

**PRAWN EXOSKELETON DERIVED CALCIUM PHOSPHATES AND
THEIR COMPOSITES FOR BONE REGENERATION**

Thesis

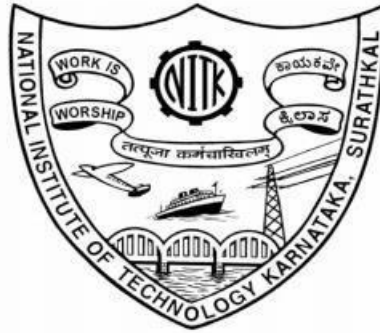
Submitted in partial fulfilment of the requirements for the degree of

DOCTOR OF PHILOSOPHY

By

PERABATHULA SATISH

(207158MT005)



**DEPARTMENT OF METALLURGICAL AND MATERIALS
ENGINEERING**

**NATIONAL INSTITUTE OF TECHNOLOGY KARNATAKA
SURATHKAL, MANGALURU – 575025**

MAY, 2024

**PRAWN EXOSKELETON DERIVED CALCIUM PHOSPHATES AND
THEIR COMPOSITES FOR BONE REGENERATION**

Thesis

Submitted in partial fulfilment of the requirements for the degree of

DOCTOR OF PHILOSOPHY

By

PERABATHULA SATISH

(207158MT005)

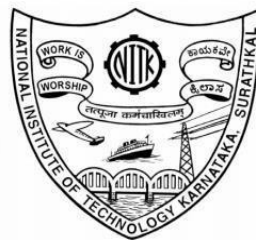
Under the guidance of

Dr. Saumen Mandal

Associate Professor

Department of Metallurgical and Materials Engineering,

NITK, Surathkal



**DEPARTMENT OF METALLURGICAL AND MATERIALS
ENGINEERING**

**NATIONAL INSTITUTE OF TECHNOLOGY KARNATAKA
SURATHKAL, MANGALURU – 575025**

DECLARATION

I hereby *declare* that the Research Thesis entitled “**Prawn exoskeleton derived calcium phosphates and their composites for bone regeneration**” which is being submitted to the National Institute of Technology Karnataka, Surathkal in partial fulfillment of the requirements for the award of the Degree of Doctor of Philosophy in the Department of Metallurgical and Materials Engineering, is a *bonafide report of the research work carried out by me*. The material contained in this Research Thesis has not been submitted to any University or Institution for the award of any degree.



Name: PERABATHULA SATISH

Register Number: 207158MT005

Department of Metallurgical and Materials Engineering

Place: NITK Surathkal

Date: 08-05-2024

CERTIFICATE

This is to certify that the Research Thesis entitled “**Prawn exoskeleton derived calcium phosphates and their composites for bone regeneration**” submitted by Mr. Perabathula Satish (Register Number: 207158MT005) as the record of the research work carried out by him, is *accepted as the Research Thesis submission* in partial fulfillment of the requirements for the award of degree of Doctor of Philosophy.

Research supervisor



Dr. Saumen Mandal

Associate Professor

Department of Metallurgical and Materials Engineering

NITK Surathkal



Chairman- DRPC

Chairman - DRPC
Dept. of Metallurgical and Materials Engineering
National Institute of Technology Karnataka, Surathkal
Post Srinivasnagar, Mangaluru - 575 025
Karnataka, India

**DEDICATED TO
THE ALMIGHTY GOD.....**

ACKNOWLEDGEMENTS

I express my sincere thanks to the almighty whose divine intervention was instrumental in the proceedings of this work. I express my sincere gratitude to my wife, parents and family for their constant and encouraging support throughout my doctoral study.

My sincere, graceful acknowledgement to my research supervisor Dr. Saumen Mandal, Associate Professor, Department of Metallurgical and Materials Engineering, National Institute of Technology Karnataka, Surathkal for his valuable guidance, support and help throughout the research. It has been an honor to be his Ph.D. student. I heartily thank him for his kindness, valuable suggestions, and constant encouragement, which I received during tough times in the Ph.D. pursuit. His constant guidance, cooperation and moral support has always kept me going ahead. The research work presented here would have been impossible without support and guidance of my supervisor. I would also like to thank his family members for their relentless love, care, and support they showered on me as part of their family.

I would like to thank Dr. Kumkum Banerjee, Head of the Department, Metallurgical and Materials Engineering, National Institute of Technology Karnataka, Surathkal for the constant encouragement and support. I would like to take this opportunity to thank members of my research programme assessment committee (RPAC), Dr. Preetham Kumar G.V., Dept. of Metallurgical and Materials Engineering and Dr. Somasekhara Rao Todeti, Dept. of Mechanical Engineering, National Institute of Technology Karnataka, Surathkal for their valuable suggestions and the comments during the progress and pre-synopsis seminars. I also express my sincere thanks to Dr. Ravishankar K.S., Ex-Head of the department, Department of Metallurgical and Materials Engineering, for the constant encouragement and support.

I am obliged to Ministry of Human Resource Development (MHRD), New Delhi, and NITK for their financial assistance to conduct my research work in the form of contingency and for the research fellowship. I would like to sincerely thank the Department of Metallurgical and Materials Engineering, National Institute of Technology Karnataka, Surathkal, for providing the labs and research facilities. I would like to thank Centre for Nano Science and Engineering (CeNSE), Indian Institute of Science, Bengaluru, and Material Research Centre, MNIT Jaipur, and Central Research Facility, National Institute of Technology Karnataka, Surathkal for

providing research facilities. I also express my sincere thanks to all research colleagues of NITK Surathkal for their constant help and support and fruitful discussions on concepts.

I express deep and sincere thanks to Dr. Komalakrushna Hadagalli, Dr. Ashritha Salian, Dr. Robbi Vivek Vardhan, Mr. Lakkimsetti Lakshmi Praveen, Mr. Mahin Saif Nowl, Mr. Vishal Gautam, Mr. Sandeep Singh, Mr. Rahul, Mr. Akhil, Ms. Ambili, Mr. Shilajit Das, Mr. Darshan, for their constant support throughout my research work.

I am thankful to all teaching and non-teaching staff of the Dept. of Metallurgical and Materials Engineering, National Institute of Technology Karnataka, Surathkal for constant support and help in various aspects of my course. Special thanks to Mrs. Sharmila Dinesh for helping me in necessary documentation at various stages of Ph.D.

The dissertation must surely bear the imprint of the prayers, sacrifices made, love, and affection showered on me by my family members. A very special thanks to my wife Mrs. Lalitha, my daughter Ms. Evangeline, my father Mr. P.T.V.S.Naidu, my mother Mrs. Ammaji, my father in law Mr. Eswararao, my mother in law Mrs. Padma who supported me throughout my life and during this study. I also express my sincere gratitude to Pastor Samuel Raju, Pastor Hosanna, Pastor Prasad Paul and all my church members for their constant prayers during my reseach. I am grateful to myparents, friends and relatives for their care and love.

Finally, I thank all my friends, well-wishers, and anonymous souls for their love and regards, prayers and wishes, that directly and indirectly helped me for completing this research work.

PERABATHULA SATISH

Abstract

In the present study, various calcium phosphates like hydroxyapatite (HA), biphasic calcium phosphates (BCP) and β -tri calcium phosphate (β -TCP) were synthesized from prawn (*Fenneropenaeus Indicus*) exoskeleton powder. The obtained calcium phosphates were investigated using X-ray diffraction (XRD), Fourier transform infrared spectroscopy (FTIR), Raman spectroscopy, X-ray photo electron spectroscopy (XPS), scanning electron microscopy (SEM), differential scanning calorimetry (DSC) and thermo gravimetric analysis (TGA). The calcination temperature of 723 °C was appropriate for the thermal decomposition of calcite to calcium oxide (CaO). Hydroxyapatite and biphasic calcium phosphates are derived from prawn shell biowaste through a wet chemical treatment of CaO. Hydroxyapatite dense scaffolds sintered at 1100 °C showed compressive strength of 26.5 MPa. In biphasic calcium phosphates, the specimens sintered at 1100 °C showed the compression strength of 56.8 MPa. X-ray diffraction (XRD) pattern revealed the phase-pure crystalline rhombohedral crystal structure of β -TCP with an average crystallite size of ~25.8 nm, prepared at 1100 °C through solid state reaction approach with Ca:P ratio of 1.5. Furthermore, the SEM and EDS opened up well-sintered uniaxial grains and the presence of trace elements like Fe, Mg, Si, and Na. A major objective of this work is to explore the mechanical properties of calcium phosphates and their composites with clay. In this study, a cost-effective method to prepare HA-clay composite was demonstrated via the mechanical mixing method, where kaolin and bentonite were used, because of their biocompatibility. Addition of 20 % kaolin to HA enhanced the compressive strength by 33.7 % and addition of 30 % bentonite to HA enhanced the compressive strength by 6 times when compared with bare HA.

Keywords: Prawn shell, hydroxyapatite, tricalcium phosphate, compression strength, sintering, clay, composite.

CONTENTS

CHAPTER 1	1
INTRODUCTION	1
CHAPTER 2	5
LITERATURE REVIEW	5
2.1 Introduction.....	5
2.2 Bioceramics	7
2.3 Calcium phosphate materials	8
2.3.1 Hydroxyapatite	9
2.3.2 Tricalcium phosphate	11
2.3.3 Octacalcium phosphate	12
2.3.4 Amorphous calcium phosphate	13
2.3.5 Dicalcium phosphate anhydrous	14
2.3.6 Dibasic calcium phosphate dihydrate	14
2.3.7 Fluorapatite	14
2.3.8 Tetracalcium phosphate	15
2.4 Requirements of calcium phosphates for medical applications	17
2.5 Bone structure and its properties	18
2.6 Marine resources	21
2.6.1 Marine benthos availability	22
2.6.2 Marine resource based minerals.....	24
2.6.3 Conversion of marine resources to biocompatible Bioceramics	27
2.7 Hydroxyapatite based Bioceramics	31
2.7.1 Synthesis methods of HA	32
2.7.1.1 Dry methods	33
2.7.1.2 Wet methods	33
2.7.1.3 High temperature methods	36
2.7.1.4 Biogenic synthesis	37
2.8 β -TCP based bioceramics	59

2.8.1 Synthesis methods	60
2.8.1.1 Solid state reaction	60
2.8.1.2 Thermal conversion	60
2.8.1.3 Precipitation	61
2.9 Biphasic calcium phosphates	62
2.9.1 Synthesis methods	63
2.10 Clay minerals.....	64
2.10.1 Types of clay	66
2.10.1.1 Type 1:1 clay mineral	67
2.10.1.2 Type 2:1 clay mineral	68
2.10.1.3 Type 2:1:1 clay mineral	71
2.10.2 Structural characteristics of clay	72
2.10.3 Formation of clay minerals	74
2.10.4 Physical and chemical properties of clay minerals	75
2.10.5 Applications of clay	76
2.11 Kaolin clay minerals	78
2.12 Bentonite clay	79
2.13 Structure of prawn exoskeleton	80
2.14 Scope and objectives of the study.....	81
CHAPTER 3	82
SYNTHESIS AND CHARACTERIZATION OF PURE HYDROXYAPATITE FROM PRAWN SHELL EXOSKELETON BIO WASTE	82
3.1 Introduction	82
3.2 Experimental procedure	83
3.2.1 Materials	83
3.2.2 Synthesis of pure hydroxyapatite	83
3.2.3 Development of dense hydroxyapatite	84
3.2.4 Characterization	84
3.2.5 In-vitro biodegradation study	86
3.3 Results and discussion	86

3.3.1 Structural analysis	86
3.3.2 Thermal analysis	88
3.3.3 Vibrational analysis	89
3.3.4 Morphological analysis	90
3.3.5 XPS analysis	91
3.3.6 Biodegradation study of HA scaffolds	93
3.4 Conclusion	93
CHAPTER 4	95
SYNTHESIS AND CHARACTERIZATION OF β-TRI CALCIUM PHOSPHATE	95
4.1 Introduction	95
4.2 Experimental procedure	97
4.2.1 Materials	97
4.2.2 Preparation of β -TCP powder from the prawn shells	97
4.2.3 Characterization	98
4.3 Results and discussion	99
4.3.1 Structural analysis.....	99
4.3.2 Microstructural and elemental analysis	100
4.3.3 Vibrational spectroscopic analysis	106
4.3.4 Thermal analysis	108
4.3.5 XPS analysis	109
4.3.6 Mechanical and physical properties	110
4.3.7 Biodegradation study	111
4.4 Conclusion	112
CHAPTER 5	115
SYNTHESIS AND CHARACTERIZATION OF BIPHASIC CALCIUM PHOSPHATES	115
5.1 Introduction	115
5.2 Experimental procedure	117
5.2.1 Materials	117

5.2.2 Preparation of biphasic calcium phosphate powder from prawn shells ...	117
5.2.3 Preparation of sintered specimens for compressive testing	118
5.2.4 Characterization	118
5.3 Results and discussion	119
5.4 Conclusion	127
CHAPTER 6	129
DEVELOPMENT OF HA-KAOLINITE COMPOSITE FOR BONE	
REGENERATION	129
6.1 Introduction	129
6.2 Materials and methods	132
6.2.1 Materials	132
6.2.2 Preparation of hydroxyapatite clay composite from the prawn shells ...	132
6.2.3 Characterization tools	133
6.3 Results and discussion	134
6.3.1 Structural and vibrational analysis	134
6.3.2 Thermal analysis	138
6.3.3 Morphological analysis	140
6.3.4 Mechanical and physical properties	141
6.4 Conclusion	143
CHAPTER 7	145
DEVELOPMENT OF HA-BENTONITE COMPOSITE FOR BONE	
REGENERATION	145
7.1 Introduction	145
7.2 Materials and methods	146
7.2.1 Materials	146
7.2.2 Preparation of hydroxyapatite bentonite clay composite from the prawn shells	146
7.2.3 Characterization tools	147
7.3 Results and discussion	148
7.3.1 Structural and vibrational analysis	148
7.3.2 Thermal analysis	151

7.3.3 Morphological analysis	153
7.3.4 Mechanical and physical properties	155
7.4 Conclusion	156
CHAPTER 8	159
CONCLUSIONS	159
8.1 Scope for future work	161
APPENDIX	163
REFERENCES	165
LIST OF PUBLICATIONS	197
LIST OF CONFERENCE PRESENTATIONS	197
BIODATA	199

NOMENCLATURE

HA	:	Hydroxyapatite
TCP	:	Tricalcium phosphate
OCP	:	Octacalcium phosphate
ACP	:	Amorphous calcium phosphate
DCPA	:	Dicalcium phosphate anhydrous
FA	:	Fluorapatite
TTCP	:	Tetracalcium phosphate
DCPD	:	Dibasic calcium phosphate dihydrate
XRD	:	X- ray diffraction
SEM	:	Scanning electron microscopy
XPS	:	X-ray photoelectron spectroscopy
EDS	:	Energy-dispersive X-ray spectroscopy
TGA	:	Thermo-gravimetric analysis
DSC	:	Differential scanning calorimetry
FTIR	:	Fourier transform infrared spectroscopy
RT	:	Room temperature
A.D.	:	Apparent density
B.D.	:	Bulk density
D	:	Dry weight
I	:	Immersed weight
S	:	Soaked weight

CHAPTER 1

INTRODUCTION

Calcium phosphates (CaP) represent the inorganic portion of major normal (bones and teeth) and pathological (i.e., those arising from different diseases) calcified tissues in mammals. Calcium phosphates comprises three primary chemical elements namely calcium (oxidation state +2), phosphorous (oxidation state +5) and oxygen (reduction state -2). The surface of our planet is abundant with these three chemical elements. The most common chemical element on Earth's surface is oxygen (47 mass%), followed by calcium (3.3–3.4 mass%) in fifth place and phosphorus (0.08–0.12 mass%) in the first twenty most common chemical elements on Earth (Dorozhkin 2009). The phrase "calcium phosphate" describes a group of substances and minerals that include both inorganic phosphate ($[\text{PO}_4]^{3-}$) anions and calcium ions (Ca^{2+}). The chemical composition of numerous calcium phosphates include hydrogen either as an acidic phosphate anion or as incorporated water. Variety of calcium phosphates are available with multiple combinations of oxides of phosphorous and calcium. The complete structure of calcium phosphates is stabilized by a network of phosphate groups, forming the foundation of its atomic arrangement. All mammalian calcified tissues primarily consist of biological calcium phosphates, while natural calcium phosphates serve as the main raw materials for phosphorus-containing fertilizers (Jeong et al. 2019). However, the chemical synthesis of calcium phosphates has shown toxicity towards normal and healthy cells. As a result, biogenic synthesis from marine and animal sources is viewed as the next-generation biomaterial, owing to its biocompatibility facilitated by mineral ion presence and substantial porous architecture, along with its bone-bonding capability.

Many calcium phosphates have exceptional biocompatibility and bioactivity because of their strong chemical resemblance to biologically calcified tissues (Canillas et al. 2017). This characteristic is often used by material scientists to create artificial bone grafts that are either surface-coated or fully composed of the physiologically appropriate calcium phosphates. For example, calcium phosphate-based self-setting hydraulic cements are beneficial for bone restoration, while titanium substitutes coated

with calcium phosphates are utilized for hip joint endoprostheses and as tooth substitutes (Lukina et al. 2023). Calcium phosphates are of particular interest in a number of interdisciplinary scientific domains, such as biology, geology, chemistry, and medicine. Bioceramics that are based on calcium phosphate and mostly consist of tricalcium phosphate or hydroxyapatite (HA) are the most similar to the minerals present in bone (Eliaz and Metoki 2017). Because of this, calcium phosphates have exceptional osteoconductivity, biocompatibility, and biodegradability (Hou et al. 2022). The ability of calcium phosphates to create molecular interactions with the surrounding tissues that lead to the surface deposition of an apatite layer is what gives them their osteoconductivity. When compared to calcium sulphates, these calcium phosphate-based bone graft alternatives degrade more slowly (Fernandez de Grado et al. 2018). Different calcium phosphates show different degradation rates, for example hydroxyapatite (HA) degrade slowly when compared with tricalcium phosphates (Stastny et al. 2019).

Calcium phosphates are plentiful in both living organisms and nature. The most significant inorganic component of biological hard tissues is calcium phosphate. They are found in tendons, teeth, and bone as carbonated hydroxyapatite (HA), which gives these tissues hardness and stability (Yu and Wei 2021). Geologically, calcium phosphates are found in different areas mainly as deposits of apatites (mostly as fluorapatite, FA) or phosphorites (sedimentary rock) under extreme conditions of temperature and pressure. Conversely biologically formed calcium phosphates are generally nano crystals that are precipitated under ambient pressure and near room temperature (Degli Esposti et al. 2020). The world deposits of calcium phosphates are estimated to be more than 150 billion tons out of 85% are phosphorites and remaining 15% are apatites (Dorozhkin 2009). Most of the natural calcium phosphates occur as smaller polycrystalline structures. Larger crystals are rarely available. The crystal structure of apatites usually have hexagonal or monoclinic system (Ptáček 2016). Because apatite is easily substituted with other atoms, a variety of compositions can be made with this mineral.

As calcium phosphates are found in vertebrates, including humans, they are especially significant in biomedicine since many diseases emerge from abnormalities

in the skeletal or dental systems (i.e., the bone or teeth). Additionally, it should be emphasized that while the existence of calcium phosphate in these hard tissues is essential for survival, there are times when the minerals in calcium phosphate crystallize erratically in undesirable places. For example, a solid mixture of cholesterol and calcium phosphate causes atherosclerosis, which blocks blood vessels. This phenomenon is called ectopic mineralization or pathological crystallization. Nowadays, biomaterials and bio ceramics based on calcium phosphate are utilized in many different bodily functions, encompassing every part of the skeleton. Applications include orthopedics, dental implants, cranio-maxillofacial reconstruction, otolaryngology, complete joint replacement (bone augmentation), spinal surgery and periodontal therapy (Al-Shalawi et al. 2023). Various calcium phosphates can be utilized based on the desired characteristics, whether it be bioresorbable or bioactive. The major driving force for utilizing calcium phosphates as bone substitute materials is their chemical resemblance to the mineral found in mammalian teeth and bones. Because of this, they are not only non-toxic but also biocompatible, do not cause the body to perceive them as alien substances, and most importantly show bioactive behavior and integrate into live tissue through the same mechanisms that remodel healthy bone. As a result, the implants and bone form a close physicochemical bond known as osteointegration (Parithimarkalaignan and Padmanabhan 2013).

In the creation of practical biomaterials for implant fabrication, calcium phosphates with therapeutic applications represent an intriguing area of study and development. Bioceramics in biomaterials play a vital role in replacing numerous parts of the human body. There are two broad categories into which bio ceramic materials can be divided: bioactive and bioinert. Bioinert ceramics are those which have no influence on the surrounding living tissue and the best example would be alumina. Whereas bioactive ceramics are those which can able to bond with surrounding living tissues. Various calcium phosphates and ceramic glasses exhibit this bioactive feature. Three types of calcium phosphates are developed from prawn shell exoskeleton via wet chemical synthesis technique and solid-state sintering. The first type of calcium phosphate developed was hydroxyapatite, the second system was biphasic calcium phosphates and the third was β -tri calcium phosphate. The current thesis is not only

restricted to calcium phosphates derived from prawn shell but also its composites with different types of clay namely bentonite and kaolin. The thesis flow is explained in the subsequent paragraph.

CHAPTER 1 of the thesis introduces the concepts of the present studies. **CHAPTER 2** is dedicated to the literature review in the current area of research. **CHAPTER 3** is devoted to the synthesis and characterization of prawn shell derived phase pure hydroxyapatite. **CHAPTER 4** is assigned to the synthesis and characterization of β -tricalcium phosphate. **CHAPTER 5** is allocated to the synthesis and characterization of biphasic calcium phosphates. **CHAPTER 6** is allocated to the development of hydroxyapatite kaolin composites and their characterization. **CHAPTER 7** is allotted to the development of hydroxyapatite bentonite composites and their characterization. Finally, **CHAPTER 8** is devoted to the conclusion and future scope of the existing studies.

CHAPTER 2

LITERATURE REVIEW

2.1 Introduction

Biomaterials, which include metal alloys, ceramics and composites have seen significant advancement in the recent few decades. Novel materials are being investigated for different medical applications to enhance human life quality. In medical applications, biomaterials are frequently employed to supplement or replace a natural function. The domain of biomaterials necessitates the integration of expertise from disparate scientific and technological fields to ensure that the material functions suitably in a living body. Because of this, biomaterials seem to be a prime example of a truly multi-disciplinary field, where the material crafted by materials scientists and engineers must be validated and carry out its function within the human body under the supervision of biologists and physicians, and where all interrelated research must coordinate and analyze the final product. Understanding of material science, chemistry and engineering appears to be crucial for biomaterials since they deal with every facet of material creation and processing (Chen and Liu 2016). However, as the primary application of biomaterials is in clinical implantology, the biological sciences take center stage in the study. These encompass histology, anatomy, physiology, and cell and molecular biology (Lam and Wu 2012). Following the identification of a specific need, a procedure is initiated. Because numerous phases need to be confirmed, including material synthesis, prosthesis design and production, multiple material tests, and biomedical evaluation, the entire process looks to be somewhat lengthy. The ultimate goal is to accomplish the proper physiologic fusion of artificial grafts with host tissues. Lastly, a prospective biomaterial needs to meet all regulatory standards (Schuh and Funk 2019).

Biomaterials are employed in various applications across the body, interfacing with biological systems *in vivo* to assess, treat, augment, or substitute any organ, tissue or function of the body (Todros et al. 2021). Biomaterials, therefore, are

exclusively related to the healthcare industry and necessitate an interface with tissues or tissue constituents. It is important to emphasize that while the skin serves as a protective barrier between the body and the outside world, any artificial materials that come into direct contact with the skin such as wearing prosthetic limbs and hearing aids do not fall under the category of biomaterials. The ability of biomaterials to persist in a biological environment without causing harm to themselves or their surroundings is the primary distinction between them and other types of materials (Huzum et al. 2021). Most of the biomaterials that are available today are solid materials. They fall into four main categories based on their composition and nature: biometals, bioceramics, biopolymers and biocomposites. The use of a particular biomaterial is determined by its composition, structure, material characteristics and ability to initiate the desired *in vivo* reactions in order to carry out a given function. Moreover, for utilizing biomaterials in medical field, researchers must also prioritize considerations such as biocompatibility, bioresorbability and toxicity (Maloo et al. 2022; Park et al. 2023). Tissue engineering requires biomaterials as a fundamental component. In order to promote cell proliferation and eventual tissue regeneration, they are made to offer an architectural framework similar to the extracellular matrix seen in real tissues (Lee et al. 2014). Different properties required for a biomaterial to be used in biomedical applications is summarized in Figure 2.1

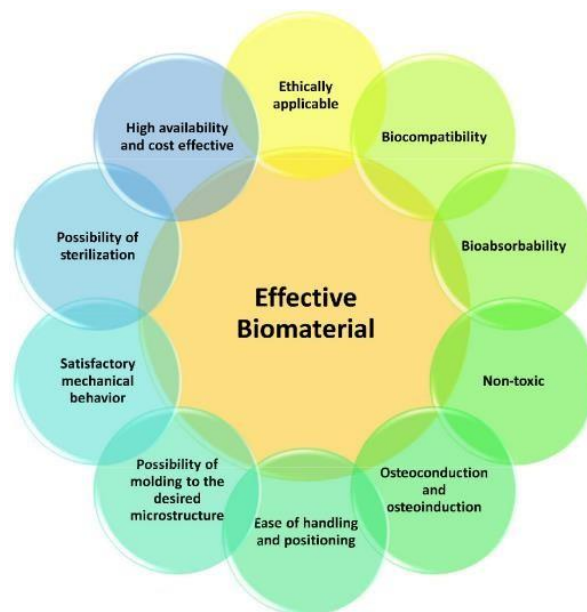


Fig. 2.1 Properties required for an effective biomaterial (Vaiani et al. 2023)

2.2 Bioceramics

Bioceramics encompass a variety of ceramics that are purposefully engineered and crafted to address the repair and reconstruction needs of diseased, damaged, or depleted parts of the body. Various types of bioceramics include silica, alumina, glass ceramic, zirconia, titanium dioxide, bioactive glass and calcium phosphate. Both dense and porous bioceramics have been widely utilized in biomedical applications (Prakasam et al. 2015). Bioceramics are categorized as either bioinert or bioactive based on how they attach to the tissue, particularly bone. Alumina (Al_2O_3) and zirconia (Zr_2O_3) are bioinert ceramics that are commonly employed in both dental and orthopaedic applications. Bioactive ceramics are either of biogenic or synthetic origin. Biogenic origin includes: natural coral, coral transformed to hydroxyapatite, apatite from bovine bone etc.. Entirely synthetic materials comprise specially formulated glasses (silica-based or phosphate based), calcium sulfate (plaster of Paris) and different types of calcium phosphates (CaP). Bioceramics have positive interactions with human tissues, which makes them useful in many biomedical applications. These include stabilisation and augmentation of the jaw bones, spinal fusion, replacements for teeth, ligaments, hips, knees and tendons, maxillofacial reconstruction, rectifying diseased periodontium, and serving as temporary bone space fillers post tumour excision. They can also be used as thromboresistant carbon coatings in prosthetic heart valves (Roy and Lee 2007)

Bioceramics are unique among biomaterials, as they have a unique combination of properties that set them apart from other biomaterials like metals or polymers. These properties include: (i) high intrinsic strength—materials like zirconia and alumina exhibit good mechanical properties like low coefficient of friction and high wear resistance, making them suitable for use in high-stress applications like dental implants or artificial joints; (ii) biocompatibility— bioceramics typically exhibit compatibility with human tissues, thereby mitigating the risk of adverse reactions or inflammation; certain bioceramics, like hydroxyapatite or bioactive glasses, in particular, exhibit bioactive behaviours that can encourage tissue regeneration and osteointegration; (iii) Versatility: Bioceramics can be composed to improve particular qualities and modelled to exact shapes. Because of all these advantages, bioceramics can be used to solve a wide range of biomedical problems. With regard to their use as

load-bearing components, fillers, joint replacements, drug-delivery platforms, veneering materials and biomimetic scaffolds, among other important uses in medicine and biotechnology, research on ceramic biomaterials is expanding quickly (Jitaru et al. 2016).

2.3 Calcium phosphate materials

Since the majority of the inorganic constituents found in human bones are calcium and phosphorous compounds, calcium phosphates are generally considered as the most crucial substances that have been thoroughly studied in bone tissue engineering (Hong et al. 2022). Calcium phosphates occupy an important position in bone repair because of their resemblance to natural bone tissue. Synthetic calcium phosphates are the most extensively used biomaterials for the repair and restoration of bone tissue defects because of their many good qualities which include bioactivity, biocompatibility, nontoxicity, osteoconductivity and nonimmunogenicity (Al-Sanabani et al. 2013). The solid tissues of human body naturally produce calcium phosphate ceramics through a process called biomineralization (Díaz-Cuenca et al. 2022). Artificial materials derived from calcium phosphates should have the best possible chemical and physiological characteristics in terms of biocompatibility. Biological calcium phosphates possess unique qualities such as low crystallinity, high substitution of compositional elements, and very small crystallite size, often closely associated with developing protein matrix.

The extraordinary functional characteristics of mineralized tissues are intimately associated with these distinguishing features. Progression of the synthesis and performance of bioceramics appears to be dependent on investigating novel pathways and procedures to produce biomimetic ceramics and composites derived from calcium phosphates. The physical and chemical characteristics of CaP materials, such as their solubility, stability, and mechanical strength, are strongly linked to their osteoconductivity and osteoinductivity and are contingent upon the species of the CaP materials (Tang et al. 2018). Thus, while creating biomaterials for use in bone regeneration, it is crucial to choose a specific type of CaP biomaterial based on its unique features. Numerous CaP biomaterials have been employed in biological research

and bone regeneration including hydroxyapatite (HA), tricalcium phosphate (TCP), octacalcium phosphate (OCP), amorphous calcium phosphate (ACP), dicalcium phosphate anhydrous (DCPA), fluorapatite (FA), tetracalcium phosphate (TTCP), dibasic calcium phosphate dihydrate (DCPD). In biological systems, several calcium phosphates do not occur naturally. They are mostly present in skeletal structures as weakly crystallized, calcium-deficient apatite. Solubility of the CaP phases is principally determined by their chemical composition, crystallographic characteristics, and the existence of cationic or anionic substitutions inside the apatite lattice (Mishchenko et al. 2023).

2.3.1 Hydroxyapatite (HA)

Hydroxyapatite (HA, $\text{Ca}_{10}(\text{PO}_4)_6(\text{OH})_2$) is an important member of the calcium apatite family. Both in terms of chemical composition and structure, it remarkably matches the structure of natural bone. In particular, for bone tissue engineering, hydroxyapatite is one of the most used biomaterials. Approximately 67 weight percent of natural bone and teeth are made up of HA. Due to its bioactive and biocompatible properties, HA has been used frequently as an implant material in the repair and regeneration of bone tissue (Basu 2017). Because of its bioactivity, HA is mostly employed for bone regeneration and various bone repairs as well as coatings on metallic artificial devices to improve their biological qualities (Tripathi and Basu 2012). Compared to other calcium phosphates, HA is the most thermally stable compound under physiological conditions (Basu 2017). Among all calcium phosphate materials, HA is second only to fluorapatite (FA) in terms of stability and insolubility (Hou et al. 2022). HA can be artificially synthesized or naturally formed. Naturally formed HA has hexagonal crystal structure and usually contain defects that can be filled by other ions. However, specific synthesis conditions may affect structural defects in synthesized HA. Synthesized HA may have two crystal structures namely monoclinic and hexagonal. When the temperature is more than 250 °C monoclinic crystal structure changes to hexagonal (Rangavittal et al. 2000). Because of its great stability, the hexagonal crystal structure of HA is the most common phase encountered in the biological environment. HA is thought to be the most stable phase of CaP after fluorapatite. In contrast, the other CaP phases in bone, such as amorphous calcium phosphate and octacalcium phosphate

are precursors or sub-precursors of HA, which changes into HA under high pH in aqueous or *in-vivo* conditions. Several CaPs typically undergo phase transformations under various circumstances. The physical, chemical and biological characteristics of HA substantially change with the Ca/P ratio and the replacement of ions in HA crystal structure. The defects of HA crystal structure can be replaced with Mg^{2+} , Sr^{2+} , Cl^- , F^- , CO_3^{2-} and other ions. The size and density of HA nanoparticles, which contribute to the unique mechanical characteristics of bones, may change as a result of Mg^{2+} replacement. Moreover, Mg^{2+} inhibits the crystallization of HA, which leads to the creation of more apatite nuclei and fewer big crystals. Stability can be increased by replacing F^- ions, and biological activity is increased by Mg^{2+} when compared to pure HA. Numerous studies have demonstrated that Mg^{2+} can affect bone metabolism, control osteoblast and osteoclast activity, and promote the formation of new bone. As a result, research has been done on artificially replaced magnesium in HA in various forms, and the results have shown enhanced bioactivity.

Since the 1980s, HA has been utilized clinically in bone regeneration in the form of implants and coatings on implants. HA has good bioactivity, biocompatibility and osteoconductive qualities. The surface of HA can serve as a nucleation site for the onset of biomineralization when Ca^{2+} and PO_4^{3-} ions are present. As a result, HA is frequently utilized in dental surgery, maxillofacial repair, long bone defects, bone nonunion, and spinal fusion operation. Coating the surfaces of metal implants with HA improves their biocompatibility, osseointegration, and bioactivity by increasing the contact area of bone and cell adhesion characteristics.

HA is chemically stable but has poor mechanical properties. Therefore, HA cannot be used as a load bearing implant and can be usually implanted as granules and porous scaffolds. Still, it is a huge challenge to enhance the mechanical properties of HA. Metal oxides include alumina, titania and zirconia are the common reinforcing agents. However, the use of these reinforcing agents, which are either bioinert or non-biodegradable, compromises the biocompatibility and biodegradation features of HA-based biomaterials. HA can be mixed with polymers to improve its mechanical properties. Natural polymers such as gelatin, chitosan, silk fibroin and hyaluronic acid are commonly used to fabricate hybrid scaffolds. It is important to note that hardness,

wear resistance and friction coefficient of dense HA are comparable to those of naturally occurring mineralized tissues. HA has good bioactivity, biocompatibility and possess good osteoconductivity but poor osteoinductivity. Therefore, HA can be combined with other materials to enhance its osteoinductivity.

2.3.2 Tricalcium phosphate (TCP)

TCP, a calcium phosphate substance that has been extensively researched, is composed of two crystalline phases namely α -TCP and β -TCP. β -TCP crystallizes in rhombohedral system, whereas α -TCP crystallizes in monoclinic system. The chemical formula of TCP is $\text{Ca}_3(\text{PO}_4)_2$ and Ca/P ratio is 1.5. As pure crystalline α -TCP is far less soluble than β -TCP, it cannot precipitate in aqueous solutions. The three methods for producing β -TCP are precipitation, thermal conversion, and solid-state reaction. Typically, the process of producing crystalline β -TCP involves heating calcium deficient hydroxyapatite (CDHA) to approximately 800 °C. Additionally, solid-state interaction between acidic CaP and CaO is another method. Furthermore, research has demonstrated that β -TCP precipitates in organic solutions, including methanol, ethylene glycol, ethyl propionate and tetrahydrofuran. Tang et al. synthesized β -TCP in organic solvents (e.g., ethylene glycol) at a comparatively low temperature around 150 °C. Furthermore, at temperatures above 1125 °C, β -TCP changes into α -TCP, so α -TCP can be thought of as the high-temperature phase of β -TCP. Although β -TCP and α -TCP have the similar chemical composition, they diverge in their crystal structure and solubility.

TCP has good stability and can be kept for a long time at room temperature in a dry atmosphere. Mg-stabilized β -TCP (Whitlockite) has been detected in renal stones, arthritic cartilage, and dental calculus formation during pathological calcification. But β -TCP is not found in bone, dentin, or enamel. Biological calcifications never contain α -TCP. Density functional analysis found that β -TCP exhibits greater stability than α -TCP. α -TCP is more reactive and has a higher specific energy in an aqueous solution than β -TCP and can be hydrolyzed to CDHA. When it comes to clinical applications, β -TCP is more osteoconductive and osteoinductive than HA and is mainly utilized in bone cements and bioceramics, whereas α -TCP is typically found in cements due to its

phase conversion to HA upon contact with water. It is noteworthy that there exists an imbalance between the processes of bone development and scaffold degradation due to the faster rate of resorption of pure α -TCP than that of new bone creation. Thus, α -TCP is typically utilized in conjunction with other CaP materials as a component of CaP cements. β -TCP, on the other hand, has a comparatively lower rate of resorption than α -TCP and makes it as a promising candidate for use in bone regeneration.

2.3.3 Octacalcium phosphate (OCP)

There is a great biological importance to OCP as it is one of the major stable components of human urinary and dental calculi. OCP plays a vital role in the *in vivo* formation of apatitic biominerals. OCP crystallizes in triclinic system and its Ca/P ratio is 1.33. Together with ACP and DCPD, OCP is a precursor to HA crystal formation, and is crucial for the formation and biomineralization of bone. Although OCP is hydrolyzed to HA it is more unstable than HA. The exact process underlying OCP hydrolysis remains unclear. Two hypotheses, namely ion diffusion-crystallization conversion and dissolution-reprecipitation mechanism are suggested to explain the hydrolysis mechanism of OCP. Under both *in vitro* and *in vivo* conditions, the transformation of OCP was observed. When the mixture of OCP and HA is placed in water with an initial pH of 7.2, the structural transition is observed after 1 h and 12 h. In six hours, the OCP was fully hydrolyzed to CDHA in deionized water. The transformation rate is affected by pH as well. Interestingly, under *in vivo* conditions, the hydrolysis of OCP into HA proceeds quite slowly. OCP can be used in coatings and as a component in biocomposites and selfsetting formulations. OCP coatings exhibit osteoinductive behavior. OCP has been tested for alveolar ridge enhancement as well as direct pulp capping material. Strong osteoconductivity and osteoinductivity of OCPs make it a viable material for use in bone graft materials and bone regeneration. Understanding the biological mechanism behind strong osteoinductivity of OCP, along with assessing how its microstructure and Ca/P stoichiometry influence its inherent biological activity, is imperative.

2.3.4 Amorphous calcium phosphate (ACP)

Amorphous calcium phosphates (ACP), are unique kind of CaP materials that have different chemical compositions. ACPs were first identified during the *in vitro* synthesis of HA, and as such, they were regarded as HA precursors. ACPs are categorized into two groups: low-temperature and high-temperature ACPs, according to the temperature at which they are prepared. Typically, low-temperature ACPs emerge as precursors when other CaP compounds precipitate. Since ACPs have a lower surface energy than HAs and OCPs, it is believed that ACPs originate during the beginning of precipitation. The amount of calcium and phosphate ions in an aqueous solution, as well as the pH value, determine the chemical composition of ACPs. An increase in calcium and phosphate ions concentration causes the recrystallization of ACPs. Moreover, in a reaction system with continuous stirring rate, ACPs may slowly recrystallize or change into CaP materials with high degree of crystallization, such as CDHA, particularly at higher reaction temperatures. As the pH value shifts from 6.6 to 11.7, the Ca/P ratio of amorphous calcium phosphates (ACPs) increases from 1.18 to 1.53, according to studies on the impact of pH. The chemical formula of ACP is $\text{Ca}_9(\text{PO}_4)_6$.

ACPs have outstanding biological qualities, such as osteoconductivity and biodegradability, which open up a wide range of applications. These include scaffolds for biological tissue engineering, CaP bone cements, and biomaterials for bone repair. Furthermore, the enormous specific surface area and pH-dependent degradation of the nano-sized clusters in the ACPs make them perfect drug delivery carriers for investigations pertaining to drug loading and controlled release. Ion-substituted ACPs, which are invariably composed of ions of Mg, Na, carbonate, and pyrophosphate, are identified biologically in pathological calcifications of soft tissues (such as calcifications of the heart valves in uremic patients). Amorphous calcium phosphate finds application in dental care for addressing early-stage dental decay. Its primary role lies in serving as an occluding agent, helping to alleviate sensitivity.

2.3.5 Dicalcium phosphate anhydrous (DCPA)

Dicalcium phosphates are produced when two phosphoric acid acidities are neutralized with calcium hydroxide. There are two crystalline forms: DCPA, also known as “Monetite”, and DCPD, commonly known as “Brushite” among mineralogists. The anhydrous form of DCPD is called DCPA. Compared to DCPD, it is less soluble because there is no water inclusion. It is possible to crystallize DCPA and DCPD from aqueous solutions, but only at 100 °C. DCPA does not arise in either pathological or normal calcifications, in contrast to DCPD. It is a component of toothpaste, calcium phosphate cements, and calcium and phosphate sources in dietary supplements such morning cereals.

2.3.6 Dibasic calcium phosphate dihydrate (DCPD)

The CaP compound that is easiest to synthesize is DCPD. In addition to being osteoconductive, biocompatible, and biodegradable, it can be changed into DCPA (pH < 6), OCP (pH \approx 6–7), or precipitated HA (pH >7). It is also called brushite. It has been observed that DCPD can degrade and be replaced by bone, or it can convert *in vivo* into precipitated HA. Brushite may appear as an intermediate phase in pathological calcifications which occur in slightly acidic media such as urinary calculi, dental calculi and urinary stones. In the medical field, DCPD is utilized in CaP cements and as an intermediate compound for teeth remineralization. DCPD is added together with the toothpaste for the protection of dental caries and as a polishing agent. Generally, DCPD can be derived by double decomposition between calcium and phosphorous containing solutions in mild acidic media. It can also be obtained by reaction of calcium containing salts such as CaCO₃ in acidic orthophosphate solutions. In DCPD crystals, lattice water molecules are interlayered between calcium phosphate chains that are oriented parallel to one another.

2.3.7 Fluorapatite (FA)

The least soluble phase among all the calcium phosphates is fluorapatite (FA). FA crystallizes in the same system as HA with fluoride ions substitute hydroxyl ions in the tunnels of apatite. It forms a solid phase easily, but the process of obtaining pure FA obtained through precipitation in aqueous solutions is difficult. Even in the presence

of high concentrations of fluoride ions, the formation of fluoridated hydroxyapatite (FHA) is facilitated by solid-state solutions stabilized through hydrogen bonds between fluoride and hydroxyl ions within the apatite tunnels. Whereas FA is mostly found in dental enamel, FHA is primarily found in bone tissue. For the development of the skeleton and teeth, saliva and plasma must include fluoride. It has been demonstrated that fluorine ions play a physiological role in promoting the mineralization of calcium phosphates during the formation of bone. Compared to pure HA, adding fluorine to hydroxyapatite improves the response of osteoblasts in terms of proliferation, differentiation, adhesion and mineralization processes. Osteoblast cell proliferation and differentiation is directly impacted by the quantity of fluoride ions produced. Compared to HA, FA has superior cell attachment and protein absorption.

2.3.8 Tetracalcium phosphate (TTCP)

The most basic CaP phase is tetracalcium phosphate (TTCP), which is hydrolyzed to $\text{Ca}(\text{OH})_2$ and HA over time in an aqueous solution or humid environment. TTCP is in a metastable state. TTCP, often observed as a by-product of HA plasma coating, results from the combination of TTCP, CaO, and α -TCP at high temperatures during the process. It is only possible to perform the chemical synthesis of TTCP in a hoover or dry air environment. It can be synthesized by using solid phase reaction process at above 1300 °C. When water vapour is present, TTCP decomposes into HA. TTCP bone cement comes in three varieties: polymer, multi component, and single component. TTCP is typically utilized in biological applications as a component in the creation of biological composites, self-curing bone cements, and root canal treatment. Bone cements with the stoichiometric composition of HA can be made by mixing TTCP with DCPA (Ca/P = 2.0). Biological calcifications never contain TTCP.

Table 2.1. List of calcium phosphates with their basic information

Name	Formula	Crystal structure	Ca/P ratio	Solubility at 25 °C (g/L)
HA	$\text{Ca}_{10}(\text{PO}_4)_6(\text{OH})_2$	Monoclinic/Hexagonal	1.67	~0.0003
α -TCP	$\alpha\text{-Ca}_3(\text{PO}_4)_2$	Orthorhombic	1.5	~0.0025
β -TCP	$\beta\text{-Ca}_3(\text{PO}_4)_2$	Rhombohedral	1.5	~0.0005
ACP	$\text{Ca}_x\text{H}_y(\text{PO}_4)_z \cdot n\text{H}_2\text{O}$, n = 3-4.5, 15–20 % H_2O	-	1.2-2.0	-
OCP	$\text{Ca}_8(\text{HPO}_4)_2(\text{PO}_4)_4 \cdot 5\text{H}_2\text{O}$	Triclinic	1.33	~0.0081
FA	$\text{Ca}_{10}(\text{PO}_4)_6\text{F}$	Hexagonal	1.67	~0.0002
DCPA	CaHPO_4	Triclinic	1.0	~0.048
DCPD	$\text{CaHPO}_4 \cdot 2\text{H}_2\text{O}$	Monoclinic	1.0	~0.088
TTCP	$\text{Ca}_4(\text{PO}_4)_2\text{O}$	Monoclinic	2.0	~0.0007

HA: hydroxyapatite, α -TCP: α -tricalcium phosphate, β -TCP: β -tricalcium phosphate, ACP: amorphous calcium phosphate, OCP: octacalcium phosphate, FA: fluorapatite, DCPA: dicalcium phosphate anhydrous, DCPD: dibasic calcium phosphate dihydrate, TTCP: tetracalcium phosphate. The solubility of ACP cannot be measured exactly. However, in acidic buffer the comparative solubility is $\text{ACP} \gg \alpha\text{-TCP} \gg \beta\text{-TCP} \gg \text{HA}$

2.4 Requirements of calcium phosphates for medical applications

In the medical field, calcium phosphates are frequently utilized as pastes, scaffolds, coatings, and cements. It may require a variety of properties in order to function correctly. The main mechanism driving bioactivity involves dissolution partly and subsequent outcome of ionic products *in vivo*. This process elevates the concentrations of calcium and phosphate ions in the local environment, prompting the formation of a biological apatite layer on the ceramic surface. All materials intended for medical use must be biocompatible, which means they can't cause the living system or tissue to react in any way, either locally or systemically. It has been found that all CaP ceramics are biocompatible. This is because of the widespread distribution inside the body, either by dissolved or solid form. CaPs mechanical properties are a major issue that prevents them to use in clinical applications broadly. Potential biomaterials and bioceramics of various kind must be resilient in a variety of conditions including sitting, standing, running, stretching, and climbing. Unfortunately, CaPs have low tensile stress (6 to 10 MPa), low impact resistance, and brittleness. Their porosity, which acts as preferred crack propagation initiation sites, is the primary cause of this. However, they have a relatively high compressive strength compared to regular bone. CaP is therefore either utilized as coating for dental and orthopaedic metallic implants or as non-load bearing implants, such as middle ear surgery and the filling of bone deficiencies in the skeleton and oral cavity.

Supporting cell adhesion/proliferation and cell integration in the CaP are aspects of osteoconduction and osseointegration. Primarily, cell adhesion is determined by CaPs capacity to adsorb extracellular matrix proteins, such as fibronectin. When it comes to CaPs, factors such as surface roughness, solubility, phase composition, grain size, particle size, surface charge, and surface energy all have a significant impact on this capacity. The capacity of a substance to draw in progenitor cells and encourage their differentiation into osteoblastic lineage is known as osteoinduction. Numerous investigations revealed that CaPs are osteoinductive. Osteoinduction, however, is dependent on a number of CaP characteristics. For example, the surface chemistry and charge of CaP could influence how proteins adhere to it, subsequently promoting

osteoblastic development via interactions with the cell's extracellular matrix. Physical characteristics like surface morphology can also have an impact.

Resorption refers to the process through which the bioceramic is absorbed by the body, either through dissolution or via cellular activity such as osteoclasts and macrophages. Particle size, crystallinity, porosity, and the phase content of CaP affect this ability. Some phases might undergo rapid resorption, effectively replacing the cement or coating with bone. Large variations in the solubility of various HA scaffolds can be explained by the involvement of lattice defects in the dissolution process. This characteristic is crucial since coatings and cements have the potential to give biologically desirable qualities temporarily before being replaced by new bone. In addition to the anatomic site, the recipient's age, sex, and overall metabolic status affect the pace of bone substitution. Because of these factors, the time it takes for bone to replace CaP can range from 3 to 36 months.

2.5 Bone structure and its properties

The fundamental component of the human skeleton is the bone. Bone facilitates mechanical movement, protects important organs, houses hematopoietic cells, carries the weight of the body, and maintains iron homeostasis. The complex and variable arrangement of structures in bone throughout a wide range of length scales is shown in Figure 2.2 that allows for a variety of biological, mechanical, and chemical activities. It is a complex, hierarchical, functionally graded material (FGM) that is composed of exterior cortical bone and inner cancellous bone. It is vital to comprehend the structural interconnection among the various levels of hierarchy of the bone. These four types of bone structure are as follows: (1) macrostructure, which includes cancellous vs cortical bone; (2) microstructure & sub-microstructure, which include haversian canal and osteons; (3) nanostructure, which includes fibrillar collagen; (4) sub-nanostructure, which includes molecular components of the mineral, collagen, and organic proteins. At macroscopic level, depending on their specific purpose, bones can have a variety of shapes. However, there are two general forms of bones: cancellous (also known as trabecular) bone and cortical (also known as compact) bone. Most of the bones outermost layer is composed of cortical bone. In vertebrae, they can achieve a thickness of several tenths of a millimetre, while in the mid-shaft of long bones, they

can reach several millimetres or even centimetres. The porosity of the bone is in the order of 6 %, making it fairly dense. Cancellous bone typically develops within bones that are subjected to compressive stress. About 80 % of trabecular bone is made up of pores (Figure 2.3). Trabeculae typically range in thickness from 50 to 300 μm , and their orientation is determined by the distribution of load within the bone. Young's modulus of 1 to 20 GPa and strength of 130 to 220 MPa have been reported for cortical bone, while 0.1 to 1.0 GPa of Young's modulus and 2 to 12 MPa of strength have been reported for cancellous bone (Morgan et al. 2018).

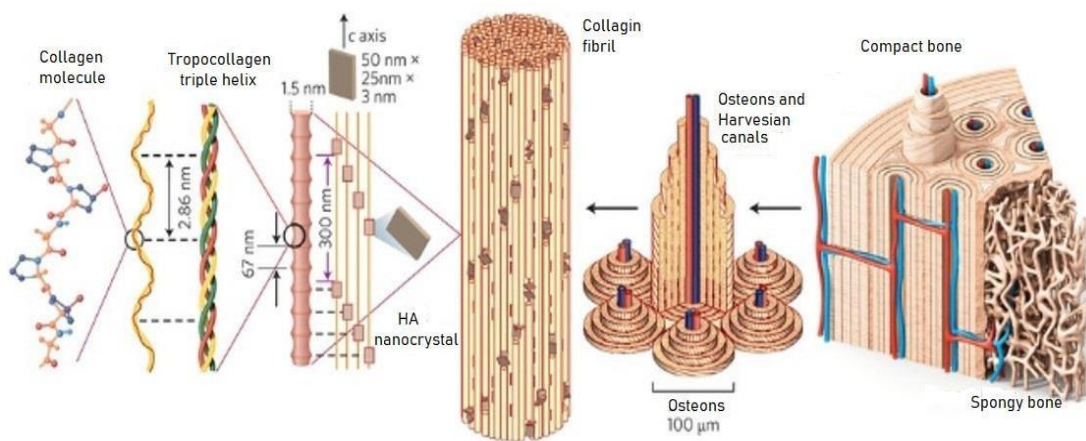


Fig. 2.2 Structural hierarchy of bone (Eliaz and Metoki 2017)

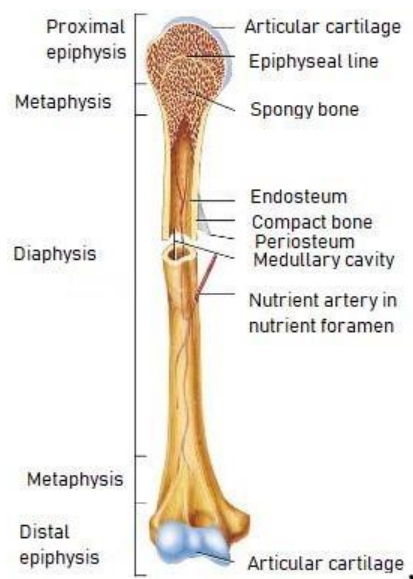


Fig. 2.3 Typical structure of long bone (Eliaz and Metoki 2017)

Mineralized collagen fibres in the microstructure of bone arrange themselves into planar structures termed lamellae, which are 3 to 7 μm wide. As demonstrated in Figure 2.2, in certain cortical bones, the lamellae create an osteon or a harversian system by wrapping in concentric layers around a central canal. The osteons have a cylinder-like appearance and generally align nearly parallel to the long axis of the bone. Woven bone refers to other types of cortical bone where no such pattern is discernible. Trabecular bone, has a distinct pattern in its microstructure. It is comparable to a fibre texture in which every mineral platelet is aligned parallel to a single direction, which corresponds to the fibre direction of collagen. This is the fundamental component that makes up bone. Collagen molecules that are 300 nm long and 1.5 nm thick are assembled to form the fibrils. Collagen is the major organic component of the matrix (type I). Osteoblasts secrete the collagen molecules, which subsequently self-assemble. The distinct crevices between the collagen fibrils are home to apatite crystals. The collagen in the fibrils restricts the crystal's ability to expand initially, making them distinct and irregular in shape. With a repeat distance of roughly 67 nm, crystals are spaced regularly along the fibrils and represent the staggered distance between neighbouring collagen molecules. It is significant to remember that the arrangement of collagen fibres and lamellae at the nanoscale improves the isotropic qualities of bone, prevents cracks from spreading, and boosts toughness.

"Biom mineralization" refers to the process of apatite formation in the extracellular area of collagen. It is crucial to remember that the procedure varies based on a number of variables, including age, location, stage (such as development or fracture healing), etc. The formation of the bone matrix is followed by a typical 13-day time period to mineralize quickly before the matrix begins. This process is known as primary mineralization and within a matter of days, the matrix will mineralize up to 70 %. Secondary mineralization is the term for the remaining 30 % of the mineral content growth that persists for several years. The majority of studies characterize bone mineral crystals as plate-like shape, although they vary widely in size; platelet thicknesses range from 1.5 to 9 nm, lengths from 15 to 200 nm, and widths from 10 to 120 nm.

The several cell types that make up bone tissue include osteoblasts, which build new bone, osteocytes, which are mature osteoblasts, osteoclasts, which resorb bone, and bone lining cells, which form a protective covering on the surface of the bone. The process of forming new bone and mineralizing existing bone involves osteoblasts and osteocytes. The chemical composition of bone consists of two phases: an inorganic phase, comprising approximately 67 %, and an organic phase, constituting roughly 33 %. Hydroxyapatite is the main component of the inorganic phase, whereas collagen (28 %) and protein (5 %), respectively, make up the organic phase as shown in Figure 2.4.

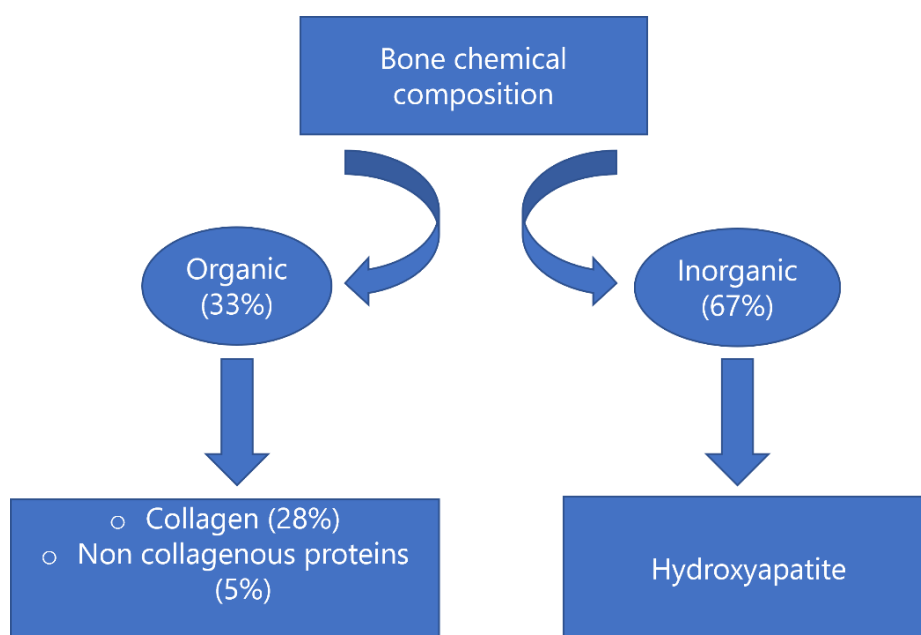


Fig. 2.4 chemical composition of human bone

2.6 Marine resources

Oceans, lakes, rivers, and other bodies of water enclose around 72 % of the planet, with 97 % of that area falling under oceans. Oceans include a wealth of food, medicine, and minerals in addition to salt water. Biomolecules derived from marine environments, including proteins, natural chemicals, etc., are becoming increasingly important in engineering and medicine. There is a significant conversion of HA due to the abundance of calcium-rich marine benthos biowaste. Marine mollusk shells, such as sea snails, nacre shells, sea coral, cuttlefish bones, etc., are among the many marine benthos. Sahin et al. reported on the synthesis of HA using raw precursors derived from

tropical sea snail shells (*Clinocardium ciliatum*) through chemical synthesis (Sahin et al. 2020). Using hotplate and ultrasonic method, Agaogullari et al. created Calcium phosphate powders, specifically CaHPO_4 and TCP, incorporating nano-sized particles from sea urchin (Ağaoğullari et al. 2012). To obtain HA, cuttlefish bones, natural calcite, and bovine bone were also utilized. HA can also be derived raw materials derived from Malaysian cockle shells (George et al. 2019).

The remains of deceased marine species were used as resources to create biocompatible hydroxyapatite. Sea snail (*trochidae infundibulum concavus*) (Tămășan et al. 2013), Sea urchins (Ağaoğullari et al. 2012), eastern oyster (*crassostrea virginica*) (Johnstone et al. 2008), sputnik sea urchin (Tămășan et al. 2013), conch shells (*strombus gigas*) (Vecchio et al. 2007), *thunnusobesus* bone (Venkatesan et al. 2011), giant clam (*tridacna gigas*) (Vecchio et al. 2007), land snail (*helix aspersa*) (Kel et al. 2011), sea snail (*cerithium vulgatum*) (Ozyegin et al. 2011), cuttlefish bone (Aminatun et al. 2019; Faksawat et al. 2015; Kim et al. 2014) and sea snail (Ozyegin et al. 2011) can be used for the synthesis of HA which can be used in biomedical engineering applications. The dorsal shield and lamellar matrix are the two types of layers found in cuttlefish bones. The lamellar matrix is preferred to synthesise hydroxyapatite due to its plentiful availability and porous nature, as opposed to the dorsal shield's dense architecture. The lamellar matrix is composed of 90 % porosity of aragonite. Biogenic CaP based bioceramics exhibit bioactive properties as they release ions upon contact with body fluids, facilitating the precipitation of apatite on their surface. This characteristic makes them suitable as scaffolds for promoting the formation of new bone tissue (Sahin et al. 2019).

2.6.1 Marine benthos availability

Benthos is the general term for the group of organisms that live on, in, or close to the seafloor. An intertidal zone, or the space between high and low tide, is characterized as a rocky shore. These intricate marine ecosystems are found along coastlines all around the world. Numerous creatures, including barnacles, sea snails, sea anemones, isopods, sea stars, mussels, sea crabs, limpets, and chitons, can be found there due to the availability of nutrients and oxygen as shown in Figure 2.5.

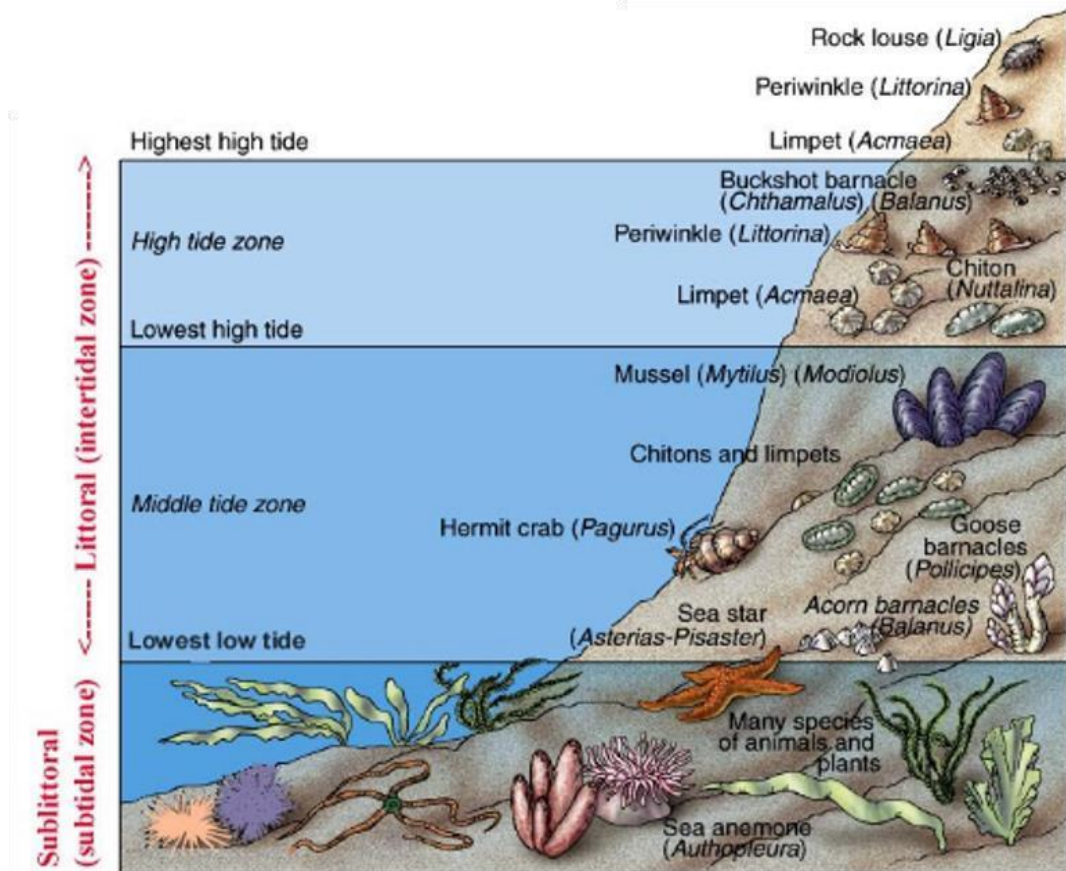


Fig. 2.5: Rocky shore zonation (Intertidal zonation) (<https://www.pathwayz.org>)

An intertidal area with solid rocks is called a rocky shore. It encompasses a wide range of biologically diverse habitat types, boulder fields, platforms, rocky cliffs, and pools of rock. It is unique because of the erosional features caused by the constant movement of the tides. The sun, wind, and other natural elements combine to produce a complex environment. The ecosystem that these organisms inhabit is always changing. To survive, benthic organisms need to withstand significant fluctuations in salinity, temperature, amount of moisture, and activity of wave. According to zonation, certain organisms are found in each coastal region. The intertidal zone can be categorized into following three zones.

- **High tide zone** is also known as high intertidal zone. High tides cause flooding in this area. Barnacles, crabs, anemones, chitons, mussels, isopods, sea stars, sea snails, and other organisms can be found here.

- **Mid tide zone** is also known as mid-littoral zone. Twice a day, this tumultuous area is covered and uncovered. Sea stars, sponges, barnacles, mussels, crabs, and snails are examples of common creatures.

- **Low tide zone** is also known as lower littoral zone. Most of the time, water covers this area. Only during exceptional cases low tide zone is exposed. The organisms inhabiting this zone are less adapted to enduring prolonged periods of dryness or extreme high temperatures compared to those found in other zones. Crabs, brown seaweed, sea cucumbers, mussels, sea urchins, prawns, snails, tube worms, are common organisms that can be found in this area.

2.6.2 Marine resource-based minerals

Advanced technologies and bio-complexity open up new avenues for the creation of innovative medical products sourced from marine resources. Given that biomaterials can be derived from both synthetic and natural sources, this field presents a vast array of natural species suitable for biomedical applications such as tissue engineering and drug delivery. There are numerous factors supporting the use of marine organisms in the quest for effective bone repair. First of all, a wide variety of species include mineral-producing structures within their bodies. Examples of these include the aragonite skeletons of cuttlefish, lobster and the submicron silica frustules of diatoms. The majority of minerals found in marine animals are either calcium carbonate in the form of aragonite or calcite, or they are silica-based (Table 2.2). The marine environment is a natural collector of porous materials, and this porous structure is more relevant in field of tissue engineering (Antoniac et al. 2016). A study of marine organisms is important because this aragonite (Ca sources) can be converted into bio ceramic powder, which can subsequently be used for biomedical applications. In addition to their mineral components, these species that bear skeletons contain organic macromolecules such as collagen, chitin, keratin, elastin, resilin, and abductin that may find application in biomedicine.

Table 2.2: List of few marine organisms along with their minerals

Phylum	Class	Common name	Skeletal mineral
Heterokontophyta	Bacillariophyta	Diatoms	Silica
Haptophyta	Prymnesiophyceae	Coccolithophorids	CaCO ₃
Radiolaria	Polycystina	Radiolarians	Silica
Foraminifera	Granuloreticulosa	Foraminiferans	CaCO ₃
Rhodophyta	Florideophyceae	Red algae	CaCO ₃ / Calcite
Ectoprocta	Stenolaemata	Bryozoans	CaCO ₃
Porifera	Demospongia	Sponges	CaCO ₃ / Silica
Cnidarians	Anthozoa	Corals	CaCO ₃ / Aragonite
Mollusca	Gastropoda	Snails, limpets	CaCO ₃ / Aragonite
	Bivalvia	Clams, mussels	
	Cephalopods	Squid, cuttlefish	
Arthropoda	Crustacea	Lobster, crab,	
Brachiopoda	Lingulata	Lampshells	CaCO ₃ / CaPO ₄
Echinodermata	Asteroidea	Starfish	CaCO ₃ / Calcite
	Echinoidea	Sea urchins	

The fact that marine species provide a vast source of silicate, carbonate, and magnesium ions (in trace amounts) all of which are crucial for bone regeneration is another noteworthy feature. As evidence supporting secondary ions role in bone repair has emerged, these once-classified contaminants are becoming more and more important. Magnesium, for instance, has been shown to promote angiogenesis in porous

materials, osteoblast adhesion, and bioresorption. Carbonated calcium phosphates and silicon-substituted calcium phosphate base have been demonstrated in *in vivo* experiments to grow bone. For example, the skeletal structures of sea urchins contain a high concentration of magnesium ions (Mg^{2+}), facilitating the formation of magnesium substituted β -tricalcium phosphate when converted into phosphate-based minerals (Vecchio et al. 2007).

2.6.3 Conversion of marine resources to biocompatible bioceramics

Numerous researchers have explored about the potential utilization of marine species as precursors in the fabrication of ceramic based tissue engineered bone replace materials. Table 2.3 contains details of earlier developed bioceramics from different marine resources.

Table 2.3 A summary of conversion of marine species to various calcium phosphates

S. No.	Marine Species	Processing technique	Calcium phosphate phase	Properties explored	References
1	Conch shells (<i>Strombus gigas</i>) & Giant clam shells (<i>Tridacna gigas</i>)	Hydrothermal method	Dense HA structures	<i>in vivo</i> study on rats and biocompatibility and bioactivity evaluation	(Vecchio et al. 2007)
2	Sea snail (<i>Cerithium vulgatum</i>)	Mechanochemical method	Biphasic HA+ β - TCP	Synthesis and structural, morphological properties were evaluated	(Gunduz et al. 2014)
3	Snail shell (<i>Rapana venosa</i>)	Hydrothermal synthesis	HA	Synthesis and structural, morphological analysis of HA	(Antoniac et al. 2016)
4	Abalone shells	Hydrothermal solid-state conversion	Hydroxyapatite nano rods	Synthesis and structural, microstructure analysis	(Chen et al. 2015)

5	Brown Mussel (<i>Mytilus sp</i>)	Wet chemical reaction synthesis	HA	Structural and microstructural analysis of coating of nano HA on Ti-6Al-4V alloy	(Santhosh and Balasivanandha Prabu 2012)
6	Tuna (<i>Thunnus obesus</i>)	Alkaline hydrolysis and thermal calcination methods.	HA crystals	Synthesis and microstructural analysis and biocompatibility evaluation	(Venkatesan et al. 2011)
7	Cuttlefish-bone	Hydrothermal reaction	HA	<i>in vivo</i> study and biocompatibility evaluation	(Venkatesan et al. 2018a)
8	Sea coral	Hydrothermal synthesis	HA	<i>in vivo</i> study on rabbit and biocompatibility evaluation	(Nandi et al. 2015)
9	Sea Urchins	Hot plate method and ultrasonication	Calcium phosphate powders (monetite and TCP)	Synthesis and structural properties evaluation	(Agaogullari et al. 2012)
10	Indian sea coral genus 'Goniopora'	Hydrothermal synthesis	Hydroxyapatite granules	Structural, thermal analysis of HA and <i>in vitro</i> study	(Sivakumar et al. 1996)
11	Sea shell (<i>Anandara Granosa</i>)	Hydrothermal method	HA	Effect of Ca/P ratio on chemical properties of HA	(Fadli et al. 2014)

12	Atlantic cod fishbone	Calcination and CaCl ₂ treatment	HA and biphasic HA+β-TCP	Bioactivity, haemocompatibility and cytotoxicity evaluation	(Piccirillo et al. 2015)
13	Snail shells (<i>rapana thomasiana</i>)	Chemical hot-plate stirring method	HA and TCP	Structural and microstructure analysis of biphasic HA	(Ozyegin et al. 2011)
14	Cuttlefish bone	Precipitation Method	HA granules	Effect of sintering temperature on crystallite size of HA	(Faksawat et al. 2015)
15	Cuttlefish bone	Hydrothermal method	HA granules	<i>in vivo</i> study on rabbits and biocompatibility and bioactivity evaluation	(Kim et al. 2014)
16	Land snail shells (<i>helix aspersa</i> and <i>helix pomatia</i>)	Ultrasonic and hotplate stirring method	Monetite (CaHPO ₄), fluorapatite (FA) Ca ₅ (PO ₄) ₃ F	Synthesis and structural, morphological analysis	(Kel et al. 2011)
17	Snail shells	Sol-gel method	Nano HA and biphasic calcium phosphate (HA+β-TCP)	Biocompatibility and bioactivity evaluation	(Anjaneyulu et al. 2016)
18	Austromegabalanus psittacus, Star fish and Sea urchin	Wet chemical synthesis	Nano crystalline HA	Structural, thermal and mechanical properties evaluation	(Jyoth et al. 2017)

19	Cuttlefish bone	Wet chemical synthesis	Submicron size HA powder	Structural and mechanical properties evaluation and biomineralization study	(Hadagalli et al. 2019)
20	Cuttlefish bone	Wet chemical synthesis	Nano crystalline HA	Structural and morphological study and antibacterial activity assessment	(Kalpana and Nagalakshmi 2023)

2.7. Hydroxyapatite based bioceramics

HA ($\text{Ca}_{10}(\text{PO}_4)_6(\text{OH})_2$) is an inorganic calcium phosphate compound which makes up most of the human bone and tooth structure. Pure HA has a hexagonal crystal structure (Fig. 2.6) with lattice parameters $a = b = 9.54 \text{ \AA}$, $c = 6.91 \text{ \AA}$. It is white in colour and has a stoichiometric Ca/P ratio of 1.67. Under physiological conditions, HA is the most thermodynamically stable compound found in body fluids.

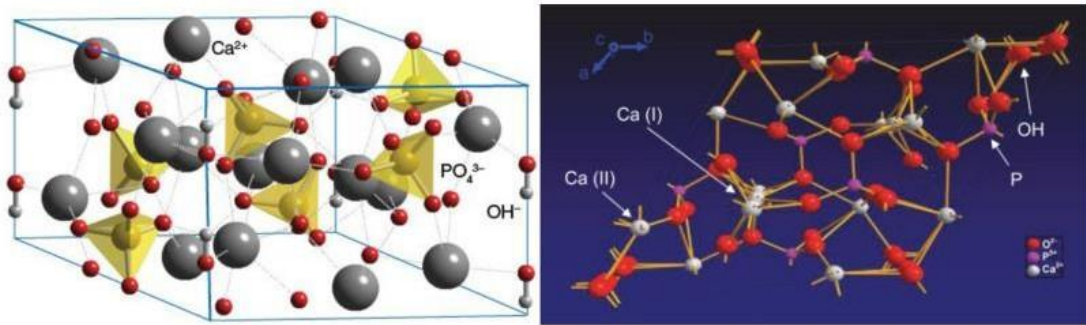


Fig. 2.6: Hydroxyapatite crystal structure (Eliaz and Metoki 2017)

Two distinct channel types, called channel A and channel B, are created across the c axis in each unit cell by the division of PO_4^{3-} ions into two planes at crystal heights of $1/4$ and $3/4$, respectively, and the possibility for calcium ions to occupy sites I and II. Phosphate group oxygen atoms and calcium type II (Ca (II)) ions are positioned at the vertices of two equilateral triangles in channel A, which are rotated by sixty degrees apart. Only type I calcium ions (Ca (I)) are present in the 2 \AA diameter channel B.

Each unit cell contains/shares:

- 14 Ca^{2+} ions, of which 6 are contained within the cell and 8 are shared with neighbouring cells, for a total of 10 Ca^{2+} ions per unit cell.
- Ten PO_4^{3-} ions total, of which two inside the cell and eight peripheral ions shared with numerous neighbouring cells—resulting in a total of six PO_4^{3-} ions per unit cell.
- 8 OH^- ions: being at the edges, they are all a part of the cell by $1/4$. = 2 OH^- ions/unit cell;

Because of its inherent bioactivity, biodegradability, and biocompatibility, HA is a desirable choice for bone filler applications as well as for use as a carrier or

delivery system for proteins, genes, or medications. Various applications of HA are summarized in Figure 2.7. Furthermore, the ability to make HA nanoparticles intrinsically magnetic or fluorescent opens up a number of possibilities for imaging and therapy (such as cancer ablation). The primary physicochemical features of HA such as its size, morphology, crystallinity, dosage, surface area, aggregation are pertinent factors to take into account when developing HA for biological applications.

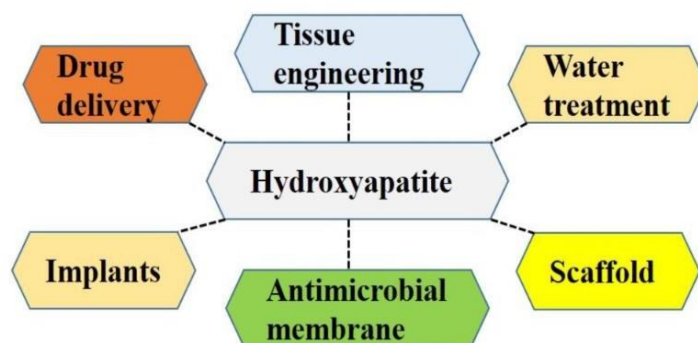


Fig. 2.7 Applications of hydroxyapatite (Kumar and Mohanty 2022)

2.7.1 Synthesis methods of HA

Several techniques exist for producing HA that has an approximate Ca/P ratio of 1.67. The available synthesis methods are wet methods, dry methods, high temperature methods, combination methods and biogenic synthesis which are listed in Figure 2.8.

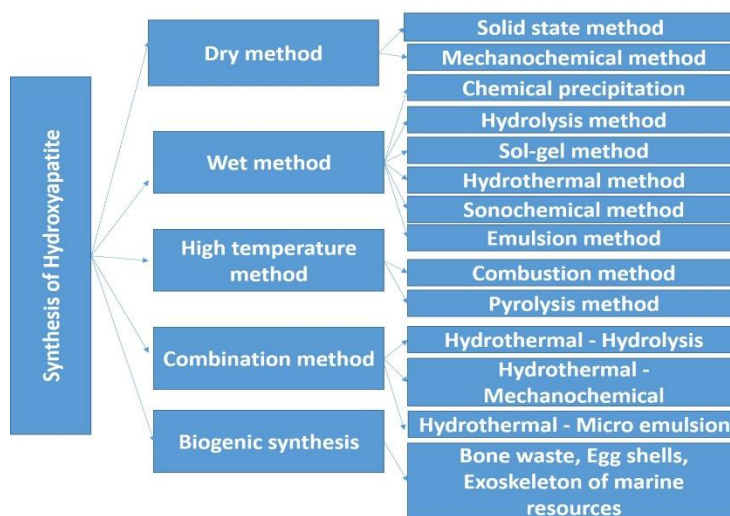


Fig. 2.8 Synthesis methods of hydroxyapatite

2.7.1.1 Dry methods

The solid-state synthesis method and the mechano-chemical method are two distinct techniques used in dry methods. Large particle sizes and irregular shapes are typical characteristics of HA powders produced by dry methods (Sadat-Shojai et al. 2013). These characteristics are frequently the result of employing inexpensive raw materials. In comparison to wet methods, the size of the particles is often larger than nanoscale, and their phase purity is reduced (Li B et al. 2017). The literature states that dry procedures don't need a solvent or special processing conditions. Solid-state synthesis is a reasonably easy process that is especially recommended for producing HA particles in large quantities. Precursors are typically pre-prepared CaP salts that are pulverised and calcined at high temperatures (approximately 1000 °C). An excellent crystalline structure forms as a result of the high calcination temperature. The final particles obtained have an irregular form and are heterogeneous.

In contrast to the solid-state method, the second strategy known as the mechanical alloying or mechano-chemical method that allows for the production of a powder with a much clearer structure because pressure causes surface-bonded species to be perturbed, improving both the thermodynamic and kinetic reactions between solids (Sadat-Shojai et al. 2013). Typically, a planetary mill is used to grind the materials, and the stoichiometric ratio is maintained in the molar ratios of the reagents. The key processing factors in this technique are the type of milling media, the kind of reagents, and the rotational speed (Sadat-Shojai et al. 2013). The procedure is relatively easy and easily reproducible. Nasiri-Tabrizi et al. have demonstrated that when milling time increases, the average size of the powder decreases, leading to an increase in lattice strain (Nasiri-Tabrizi et al. 2009). The best techniques for producing large quantities of HA microparticles are dry methods because of their great repeatability and inexpensive processing costs.

2.7.1.2 Wet methods

Wet methods, as opposed to dry methods, enable the production of HA with a consistent morphology. They are therefore the most used techniques for creating nano powders. The six subgroups of these techniques are as follows: sol-gel, hydrolysis,

hydrothermal method, emulsion method, traditional chemical precipitation, and sonochemical method.

One of the simplest wet techniques for making HA powder is chemical precipitation. It is predicated on the observation that HA is typically stable and poorly soluble in an aqueous solution at pH 4.2 and ambient temperature; however, the precipitation process is often carried out at pH > 4.2 (Sadat-Shojai et al. 2013). Generally, the reagents should be introduced gradually, with gentle stirring and mild conditions, while monitoring to make sure the molar Ca/P ratio stays around 1.67. Subsequently, the suspension is either reduced to powder right away or aged for a while at atmospheric pressure following meticulous filtering and drying (Sadat-Shojai et al. 2013). The precipitation reaction has to be carried out at a higher temperature or a higher pH, or both in order to produce powders with higher phase purity; doing so also reduces the possibility of phase impurity formation.

In hydrolysis, by hydrolysing various CaP phases, such as DCPD, TCP under specific circumstances, and octacalcium phosphate (OCP), HA nanoparticles are prepared. OCP has been almost abandoned until this point since it tends to absorb contaminants when transforming into HA (Sadat-Shojai et al. 2013). The synthesis of HA from TCP was reported by Tenhuisen et al., who also noted a linear relationship between hydrolysis temperature and surface area of HA that was produced (TenHuisen 1998). It was also observed that the regularity of the crystals increased with an increase in reaction temperature.

The reagents are mixed at the molecular level in the sol-gel method, which enables the use of low processing temperatures to produce fine and homogenous powders. From a colloidal solution (liquid sol), the pertinent processes result in the production of a solid gel. Salts of organic acids, alkoxides, or inorganic salts are frequently used as starting materials for the synthesis of sols (Sadat-Shojai et al. 2013). Following a sequence of hydrolysis and reactions of polymerization, the precursors become a colloidal suspension (sol), which gradually changes into a gel over time or in response to temperature changes or catalyst action. To remove any remaining organic material, the gel is subsequently allowed to age at room temperature, dried, and then subjected to a high temperature calcination. Due to the extremely slow interaction

between the calcium and phosphorus precursors, a lengthy ageing period is required for the synthesis of HA. The kind of precursors utilized has a significant impact on the type of solvent employed, the velocity of gelation and temperature and pH settings selected for the procedure. According to *in vitro* studies, HA produced by the sol-gel process in nano size has a bio-absorbability rate that is comparable to that of biological apatite (Fathi et al. 2008). The high cost of the raw ingredients and the possibility of producing CaO in the finished product are the main drawbacks of this process.

High operating temperatures and pressures are characteristics of the hydrothermal process. The ageing process is carried out at a high temperature, making it comparable to a chemical precipitation approach (Sadat-Shojai et al. 2013). In an autoclave, where the process is conducted, the high temperature and enclosed space encourage the generation of solvent vapour and an increase in pressure. An acceptable Ca/P ratio and a high phase purity than that of conventional sol-gel procedures are obtained by using a high temperature. However, compared to other wet approaches, this process is more expensive due to the high temperatures and pressures that demand expensive equipment (Sadat-Shojai et al. 2013). The hydrothermal approach generally yields HA crystals with irregular morphology.

By preventing particle agglomeration, the emulsion method is best technique for lowering particle size and attaining a regulated morphology and fine structure. Originally, porous materials were created using this approach (Chun H J et al. 2018). Phosphoric acid and calcium nitrate are the most often used reagents because they are readily available and reasonably priced (Zhu et al. 2008). The three most often used surfactants are dioctyl sodium sulfosuccinate salt, cetyltrimethyl ammonium bromide, and polyoxyethylene. It is a fairly straightforward procedure that operates at modest synthesis conditions and low processing temperatures (Guo et al. 2005; Li et al. 2008; Sun et al. 2006).

The foundation of the sonochemical method is chemical reaction triggered by intense ultrasonic pulses. The synthesis takes place by the physical mechanism of bubble cavitation in aqueous phase. Chemical reactivity is increased to speed up heterogeneous reactions involving liquid and solid reagents. It has been recently shown that the HA particles produced using this method have smaller, more homogeneous

crystals (Sadat-Shojai et al. 2013). Hazar et. al have demonstrated that raising the ultrasonic powder up to 300 W leads to a considerable decrease in the HA particle size (Hazar Yoruç and İpek 2012). The rapid speed and high kinetic energy during synthesis make it more probable for HA particles to collide and create a more homogeneous crystal lattice. This characteristic has the potential to enhance the mechanical properties of the final product.

2.7.1.3 High temperature methods

High temperatures are required for these processes in order to partially or totally burn the precursors. There are two methods namely pyrolysis and combustion.

Using the combustion approach, highly pure powder can be produced fast in a single operation. Because the components are intimately mixed, this method produces a synthesised powder with good chemical homogeneity and relatively simple process execution. An organic fuel (such as succinic acid, citric acid, glycine, urea, and sucrose) and oxidants (such as calcium nitrate $\text{Ca}(\text{NO}_3)_2$ or nitric acid (HNO_3)) combine to form an exothermic and self-sufficient redox reaction. Initially, aqueous solutions of calcium nitrate ($\text{Ca}(\text{NO}_3)_2$) and ammonium sulfate ($(\text{NH}_4)_2\text{HPO}_4$) are combined together. Following this, nitric acid (HNO_3) is introduced to dissolve any precipitate formed. Afterwards, a blend of fuels, either two varieties or sometimes just one, is introduced. To kickstart the reaction, the mixture undergoes heating in an oven at a relatively low temperature, around 300 degrees Celsius. As combustion occurs, there is a rapid rise in temperature, reaching to its maximum. In order to achieve maximum nucleation and prevent undesired additional particle growth, the mixture is finally rapidly chilled. The heat produced by the exothermic combustion reaction keeps the system temperature stable and eliminates the requirement for outside heating. Numerous factors, including the fuel/oxidant ratio, the starting furnace temperature, and the composition of fuels used, affect the maximum reaction temperature and, in turn, the end powder's properties. Usually, an aggregation of extremely small particles is the end outcome.

Pyrolysis does not require post-treatments or prolonged aging at high temperatures, as it can be completed quickly and easily while yet ensuring the formation of highly crystalline, stoichiometric particles (Sadat-Shojai et al. 2013). Because the

precursor solutions are sprayed within a heated oven using an ultrasonic generator, the pyrolysis process is also known as "pyrolysis spray." The production of the finished powder comes next, as a result of the reaction between the high-temperature gases and vapours. The precursors completely evaporate at the high temperature, and then the nanoparticles nucleate and develop in the gaseous phase. The main drawback of this technique lies in the formation of secondary aggregations, which would reduce the specific surface area.

2.7.1.4 Biogenic synthesis

HA synthesized entirely or partially from biogenic resources will be well accepted by the living organs due to its chemical similarity with the apatite of human bone. Despite the wide range of HA synthesis techniques available, only a handful of them operate well and are economically viable, mostly because of the variety of ingredients required in the synthesis of HA. The production of HA using a range of biogenic materials is depicted in Figure 2.9 (Sadat-Shojai et al. 2013). Five distinct biogenic sources of HA include the production of HA from eggshells, biomembranes, the exoskeleton of marine species, minerals extracted from biowaste, and with the help of naturally occurring biomolecules.

Animal by products from mammalian resources such as bovine bone, porcine bone, fish bone, ostrich bone, as well as shells (eggs and marine) comprise both organic and inorganic matter. Natural HA obtained from these sources involve elimination of organic matter from the mineral matrix to obtain HA directly. Several methods can be used to extract HA from these biomaterials which include calcination, precipitation, hydrolysis, hydrothermal and combination of these techniques. Compared to HA produced from other methods, HA produced from natural sources is non stoichiometric as it contains various trace elements like Mg^{2+} , Na^+ , Zn^{2+} , K^+ , Sr^{2+} , Ba^{2+} , Si^{2+} , F^- and CO_3^{2-} (Venkatesan and Anil 2021). These trace elements aid in rapid bone regeneration and mimics the human bone produced apatite. These ions are crucial because they are present in several protein complexes (enzymes) that regulate the habitats and physiological processes of osteoblasts, osteoclasts, and osteocytes as well as the equilibrium conditions within them. Furthermore, by releasing biologically active ions that affect cellular activities to direct cellular ingrowth and, as a result, tissue

regeneration, these ions would directly affect the process of bone repair. The trace elements present in few biogenic resources are summarized in table 2.6. The biological effects of these trace elements are summarized in table 2.7.

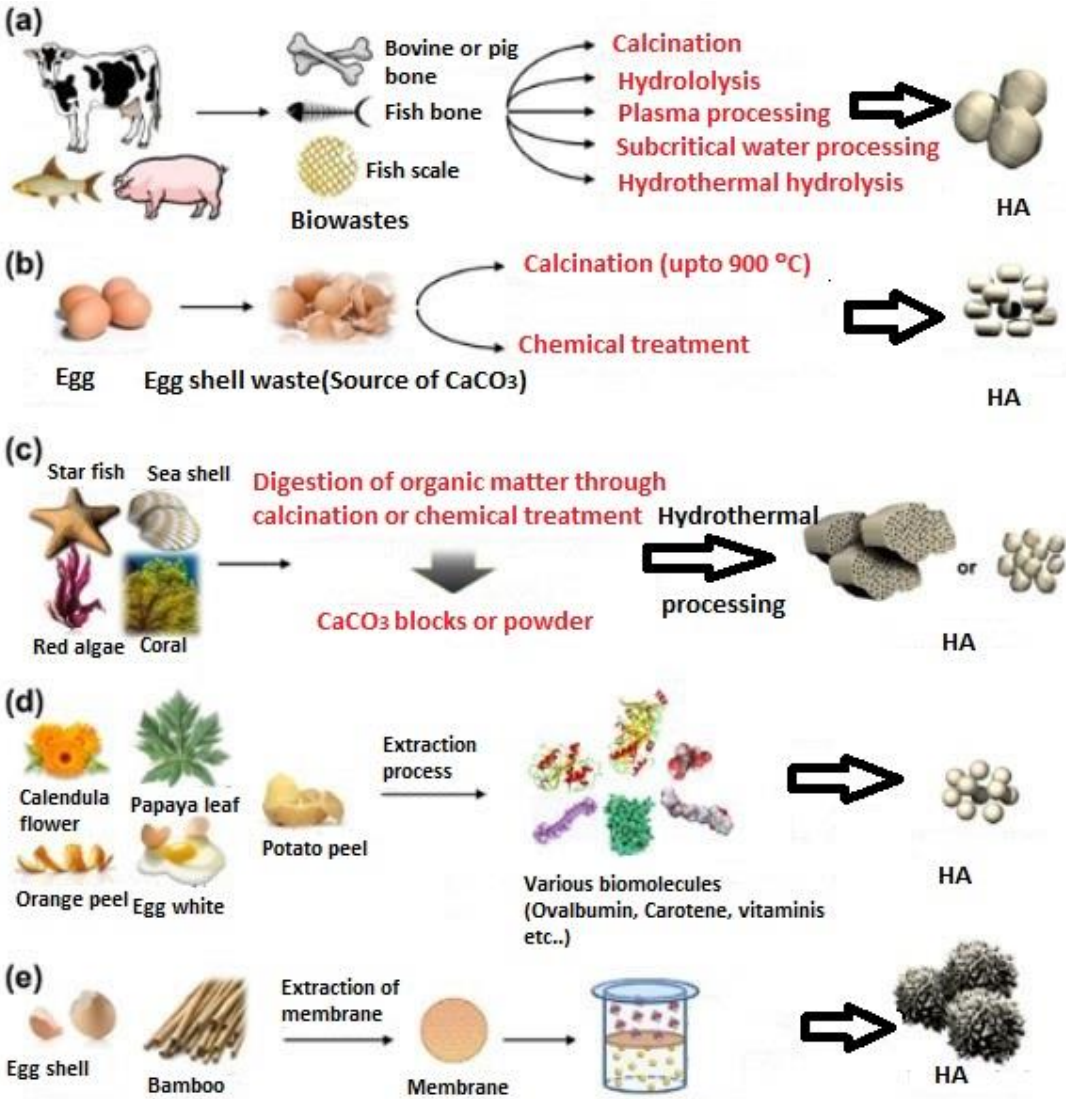


Fig. 2.9 Synthesis of HA via various biogenic resources (a) from biowaste (b) from egg shells (c) from the outer shells of marine organisms (d) from naturally derived biomolecules (e) from biomembranes (Sadat-Shojai et al. 2013)

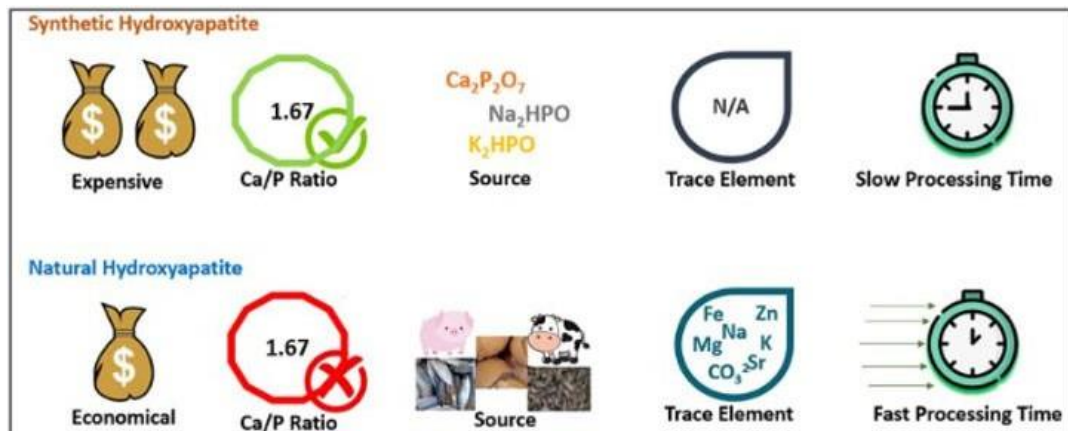


Fig. 2.10 Hydroxyapatite obtained from synthetic sources vs natural sources (Firdaus Hussin et al. 2022)

HA obtained from natural and synthetic resources is compared in Figure 2.10. The presence of trace elements and the faster processing time to synthesize HA made the natural HA as a promising candidate in biomedical applications. Wet chemical synthesis method is used in producing HA in the current work and the list of published work on wet chemical method is represented in Table 2.4. Also, various synthesis methods of HA from different biogenic resources are represented in Table 2.5.

Table 2.4 List of published work on the synthesis of HA from chemical precipitation method

S. No.	Brief description	Characteristics of HA powder	Reference
1	Combining $(\text{NH}_4)_2\text{HPO}_4$ solution with $\text{Ca}(\text{NO}_3)_2$ solution, and then introducing HNO_3 and urea, followed by heating at $95\text{ }^\circ\text{C}$ for 0.5 to 24 h and followed by aging for 12 h	HA whiskers with aspect ratio of 25	(Chen et al. 2011)
2	Slow mixing of $(\text{CH}_3\text{COO})_2\text{Ca}$ and KH_2PO_4 solutions within a glass beaker by vigorous stirring, followed by aging for 1 h	Elongated HA nanorods of 50 nm diameter with average aspect ratio of 20	(Swain and Sarkar 2011)
3	Dropwise addition of $(\text{NH}_4)_3\text{PO}_4$ solution to a solution containing $\text{Ca}(\text{NO}_3)_2$ and sodium citrate at $90\text{ }^\circ\text{C}$, followed by aging for 4 h at $90\text{ }^\circ\text{C}$	Citrate-stabilized hydrocolloids of HA nanoparticles	(Li et al. 2011)
4	Dropwise addition of $\text{NH}_4\text{H}_2\text{PO}_4$ solution to a solution containing $\text{Ca}(\text{NO}_3)_2$, NH_4OH , and CTAB or PVP (polyvinylpyrrolidone,), followed by aging at room temperature for 72 h	Prism-like HA nanoparticles	(Song et al. 2011)

5	Synthesis by employing “crystallization mushrooms” in which crystallization can occur in micro-droplets consists of high initial concentrations of $\text{Ca}(\text{CH}_3\text{COO})_2$ and $(\text{NH}_4)_2\text{HPO}_4$ along with diffusion of NH_3 and CO_2 generated through decomposition of NH_4HCO_3 solution	Carbonate-substituted HA nanorods of 100 nm dimensions	(Iafisco et al. 2011)
6	Mixing of $\text{Ca}(\text{OH})_2$ and H_3PO_4 aqueous solutions using a microreactor system under a given flow rate and preparation temperature	Rod-like HA nanoparticles of ~2 nm diameter and ~15 nm length	(Kandori et al. 2011)
7	Dropwise adding H_3PO_4 blended with ethylene glycol to a ethylene glycol solution comprising oxalic acid and CaCl_2 under stirring and pH 9	Fine elongated, stoichiometric HA powder with grain size of 440 nm in width and 680 nm in length	(Gopi et al. 2011)
8	Slow titration of a solution comprising CaCl_2 and silk sericin with Na_2HPO_4 solution at 50 °C along with adjusting pH using NaOH at 7.4, 10 or 12	Assemblies of poor crystallized HA with an enamel prism-like structure	(Cai et al. 2010)

9	Dropwise adding ethanol/water solution of ammonium phosphate to a ethanol/water solution comprising $\text{Ca}(\text{NO}_3)_2$ and ethanolamine, citric acid or PEG (as dispersant) under various temperatures and pHs, followed by aging at RT for 24 h, washing, and finally calcination at 700 °C for 1 h	HA nanoparticles of various morphologies, such as rod, sphere and needle	(Wang et al. 2010)
10	Dropwise adding $\text{Ca}(\text{NO}_3)_2$ solution to a solution comprising $(\text{NH}_4)_2\text{HPO}_4$ and cationic surfactant cetrimide at pH of 11.5, and then calcination of resultant powder at various temperatures for 8 h	Mesoporous shell-like HA nanospheres of 200 nm size	(Shanthi et al. 2010)
11	Constructing a CO_2 bubble template through heating a mixed solution comprising $\text{Ca}(\text{NO}_3)_2$, $(\text{NH}_4)_2\text{HPO}_4$, HNO_3 , urea, and chelating agent (Na_2EDTA or trisodium citrate) at 94 °C for 5 h and then aging for 12 h	Flower-like carbonated HA microsphere	(Cheng et al. 2010)
12	Slow adding $\text{Ca}(\text{NO}_3)_2$ solution of pH 9 to a ethanol/water solution comprising H_3PO_4 and nonionic surfactants (P123 and Tween-60) with or without citrate at 90 °C, followed by refluxing for 48 h and then calcination at 300 °C for 3 h	HA hollow nanospheres and nanotubes	(Ye et al. 2010)
13	Dropwise adding H_3PO_4 solution to $\text{Ca}(\text{OH})_2$ solution, followed by adjusting pH at 10 and then aging at RT for 12 h under stirring	Rod-like HA nanoparticles of 50–100 nm length	(Catros et al. 2010)

14	Mixing $\text{Ca}(\text{OH})_2$ suspension with H_3PO_4 solution under stirring, followed by aging for various lengths of time	Nanophase HA particles	(Koutsopoulos et al. 2009)
15	Mixing a $\text{Ca}(\text{NO}_3)_2$ solution of pH 2 with a $(\text{NH}_4)_2\text{HPO}_4$ solution of pH 2 and adjusting pH at 4 using NH_3OH and then adding urea and heating at 85 °C for 48 h, followed by adding NH_3OH and aging at 85 °C for 24 h	Needle-like HA nanocrystals	(Zhang et al. 2009)
16	Dropwise adding $(\text{NH}_4)_2\text{HPO}_4$ solution to an aged solution comprising CaO and saccharose at controlled pH of 11, followed by heating at 60 °C for 30 min	Nanocrystalline HA containing saccharose	(Safronova et al. 2009);
17	Dropwise adding $\text{Ca}(\text{NO}_3)_2$ solution to a solution comprising $(\text{NH}_4)_2\text{HPO}_4$, CTAB, and NaOH (pH 9.5), followed by aging at RT for 15 h and then calcination at 500 °C for 8 h	HA nanorods of ~20 nm diameter and 100–120 nm length	(SL Shanthi et al. 2009)
18	Adding sodium citrate solution to a calcium nitrate solution at a given temperature, followed by adding $(\text{NH}_4)_3\text{PO}_4$ solution, aging at 90 °C for 0.5 h, and finally adding sodium hexametaphosphate solution to the resulting suspension	Rod-like HA nanoparticles of 40–60 nm width and 300–400 nm length with high zeta potential	(Tan et al. 2009)

19	Dropwise adding a H_3PO_4 solution to a solution comprising $\text{Ca}(\text{CH}_3\text{COO})_2$ and a given amino acid (alanine, arginine and aspartic acid) along with keeping pH at 10 using NH_4OH , followed by aging at RT for 24 h	Amino acid-functionalized Ca-deficient HA nanoparticles of needle-like morphology	(Palazzo et al. 2009)
20	Titration of a suspension comprising $\text{Ca}(\text{OH})_2$ and citrate reagent with H_3PO_4 solution, followed by aging at RT and then calcination at $800\text{ }^\circ\text{C}$ for a dwell time of 2 h	Nanocrystalline HA particles of 50–60 nm	(Li 2009)
21	Mixing CaCO_3 suspension with ammonium phosphate dissolved in water, followed by stirring at $60\text{ }^\circ\text{C}$ under air atmosphere	HA microparticles	(Verwilghen et al. 2009)
22	Mixing a solution of poly (ethylene oxide)-b-poly(L-lysine) copolymer and CaCl_2 with a solution of same copolymer and $(\text{NH}_4)_2\text{HPO}_4$, followed by adjusting pH at 5 or 8 using KOH and then aging and annealing	HA nanorods	(Shkilnyy et al. 2009)
23	Mixing H_3PO_4 and PVP (capping agent) with a solution comprising $\text{Ca}(\text{NO}_3)_2$ and HNO_3 , followed by dropwise adding NH_4OH and subsequently aging at $60\text{ }^\circ\text{C}$ for 2–7 days	Rod-like HA nanoparticles with aspect ratio up to 20–30	(Zhang and Lu 2008b)

24	Adding aqueous solution of $\text{Ca}(\text{NO}_3)_2$ and H_3PO_4 to a solution comprising nonionic surfactants P123, Tween-60 and ethanol, followed by mixing with urea and then NH_4OH and finally refluxing at 60 °C	Oriented bundles and raft-like complexes of HA nanorods	(Ye et al. 2008)
25	Mixing a $\text{Ca}(\text{NO}_3)_2$ solution of pH 2 with a $(\text{NH}_4)_2\text{HPO}_4$ solution of pH 2, then adjusting pH at 4 and adding urea into the mixture and heating at 85 °C for 48 h, followed by immersing the resulting powders in a NH_4OH solution (pH 12) at 60 °C for 48 h	HA nanorods and dandelion-like spheres assembled by HA nanorods	(Zhang and Lu 2008a)
26	Mixing aqueous citric acid solution having various pHs (7.4 to 8.5) with appropriate amounts of $\text{Ca}(\text{NO}_3)_2$ and $(\text{NH}_4)_2\text{HPO}_4$ solutions, followed by filtering the solution and aging the resulting solution at 37 °C for 24 h	Dumbbell-like HA microparticles	(Martins et al. 2008)
27	Titration of a H_3PO_4 solution diluted with deionized water or ethanol with a solution comprising $\text{Ca}(\text{OH})_2$ and citric acid until falling the pH to 10, followed by ripening for 24 h and finally calcination at 800 °C for 2 h	Nanocrystalline HA particles of 55 and 85 nm size	(Li and Meng 2008)

28	Spreading $\text{Ca}(\text{NO}_3)_2$ and $(\text{NH}_4)_3\text{PO}_4$ in 100 ml and 25 ml beakers, respectively, followed by putting one beaker inside another, and then incorporating PEG watery solution with pH of 10.5 into the beakers one by one and finally aging the resultant suspension at RT for 5 days	Spherical HA nanoparticles of 30–50 nm diameter	(Qiu et al. 2008)
29	Biomimetic mineralization on the 1-D fibrinogen fibrils and 2-D fibrinogen fibril networks as novel protein fibrils-based templates, in a 1.5 SBF at 37 °C for various lengths of time	Spherical HA crystals of 1–2 μm diameter	(Wei et al. 2008)
30	Dropwise adding a solution of pH 5 comprising Na_2HPO_4 , hexamethylenetetramine (pH regulator), and HCl into a solution of pH 5 comprising calcium bis(2-ethylhexyl) sulfosuccinate, hexamethylenetetramine, and HCl, followed by refluxing at 100 °C	Ribbon-shaped, single crystal HA particles of 3–6 μm width and 10–30 μm length	(Tao et al. 2007)
31	Spreading $\text{Ca}(\text{NO}_3)_2$ and $(\text{NH}_4)_3\text{PO}_4$ in 400 ml and 100 ml beakers, respectively, followed by putting one beaker inside another, and then incorporating chitosan solution into the beakers one by one and finally aging the resultant suspension at RT for several days	Thermally stable, spindle-shaped HA of 7–8 nm width and 30–40 nm length	(He et al. 2007)

32	Dropwise adding a $\text{NH}_4\text{H}_2\text{PO}_4$ solution into a solution of $\text{Ca}(\text{OH})_2$ and then refluxing at 70 or 90 °C for 3 h, followed by aging for 24 h and thermal treatment at 800 °C	Mesoporous HA microparticles	(El Hammari et al. 2007)
33	Mixing a solution comprising $\text{Ca}(\text{NO}_3)_2$, sodium dodecyl sulphonate (template), and ethanol with an ethanol/water solution of $(\text{NH}_4)_2\text{HPO}_4$, followed by adding ethanol/water solution of NaOH and refluxing at 83 °C for 14 h	Ordered lamellar HA nanostructures	(Liu et al. 2007)

Table 2.5. List of published work on the synthesis of HA from biogenic sources.

S.No.	Biogenic source	Brief description	Characteristics of HA powder	References
1	Porcine bone	Hydrothermal treatment of bones followed by calcination at 900-1200 °C	Submicron size HA powder with intergranular porosity	(Forero-Sossa et al. 2021)
2	Chicken bone	Treatment of chicken bones with acetone followed by calcination at different temperatures such as 700, 900, 1100 °C for 3 hours	Nano HA	(Vinoth Kumar et al. 2021)
3	Ostrich bone	Ostrich bone powder subjected to alkaline hydrothermal process at 250 °C followed by calcination at 950 °C	HA nano particles of size 36.44 nm	(Malla et al. 2020)
4	Chicken bone	Calcination of chicken bones after removing bone marrow at different temperatures between 600-1000 °C and at different times like 4 h, 12 h and 20 h.	Spheroidal like aggregate structure with interconnected porous morphology	(Bee and Hamid 2019)
5	Nacre shell	Mixing CaCO ₃ microspheres, obtained from nacre, with Na ₂ HPO ₄ solution, followed by hydrothermal treatment at 140 °C for 12 h	Carbonated HA microspheres consisting nanoparticles	(Guo et al. 2011)

6	Eggshell	Mixing of CaCO_3 and $\text{Ca}(\text{OH})_2$, obtained respectively from uncalcined and calcined eggshell with respectively HNO_3 and H_3PO_4 followed by aging and thermal treatment	Carbonated HA powder of various crystallinities	(Meski et al. 2011)
7	Bamboo membrane	Crystallization of HA at 37 °C from K_2HPO_4 and $(\text{CH}_3\text{COO})_2\text{Ca}$ solutions of pH 7.4 separated using a bamboo membrane, for various holding times	Flower-like HA agglomerates of nanowire-like crystals	(Zhang et al. 2011a)
8	Fish scale	Enzymatic hydrolysis of a tilapia fish-scale using protease N for 2.5 h, and flavourzyme for 0.5 h at an optimal pH and temperature, followed by stirring in a boiling water bath for 10 min and subsequent sintering at 800 °C	Agglomerated HA nanoparticles	(Huang et al. 2011)
9	Egg shell inner membrane	Crystallization of HA from $(\text{NH}_4)_2\text{HPO}_4$ solution and CaCl_2 solution of pH 9–11 separated using inner membrane of eggshells, under stirring for 24 h	HA nanorods of 2–5 nm diameter and 50–100 nm length	(Neelakandeswari et al. 2011)
10	Bovine bone	Bovine bone processing by transferred arc plasma process at 5 kW for 30–120 sec	Poor crystallized HA powder	(Yoganand et al. 2011)

11	Egg shell inner membrane	Crystallization of HA at 15–50 °C from K_2HPO_4 and $(CH_3COO)_2Ca$ solutions of pH 6–11 separated using inner membrane of hen eggshells for various holding times (3–12 days)	Flower-like HA agglomerates	(Zhang et al. 2011b)
12	Crocodile egg shells	Mixing $Ca(OH)_2$ or $CaCO_3$, obtained respectively from calcined and uncalcined crocodile eggshells, with $(NH_4)_2HPO_4$, $Ca_3(PO_4)_2$, or H_3PO_4 , followed by hydrothermal treatment at 250 °C for up to 48 h	Agglomerated plate-like HA of various phase purities	(Boonyang et al. 2010)
13	Egg shells	Thermal treatment of eggshell at 900 °C for up to 3 h, followed by milling with H_3PO_4 at 4000 rpm for 5 h (attritor milling) or 350 rpm for 10 h (ball milling) and then sintering	HA aggregates of nanometer or micrometer size grains	(Gergely et al. 2010b; a)
14	Fish scale	Treatment of <i>Labeo rohita</i> fish-scale using HCl and then NaOH, followed by stirring in a boiling water bath for 20 min and subsequent calcination at various temperatures (800–1400 °C)	Submicron size HA powder	(Mondal et al. 2010)

15	Chicken bone	Thermal treatment of a deproteinized and defatted bone pulp (bone sludge) using a two-step calcination at 600–950 °C	Phase-pure HA of various crystallinities	(Sobczak et al. 2009)
16	Bovine bone	Thermal treatment of a cortical bovine bone at 900 °C for 2 h, followed by crushing the resultant mass	HA powder of an irregular morphology	(Herliansyah et al. 2009)
17	Bovine serum albumin (BSA)	Rapid mixing of Ca(OH) ₂ solution with MCPM solution and subsequently with bovine serum albumin along with ultrasonic irradiating for 8 min, followed by freeze-drying the resultant colloidal protein precursors and finally thermolysis at a given temperature for 1 h	Rod like HA nano crystals	(Han et al. 2007, 2009)

18	Egg shell, potato peel, orange peel, papaya leaf, calendula flower	1) Aging a solution comprising dissolved eggshell in HCl, $(\text{NH}_4)_2\text{HPO}_4$ and NH_4OH at RT for a week; 2) Extraction of various biomolecules from orange peel, potato peel, papaya leaf, and calendula flower in a boiling water, then mixing the extracts with alkaline $\text{Ca}(\text{NO}_3)_2$ solution and aging for 24 h, followed by mixing with alkaline $(\text{NH}_4)_2\text{HPO}_4$ solution and aging for a week	HA nanoparticles of various sizes and morphologies	(Nayar and Guha 2009)
19	Bovine bone	Extraction of HA from bovine bones using three methods: thermal decomposition of grinded bone at $750\text{ }^\circ\text{C}$ for 6 h; subcritical water processing in water at $275\text{ }^\circ\text{C}$ for 1 h; and alkaline hydrothermal hydrolysis in a NaOH solution at $250\text{ }^\circ\text{C}$ for 5 h	Pure HA nanoparticles of flake like and rod like morphologies	(Barakat et al. 2009)
20	Egg white	Dropwise adding a $\text{Ca}(\text{NO}_3)_2$ solution to a solution of pH 8.5 comprising $(\text{NH}_4)_2\text{HPO}_4$, NH_4OH , and ovalbumin extracted from egg white, followed by aging at RT for 3 days and subsequent calcination at $300\text{--}700\text{ }^\circ\text{C}$	Agglomerated carbonated HA nanorods	(Zhao et al. 2008a)

21	Egg white	Mixing a CaCl ₂ solution, obtained by dissolving eggshell in HCl, with H ₃ PO ₄ and then aging at RT for 5 days, followed by adding ovalbumin, extracted from egg white, and adjusting pH at 5.5 using NH ₄ OH and subsequent aging for a month	Large spindle-like HA-ovalbumin composite of 0.8 mm length consisting needle-like nanocrystals	(Zhao et al. 2008b)
22	Red algae	Thermal treatment of red algae at 650–700 °C for 12 h, followed by mixing with NH ₄ H ₂ PO ₄ solution under stirring at 100 °C and pH 11 for 12 h and subsequent washing with acetic acid	Microporous HA	(Walsh et al. 2008)
23	Bovine bone	Thermal treatment of bovine bone at 800 °C for 3 h, then grinding and ball milling for 24 h, followed by vibro-milling using ethanol for various milling times	Needle-like HA nano powder of ~100 nm size	(Ratnayake et al. 2008)
24	Egg shells	Calcination of hen eggshells at 900 °C for 2 h to produce CaO and then preparing Ca(OH) ₂ , followed by mixing with (NH ₄) ₂ HPO ₄ solution and subsequent irradiating in a microwave oven	Carbonated HA nanorods of 33-50 nm length and 8–14 nm width	(Siva Rama Krishna et al. 2007)

25	Bovine bone	Annealing bovine bone at various temperatures (400–1200 °C)	Porous HA with interconnected structure	(Ooi et al. 2007)
26	Fish bone	Thermal treatment of bones originated from Brazilian river fish at 900 °C for 4–12 h, followed by milling at 300 rpm for 2–16 h using a high-energy milling	Irregular stoichiometric HA nanoparticles of various sizes	(Coelho et al. 2006)
27	Oyster shell	Mixing various milled oyster shell powders and $(\text{NH}_4)_2\text{HPO}_4$ solution with or without KH_2PO_4 , followed by hydrothermal treatment at 200 °C for various lengths of time	Carbonated HA nanoparticles of ~100 nm size	(Lemos et al. 2006)
28	Egg shell	Mixing $\text{Ca}(\text{OH})_2$, obtained using calcination of eggshell at 900 °C, with $(\text{NH}_4)_2\text{HPO}_4$ along with adjusting pH at 7.4 using NH_4OH or HCl , followed by hydrothermal treatment at various temperatures and pressures	Agglomerated carbonated HA nanoparticles of 10–63 nm size	(Lee et al. 2003)
29	Pig bone	Treatment of pig bone in hot NaOH solution at 100 °C for 48 h, followed by heating at 350 °C	Carbonated HA of plate-like morphology	(Haberko et al. 2006)

30	Starfish skeleton	Mixing CaCO ₃ , extracted from starfish skeleton of Mexico coast using treatment with a dilute NaCl solution and thermal treatment at 300 °C, with DCPD solution, followed by hydrothermal synthesis at 200 °C and 6 MPa for 2–20 h	Bundle of HA fibers with 0.5 μm diameter and 5 μm length	(Rodríguez-Lugo et al. 2005)
31	Egg shell	Calcination of an uncrushed eggshell at 900 °C for 1 h, and then mixing with H ₃ PO ₄ solution under various ratios, followed by ball-milling with zirconia ball media under isopropyl alcohol solvent for 12 h and subsequent thermal treatment at various temperatures	Pure HA and β-TCP powders	(Lee and Oh 2003)
32	Bovine bone	Thermal treatment of bovine bone at 700 °C overnight, followed by mixing with HF at 250 °C for 30 min or grinding with NaF and heating at 900 °C for 12 h	Fluoride substituted HA powder	(Murugan et al. 2002)

33	Porites coral	Mixing MCPM or DCPA with an aqueous mixture of H_3PO_4 and Porites coral, followed by hydrothermal treatment at 160 or 200 °C.	HA rods with 500nm size	(Jinawath et al. 2002)
34	Porites coral	Mixing of Porites coral and $(NH_4)_2HPO_4$ solution, with or without the mineralizer KH_2PO_4 , followed by hydrothermal treatment for various lengths of time	Porous HA with interconnected structure	(Xu et al. 2001)
35	Algae	Adding $CaCO_3$, extracted from algae of Brazilian coast through treatment with a dilute $NaClO$ solution, to $(NH_4)_2HPO_4$ solution with or without NH_4F along with adjusting pH at 9 using NH_4OH , followed by hydrothermal method at 200 °C for 24–48 h	Carbonated HA of interconnected porous structure	(Felício-Fernandes and Laranjeira 2000)

Table 2.6 List of trace elements present in biogenic resources

S. No.	Biogenic resource	Trace elements	References
1	Egg shell	Mg, Sr	(Wu et al. 2023)
2	Bovine bone	Na, K, Mg, Sr, Zn	(Ratnayake et al. 2024)
3	Fish scale	Mg, Sr, Na, and K	(Paul et al. 2017)
4	AMBP	Na, Fe, Mg	(Jyoth et al. 2017)
5	Starfish	Na, Fe, Mg	(Rodríguez-Lugo et al. 2017)
6	Sea urchin	Na, Fe, Mg	(Gómez Vázquez et al. 2020)
7	Cuttlefish bone	Na, Fe	(Venkatesan et al. 2018)
8	Goose barnacle	Na, Fe, Mg	(Albuquerque et al. 2016)
9	Sea Crab	Mg	(Gibbs and Bryan 1972)
10	Sand dollar	Mg	(Ehrlich et al. 2010)

Table 2.7 Trace elements and its biological effects

Trace element	Biological effects	References
Zinc	Inhibit osteoclast cell formation	(Shepherd et al. 2014; Webster et al. 2002)
	Avoid osteoporosis	(Ito et al. 2005)
	Increase angiogenesis	(Lima et al. 2010)
	Improve the differentiation of osteogenic cells	(Bhattacharjee et al. 2014; Cuzzo et al. 2020; Ishikawa et al. 2002; Matsunaga 2008; Yu et al. 2017)
Magnesium	Cell adhesion and enhance bioactivity	(Silva et al. 2020)
	Stimulate cell differentiation	(Wu et al. 2019)
Fluoride	Stimulate osteoblast activity	(Li et al. 2015b)
	Avoid osteoporosis	(Aoba 1997)
	Hinder osteoclast proliferation	(Liu et al. 2019)
	Enhance strength and corrosion resistance	(Chen and Miao 2004)
Silicon	Enhance cell differentiation	(Gao et al. 2016)
	Improve osteogenic differentiation	(Sun et al. 2018)
	Enhance mechanical property	(Rodrigues et al. 2017; Yamada et al. 2019)
Strontium	Absence of cytotoxicity	(Ge et al. 2018)
	Enhance osteoblast activity and proliferation	(Olivier et al. 2020)

2.8. β -TCP based bioceramics

β -tricalcium phosphate (β -TCP) is a widely utilized and effective artificial bone substitute. It is osteoinductive in addition to osteoconductive. β -TCP is resorbable and easily replaced by new bone, in contrast to sintered HA. Because of its solubility, which is similar to that of bone mineral, β -TCP is not soluble under physiological conditions. Instead, it is resorbed by cells, most often osteoclasts, which cause a local acidity that causes β -TCP to dissolve. β -TCP crystallizes in rhombohedral space group with lattice parameters $a=10.439 \text{ \AA}$, $c=37.375 \text{ \AA}$ (Dickens et al. 1974). There are 42 PO_4 groups and 63 Ca atoms in a single β -TCP unit cell. Ca atoms are dispersed across five distinct Ca locations as shown in Figure 2.11. The sites Ca (1), Ca (2), and Ca (3) have eight to nine coordinated oxygens in their general positions, whereas the sites Ca (4) (highlighted in yellow) and Ca (5) have a peculiar position with an effective multiplicity of one-third of the other cation sites. Growing use of β -TCP as a biocompatible coating for apatites and bone prostheses or repair of missing bone has been observed. Additionally, TCP can be used as a precursor to make apatites. β -TCP has a solubility in water that is approximately double that of hydroxyapatite. β -TCP can be synthesized by solid-state reaction, thermal conversion, and precipitation.

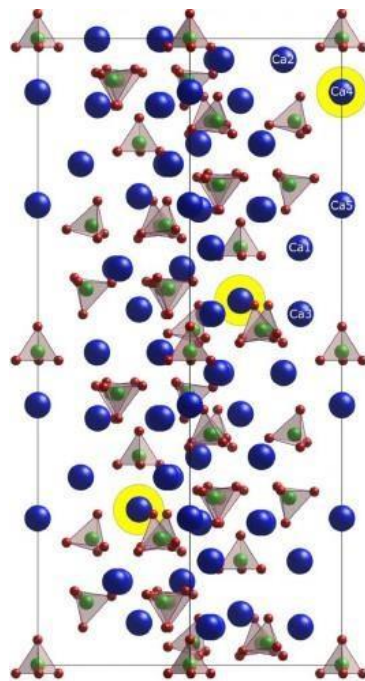


Fig. 2.11. Crystal structure of β -TCP

2.8.1 Synthesis methods

2.8.1.1 Solid-state reaction

β -TCP can be synthesized through the solid-state reaction of a calcium-rich phase, such as calcium carbonate (CaCO_3 ; CC) (Bigi 1997; Enderle et al. 2005; Famery et al. 1994; Jinlong et al. 2001), calcium hydroxide (Ca(OH)_2) (Jinlong et al. 2001) and HA (Bohner et al. 1997; Lin et al. 1998) with a phosphate-rich phase, such as dicalcium phosphate (CaHPO_4 ; DCP) (Famery et al. 1994; Jinlong et al. 2001), dicalcium phosphate dihydrate ($\text{CaHPO}_4 \cdot 2\text{H}_2\text{O}$; DCPD) (Bigi 1997), calcium pyrophosphate ($\text{Ca}_2\text{P}_2\text{O}_7$; CPP), or ammonium phosphate ($(\text{NH}_4)_2(\text{HPO}_4)$) (Enderle et al. 2005). The reaction between DCP and CC can be expressed as:

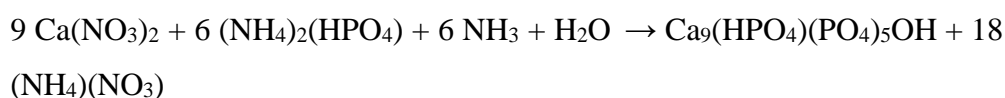


It is essential to take extra precautions to ensure thorough mixing of the two raw materials in order to achieve phase pure β -TCP. Inhomogeneous distribution of two components can lead to the appearance of contamination phases, such as β -CPP in phosphate-rich domains and HA in Ca-rich domains. For this purpose, an intermediate pre-sintering and homogenization process (for example, at 900 °C) would be helpful (Bohner et al. 1997). Additionally, it is recommended to utilize raw materials with compositions similar to β -TCP (Ca/P molar ratio = 1.50), such as hydroxyapatite (Ca/P = 1.67) and dicalcium phosphate (Ca/P = 1.00). However, obtaining pure calcium carbonate (Ca/P = ∞) or ammonium phosphate (Ca/P = 0.00) powders is far simpler than obtaining pure calcium phosphate phases. The introduction of ammonium phosphate in a solid-state process induces melting, leading to the formation of β -tricalcium phosphate (β -TCP) characterized by strong agglomeration (TenHuisen and Brown 1999). Furthermore, ammonia vapours are extremely corrosive and toxic, which can harm metallic labware.

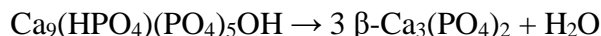
2.8.1.2 Thermal conversion

A popular approach for producing β -TCP is thermal conversion of either calcium-deficient hydroxyapatite ($\text{Ca}_9(\text{PO}_4)_5(\text{HPO}_4)\text{OH}$; CDHA) (Akao et al. 1982; Brazete et al. 2018; Chaair et al. 2017; Destainville et al. 2003; Eder et al. 2014; Gibson et al. 2000; Grigoraviciute-Puroniene et al. 2017; Ishikawa et al. 1993; Jarcho et al. 1979; Kannan et al. 2009; Raynaud et al. 2002; Torres et al. 2016) or amorphous

calcium phosphate (ACP) (Bohner et al. 2008; Kanazawa et al. 1982; Maciejewski et al. 2008; Somrani et al. 2003; Vecbiskena et al. 2015) above 650-750 °C. Calcium nitrate ($\text{Ca}(\text{NO}_3)_2$) (Brazete et al. 2018; Enderle et al. 2005; Ishikawa et al. 1993; Jarcho et al. 1979; Kannan et al. 2009; Lin et al. 1998; Ruiz-Aguilar et al. 2018; Sanosh et al. 2010), calcium hydroxide (Akao et al. 1982), ammonium phosphate ($(\text{NH}_4)_2(\text{HPO}_4)$) (Brazete et al. 2018; Enderle et al. 2005; Grigoraviciute-Puroniene et al. 2017; Jarcho et al. 1979; Kannan et al. 2009; Lin et al. 1998; Ruiz-Aguilar et al. 2018; Torres et al. 2016), and phosphoric acid (H_3PO_4) (Akao et al. 1982; Chaair et al. 2017) are common raw materials utilized for the aqueous precipitation of ACP and CDHA. Ammonia (NH_3) is added to the precipitation procedure to maintain a consistent pH while using calcium nitrate and ammonium phosphate:



The final thermal transformation into β -TCP is:



β -TCP produced through conversion of ACP or CDHA is more homogenous than that produced by solid-state reactions (Torres et al. 2016). Moreover, it provides a chance to add elemental impurities, such as zinc (Kannan et al. 2009) or magnesium (Torres et al. 2016), by mixing zinc or magnesium nitrate in the solution. However, particles are still agglomerated.

2.8.1.3. Precipitation

It has been demonstrated that β -TCP precipitates in organic environments, such as methanol (Bow et al. 2004), tetrahydrofuran (Makarov et al. 2010), ethyl propionate (Kjellin et al. 2016), and ethylene glycol (Erhart et al. 2012; Galea et al. 2013; Stähli et al. 2016; Tao et al. 2008, 2009). Additionally, it has been noted that β -TCP can be produced while autoclaving ACP (TOYAMA et al. 2002; Vani et al. 2009) and α -TCP (Galea et al. 2015; Raymond et al. 2018). Phase-pure β -TCP has occasionally been produced by combining chemical synthesis with autoclaving (Zhu et al. 2015).

Typically, the β -TCP particles produced through this process are in the nanometer range.

2.9. Biphasic calcium phosphates

Biphasic calcium phosphates (BCP) are made up of two distinct phases of CaP, usually from a more soluble phase (β -TCP) and a more stable phase (HA), in varying amounts. Compared to previous CaP bioceramics, this combination offers a number of advantages, including improved control over bioactivity and biodegradation, which ensures the stability of the biomaterial and encourages bone ingrowth. BCP ceramics have the potential to become osteoinductive and are osteoconductive. The chemical composition and physical characteristics of BCP ceramics influence the biological response, which can result in varying rates and patterns of bone regeneration. It is important to distinguish the term BCP from composite that is composed of two or more constituents having notably dissimilar physicochemical properties. There are two main categories of BCP formulations: 1) BCP that includes CaP phases with comparable molar Ca/P ratios (like α -TCP and β -TCP, where Ca/P = 1.5 for both); 2) BCP that includes CaP phases with distinct molar ratios (like β -TCP and HA, where Ca/P = 1.5 and 1.67, respectively). The primary idea behind the application of BCP is to increase the biological qualities of bio ceramic materials, such as their bioactivity, bioresorbable, osteoconductive, and osteoinductivity, in order to promote the production of new bone tissue (Lobo and Livingston Arinzeh 2010). It is important to emphasize that the rate and pattern of the production of new bone might be affected by a delayed or quick biodegradation rate. Consequently, the primary benefit of the BCP has the ability to adjust the ratio of more stable to more biodegradable phases to maximize the rate of biodegradation and improve the process of bone regeneration for a given application.

Particle sizes, crystallinity, specific surface area, porosity, and chemical composition are some of the variables that affect how quickly BCP degrades. It is established that the biodegradation of BCP *in vivo* and *in vitro* both adhere to a similar pattern. The following is a widely acknowledged pattern of the biodegradation of the several BCP stages in ascending order: HA < β -TCP < α -TCP; α -TCP exhibiting the greatest rate of biodegradation. The types of accessible chemical phases (HA/TCP) and

their percentage ratio determines the biodegradation kinetics of BCP with equal particle size and porosity; more the ratio of TCP, more the biodegradation rate of BCP. But there are other elements that affect the biodegradation process as well. For example, reduced porosity and surface area or increased crystallinity and larger particle sizes are linked to a slower rate of biodegradation (Radin and Ducheyne 1994). BCP biodegradation *in vivo* is typified by a rise in overall porosity and a decrease in crystal size (LeGeros et al. 2003). The scaffolds used in bone tissue engineering should mimic the physicochemical characteristics of the bone extracellular matrix (ECM). BCP bioceramics, which have a mineral composition similar to that of natural bone, best represent the inorganic phase of the bone extracellular matrix. During the biodegradation process, the less stable TCP phase creates space for new bone ingrowth, while the more stable HA phase can act as a structural framework to support the scaffold and newly formed bone.

2.9.1 Synthesis methods

In order to develop BCP bioceramics with varied HA/ β -TCP ratios that mimic the biological and physical characteristics of real bones, several methods have been established. However, the creation of bone substitute materials that resemble real bone has only been somewhat successful up to this point, which highlights how intricate natural structures are. The most common method for preparing BCPs that is currently accessible involves sintering non-stoichiometric CaP (such as CDHA and ACP) at temperatures higher than 750 °C (Natasha et al. 2014). Compared to other preparation methods, this one is easier to use, more affordable, and avoids the labor-intensive purifying step. ACP and CDHA have also been sintered using a variety of modifications, including two-step sintering (Lukić et al. 2011) and microwave heat processing (Farzadi et al. 2011; Manjubala and Sivakumar 2001; Veljović et al. 2010b; a). The chemical reaction of a thermal decomposition of CDHA is.



BCP which consists of HA and β -TCP can be produced because of this reaction. Based on the diffusion of OH^- and Ca^{2+} ions, a suitable solid-state transition mechanism was provided for this decomposition (Dorozhkin 2003; Dorozhkina and Dorozhkin 2002).

It is significant to note that, under precisely equal conditions, the initial numerical Ca/P ratio of CDHA affects the sintered grain sizes of BCP, with the average grain size decreasing as the Ca/P ratio increases (Descamps et al. 2013).

An alternative method of preparation relies on high-temperature solid-state reactions between two solid substances. Examples include the solid state reactions between TCP and Ca(OH)_2 (RAO et al. 1997), monocalcium phosphate monohydrate ($\text{Ca(H}_2\text{PO}_4)_2 \cdot \text{H}_2\text{O}$) and CaCO_3 (Hsu 2003; Jaw 2006), calcium hydrogen phosphate dihydrate (brushite, $\text{CaHPO}_4 \cdot 2\text{H}_2\text{O}$) and calcium carbonate (calcite, CaCO_3) (Tadjiev et al. 2007; Yang and Wang 1998). Therefore, in order to prepare BCP, the selected compounds containing Ca and P are first mixed in known amounts to obtain the required Ca/P ratio (1.50–1.67), which is then followed by heating and sintering. Furthermore, BCP can also be produced by mechanically combining the required quantities of either the separate powders of HA and TCP (Kreethawate et al. 2014; Nilen and Richter 2008; Yang et al. 2006; Zhang et al. 2007a; b) or their precursors. When compared to BCP bioceramics made by thermally decomposing CDHA powder, mechanically blended bioceramics were found to have both an increased amount of dissolution (Bouler et al. 1996) and a lower sintering performance (Jun et al. 2006). However, it was discovered that the mechanically blended BCP had a higher weight gain than the precipitated BCP when it came to soaking in simulated bodily fluid (Yang et al. 2006).

2.10 Clay minerals

Clay minerals are unique types of minerals that are found on earth in environments close to the planetary surface. These environments contain various amounts of ions such as calcium, magnesium, iron, alkali metals, alkaline earth metals and other cations. They originate from the diagenetic and hydrothermal modification of rocks in the presence of water and are regarded as significant components of soil. Fine-grained sedimentary rocks like mudstone, siltstone, and shale are frequently home to them. Because they have an uneven electrical charge on their surface, clay minerals can absorb water and dissolved plant nutrients that have been stripped from other minerals, making them behave as "chemical sponges". Since water is necessary for the formation of clay minerals, most clay minerals are referred to as hydrous aluminium silicate or hydrous aluminium phyllosilicate. Clay minerals have historically been used mostly in

industrial and cosmetic items, but their range of uses is constantly growing to include pharmaceuticals, which includes tissue engineering and drug delivery. In the last several years, the scientific world has been much more interested in clays because of their easily modifiable composition and structure for a variety of uses. Clay nanostructure can be tailored to adjust its mechanical and rheological characteristics as well as its ability to trap moisture for a specific purpose, largely because of its small particle size and structural flexibility. Different biomolecules can intercalate between clay layers due to the nature of clay. These biomolecules have controlled release capabilities that make them useful for drug delivery applications.

Clays are finely grained, layered, phyllosilicate minerals that occur naturally. In general, they are made of water, silica, alumina, and magnesia. Clays have been utilized for a wide range of purposes since the dawn of human civilization. Indigenous tribes in Asia, Africa, and America use them as antiseptics and as cures for skin, fever, and digestive issues due to their proven natural healing properties (Gaharwar et al. 2019). These days, with the field of biomedical research seeing unparalleled progress, clays are an intriguing class of building blocks for the development of new hybrid functional materials. Because of their intriguing structural diversity and chemical qualities, clays have been used in medicine in addition to being used as stabilizers and reinforcing agents in a variety of paint and polymer industries (Murugesan and Scheibel 2020).

Engineered clay nanomaterials are a broad range of hybrid nanocomposites that combine clays with different biomaterials, inorganic nanoparticles, and a variety of polymers (Ghadiri et al. 2015; Guo et al. 2018). The physicochemical properties of polymer-clay nanocomposites (PCNCs) are superior to those of natural clay. These properties include increased strength and density, increased surface area, increased flame retardant ability, and tailored electrical, optical and magnetic properties. As a result, PCNCs find applications in a variety of fields, including pharmaceuticals, wastewater treatment, aeronautical engineering, house building, and the oil and automotive industries (Guo et al. 2018).

For example, Ajmal et al. created biodegradable implants using vinyl triethoxysilane-grafted sepiolite clay with Poly-3-hydroxybutyrate-hydroxyvalerate

(PHBV) (Ajmal et al. 2018). Sheikhi et al. have demonstrated the potential benefits of laponite clay composite combined with doxorubicin hydrochloride (DOX), alginate acid, and sodium salt for the treatment of cancer (Sheikhi et al. 2018). Drug delivery has been attempted by Wang et al. using hydrotalcite clay combined with chemically synthesized poly (acrylic acid-isopropyl acrylamide) (Wang et al. 2012). Posati et al. have shown how polyurethane containing aromatic polyether soft segments can be used in conjunction with sodium montmorillonite (Na-MMT) composite to promote wound healing (Posati et al. 2014).

An intriguing variety of engineered clay nanomaterial is organoclay (Jain and Datta 2014). Hydrophobic clays are necessary for the transportation of organic materials, including DNA molecules and drugs. Consequently, the hydrophilic clay undergoes organic alteration to provide it hydrophobicity. For instance, Lin et al. modified MMT with hexadecyltrimethylammonium (HDTMA) to create a new organoclay that intercalates DNA in its interlayer spacing quickly (LIN et al. 2006). Lee et al. opined that these hydrophobic organoclays are easily able to build composites with various polymer types to create new hybrid functional materials that are beneficial for biomedical applications such as drug delivery and tissue engineering (Lee and Fu 2003). They are ready to be used in combination with hydrophobic polymers for delivery of drugs. For instance, PDMS (polydimethylsiloxane) is used to create a composite from Closite30B (commercial name of organoclay), which is essentially organically modified MMT, in order to deliver the drug metronidazole (Vasilakos and Tarantili 2012).

2.10.1. Types of clays

Clays can be broadly classified into two basic varieties based on where they come from: natural clay and synthetic clay. Generally, tetrahedral silica and octahedral alumina or magnesia alternate in various ratios to form clays. Three types can be distinguished from clays based on this structural factor as shown in Figure 2.12. These include (a) 1:1 structure, characterized by one octahedral layer linked to one tetrahedral layer, found in minerals such as kaolinite, halloysite and rectorite; (b) 2:1 structure, where two tetrahedral sheets are attached to each side of an octahedron, as observed in minerals like montmorillonite, bentonite, saponite, hectorite, laponite,

vermiculite and sepiolite; and (c) 2:1:1 structure, such as in chlorites, where brucite like layers are intercalated between the tetrahedral-octahedral-tetrahedral layers of aluminosilicates (Nazir et al. 2016; Uddin 2008).

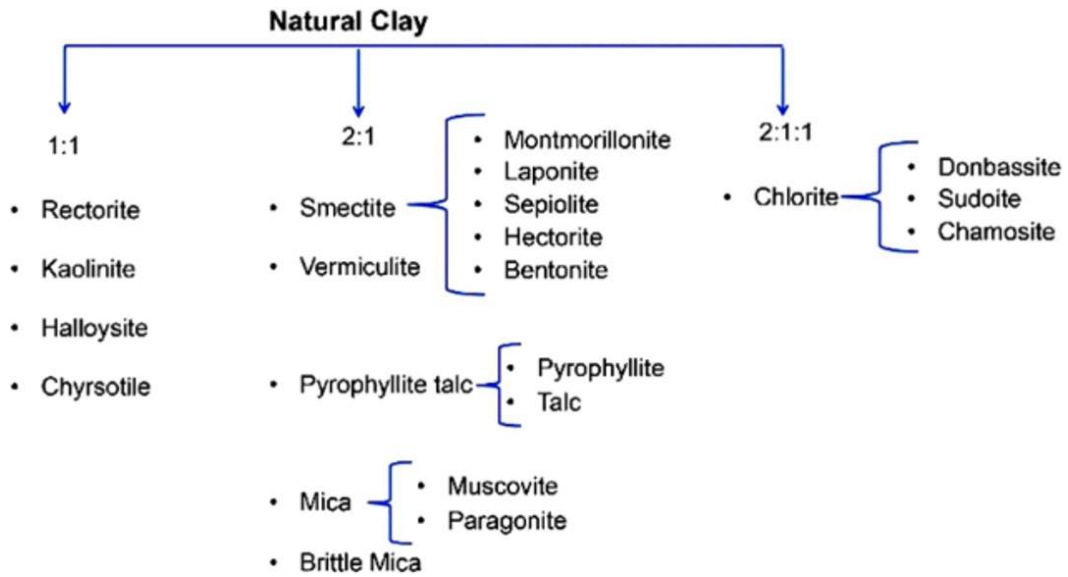


Fig. 2.12 Different types of clay (Singh 2022)

2.10.1.1. Type 1:1 clay mineral

The most common 1:1 clay mineral in soils is the kaolinite group, which comprises dickite, nacrite, halloysite, and kaolinite. Each crystalline unit of these has one silicon tetrahedral and one aluminium octahedral sheet. The oxygen anions, shared by both the silicon and aluminum cations within their respective sheets, play a crucial role in tightly binding the tetrahedral and octahedral sheets within a layer of a kaolinite crystal. Hydrogen bonding, in turn, holds these layers together. As a result, when the clay is wetted, the structure is fixed and there is typically no expansion between layers. A 1:1 type mineral particle's structural layers prevent the entry of cations and water. Kaolinite's effective surface is limited to its external surface area or its outer sides. Typically, kaolinite crystals have a hexagonal form. The strong binding forces that hold kaolinite particles together prevent them from easily breaking down into incredibly thin plates. Kaolinite shows very little cohesiveness, swelling, shrinking, or plasticity.

2.10.1.2. Type 2:1 clay mineral

An octahedral sheet positioned between two tetrahedral sheets defines the crystal units (layers) of these types of minerals. This fundamental crystal structure belongs to three broad groupings. Smectite and vermiculite are two of the expanding type clay minerals while the third one mica group (illite) is non expanding. The minerals montmorillonite, beidellite, nontronite, bentonite and sepiolite are members of the smectite group. The structure of smectite is shown in Figure 2.13. When wetted, the interlayers in this group of minerals swell and expand. As soon as water enters the interlayer gap, the layers are forced apart. The most common member of this category in soils is montmorillonite. Smectite's flake-like crystals are made of a clay mineral with an expanding lattice 2:1 type. An octahedral sheet is layered between two tetrahedral (silica) sheets to form each layer. Extremely weak links between oxygen and cations and between oxygen and oxygen hold the layers together slackly. The crystal lattice expands as a result of exchangeable cations and related water molecules being drawn between layers. The internal surface of clay crystal is larger than its outward surface. In certain locations of the octahedral sheet of montmorillonite, magnesium replaces aluminium. Similarly, aluminium may take the place of some silicon atoms in the tetrahedral sheet. These replacements result in a negative charge. These minerals exhibit strong swelling, shrinking, and cation exchange capacities. When dried, wide cracks frequently appear in soils with a smectite predominance (such as Vertisols). Tilling such soils is challenging due to the extremely hard dry pebbles, or clods.

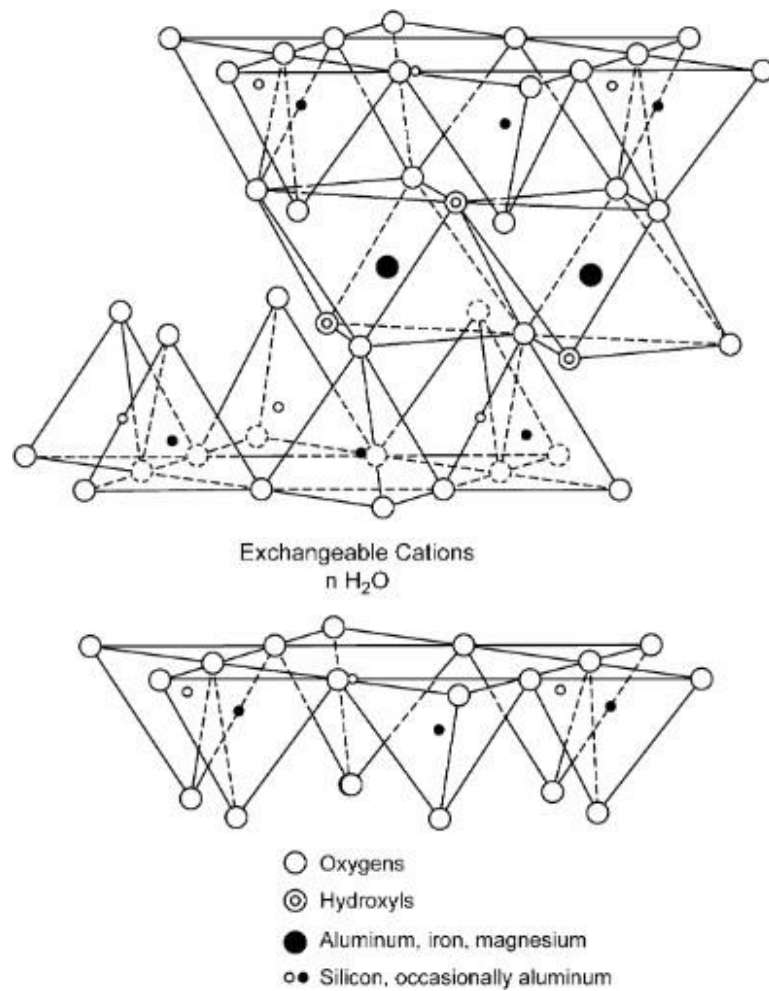


Fig. 2.13 Structure of smectite (Murray 2006)

Vermiculites resemble montmorillonite in their structure since they feature an octahedral sheet sandwiched between two tetrahedral sheets. Most vermiculite has a tetrahedral layer with silicon in most of the locations where aluminium used to be. The majority of the extremely high net negative charge connected to these minerals can be explained by this. In the interlayer space of vermiculites, water molecules are firmly adsorbed along with magnesium and other ions. Rather than functioning as wedges that pull the units apart, they essentially serve as bridges keeping them together. Compared to smectite, vermiculites swell to a lesser extent. Vermiculites are therefore regarded as limited expansion clay minerals since they expand more than kaolinite but substantially less than smectite. Because of the exceptionally high negative charge in the tetrahedral sheet, vermiculite has a higher cation exchange capacity (CEC) than any other silicate

clay. The crystals of vermiculite are significantly smaller than those of kaolinite, although they are larger than those of smectite. Illite, or micaceous minerals, share a basic structure with montmorillonite. The structure of illite is shown in Figure 2.14. Nevertheless, compared to smectite, the particles are substantially bigger. In the tetrahedral sheet, aluminium ions partially replace silicon ions (20%). Potassium ions balance the net negative charge in the tetrahedral sheet. By acting as a binding agent, potassium stops the crystal from expanding. As a result, micas with fine grains are not expanding at all. Fine-grained micas have less intense forms of hydration, cation adsorption, swelling, shrinkage, and plasticity.

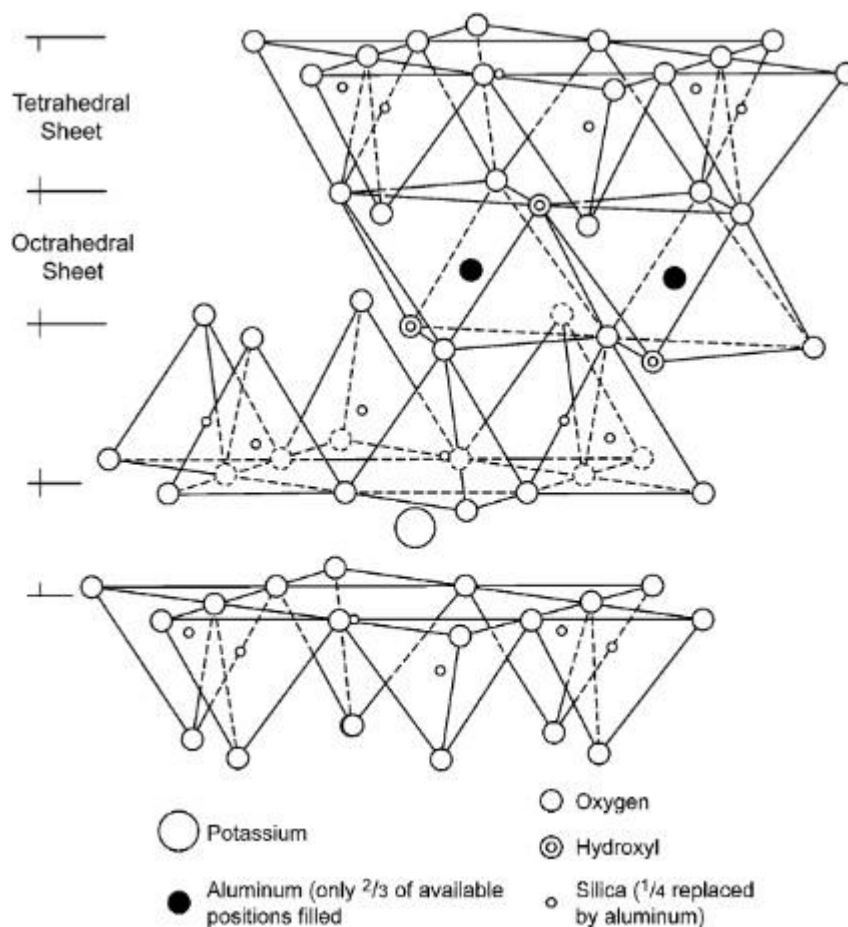


Fig. 2.14 Structure of illite (Murray 2006)

2.10.1.3. Type 2:1:1 clay mineral

Chlorites are representatives of this category. One 2:1 unit, such as mica or montmorillonite, and one octahedral unit, brucite, $Mg_3(OH)_6$ layer, make up the crystal unit of 2:1:1 type clay mineral. The 2:1 unit's octahedral sheet is dominated by magnesium. The non-expanding nature of this mineral is explained by the absence of water adsorption between the units of the chlorite crystal. The structure of chlorite is shown in Figure 2.15.

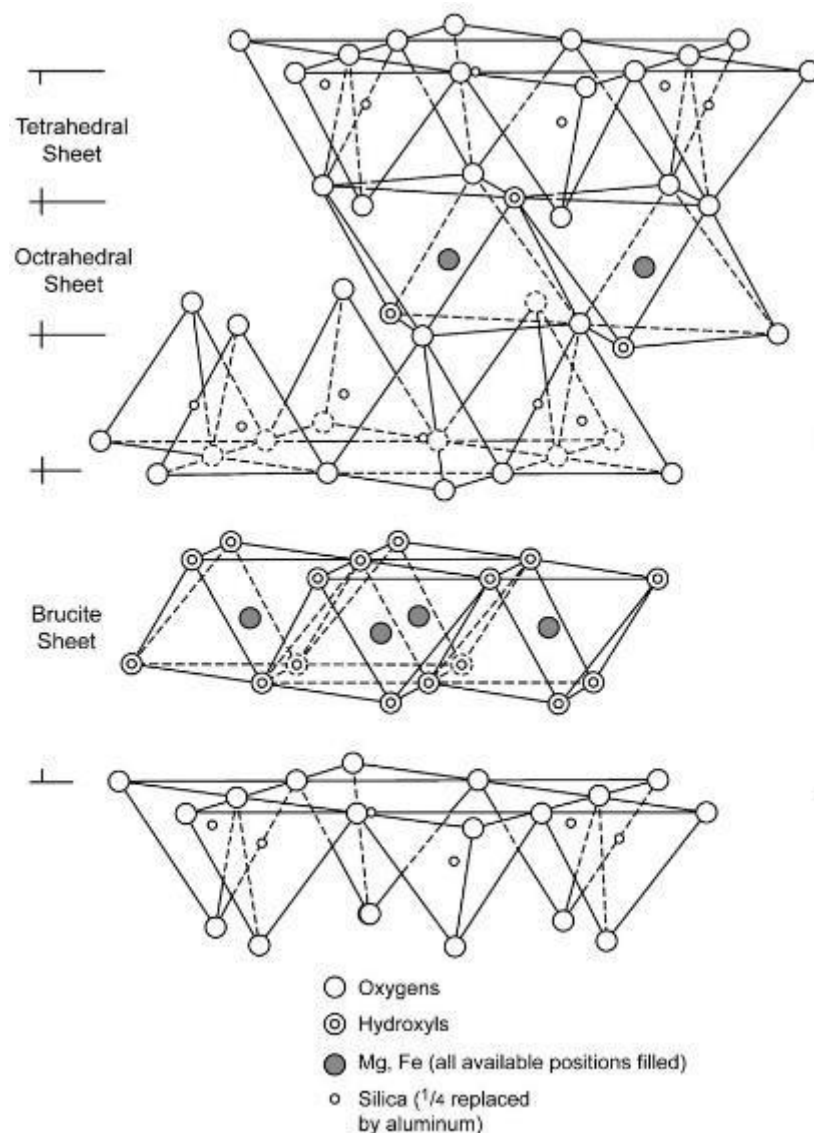


Fig. 2.15 Structure of chlorite (Murray 2006)

2.10.2. Structural characteristics of clay

The fundamental building blocks of clays are octahedral hydroxide and tetrahedral silicates, which are stacked in layers. The chemical compounds found in clay minerals, their symmetrical atomic and ion arrangements, and the forces holding them together define the characteristics of clay minerals. The complex silicates of different ions, including aluminium, magnesium, and iron, are the primary form of identification for clay minerals. The basic crystalline units of clay minerals can be classified into two categories based on the arrangement of these ions:

- The silicon-oxygen tetrahedron consists of four oxygen atoms encircling silicon, which comes together to create the silica sheet as shown in Figure 2.16 (a).
- The aluminium or magnesium octahedron is made up of six hydroxyl units encircling the aluminium atom, which joins to create a gibbsite sheet when the aluminium atom is the major dominating atom and a brucite sheet when the magnesium atom is the primary dominating atom as shown in Figure 2.16 (b).

The Si^{4+} cation is the most dominant atom in the tetrahedral sheet. A unit of Si atom surrounded by four oxygen atoms is known as a silica tetrahedra, and it is the fundamental building block of a tetrahedral sheet. As shown in Figure 2.16, the tetrahedral sheet is created by sharing three of each tetrahedra's oxygen with the three neighbouring tetrahedra. These oxygen atoms, referred to as basal oxygen, roughly unite all tetrahedra pairs in a single plane, while the fourth oxygen atom stays free and forms an apical oxygen. The apical oxygens join the octahedral and tetrahedral sheets together, and they are all located in a different plane. The eight-sided building unit known as an octahedron is created by the major dominant atoms in octahedral sheets, which are Al^{3+} or Mg^{2+} , surrounded by six oxygen atoms or hydroxyl groups.

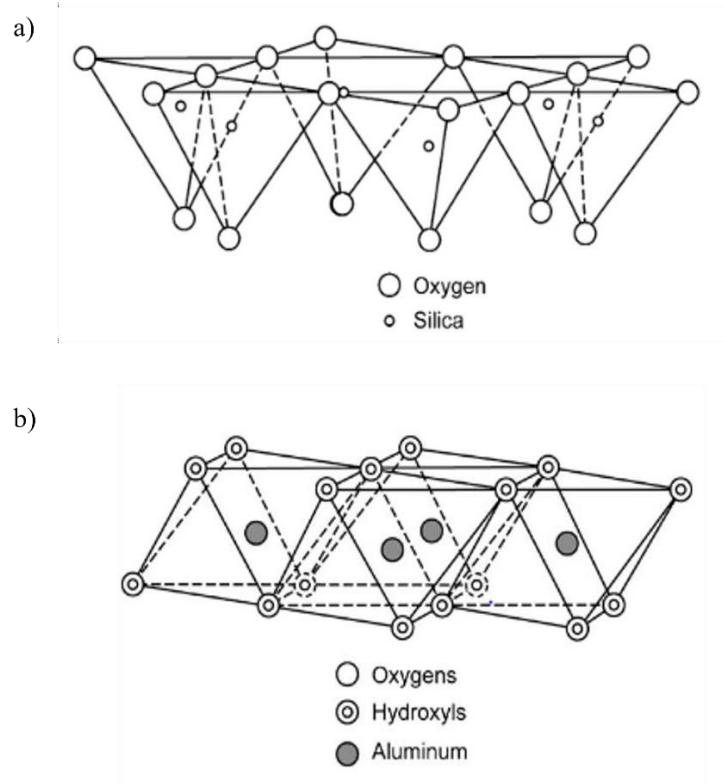


Fig. 2.16 Schematic of a) Tetrahedral sheet b) Octahedral sheet (Murray 2006)

It is essential to identify and distinguish between the various clay minerals based on this layering arrangement in the form of sheets. There are two kinds of clay minerals: negatively and positively charged. Clay minerals are employed as ion exchangers because of their distinct layered structure and charge content. In general, clay minerals can be divided into two classes based on their charge: cationic and anionic clay minerals. The negative-charged cationic clay minerals, such as smectite, are frequently found in nature. In smectite clay minerals, two tetrahedral sheets of silica are sandwiched by an octahedral metal oxide sheet (often Mg^{2+} or Al^{3+}). Anions in the interlayer spaces of anionic clay minerals, also known as layered double hydroxides (LDH), can change, and they can occupy a positive charge. LDHs can be used to produce a wide range of chemical compounds and several polymer clay nanocomposites. For instance, the cationic nanoparticles of an aluminosilicate like montmorillonite (MMT), have high interior surfaces and quadrilateral and octahedral sheets. Cationic clay minerals are composed of two quadrilateral plates with an octagonal twisted sheet integrated between them. The tetrahedral and octahedral sheets

have been arranged in ratios like 1:1 and 2:1 to introduce different kinds of clay minerals. An octahedral sheet between two tetrahedral sheets produces 2:1 clay mineral as shown in Figure 2.17 (such as smectite, chlorite, and vermiculite), whereas one tetrahedral and one octahedral sheet produces 1:1 clay minerals (such as kaolinite and serpentine). Clay minerals are classified as di-octahedral or tri-octahedral depending on the metal ions that are present on the octahedral sheets. Trivalent metal ions like Al^{3+} make a di-octahedral clay mineral, while divalent metal ions like Mg^{2+} and Fe^{2+} form a tri-octahedral clay.

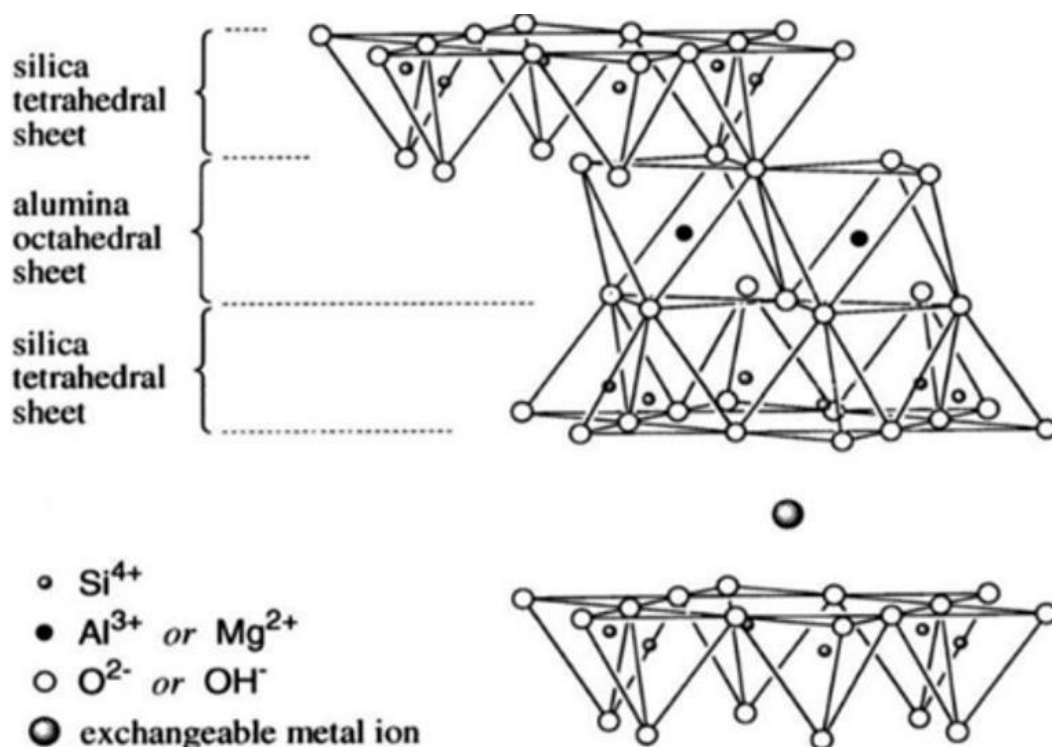


Fig. 2.17 Structure of 2:1 clay mineral (Murray 2006)

2.10.3. Formation of clay minerals

Other minerals undergo weathering and modification to become clay minerals. Numerous processes, including as chemical weathering, hydrothermal alteration, and sedimentation, can result in the creation of clay minerals as shown in Figure 2.18. The parent rock and the surrounding conditions determine the particular process that results in the production of clay minerals. Clay minerals are frequently formed by a process known as chemical weathering. Through chemical reactions with water and ambient

- **Small particle size:** The average particle size of clay minerals is less than 2 microns. Because of their small size and high surface area per unit weight, they are efficient ion exchangers and adsorbers.
- **High surface area:** Adsorbing and exchanging ions as well as adsorbing organic substances is made possible by the vast surface area of clay minerals.
- **Cation exchange capacity (CEC):** Clay minerals are able to absorb and exchange positively charged ions including calcium, magnesium, and potassium due to their high cation exchange capacity. They are beneficial to soil chemistry because of this characteristic, which helps to retain nutrients needed for plant growth.
- **Plasticity:** Because of its small particle size and large surface area, clay minerals can be moulded and shaped when combined with water.
- **Cohesion:** Clay minerals plate-like structure enables them to bind together to form a cohesive mass that can be molded and shaped.
- **Absorption and desorption:** Clay minerals may adsorb organic compounds, heavy metals, and contaminants, and can also absorb and retain water molecules.
- **Swelling:** Some clay minerals such as smectites may swell when hydrated, which makes it ideal for a number of uses, including drilling muds.
- **Chemical reactivity:** Minerals found in clay can react chemically with other substances to generate new minerals or change already existing minerals.

2.10.5 Applications of clay

Clay minerals like kaolinite and halloysite are frequently employed in the manufacturing of ceramics due to their ability to create strong, heat-resistant materials. Clay minerals like kaolinite and illite are employed in paint industry as fillers and pigments to improve the texture, durability, gloss of the final product. Additionally, kaolinite is utilized in the making of paper, where it serves as a coating and filler to increase the strength and brightness of the finished product. Because they can increase the end product's strength and longevity, clay minerals like smectite and illite are used to make bricks, cement, and other building materials. In environmental remediation, clay minerals like bentonite and montmorillonite are used to absorb and eliminate

pollutants from contaminated soils and water. These minerals are efficient at eliminating organic molecules, heavy metals, and other pollutants because of their large surface area and cation exchange capacity. Because of its distinctive tubular structure, halloysite is being investigated as a possible drug delivery system. This could assist to increase drug solubility and bioavailability. Drilling muds use clay minerals like bentonite and montmorillonite to regulate the drilling fluid's viscosity and pressure, as well as to cool and lubricate the drill bit. In order to lower greenhouse gas emissions, carbon dioxide can be sequestered that is, it can be trapped and stored underground using clay minerals. These minerals are good at absorbing carbon dioxide from the atmosphere because of their large surface area and adsorption capabilities. Several other applications of clay are represented in Figure 2.19.



Fig. 2.19 Different applications of clay minerals (Awasthi et al. 2019)

2.11 Kaolin clay minerals

One layer of a single tetrahedral sheet and one single octahedral sheet makes up the fundamental kaolin mineral structure, which is made up of the mineral's kaolinite, dickite, nacrite, and halloysite. The structure of kaolinite is shown in Figure 2.20. The apical oxygens of the silica tetrahedrons all point in the same direction, allowing the silicon atoms in the tetrahedral sheet and the aluminium in the octahedral sheet to share these oxygens and/or hydroxyls, which may be present to balance the charges. The structural formula for kaolinite is $\text{Al}_4\text{Si}_4\text{O}_{10}(\text{OH})_8$ & the chemical composition of kaolinite is SiO_2 , 46.5 %; Al_2O_3 , 39.5 %; and H_2O , 14 %. Kaolinite is a layered aluminosilicate, which is 1:1 dioctahedral phyllosilicate.

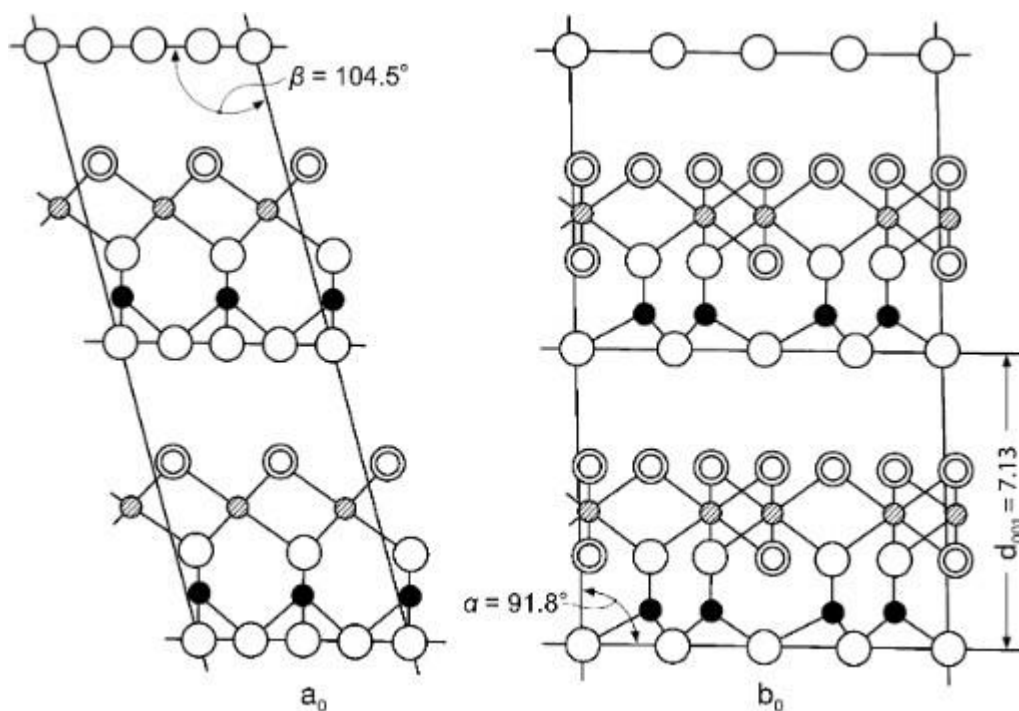


Fig. 2.20 structure of kaolinite (Aboudi Mana et al. 2017)

An aluminium atom only occupies two thirds of the octahedral positions. There are eight hydroxyls and four oxygen atoms surrounding each aluminium atom. The kaolinite structure charges are balanced. The minerals referred to as 1:1 layers consist of combined tetrahedral and octahedral sheets, which extend continuously in the a- and b-axis directions and are stacked one on top of the other in the direction of c-axis, make up the kaolin group's minerals such as, kaolinite, dickite, nacrite, and halloysite etc..

The way the unit layers are layered on top of one another determines the variations in the kaolin minerals. The unit layer thickness is 7.13 Å.

2.12 Bentonite clay

Bentonite is a clay that is commonly produced when volcanic ash is altered. The structural formula for bentonite is $\text{Al}_2\text{O}_3 \cdot 4(\text{SiO}_2) \cdot \text{H}_2\text{O}$. It is mostly composed of smectite minerals, most commonly montmorillonite. A cluster of lamellar platelets bound by electrochemical forces and containing interstitial water is known as montmorillonite. Three sandwich-arranged layers make up each platelet: two tetrahedral silica (SiO_2) layers and a core central octahedral alumina (Al_2O_3) layer as shown in Figure 2.21. Iron and magnesium are examples of lower valence metals that can isomorphously replace silicon and aluminium ions. Consequently, exchangeable cations, specifically calcium (Ca^{2+}), magnesium (Mg^{2+}), and sodium (Na^+) ions, as well as water molecules bound by ion-dipole forces, counteract the charge imbalance caused by these substitutions. These ions are the primary source of hydration in the crystal lattice because they are no longer able to remain inside the reticular structure and migrate to the exterior silica layers.

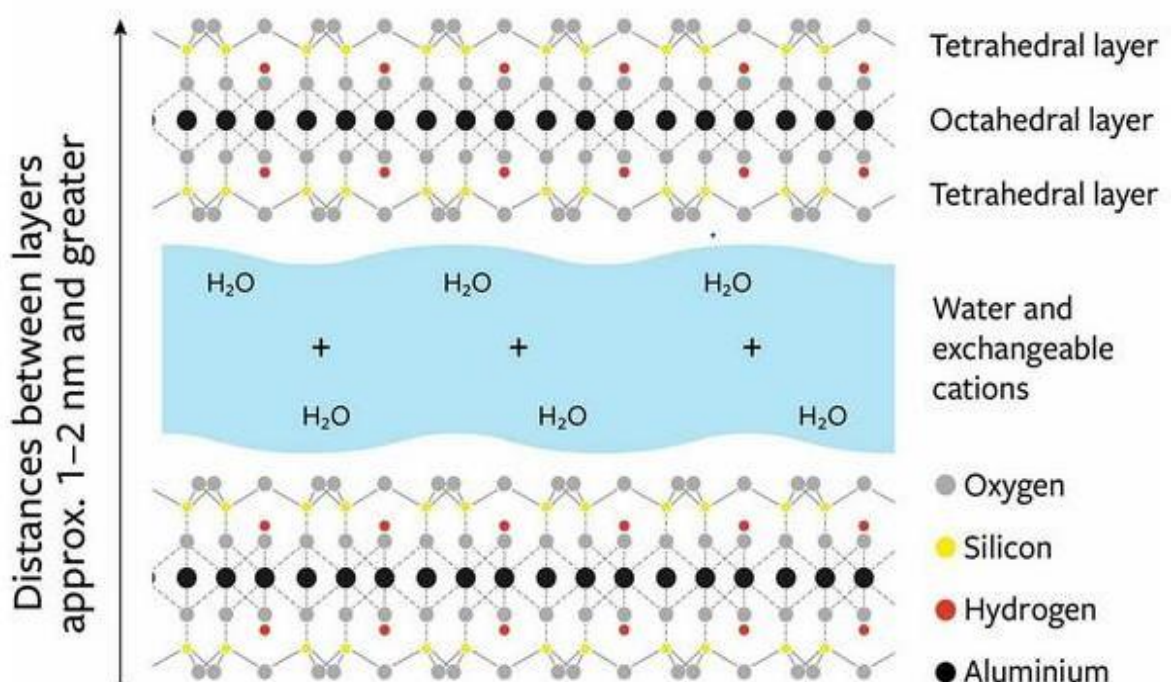


Fig. 2.21 Structure of bentonite (<https://www.scottlab.com>)

2.13 Structure of prawn exoskeleton

About 55–65 % of the weight of prawns are edible, with the remaining 35–45 % being biowaste that is used as fertilizer, animal feed mix, and a source of chitin and chitosan (Hansen and Illanes 1994). The structure of the prawn exoskeleton is shown in Figure 2.22. The exoskeleton/shell of prawns is composed of (a) 30–50 % calcite, (b) α -chitin (20–30 %), a nitrogen-containing polysaccharide, and (c) 30–40 % proteins, with trace amounts of calcium phosphates, magnesium, and other elements (Hansen and Illanes 1994; Shahidi et al. 1999). The multilayer stacking of chitin-protein fibres, which are sporadically arranged in the shape of a twisted woven structure to create a composite of chitin-protein, makes up the structure of prawn shells (Raabe et al. 2005). The gap between the fibers is filled with bio-minerals and proteins. The majority of the biominerals are crystalline calcium carbonate, or calcite (CaCO_3), however certain species may result in amorphous calcium carbonate as well. The most defining level of the overall hierarchy is known as a twisted plywood or Bouligand pattern, and it may be seen even under an optical microscope. The helicoidal stacking sequence of the fibrous chitin-protein layers forms this shape.

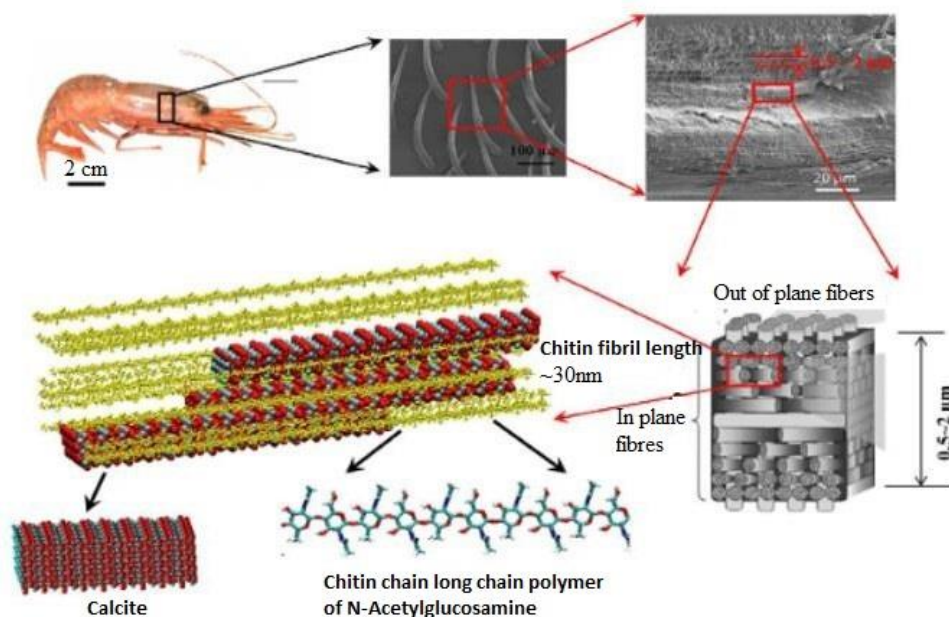


Fig. 2.22 Structure of prawn exoskeleton (Qu et al. 2015)

2.14 Scope and objectives of the study

Scope:

In tissue engineering, demand is more for innovative biomaterials with optimal mechanical, biological, and growth factor properties to trigger the body's inherent bone repair mechanisms. The use of scaffolds in scaffold-based tissue engineering is based on the effective fusion of biomolecules, living cells to support bone tissue regeneration and repair. The extraction and synthesis of biomaterials particularly calcium phosphates, produced from prawn shell exoskeleton opens up new avenues for the development of innovative medical products with potential uses in tissue engineering and other biomedical fields. Hydroxyapatite combined with clays such as kaolin and bentonite can be used as biomaterials for making scaffolds for bone tissue regeneration process. By doing this, the scaffold's biocompatibility with living cells will be increased. Kaolin and bentonite clays are abundant in nature and generally considered to be bioinert.

Objectives:

- To synthesize and characterize hydroxyapatite and biphasic calcium phosphate from prawn shell bio waste via wet chemical precipitation method.
- To synthesize and characterize β -TCP from prawn shell bio waste using solid state synthesis method.
- To fabricate and characterize dense calcium phosphate scaffolds with tailoring mechanical and physical properties.
- To develop hydroxyapatite-kaolin and hydroxyapatite-bentonite clay composites via solid state sintering method

CHAPTER 3

SYNTHESIS AND CHARACTERIZATION OF PURE HYDROXYAPATITE FROM PRAWN SHELL EXOSKELETON BIO WASTE

3.1 Introduction

The growing need for organ repair and replacement represents a global health concern for people. Most often, autologous and allogenic transplants are used to treat injured tissue. The significant risk of disease transmission and the lack of suitable donors pose limitations to these approaches. Artificial prostheses that can heal damage or failure or that can regenerate tissues are notable advances in the field of tissue engineering. With absence of the contributions of biomaterials mostly in the form of scaffolds that satisfy the criteria for ideal tissue growth, these advancements would not have been possible. Now, natural biomaterials play vital role in the design and manufacture of biocompatible prostheses, biomimetics, the creation of organized matrices for tissue regeneration and the understanding of specific cell functions (Brovold et al. 2018).

For application in bone tissue engineering, biomaterials having characteristics like those of bone tissue have been the subject of ongoing research. One useful method for simulating the extracellular matrix of bone tissue is the use of composites made of type I collagen and calcium phosphates. Through an osteoconductive mechanism, the bioactivity of hydroxyapatite (HA) ceramics can strengthen the formation of bone-bonds with other tissues (Ducheyne and Qiu 1999). HA can be extracted from natural sources like Mammalian (bovine bone, pig bone), marine resources (fish bone and fish scale), and shells (eggshells, sea shells, cockle shells and mussle shells) (Mohd Pu'ad et al. 2019). Origins of pork and bovine are frequently linked to religious beliefs and disease transmission (Nahar et al. 2015). Given the large evolutionary distance between marine resources and humans, marine sources are probably far safer and have a lower potential for disease transmission. Furthermore, marine resource byproducts are plentiful, and using them in biomedical applications would lessen environmental contamination and the risk of biohazards to people.

Powders of HA find primary application in the production of coatings for metallic implants, serving as initial ingredients for scaffold fabrication, or acting as fillers in polymer-matrix composites. Porous HA serves a significant role in the controlled release of drugs for bone-related conditions like bone tumors or osteoporosis. Loading drugs into porous HA granules or scaffolds facilitates localized and sustained drug release, thereby accelerating bone healing. While primarily utilized for bone defect repair, HA has recently garnered attention for emerging applications involving soft tissues, such as ophthalmology, wound regeneration, and anticancer therapies (Eliaz et al. 2017). HA is developed from prawn shell in the present work through wet chemical synthesis method. This work proposes that HA from prawn exoskeleton is an outstanding biomaterial candidate for bone tissue engineering applications.

3.2 Experimental procedure

3.2.1 Materials

Prawn (*Fenneropenaeus Indicus*) shells were collected from the local fish market which are abundantly available. Prawn exoskeleton is a raw source of CaCO_3 . The prawn shells were thoroughly cleaned with tap water and then with hot water. After washing, the prawn shell was dried in an oven at $150\text{ }^\circ\text{C}$ for 6 hours and then crushed to powder using agate mortar and pestle. This powder is subjected to calcination in muffle furnace to obtain calcium oxide (CaO). This CaO can be used as a raw precursor to derive hydroxyapatite.

3.2.2 Synthesis of pure hydroxyapatite

Wet chemical synthesis method is used to produce pure hydroxyapatite as shown in Figure 3.1. The prawn shell which is a source of calcite was calcined in a muffle furnace at $900\text{ }^\circ\text{C}$ for 12 hours at a rate of $10\text{ }^\circ\text{C}/\text{min}$ to obtain calcium oxide (CaO). This calcium oxide was mixed with distilled water and stirred with the help of magnetic stirrer continuously in a beaker. Meanwhile, orthophosphoric acid (85% H_3PO_4) was added very slowly dropwise to advance the reaction. Ammonia solution was employed to maintain the pH of the solution at 10 consistently during the reaction. Later this solution was transferred to closed container and stirred for 48 hours at room temperature. After process completion, a thick white solution of HA was precipitated; and then it was dried at $100\text{ }^\circ\text{C}$ in a hot air oven.

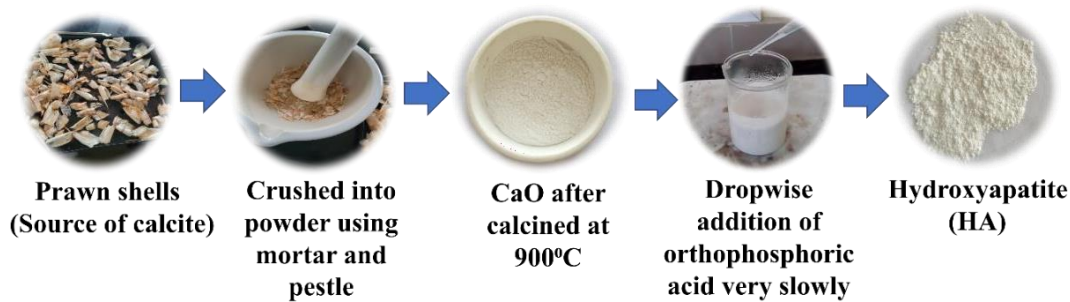
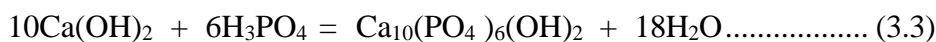
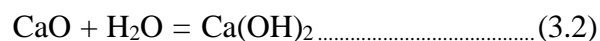
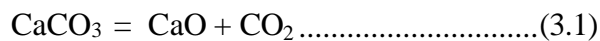


Fig. 3.1. Process flow diagram for synthesis of hydroxyapatite (HA)

The following reactions are involved in the synthesis of HA powder



3.2.3 Development of dense hydroxyapatite

A certain amount of HA powder (3gm.) is weighed and placed in the cleaned die and plunger. Cylindrical pellets were prepared with a length-to-diameter (L/D) ratio of 1.45 from HA powders by using a uniaxial hydraulic press with a load of 12.5 kN. These pellets were subjected to solid state sintering at 1100 °C (Ramesh et.al. 2012) for 2 hours, utilizing a heating rate of 10 °C/min in a high temperature programmable furnace. This process resulted in the formation of sintered dense HA pellets.

3.2.4 Characterization

The raw calcite (CaCO₃) powder which is derived from prawn exoskeleton is subjected to thermal analysis using a technique called differential scanning calorimetry (DSC, NETZSCH DSC 404 F1, Germany). This analysis aims to determine the appropriate calcination temperature (CaCO₃ to CaO). To determine the crystalline phases, present in calcite, calcined calcite and HA powder, X-ray diffraction (Empyrean 3rd Gen, Malvern PANalytical, Netherlands) method was used with the source of Cu K α radiation. XRD data was collected at room temperature over the 2 θ range of 10°-90° with a scan rate of 2°/min. Scherrer's equation, which is often used to calculate crystallite size based on diffraction peak width, is a well-known technique for analyzing X-ray diffraction patterns. Scherrer's formula, however, underestimates the crystallite size or only gives a lower bound since it fails to account for peak broadening caused by

other significant factors including instrumental effects and inhomogeneous strain. The X-ray diffraction peak broadening is typically caused by lattice strain in the material, instrumental broadening, and crystallite size. The diffraction peaks are generally widened because of the complex contributions of each of these phenomena. Adjusting for the instrumental effect is required prior to determining the size of the crystallite. The formula for estimating the instrumental corrected broadening β_{hkl} , which corresponds to the diffraction peak of HA is

$$\beta_{hkl} = [(\beta_{hkl} (measured))^2 - (\beta_{hkl} (Instrumental))^2]^{1/2} \dots \dots \dots (3.4)$$

The crystallite size “D” can be calculated by using Scherrer’s equation

$$D = \frac{K\lambda}{\beta \cos\theta} \dots \dots \dots (3.5)$$

where K is a dimensionless shape factor 0.9, λ is X-ray wavelength, β is full width at half maximum (FWHM) and θ is diffraction angle (Rabiei et al. 2020). Fourier transform infrared spectrometry (FTIR, PerkinElmer Frontier) was conducted to identify the chemical bonds in HA. Raman spectroscopy (Renishaw, UK) was used to identify the vibrational modes in HA from laser light of wavelength 530 nm. Field emission scanning electron microscopy (FESEM – 7610FPLUS, Jeol, Japan) coupled with Energy Dispersive Spectroscopy (EDS) at an accelerating voltage of 20 kV was used to investigate the surface morphology and microstructure. In order to determine the chemical states present in elements and composition of HA, X-ray photo electron spectroscopy (XPS) was used. The density measurement kit (CONTECH, India) was utilized to measure bulk density (B.D.), apparent density (A.D.) and apparent porosity (% of the open pore) (A.P.) by using equations 3.6, 3.7 and 3.8 respectively.

$$\text{Apparent density A. D.} = \frac{D}{D-I} \dots \dots \dots (3.6)$$

$$\text{Bulk density B. D.} = \frac{D}{S-I} \dots \dots \dots (3.7)$$

$$\text{Open porosity} = \frac{S-D}{S-I} \times 100 \dots \dots \dots (3.8)$$

Where D = Dry weight, I = Immersed weight, S = Soaked weight.

Mechanical properties such as compressive strength and compressive modulus were determined through a compression test by using a universal testing machine (UTM, SHIMADZU AG X-Plus 100kN, Japan) in accordance with ASTM F2027.

3.2.5 *In-vitro* biodegradation study

The controllable degradation behaviour of HA plays a crucial role in successful long-term implantation of a bone tissue substitute. The biodegradation of dense scaffolds which are prepared by uniaxial compaction of HA powders followed by sintering at 1100 °C was analysed in Tris-HCl buffer solution at different time points. 0.05 M Tris-HCl buffer solution was prepared using tris(hydroxymethyl)aminomethane (Tris) and distilled water. The solution's pH was regulated to approximately 7.4 at 37°C by adding 1 M HCl. At various time intervals (1 day, 3 days, 5 days, and 7 days), the scaffolds were extracted from the solution and subsequently dried. The initial weight (w_o) of scaffolds and final weight (w_t) of the scaffolds after removing from Tris solution at different time points has been recorded. To assess bioresorbability, the weight loss of the scaffolds (%) can be determined using the following equation.

$$\text{Weight loss (\%)} = \frac{w_o - w_t}{w_o} \times 100 \dots\dots\dots (3.9)$$

w_o = Initial weight of the scaffolds (g),

w_t = Final weight of the scaffolds (g) after soaking in Tris-HCl solution at different time points.

3.3. Results and Discussion

3.3.1 Structural analysis

The X-ray diffraction pattern of raw prawn shell and calcium oxide (CaO) obtained from prawn shell after calcination is shown in Figure 3.2. In Figure 3.2(a) XRD pattern of raw prawn shell powder confirmed the presence of CaCO₃ which is in the form of calcite with reference to ICDD: 00-047-1743. Interestingly, the prawn shell raw powders revealed the existence of α-chitin also along with the calcite. The peak positions of α-chitin along with their corresponding planes are 19.4° (110), 21.2° (120) and 23.7° (130). Calcite present in the raw prawn shell powders was converted into

calcium oxide through calcination at 900 °C. XRD pattern of calcium oxide is shown in Figure 3.2(b) with ICDD: 00-037-1497. This calcination temperature of 723 °C was obtained from DSC analysis which is shown by an endothermic peak (Figure A, Appendix).

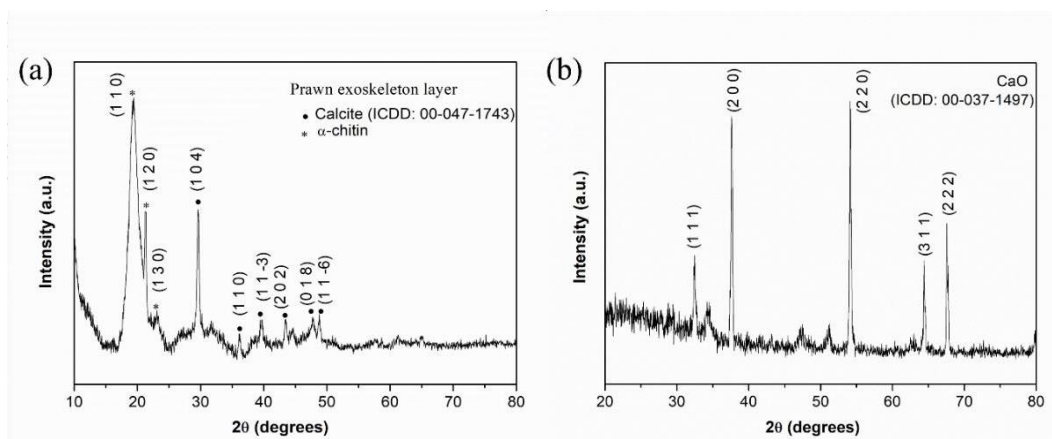


Fig. 3.2 XRD pattern of (a) as collected prawn shell (b) CaO (calcination at 900 °C) derived from prawn shell

X-ray diffraction pattern of as synthesized HA is shown in Figure 3.3. All peaks are well matched with the standard ICDD peaks of HA (ICDD: 01-074-0565). There were no secondary phases detected and the presence of sharp and distinct peaks indicates that obtained HA was pure and highly crystalline. The average crystallite size by using Scherrer's equation was found to be 65.3 nm.

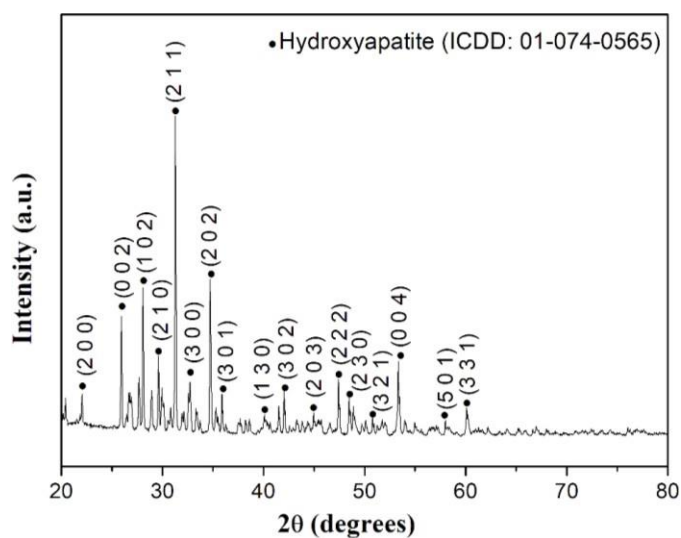


Fig. 3.3 XRD pattern of as-synthesised HA from prawn shell

3.3.2 Thermal analysis

The weight loss (%) versus temperature profile of prawn exoskeleton from the thermogravimetric analysis is displayed in Figure 3.4 (a). The derivative of TGA is represented by the blue line.

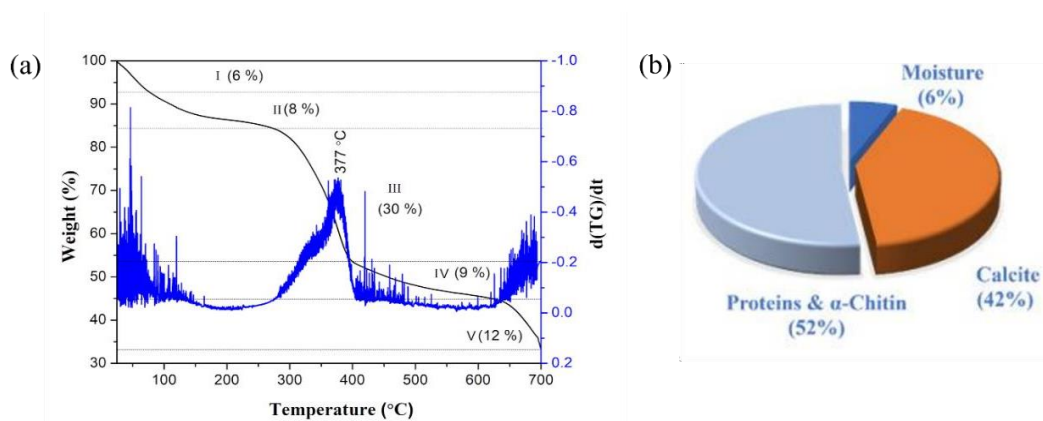


Fig. 3.4. (a) TGA plot of raw prawn shell powder (b) Prawn shell composition (weight%) drawn from TGA

The weight loss profile is broken down into five phases, ranging from stage I to stage V (Table 3.1). Proteins, α -chitin, and calcite make up the prawn shell. Stage I is the temperature range between 30 °C and 95 °C, during which water evaporates and causes a weight loss of about 6 %. Stage II temperatures vary from 95 to 270 °C, and the reason for the weight loss of approximately 8 % is the elimination of water and deproteinization. During stage III, there is a noticeable weight loss of approximately 30 % between 270 and 400 degrees Celsius. This weight loss is associated with (a) the molecule's saccharide structure degradation in α -chitin fibre, which includes the dehydration of saccharide rings, and (b) the α -chitin's decomposition. Stage IV temperature ranges between 400 °C to 625 °C are linked to a weight loss of less than 9 % because of the α -chitin's complete decomposition. Ultimately, stage V, which occurs between 625 and 700 °C, is similar to the calcination of calcite to CaO (weight loss ~ 12 %). As a result, even after heating to 900 °C, 27 % of the residual mass remains as CaO. Figure 3.3(b) shows the full compositional image of the prawn shell obtained from TGA. It contains 6 % moisture, 42 % calcite, and the remaining 52 % organic matter, which comprises proteins and α -chitin; these results are in good agreement with the existed literature.

Table 3.1: An overview of the weight loss profile of prawn shell from TGA.

Stage	Temperature interval (°C)	Weight loss (%)	Reasoning
I	30 - 95	6	Extraction of moisture
II	95 - 270	8	Extraction of moisture, deproteinization
III	270 - 400	30	Deproteinization, the breakdown of the saccharide structure within α -chitin and the subsequent decomposition of the α -chitin
IV	400 - 625	9	Decomposition of the α -chitin
V	625 - 700	12	Calcination of CaCO_3

3.3.3 Vibrational analysis

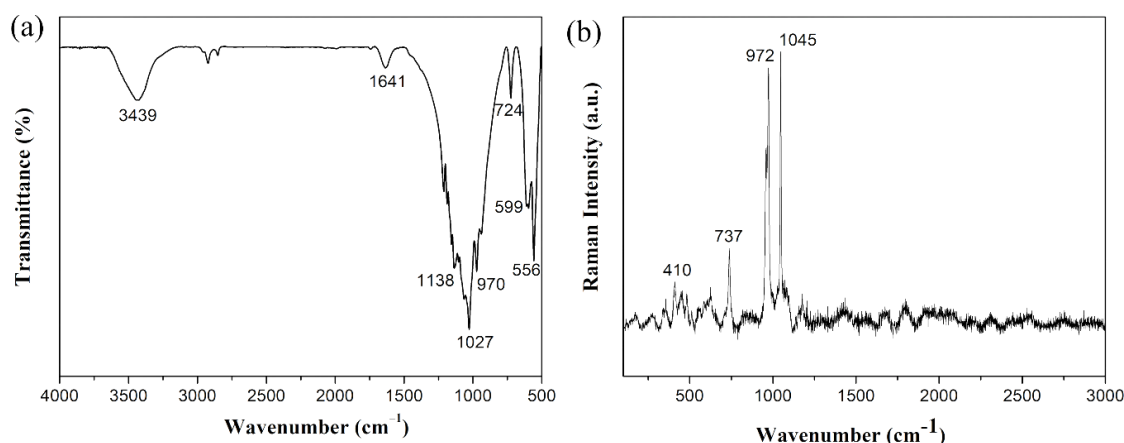


Fig. 3.5. (a) FTIR and (b) Raman spectra of as synthesized HA from prawn shell

FTIR spectra of as synthesized HA from prawn shell is shown in Figure 3.5

(a). The FTIR spectrum reveals the characteristic peaks around wavenumbers 556, 599, 724, 970, 1027, 1138 cm^{-1} due to the presence of phosphate group in HA. The peaks at 556, 599, 724 cm^{-1} are due to phosphate bending vibrations and the peaks at 970, 1027, 1138 cm^{-1} are due to phosphate stretching vibrations. A weak peak at 1641 cm^{-1} is due to traces of carbonate ions. Another broad peak which is at 3439 cm^{-1} corresponds to the stretching of structural OH^- band. Figure 3.5 (b) shows the Raman spectra of as synthesized HA derived from prawn shell. The band observed at 972 cm^{-1} corresponds

to the stretching (ν_1) symmetric vibrational mode of P–O. Additionally, the bands positioned near 410 cm^{-1} and 737 cm^{-1} correspond to the ν_2 (doubly bending mode) and ν_4 (triple degenerate bending mode) vibrational modes of PO_4 , respectively. Moreover, the ν_3 (triple degenerate antisymmetric stretching mode) vibrational mode of PO_4 was identified at 1045 cm^{-1} (Amenta et al. 2018).

Table 3.2 vibration modes in the FTIR spectrum of HA

Wavenumber, [cm^{-1}]	Stretching mode	Functional group
556, 599, 724	Asymmetric bending	PO_4^{3-}
970	Symmetric stretching	PO_4^{3-}
1027, 1138	Asymmetric stretching	PO_4^{3-}
1641	Asymmetric stretching	CO_3^{2-}
3439	stretching of OH^-	OH^-

Table 3.3 vibration modes in the Raman spectrum of HA

Wavenumber, [cm^{-1}]	Assignment	Vibration groups
972	Symmetric vibrational mode of P-O (stretching mode)	$\nu_1 \text{PO}_4^{3-}$
410	Doubly bending mode	$\nu_2 \text{PO}_4^{3-}$
1045	Triply generate antisymmetric stretching mode	$\nu_3 \text{PO}_4^{3-}$
737	Triply degenerate bending mode	$\nu_4 \text{PO}_4^{3-}$

3.3.4 Morphological analysis

SEM images of as synthesized HA from prawn shell and sintered HA are shown in Figure 3.6 (a-b). It demonstrated the existence of irregularly shaped, smaller, and more agglomerated particles with varying dimensions. An equiaxed grain structure was observed in sintered HA with an average size of $2.6 \pm 0.8\ \mu\text{m}$. The energy dispersive X-ray spectroscopy is conducted for prawn shell derived HA and results are shown in Figure 3.7. EDS spectrum reveals the presence of calcium, phosphorus, oxygen and various other trace elements like Mg, Na, Si, Fe. The weight percentage of Ca and P

are obtained as 40.6 % and 24.6 %. From this Ca/P ratio of obtained HA is 1.65. The weight percentages of other trace elements like Mg, Na, Si, Fe are obtained as 2.4 %, 0.8 %, 0.4 %, 0.6 % which help in rapid bone regeneration. During biomineralization and other bioactivities, trace elements are helpful. These ions can be very important since they directly promote the many metabolic processes related to bone metabolism in bone regeneration and repair (Akram et al. 2014).

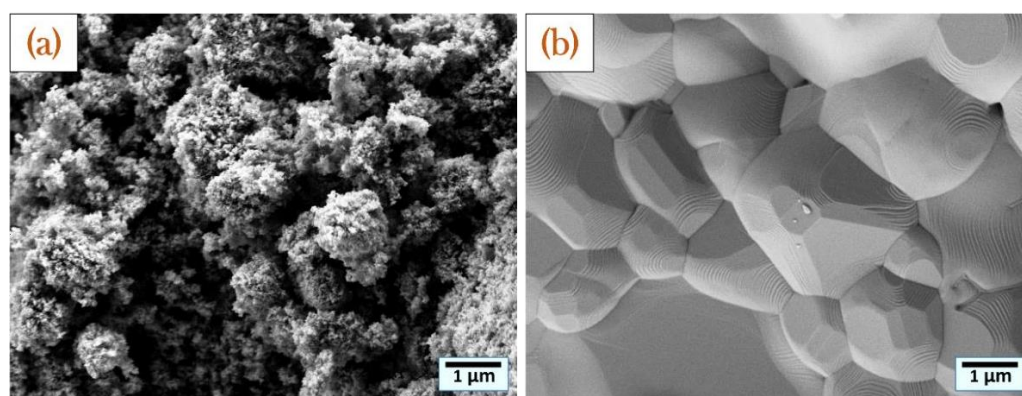


Fig. 3.6. SEM images of (a) as-synthesized HA powder (b) sintered HA (1100 °C) from prawn shell (*Fenneropenaeus indicus*)

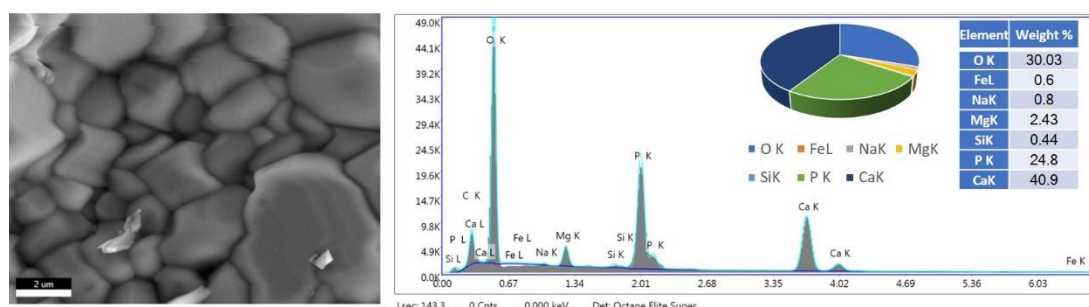


Fig. 3.7. Energy dispersive X-ray spectroscopic analysis of sintered HA

3.3.5 X-ray photoelectron spectroscopic (XPS) analysis

X-ray photoelectron spectroscopy is carried out for prawn shell derived hydroxyapatite to determine the chemical elements present and identify their chemical states. Figure 3.8 shows the survey spectrum and deconvoluted high-resolution spectra of various elements of hydroxyapatite and other elements respectively. XPS wide scan spectrum as shown in Figure 3.8 (a) confirms the peaks of the elements C 1s, O 1s, Ca

2p, P 2p, Si 2p, Na 1s, and Mg 1s. XPS spectra of Ca 2p peaks are identified at 347.42 eV ($2p_{3/2}$) and 351.02 eV ($2p_{1/2}$) (Figure 3.8(b)), which corresponds to Ca bonds in HA (Gomes et al. 2017). Figure 3.8(c) shows the high-resolution spectra of P 2p peaks where binding energies are identified at 133.44 eV and 134.49 eV. Binding energy at 133.44 eV attributes to P–C (Peng et al. 2017), and binding energy at 134.49 eV belongs to P–O bond in HA (Chusuei et al. 1999). Figure 3.8(d) shows the high-resolution spectra of O 1s peaks where binding energies at 531.67 eV, 533.38 eV are due to HA (Ortiz et al. 2022). Figure 3.8(e) shows the high-resolution spectra of Na 1s where binding energy at 1072.39 eV is assigned to the +1 state (Bharathi et al. 2019). Figure 3.8(f) shows the high-resolution spectra of Si 2p, where binding energy at 103.35 eV is assigned to the +2 state (Dora et al. 2020). Figure 3.8(g) shows the high-resolution spectra of Mg 1s where binding energy at 1305.07 eV is assigned to the +2 state (La et al. 2017).

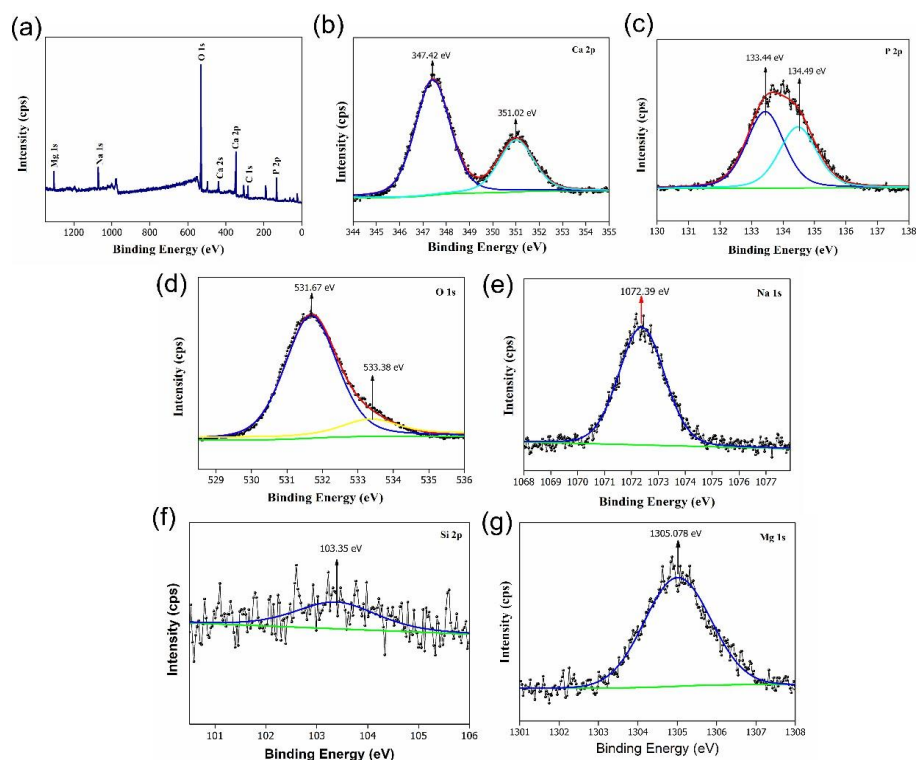


Fig. 3.8. XPS analysis validates the formation of phase pure HA from prawn shell. (a) Survey spectrum and deconvoluted high-resolution spectra of (b) Ca 2p, (c) P 2p, (d) O 1s, (e) Na 1s, (f) Si 2p, (g) Mg 1s

3.3.6 Biodegradation study of HA scaffolds

The biodegradation study was performed in accordance with ASTM F2150 standard. Figure 3.9 shows the weight loss of dense HA scaffolds after immersion in Tris-HCl solution at different time points (1, 3, 5, and 7 days). The initial profile exhibits a very slow rate of degradation for up to 5 days, which increases more after 7 days. This is due to ionic dissolution from HA surface into the Tris-HCl solution. The weight loss of dense scaffolds was calculated using equation 3.9 which was 1.2 % after 7 days. The factors influencing solubility or dissolution properties, such as the degree of micro porosity and macro porosity, chemical composition, and crystallinity bear a resemblance to those influencing biodegradation or bioresorption.

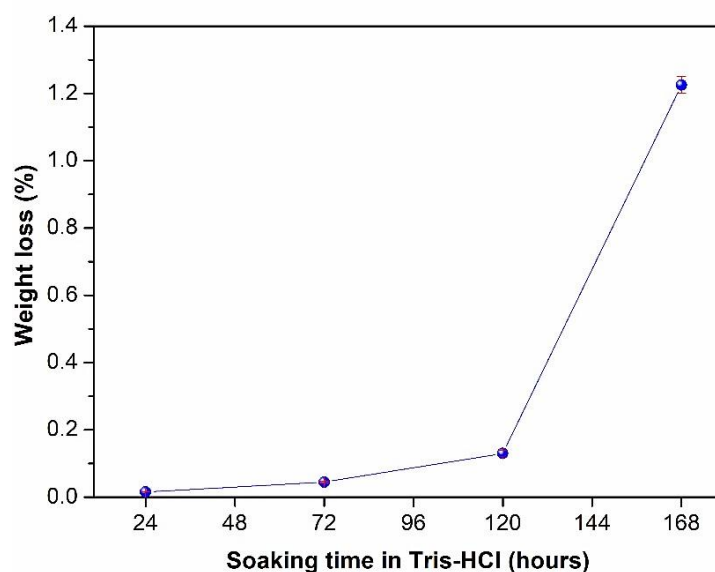


Fig. 3.9. Weight loss of dense HA scaffolds after immersion in Tris-HCl solution (pH 7.4)

3.4 Conclusion

Prawn (*Fenneropenaeus indicus*) shell exoskeleton was used to synthesize biogenic HA through wet chemical synthesis method. Thermal analysis of prawn shell reveals that prawn shell contains 42 % calcite, and 52 % organic matter, which comprises proteins and α -chitin and the remaining 6 % moisture. DSC reveals that the decomposition of calcite phase occurs at 723 °C to form calcium oxide. XRD pattern confirms the formation of phase-pure HA with hexagonal crystal structure. SEM

micrograph of sintered HA reveal that formation of well-sintered equiaxed grains. Elemental analysis shows the existence of trace elements Na, Si, Mg, Fe, etc., and the Ca: P ratio of 1.65. The biodegradation study of HA scaffolds revealed that 1.2 % of weight loss was observed after 7 days.

CHAPTER 4

SYNTHESIS AND CHARACTERIZATION OF β -TRI CALCIUM PHOSPHATE

4.1 Introduction

A variety of synthetic bone graft materials have been introduced as alternatives to traditional natural bone substitutes, which include ceramics, polymers, and metals. The most suitable materials, among these, are calcium phosphate ceramics, such as hydroxyapatite (HA), carbonated hydroxyapatite (cHA) and β -TCP. Notably, human hard tissues also contain various organic molecules (collagen and non-collagenous proteins) and inorganic phosphates in addition to pure HA or beta TCP (Hughes et al. 2019). These organic molecules and inorganic phosphates are further substituted with numerous ions like Sr^{2+} , Mg^{2+} , K^+ , Na^+ in trace level in human hard tissue (Venkatesan and Anil 2021). The presence of these trace elements plays an important role in the biological processes in the body. The physicochemical properties of calcium phosphates are responsible for their biological behavior. Hydroxyapatite with Ca/P ratio 1.67 is marginally soluble in biological fluids and therefore its *in vivo* degradation rate is less (Hanh et al. 2021). β -TCP with Ca/P ratio 1.5 degrade more quickly than hydroxyapatite-based bone graft substitutes (Ghanaati et al. 2010). It was found that when HA is co-doped with Zn, Mg, Cu, Mn, Co, Cr, Fe, Na, F, I, Mo, Se, its biological properties has been improved (Ergun et al. 2011; Yilmaz et al. 2019). Ammer et.al (Alshemary et al. 2018) extracted biological HA from chicken beaks and found that it contained trace amounts of K^+ , Na^+ , Mg^{2+} , Si^{4+} ions as well as this biological HA was stable up to 1000 °C. Evis et. al (Evis and Webster 2011) studied that osteoblast attachment values on HA doped with different ions like Mg^{2+} , Zn^{2+} , La^{3+} , Y^{3+} , In^{3+} , Bi^{3+} changed greatly.

The global requirement for the bone grafts in treatment of fractures increasing each year (Archunan and Petronis 2021). Autologous bone grafting often involves bone graft taken from the patients themselves in most cases. However, there is a growing need for alternative sources of bone grafts due to the associated expense

and morbidity of the surgical operation (Roberts and Rosenbaum 2012). Other bone grafts include xenografts (animal-derived), allografts (human-derived), and grafts derived from synthetic sources. Synthetic materials stand out among these substitutes since there is no risk of disease transmission and their chemical makeup can be replicated. Polymers, metals, and ceramics are few examples of the wide range of synthetic materials that have been suggested and used as bone grafts (Shi et al. 2016). However, among the calcium phosphate ceramics, particularly hydroxyapatite and beta-tricalcium phosphate are the most extensively investigated materials.

Although HA is an active bioceramics that forms strong bonds with bone, it has the disadvantage of inadequate solubility in physiological conditions (Dorozhkin 2013). In spite of its bioresorbable nature, β -TCP holds the advantage of being replaced by the forming bone tissue. Therefore, this material can be used extensively in bone reconstructions (Liu and Lun 2012). Driskell introduced beta-tricalcium phosphate as a substance to heal bone abnormalities brought on by trauma in 1973 (Bohner et al. 2020; DRISKELL T. D. 1973). Due to its remarkable bioactivity and biocompatibility, orthopedic surgeons uses β -TCP along with HA for bone repair, which can serve as a potential candidate for bone graft substitutes (Ana et al. 2018; Bohner et al. 2020; Sariibrahimoglu et al. 2014). β -TCP is a bioceramic substance employed in the dental and medical fields; which can be used in pulp capping, endodontics, periodontics, and maxillofacial surgery, protein purification (Guerrero-Gironés et al. 2021). It is both osteoinductive and osteoconductive (Putri et al. 2020). In recent years, several methods like solid-state reaction, sol-gel method, combustion spray synthesis, and chemical precipitation method are used to prepare β -TCP powders (Chaair et al. 2017). Among all these, the solid-state reaction method is an easy cost-effective synthesis technique. Ofudje et al. (Ofudje et al. 2022) synthesized β -TCP from waste snail shells using a one-step procedure that involved thermal decomposition and chemical precipitation. Kiagus et al. reported the extraction of β -TCP via precipitation reaction between CaO derived from egg shells and ortho-phosphoric acid (Dahlan and Nuzulia 2015). The calcite-rich fish bone serves as a biogenic source for the synthesis of biphasic calcium phosphate comprising of β -calcium pyrophosphate (β -CPP) and β -tricalcium phosphate (β -TCP) in 2:1 ratio (Amaral Corrêa and França Holanda 2019). Tahmasebifar et al.

(Tahmasebifar and Evis 2013) synthesized tricalcium phosphate by precipitation method and doped with Al^{3+} and F^- ions to investigate its mechanical and microstructural properties. They reported that Al^{3+} ions in high amounts had negative effect on the mechanical properties and incorporation of F^- ions improved the mechanical properties. Ali et al. reported that addition of lanthanum lowered degradation rate of doped β tricalcium phosphates and *in vitro* cell culture analysis showed lanthanum doped β -TCP powder was cytocompatible (Motameni et al. 2020). The focus of the present study is the synthesis of β -TCP powders derived from prawn shell biowaste. In this work, the pure-phase of β -TCP was synthesized via solid state reaction with help of prawn shell derived calcite as raw source. The effect of different processing temperatures 900, 1000, 1100 and 1200 °C on formation of β -TCP was analyzed and correlated with XRD analysis. Well-sintered powder's morphology was observed from SEM. Also, the presence of trace elements was identified in β -TCP derived from prawn shell exoskeleton which may be useful in bio-implants and bone-repair applications.

4.2. Experimental procedure

4.2.1 Materials

The prawn shells were collected from the local fish market. They were cleaned thoroughly with tap water followed by hot water cleansing. After washing, these shells were dried in hot-air oven at 150 °C for 6 hours and then, crushed into fine powder. Another material that was used to synthesize β -TCP is commercially available dicalcium phosphate CaHPO_4 (98% purity, Otto).

4.2.2 Preparation of β -TCP powder from the prawn shells

Prawn shell is a source of CaCO_3 (in the form of calcite). Prawn shell comprises 30-50 % calcite, 20-30 % α -chitin, and 30-40 % proteins along with traces of calcium phosphates, Mg, and few other elements (Hadagalli et al. 2020). The prawn shell powder was calcined at 600 °C for 12 hours to remove all the organic matter and to get phase pure calcite (CaCO_3).

The traditional solid-state reaction approach was used to prepare phase-pure β -TCP powders (Oliveira et al. 2007). The β -TCP powders were synthesized at different

temperatures 900, 1000, 1100, 1200 °C for 5 hours, where dicalcium phosphate (CaHPO_4) and calcium carbonate (CaCO_3) were used as starting materials. The schematic of the flowchart depicting the β -TCP synthesis is shown in Figure 4.1. Cylindrical pellets were prepared with a length-to-diameter (L/D) ratio of 1.4 from β -TCP powders by using a uniaxial hydraulic press with a load of 12.5 kN. These pellets were subjected to solid state sintering at corresponding sintering temperatures for 2 hours.

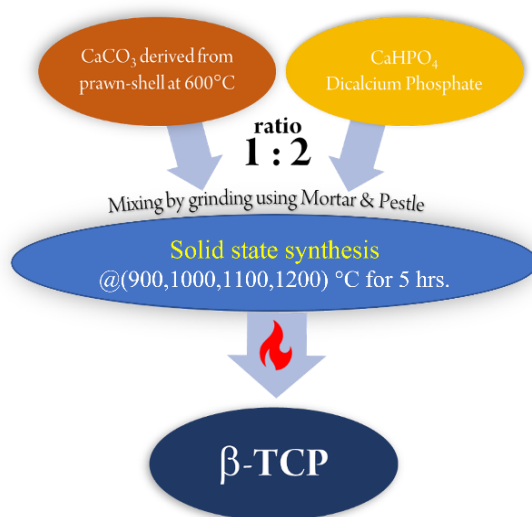


Fig. 4.1: Flowchart representing the synthesis of β -TCP

4.2.3 Characterization

X-ray diffraction (Empyrean 3rd Gen, Malvern PANalytical, Netherlands) was used with the source of $\text{Cu K}\alpha$ radiation at a scanning rate of $2^\circ/\text{min}$ to analyse the phases present and structural characteristics of synthesized powders. Field emission scanning electron microscopy (FESEM – 7610FPLUS, Jeol, Japan) coupled with energy dispersive X-ray analysis was used to determine the microstructural properties and elemental composition of the samples. The Raman analysis was carried out using a Raman spectrometer (Renishaw, UK) using 532 nm laser excitation at power of 50 mW. FTIR analysis was carried out by using a FTIR spectrometer (PerkinElmer Frontier) with a resolution of 4 cm^{-1} in the attenuated total reflection mode (ATR) in $400\text{--}4000\text{ cm}^{-1}$ wavenumber region. Differential scanning calorimetry (DSC, Netzsch 404 F1, Germany) analysis was done to detect endo and exothermic transitions at a constant heating rate of $10\text{ }^\circ\text{C}/\text{min}$ in the temperature range of $30\text{ }^\circ\text{C} - 900\text{ }^\circ\text{C}$. The

weight loss in the sample was observed within temperature range of 30 °C – 700 °C, at a constant heating rate of 10 °C/min using Thermo-gravimetric analyzer (TGA, PerkinElmer, Singapore) under nitrogen atmosphere with a flow rate of 50 ml/min. A sample of weight 24.07 mg was placed in a platinum pan and a continuous record of sample weight and heat flow was measured with respect to temperature. The particle sizes of β -TCP powders were determined by dynamic light scattering (Zeta sizer TM500, Anton-Paar, Austria). Suspended particles were dispersed in double distilled water.

4.3. Results and Discussion

4.3.1 Structural analysis

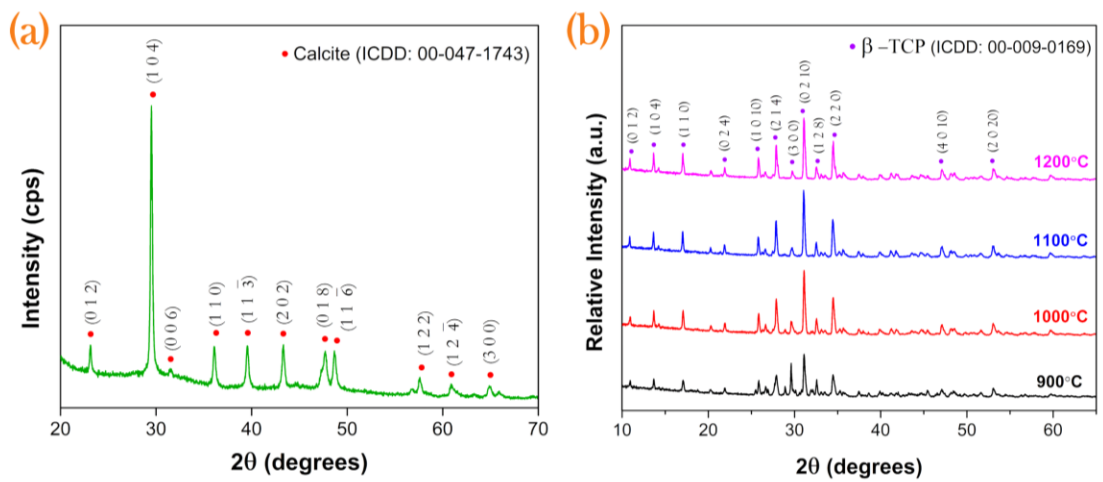


Fig. 4.2: XRD of (a) calcined prawn shell powder at 600 °C for 12 hrs and (b) β -TCP powders prepared at various sintering temperatures

XRD analysis was used to determine the purity and phase crystallinity of sintered powders. The XRD pattern of calcined prawn shell (at 600 °C) powder as shown in Figure 4.2 (a), confirms that all peaks are well-matched with the calcite (rhombohedral crystal structure, ICDD: 00-047-1743). The thermogravimetric analysis shows that calcination of prawn shell powder at 600 °C confirms the removal of carbonaceous content retaining calcite phase. The XRD of β -TCP powders prepared at various sintering temperatures is shown in Figure 4.2(b). Regardless of temperature, all samples crystallized to the β -TCP phase. The increase in intensity depicts formation of high crystalline facets of (0 2 10) with progressive increment in temperature

(Sariibrahimoglu et al. 2014). All diffraction peaks coincide with standard XRD data of rhombohedral β -tricalcium phosphate (ICDD:00-009-0169) and no secondary phases are detected. The average crystallite sizes are approximated as 18, 21.6, 25.8, 22.7 nm at 900, 1000, 1100, 1200 °C respectively. The increment in the crystallite size from 900 °C to 1100 °C could be attributed to coalescence of the grains caused by grain-boundary diffusion. The reconstructive transformation from β -TCP to α -TCP at 1125 °C could be the reason for the decrease in the crystallite size of β -TCP synthesized at 1200 °C (Guinier 1952; M. J. Buerger 1948). However, there is no evidence revealing the formation of α -TCP phase from XRD, which indicates that the sintering temperature and time is nominal for initiation of β -TCP to α -TCP transformation.

4.3.2 Microstructural and elemental analysis

The FESEM images of the synthesized β -TCP powders clearly indicate a microstructural evolution of grains with increase in the sintering temperatures, which is shown in the Figure 4.3(a-d). The increase in the grain size is clearly evident with increase in the sintering temperature. This is explained by the coalescence of smaller grains to form larger grains, which is caused by the creation of lowering surface energy regions at the grain boundaries. The increase in the sintering temperature causes the two or multiple grains to coalesce via grain boundary diffusion. The excess free energy at the grain boundaries serves as a driving force for grain growth (Mullins 1956).

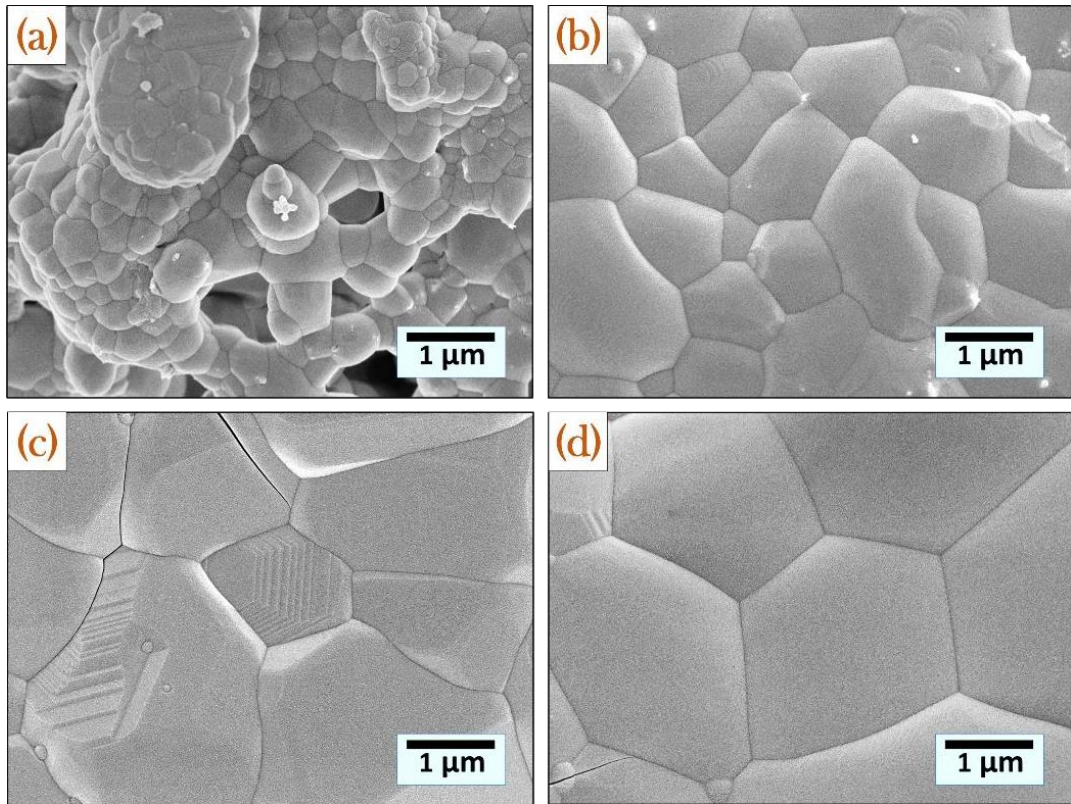


Fig. 4.3. FESEM of β -TCP powders prepared at (a) 900 °C, (b) 1000 °C, (c) 1100 °C and (d) 1200 °C.

Figure 4.4(a-d) depicts the grain size histogram plots of β -TCP powders synthesized at various sintering temperatures generated using the respective FESEM micrographs in the background. The histogram shows a unimodal grain size distribution for all the synthesized β -TCP powders. The coalescence of smaller grains led to formation of larger grains with increase in temperature resulted in uniform distribution at higher sintering temperatures. At 1100 °C, there is a gaussian distribution with wide range of grain sizes. The grain-size distribution at 1200 °C is extended towards right which indicates formation of larger sized grains.

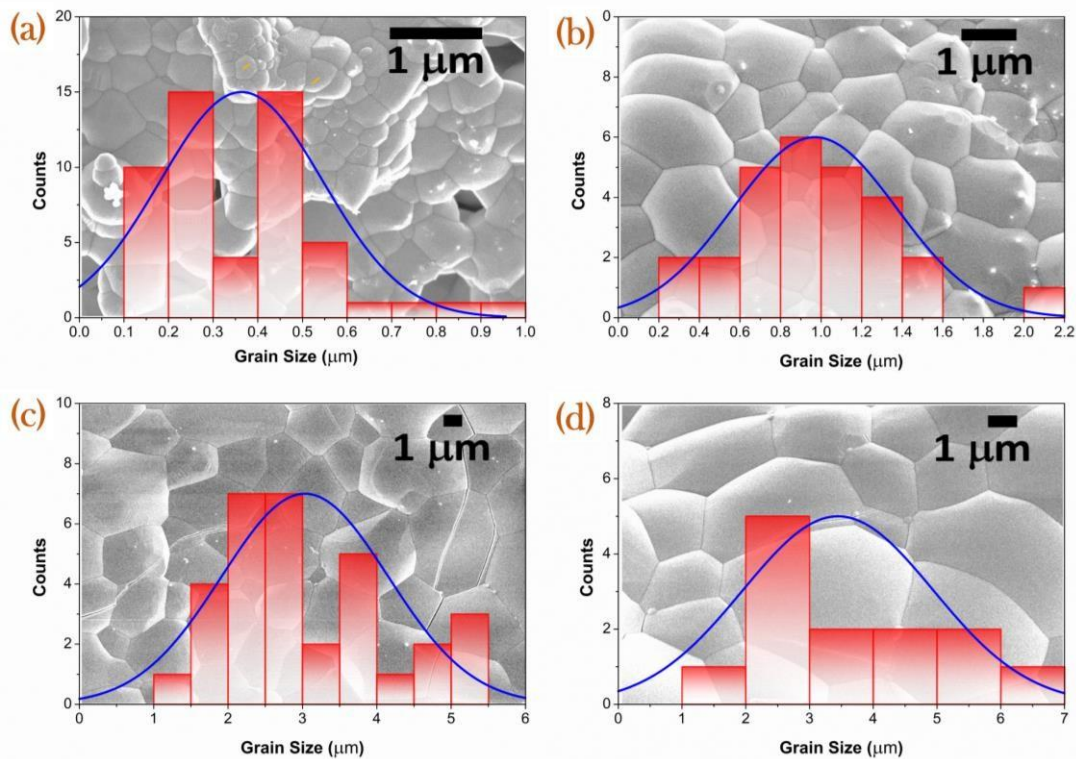


Fig. 4.4. Histogram showing the grain size distribution of β -TCP powders synthesized at 900 °C, (b) 1000 °C, (c) 1100 °C and (d) 1200 °C.

The variation in the crystallite size and grain size with increase in the sintering temperature is evident from the Figure 4.5 (a), (b) respectively. The grain-size calculated using image-J software, is found to be increased with an increase in sintering temperature. The average grain sizes were estimated as 0.37, 0.96, 3.07, 3.48 μm at 900 °C, 1000 °C, 1100 °C, and 1200°C respectively. The crystallite size variation with sintering temperature revealed that the effective temperature for obtaining phase-pure β -TCP with high intense Bragg reflections, nominal grain size and good sintering properties was 1100 °C.

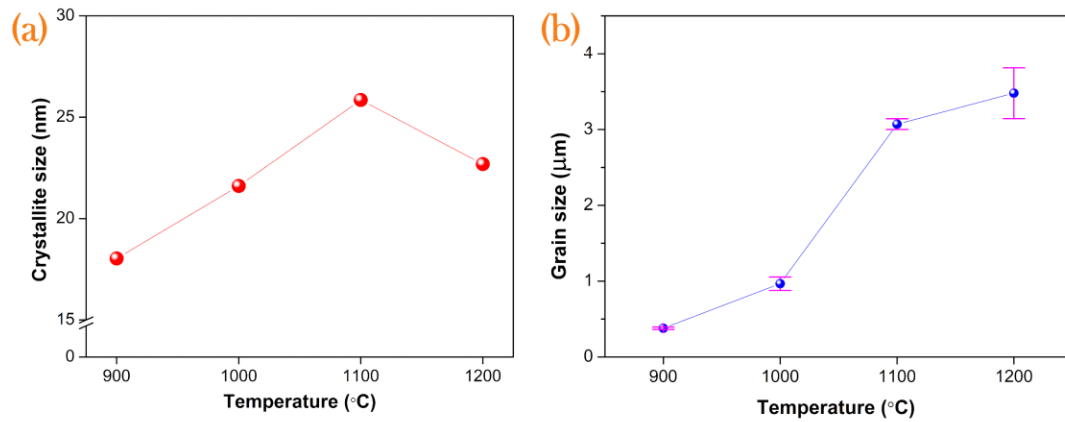


Fig. 4.5: Variation of (a) crystallite size and (b) grain size of β -TCP with sintering temperature.

The β -TCP powders synthesized at different sintering temperatures were evaluated for their sizes using dynamic light scattering (DLS) technique. The particle size distribution of β -TCP powders is shown in Figure 4.6 (a)-(d). From DLS particle size distribution, the synthesized powders at 900 °C, were found to have unimodal distribution with a mean particle size of 1.6 μm . At 1000 °C, a successive bimodal distribution was observed ranging within 0.3 to 4.8 μm . At 1100 °C, A clear distinct bimodal distribution was observed with two gaussian peaks ranging between 0.3 to 0.4 μm and 6.6 to 13.8 μm respectively. Similarly, two gaussian peaks were observed at 1200 °C ranging between 0.1 to 0.17 μm and 3.2 to 19 μm respectively. This variation in unimodal to bimodal distribution is due to the sintering between the β -TCP powders with increase in the temperature, which is clearly evident from the FESEM micrographs, shown in Figure 4.4.

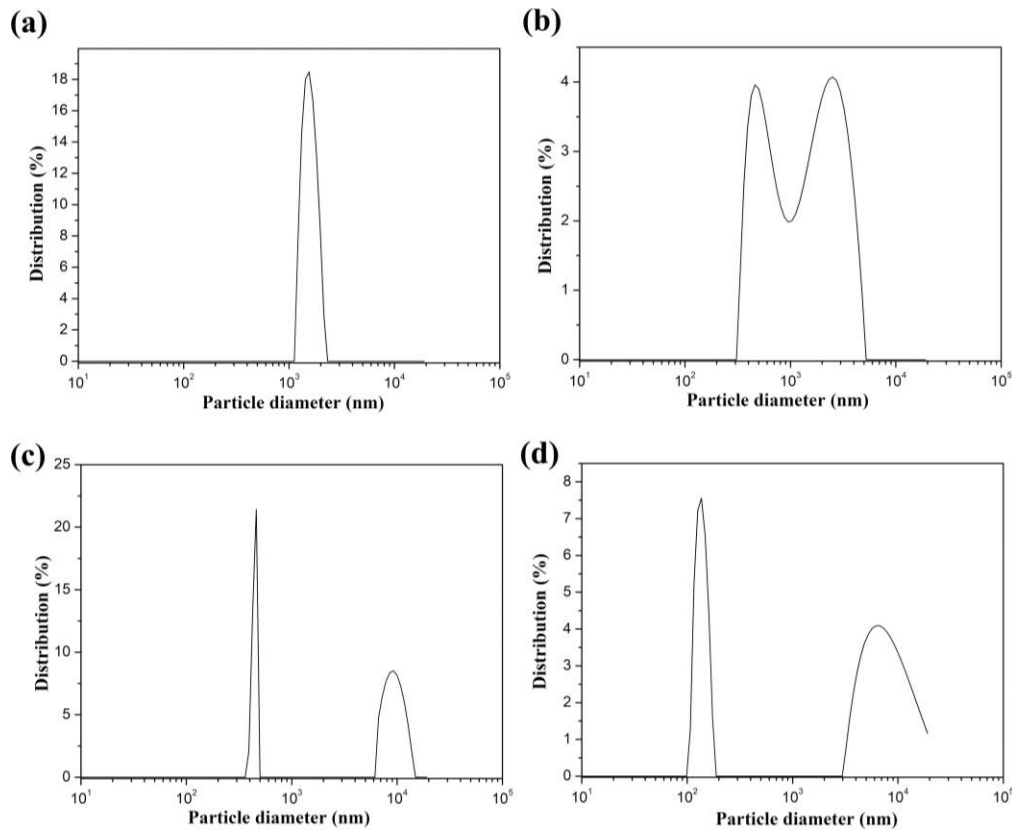


Fig. 4.6: Particle size distribution of β -TCP powders synthesized at (a) 900 °C, (b) 1000 °C, (c) 1100 °C, and (d) 1200 °C.

EDX spectroscopy is used to determine the elemental distribution of β -TCP powders synthesized at different sintering temperatures. Figure 4.7(a-d) shows EDX spectra of the synthesized β -TCP powders at various sintering temperatures 900, 1000, 1100, and 1200 °C. It confirms the presence of elements Ca, P and O along with other trace elements like Na, Mg, Si, and Fe which helps in bone regeneration and the treatment of bone defects (Nayak et al. 2022). The elemental composition (atomic percentage) with different sintering temperatures is shown in Figure 4.7, whose Ca:P ratios are calculated and tabulated in Table 4.1 and compared with the theoretical Ca:P ratio of β -TCP which is 1.5. It is observed that the Ca:P ratio decreases with an increase in sintering temperature. However, at 1100 °C, Ca:P ratio clearly matches with the theoretical Ca:P ratio of β -TCP. There is a subsequent decrease in the Ca:P ratio which might be caused due to the formation calcium deficient phase such as calcium

pyrophosphate with an increase in sintering temperature (Bian et al. 2004; Brunner et al. 2007).

Table 4.1: Ca:P ratio of β -TCP powders synthesized at various sintering temperatures assessed by EDX.

Sintering temperature (°C)	Elemental composition (atomic%)			Ca:P ratio
	Ca	P	O	
900	23.5	14.4	59.8	1.63
1000	23.9	15.2	57.3	1.57
1100	21.7	14.3	61.2	1.51
1200	20.4	13.7	63.6	1.48

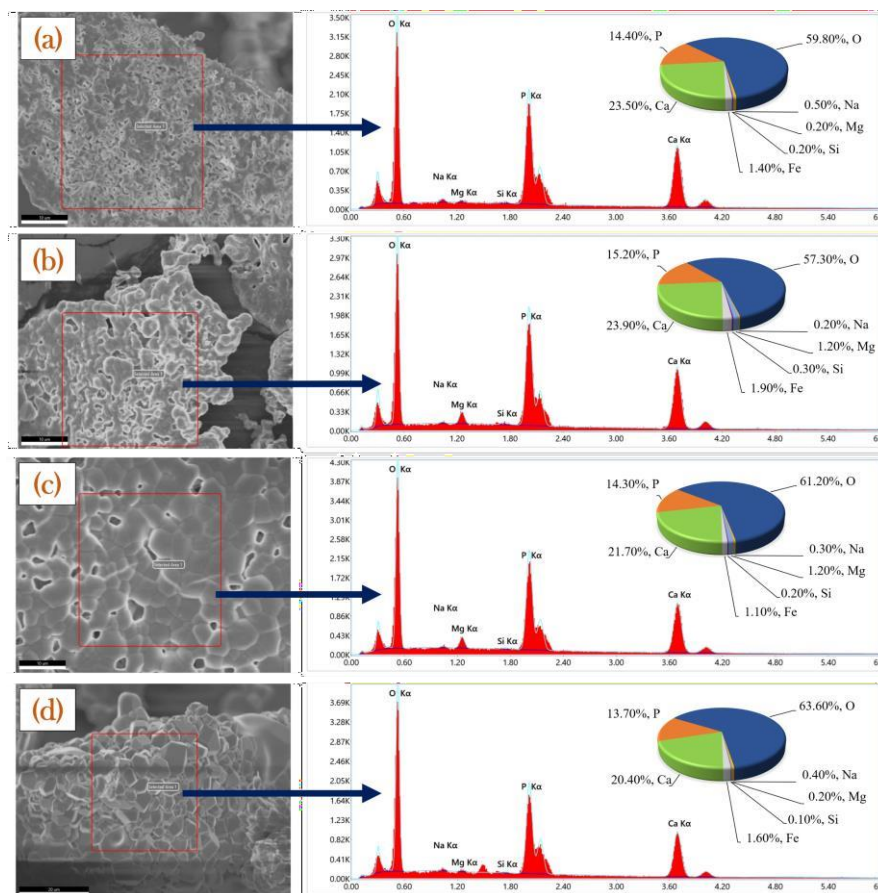


Fig. 4.7: Topological FESEM images of β -TCP powders prepared at (a) 900 °C, (b) 1000 °C, (c) 1100 °C, and (d) 1200 °C with energy-dispersive X-ray spectroscopic analysis.

4.3.3 Vibrational spectroscopic analysis

The Raman spectra of all the synthesized β -TCP powders is shown in Figure 4.8. The designated peaks in the β -TCP's Raman spectrum are indicative of the internal vibration of the PO_4^{3-} tetrahedral groups. An isolated phosphate (PO_4^{3-}) ion has tetrahedral symmetry with four normal internal vibrational modes which are represented as $A_1(\nu_1)$, $E(\nu_2)$ and $F_2(\nu_3$ and $\nu_4)$. The ν_1 vibrational mode, which is located in the $950\text{--}1000\text{ cm}^{-1}$ range, dominates all the observed spectra.

The peaks with maximum intensities of β -TCP powders at 1000 , 1100 , and 1200°C at 950 cm^{-1} and 970 cm^{-1} correspond to strong symmetric stretching (ν_1) of P-O bonds of the tetrahedron (Alrefeai et al. 2021). These bonds may form as a result of the ν_1 fundamental vibrational mode matching with the symmetric P-O stretching vibration of the phosphate ion splitting into factor groups. The triply degenerate asymmetric P-O stretching mode, (ν_3) is observed at 1046 cm^{-1} for 900°C sample. The double (ν_2) and the triple degenerate bending modes (ν_4) corresponds to the O-P-O bond bending vibrations and give rise to bands in range of $400\text{--}500\text{ cm}^{-1}$ in all the samples respectively (Fadeeva et al. 2021; Jillavenkatesa and Condrate 1998; Sinusaite et al. 2020).

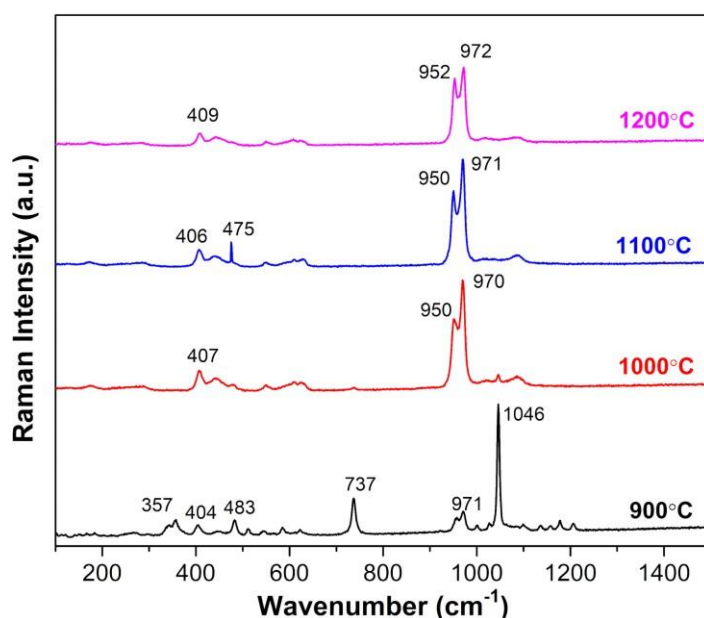


Fig. 4.8: Raman spectra of β -TCP powders prepared at various sintering temperatures.

Table 4.2: Vibration modes in the Raman spectrum of β -TCP powders

Wavenumber, cm^{-1}	Mode	Type	Assignment
400-500	double (ν_2), triple (ν_4) degenerate bending	Symmetric	O-P-O
1046	Degenerate P-O stretching (ν_3)	Asymmetric	P-O
950,970	Degenerate P-O stretching (ν_1)	Symmetric	P-O

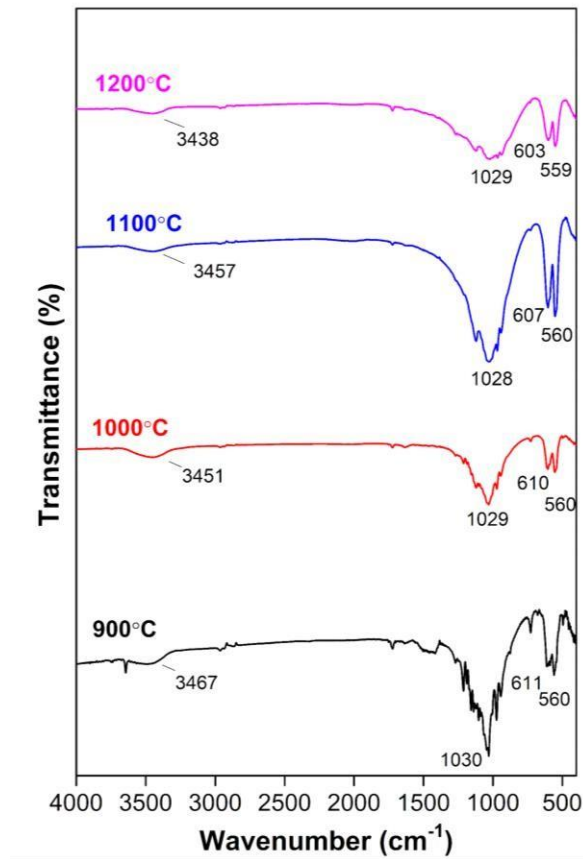


Fig. 4.9: FTIR spectra of β -TCP powders prepared at various sintering temperatures

Table 4.3: Vibration modes in the FTIR spectrum of β -TCP powders

Wavenumber, cm^{-1}	Mode	Type	Assignment
560-610	Doublet bending of PO_4^{3-}	Symmetric	O-P-O
1020-1030	Singlet stretching of PO_4^{3-}	Asymmetric	P-O
3000-3500	Wide band	Symmetric	-OH

Figure 4.9 shows the characteristic FTIR spectra of the β -TCP powders prepared at various sintered temperatures. The vibrations bands are assigned from the FTIR spectrum as shown in Table 4.3. The peaks in the range of 560-610 and 1020-1030 cm^{-1} are attributed to the phosphate group (PO_4^{3-}) (Duta et al. 2013; Fadeeva et al. 2021). The transmittance peaks in the range of 559-611 cm^{-1} are attributed to symmetrical bending of PO_4^{3-} group whereas the peaks in the range of 1020-1030 cm^{-1} can be assigned to asymmetrical stretching of PO_4^{3-} group (Jillavenkatesa and Condrate 1998). The wide bands around 3450 cm^{-1} represent O-H stretching. The vibrational and stretching mode of OH peaks around 3000-3500 cm^{-1} indicates presence of water molecules within β -TCP lattice, whose intensity decreases with increases with increase in sintering temperature.

4.3.4 Thermal analysis

Figure 4.10(a) represents the DSC analysis of β -TCP powder sintered at 1100 $^{\circ}\text{C}$. Three endothermic peaks were observed at 80 $^{\circ}\text{C}$, 480 $^{\circ}\text{C}$, 726 $^{\circ}\text{C}$ respectively. The endothermic peak at 80 $^{\circ}\text{C}$ corresponds to the removal of adsorbed water. Another broad endothermic peak at 480 $^{\circ}\text{C}$ was attributed to the crystal water (Ben et al. 2017). Also, the endothermic peak at 726 $^{\circ}\text{C}$ shows the decomposition of calcite which was one of the raw materials in creating β -TCP powders. (Carbajal et al. 2012). Figure 4.10(b) shows the weight loss percentage of sintered β -TCP powder during heating, which was found to be less than 1%, confirms its stability at higher temperatures.

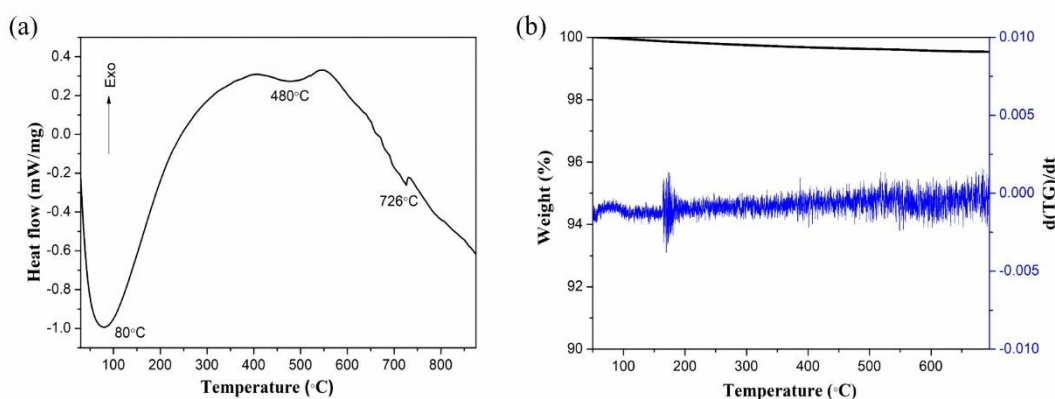


Fig. 4.10 (a) DSC analysis, and (b) TGA analysis of β -TCP sintered at 1100 $^{\circ}\text{C}$.

4.3.5 XPS analysis

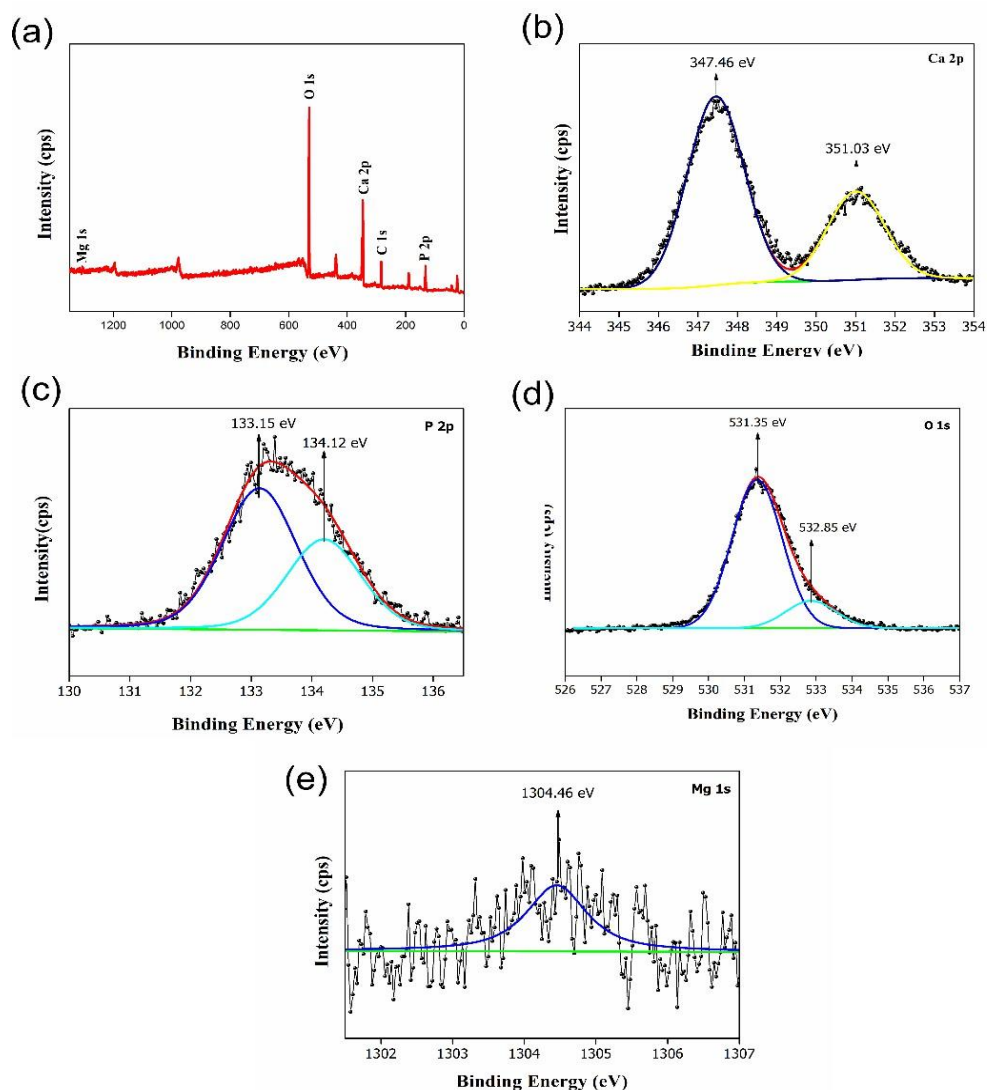


Fig. 4.11. XPS analysis validates the formation of phase pure β -TCP from prawn shell. (a) Survey spectrum and deconvoluted high-resolution spectra of (b) Ca 2p, (c) P 2p, (d) O 1s, e) Mg 1s.

XPS survey spectrum of prawn shell derived β -TCP powder exhibits C 1s, Ca 2p, P 2p, O 1s, Mg 1s peaks as shown in Figure 4.11 (a). Figure 4.11 (b), (c), (d), (e) show the high-resolution spectra of individual elements namely Ca, P, O, Mg. The binding energies of Ca 2p are 347.46 eV ($2p_{3/2}$), 351.03 eV ($2p_{1/2}$) (Figure 4.11 (b)), whereas P 2p binding energies are designated with 133.15 eV ($2p$) and 134.12 eV ($2p$) (Figure 4.11 (c)). These specified chemical elements (Ca 2p, P 2p) with binding

energies are corresponding to β -TCP. O 1s with 531.35 eV is attributed to P-O group and 532.85 eV belong to O-P-O bond present in β -TCP. Binding energy at 1304.46 eV confirms the presence of Mg in prawn shell derived β -TCP.

4.3.6 Mechanical and physical properties

With respect to mechanical properties, Figure 4.12 (A) shows the stress strain curves of sintered β -TCP specimens at various temperatures 900 °C, 1000 °C, 1100 °C, 1200 °C. It was observed that β -TCP sintered at 900 °C exhibited a compressive strength of 2.82 ± 0.7 MPa; whereas β -TCP sintered at 1000 °C, 1100 °C, 1200 °C displayed compressive strength values of 3.23 ± 1.1 MPa, 6.24 ± 0.4 MPa, 6.89 ± 0.8 MPa respectively. It is found that compressive strength increases with increase in sintering temperature as shown in Figure 4.12 (B). This is due to formation of dense microstructures obtained as shown in Figure 4.3. The obtained mechanical measurement data affirms that prawn shell derived β -TCP scaffolds can be served as an alternative for human trabecular bone whose compression strength lies in the range of 2-12 MPa (Morgan et al. 2018).

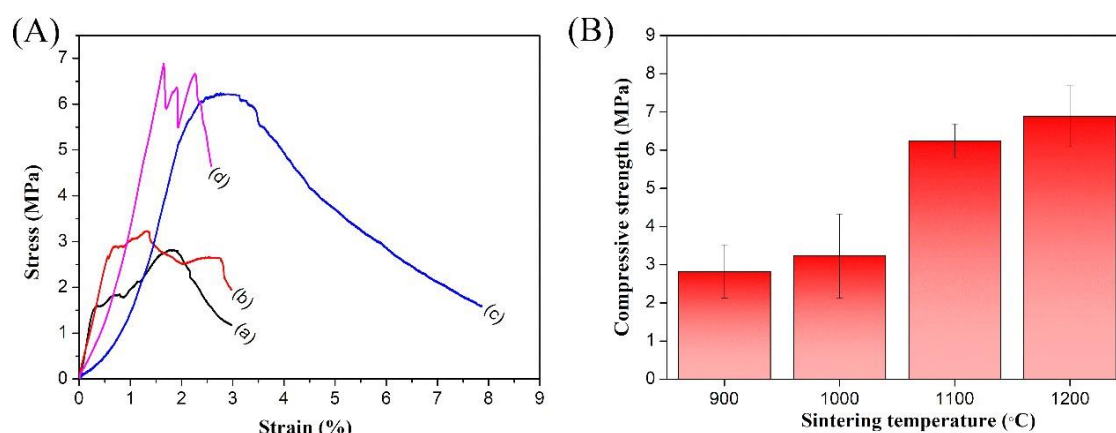


Fig. 4.12. (A) stress strain curves of β -TCP specimens sintered at (a) 900°C (b)1000 °C (c)1100°C (d)1200°C (B) Variation of compressive strength with sintering temperature

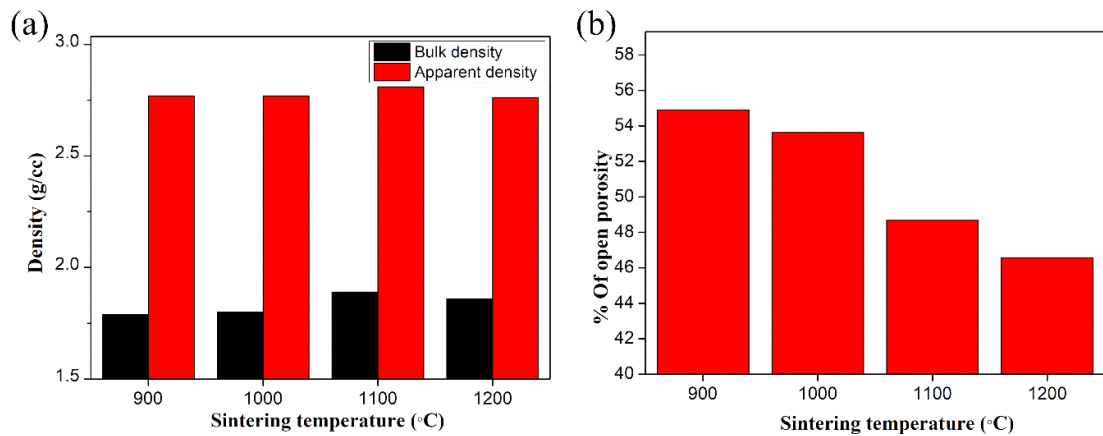


Fig. 4.13. The variation of physical properties of β -TCP with sintering temperatures
(a) bulk and apparent densities (b) open porosity

The physical properties of β -TCP are determined by open porosity, bulk density and apparent densities. Figure 4.13(a) shows the variation in apparent density and bulk density with respect to sintering temperature (900 °C, 1000 °C, 1100 °C, 1200 °C). Figure 4.13(b) shows the variation in open porosity with sintering temperature. The bulk and apparent densities of β -TCP sintered at 900°C, 1000 °C, 1100°C, 1200°C were found to be 1.79 g/cc, 2.77 g/cc, 1.8 g/cc, 2.77 g/cc, 1.89 g/cc, 2.81 g/cc, 1.86 g/cc, 2.76 g/cc, respectively. As shown in Figure 4.13, a clear trend was observed where an increase in % relative density correlated with an increase in compressive strength. This can be attributed to the reduction in porosity, which enhances the material's ability to withstand applied loads and thereby increasing its compressive strength. The open porosity of β -TCP sintered at 900 °C was found to be 54.91 % and this value is found to be decreased with increase in sintering temperature. The open porosity values of β -TCP sintered at 1000 °C, 1100 °C, 1200 °C were found to be 53.63 %, 48.68 %, 46.57 % respectively. The microstructure in Figure 4.3 indicates the grain size increases with increase in sintering temperature that leads to the decrease of number of open pores.

4.3.7 Biodegradation study

The biodegradation study was performed in accordance with ASTM F2150 standard. Figure 4.14 shows the weight loss of β -TCP scaffolds after immersion in Tris-HCl solution at different time points (1, 3, 5, and 7 days). The initial profile shows a gradual degradation rate within the first 5 days, which then accelerates noticeably by

the 7th day. Using equation 3.9, the weight loss of dense β -TCP scaffolds was determined to be 5.6 % after 7 days. This weight loss observed in the Tris buffer solution at pH 7.4 can be associated with the bioresorbability of the scaffolds, which is a crucial property for their bioactivity.

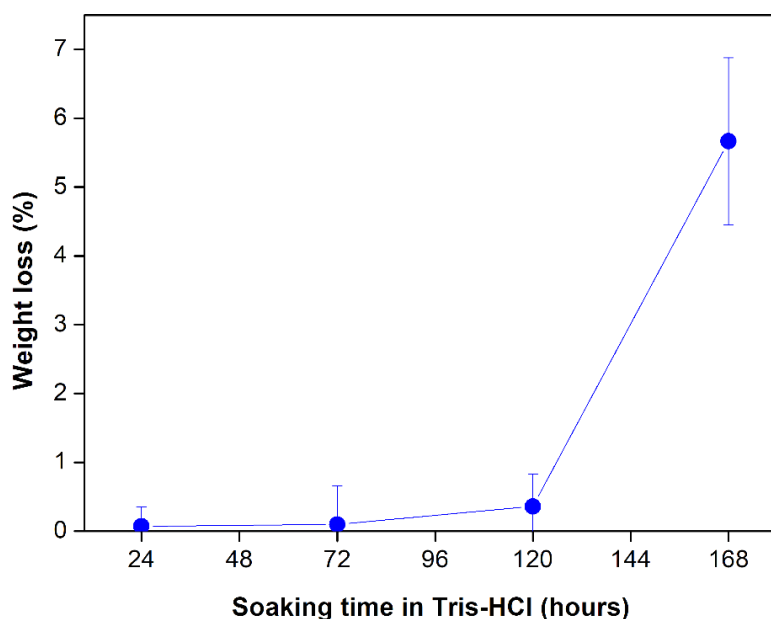


Fig. 4.14. Weight loss of β -TCP scaffolds after immersion in Tris-HCl solution (pH 7.4)

4.4 Conclusion

Phase-pure β -TCP was successfully synthesized using prawn shell biowaste as the raw source, via solid-state reaction method. A study of different processing temperatures to prepare β -TCP reveals no secondary phase formation and XRD patterns confirm the formation of phase-pure β -TCP with rhombohedral crystal structure. An increase in crystallite size with an increase in sintering temperature is observed till 1100 °C and then, it decreases at 1200 °C. SEM micrographs reveal that increase in sintering temperature resulted in the formation of well-sintered equiaxed grains with progressive increment in grain size. DSC reveals that the decomposition of calcite phase occurs at 726 °C in the synthesis of β -TCP powders. Elemental analysis shows the existence of trace elements Na, Si, Mg, Fe, etc., and also, the Ca:P ratio of 1.51 at 1100 °C which matches with the theoretical ratio of β -TCP (Ca:P =1.5). The compressive strength of

sintered β -TCP specimens increased with increase in sintering temperature. It is observed that β -TCP scaffolds sintered at 1200 °C exhibited highest compressive strength value of 6.89 ± 0.8 MPa. The biodegradation study of β -TCP scaffolds revealed that 5.6 % of weight loss was observed after 7 days. Therefore because of its better *in vitro* degradation, β -TCP has emerged as a potential material for bone regeneration applications.

CHAPTER 5

SYNTHESIS AND CHARACTERIZATION OF BIPHASIC CALCIUM PHOSPHATES

5.1 Introduction

Different biomaterials with biological or synthetic origins have been developed during the past few decades to serve as extracellular matrix composite scaffolds to produce new bone tissue (Pilliar et al. 2001). Meanwhile, various biomaterial characteristics, including osteoconduction, osteoinduction, bioactivity, biocompatibility, and biodegradation, are necessary for clinical applications (Mozafari et al. 2010). Many biomedical applications involve biomaterials, and it is crucial to fully grasp both the biological and material components to achieve successful natural outcomes (Todros et al. 2021). The most common family of bioceramics among biomaterials is calcium phosphates (CaP), which is well known for its usage in biological applications. Different types of calcium phosphates include Dicalcium phosphate, Dicalcium phosphate dihydrate, Octacalcium phosphate, β -Tricalcium phosphate, α -Tricalcium phosphate, Hydroxyapatite (Macha et al. 2013). Among all these, hydroxyapatite (HA-Ca₁₀(PO₄)₆(OH)₂) is a widely used bioceramic material in bone tissue engineering due to its chemical composition, which is similar to human bone and physical properties (Bogdanoviciene et al. 2006). In addition to that, HA has excellent bioactivity and biocompatibility (Ismail and Mohamad 2021). The mechanical stability of HA is high, and it is osteoconductive. Compared with HA, β -TCP has low mechanical stability and a faster degradation rate. So, research interest has grown for biphasic calcium phosphate scaffolds, favoring bone material deposition (Impens et al. 2009). HA can be obtained from both natural resources and synthesized from various precursors, especially calcium and phosphorous-based (Sossa et al. 2018). However, stoichiometric HA made with these processes lacks trace elements of ions in its lattice structure (de Santis et al. 2017). Due to tiny amounts of ions in its HA lattice, bone is considered a nonstoichiometric HA, which favors its structure and usage as calcium phosphate-based implants (Akram et al. 2014; Pajor et al. 2019).

Meanwhile, HA obtained from natural resources is nonstoichiometric. HA received from natural resources has recently gained more attention in bone grafting applications (Pokhrel 2018; Szcześ et al. 2017). HA can be extracted from marine resources such as fish bones, corals, and seashells like razor shells, oyster shells, and mussel shells. HA obtained from marine resources contains carbonate groups, small magnesium-sodium admixtures, and traces of other metals (Akram et al. 2014; Milovac et al. 2014; Mohd Pu'ad et al. 2019; Venkatesan and Anil 2021). HA can be synthesized using methods like wet chemical precipitation, hydrothermal, sol-gel, spray pyrolysis, and combustion (Mondal et al. 2010). The development of synthetic bone grafts with adjustable resorption rates led to the introduction of biphasic calcium phosphates (BCPs) in the late 1980s (Daculsi et al. 1989). To be used as synthetic bone grafts, biphasic calcium phosphate (BCP) bioceramics made of two phases of apatites must possess specific characteristics, such as bioactivity, tunable resorption, and intrinsic osteoinduction (Gallinetti et al. 2014; Kannan et al. 2007; Mofakhmi and Salahinejad 2021). BCP nano composites which comprises HA nanofibers in β -TCP matrix exhibited a compressive strength of 9.8 MPa like cancellous bone (Buschmann 2016).

The industrial processing of marine products generates a large amount of waste. Globally, 6 million to 8 million tonnes of discarded crab, shrimp and lobster shells are produced yearly, with 1.5 million tonnes produced in Southeast Asia (Terkula Iber et al. 2022). India is one of the largest exporters of shrimp/prawns to the world market. About 45 % of processed seafood consists of prawns; a significant share of industrial waste comes from its exoskeleton. Prawns consist of approximately 55 to 65% by weight of edible components, while the remaining 35 to 45% is considered bio-waste. This bio-waste is repurposed for various uses including animal feed mix, as a source of chitin and chitosan and as a fertilizer. The exoskeletons of prawns contain a large amount of calcium carbonate. Prawn shells consist of 30-50 % calcium carbonate in the form of calcite, 20-30 % α -chitin, and 30-40 % protein, along with traces of calcium phosphates, Mg, and few other elements. Because of its osteoconductive and bioactive attributes, hydroxyapatite has attracted much interest in bone grafting in recent years (Wang and Yeung 2017). The current chapter focuses on the precipitation of biphasic calcium phosphate powder from dry prawn shell powders. The obtained

BCP powder, which is the mixture of HA and octacalcium phosphate, is made into cylindrical pellets and sintered at high temperatures. All pellets are subjected to compression testing using UTM to measure the compressive strength after sintering. The structure, morphology, and elemental composition were investigated using XRD, SEM, EDX, and XPS.

5.2 Experimental procedure

5.2.1 Materials

Prawn shells (*Fenneropenaeus Indicus*) were collected from the local fish market, abundantly available as an inedible. Prawn shell is used as a source of CaCO_3 . The prawn shells were scrubbed in the tap water before being rinsed in distilled hot water. After washing, the prawn shell was dried in an oven at $150\text{ }^\circ\text{C}$ for 6 hours and then ground to powder. CaCO_3 was converted into CaO by calcination in muffle furnace. This CaO can be used as a precursor to derive biphasic calcium phosphates.

5.2.2 Preparation of biphasic calcium phosphate powder from the prawn shells

The wet chemical synthesis method of biphasic calcium phosphate is shown in Figure 5.1 (a) through pictorial representation. The prawn shell, a calcite source, was calcined in a muffle furnace at $900\text{ }^\circ\text{C}$ for 12 hours at a rate of $10\text{ }^\circ\text{C}/\text{min}$. As the prawn exoskeleton consists of calcite, α -chitin and proteins (Hadagalli et al. 2020), hence calcination helps in complete removal of unwanted carbons. The calcite was converted into calcium oxide (CaO) by releasing carbon dioxide. The intrinsic advantage of using CaO as raw material derived from marine resource is the presence of trace elements which play a crucial role in the rapid bone regeneration (Akram et al. 2014). Other advantages include it is less expensive than inorganic source and this CaO is derived from the waste which is not useful for anything. CaO powder was dissolved in distilled water, and orthophosphoric acid (H_3PO_4) was added drop by drop rapidly to keep the stoichiometric molar ratio of Ca/P at 1.66 using the wet chemical synthesis method. The pH value is maintained at ten throughout the experiment by adding ammonia solution dropwise. This reaction was carried out using a hot plate with a magnetic stirrer with a temperature of $80\text{ }^\circ\text{C}$ and 200 rpm for 2 hours. Once the reaction had been completed successfully, the finished product was placed in a hot air oven at $100\text{ }^\circ\text{C}$ overnight to eliminate any remaining moisture. Again, the color and shape of the green

and sintered pellet at four different temperatures (900, 1000, 1100, and 1200 °C) are displayed in Figure 5.1 (b).

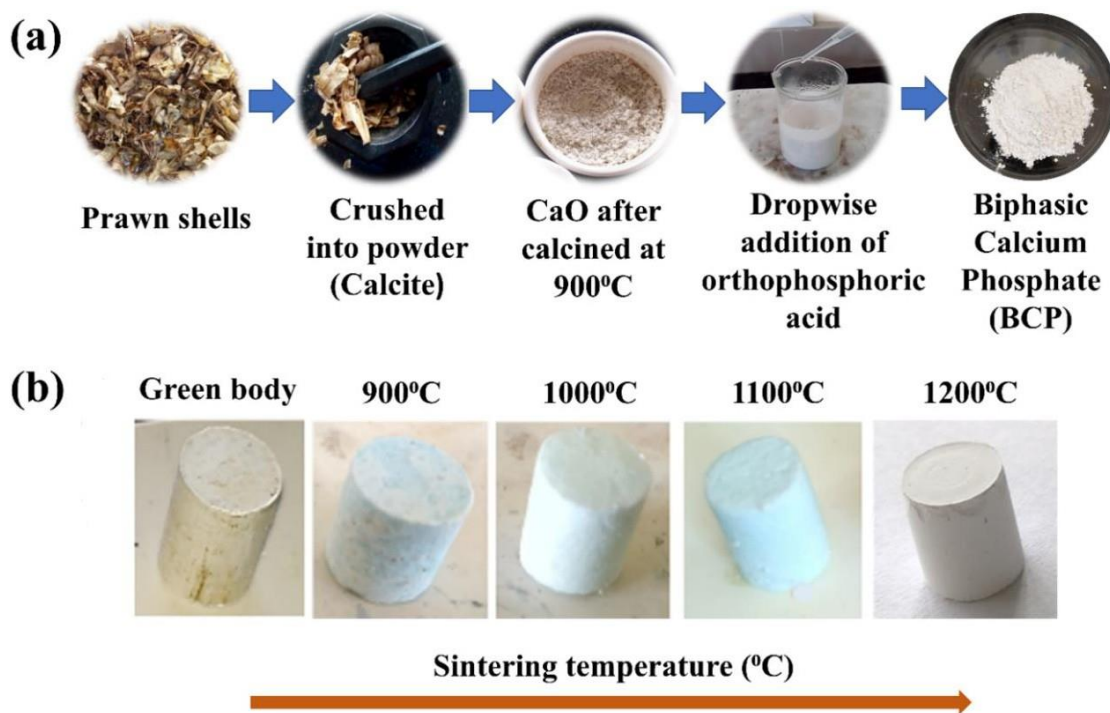


Fig. 5.1. (a) Process flow diagram of biphasic calcium phosphate (BCP) powder preparation, (b) sintered pellets at different temperatures.

5.2.3. Preparation of sintered specimens for compressive testing

Cylindrical pellets were prepared with a length-to-diameter (L/D) ratio of 1.45 from biphasic calcium phosphate powders obtained through prawn shells using a uniaxial hydraulic press with a load of 12.5 kN. These pellets were sintered at temperatures like 900,1000,1100, and 1200 °C for 2 hours in a tubular furnace at a heating rate of 10 °C/min.

5.2.4. Characterization

To determine the phase structures of sintered pellets, X-ray diffraction (Empyrean 3rd Gen, Malvern PANalytical, Netherlands) was carried out with the source of Cu K α radiation at a scanning rate of 2 °/min. Field emission scanning electron microscopy (FESEM – 7610FPLUS, Jeol, Japan) coupled with Energy Dispersive Spectroscopy (EDS) at an accelerating voltage of 20 kV was used to determine the

microstructural properties and elemental composition of the sample. The compressive strength is measured for sintered pellets using a universal testing machine (UTM, SHIMADZU AG X-Plus 100kN, Japan). The physical properties of sintered pellets, like bulk density and apparent density, were measured by Archimedes' principle using a density measurement kit (Contech-CAS 44). Open pore porosity was calculated from the sample's estimated soaked and dry weight. The element's chemical state and composition were determined by X-ray photoelectron spectroscopic (XPS, Kratos Axis Ultra DLD, Japan) analysis for samples sintered at 1100 °C and 1200 °C. The X-ray source for XPS was the monochromatic Al K α . A base pressure of 10⁻¹⁰ Torr was kept in the ultra-vacuum system. The scale of binding energy was expressed in "eV". The received spectra have been calibrated using the C-H peak of the adventitious carbon, which is located at 284.6 eV. The peak fit analysis was conducted utilizing the product of Gaussian and Lorentzian function with fixed G/L (30%) ratio and full-width half maxima (FWHM) of synthetic peaks fitted by software. To prevent inconsistent peak fitting, the FWHM of the synthetic peaks in the spectra was limited to the same. The software CASAXPS 2.3.22PR1.0 was used to carry out the peak fit analysis.

5.3 Results and discussion

The X-ray diffractogram of as-synthesized powder is shown in Figure 5.2(a). It is observed that the synthesized powder is a mixture of hydroxyapatite (ICDD: 01-074-0565) and octacalcium phosphate (ICDD: 00-026-1056). Figure 5.2(b) shows the XRD patterns of specimens sintered at 900, 1000, 1100, and 1200 °C. It is observed that an increase in sintering temperature leads to a change in the phases of calcium phosphates. The mixture phase of hydroxyapatite and β -tricalcium phosphate (ICDD: 00-009-0432) is observed at 900 °C, which retains up to 1100 °C. But at 1200 °C, the sintered pellet is a mixture of hydroxyapatite and α -tricalcium phosphate (ICDD: 00-029-0359). The phase change occurs from β -tricalcium phosphate to α -tricalcium phosphate when the sintering temperature changes from 1100 °C to 1200 °C (Safronova et al. 2020). The crystallite size "D" can be calculated by using Scherrer's

equation $D = \frac{K\lambda}{\beta \cos\theta}$ where K is a dimensionless shape factor of 0.9, λ is x-ray

wavelength, β is full width at half maximum (FWHM), and θ is diffraction angle (Rabiei

et al. 2020). The crystallite size of synthesized biphasic calcium phosphate powder is estimated as 19.1 nm.

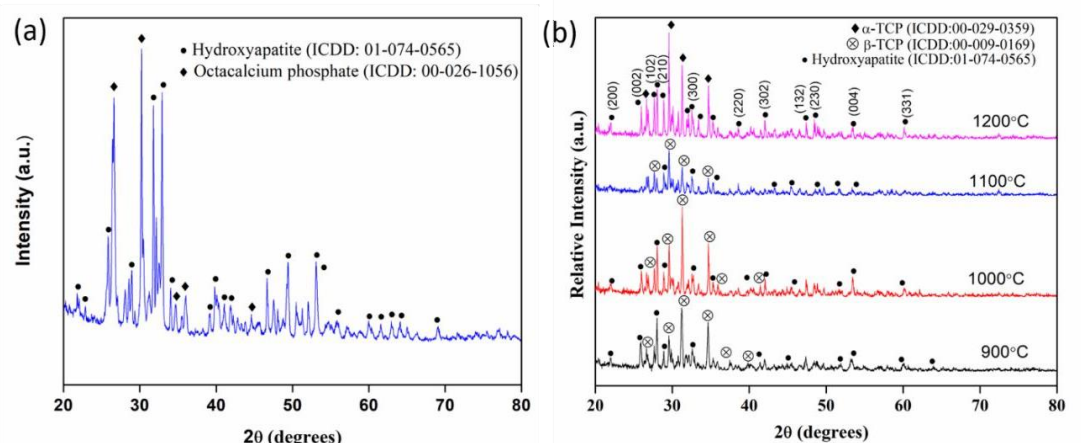


Fig. 5.2. XRD pattern of (a) as-synthesized biphasic calcium phosphate powder and (b) biphasic calcium phosphates sintered at 900, 1000, 1100, and 1200 °C.

Various biphasic calcium phosphates obtained before and after sintering are shown in Figure 5.3. The mixture of hydroxyapatite and octa calcium phosphate is obtained through wet chemical synthesis which can be considered as biphasic calcium phosphate. This mixture is sintered at 900, 1000, 1100, 1200 °C to get other biphasic calcium phosphates.

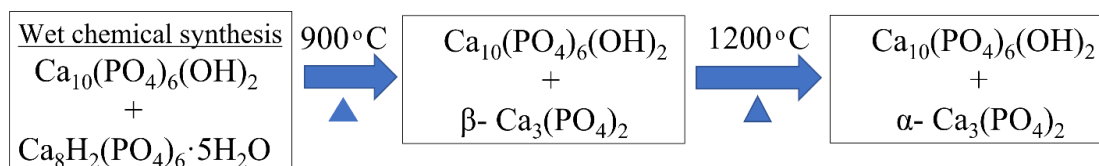


Fig. 5.3. Biphasic calcium phosphates before and after sintering

The morphology of biphasic calcium phosphates at various temperatures is shown in Figure 5.4. The open pores are present on the sintered surface. Well-sintered grains were observed, with the average grain size increasing from 0.8 μm to 3.7 μm as the sintering temperature increased from 900 to 1200 °C. Dense morphology is observed at 1100 °C with closely packed grains, as shown in Figure 5.4 (c). Uncontrolled grain growth at 1200 °C leads to micro-cracks on the pellet's surface, as shown in Figure 5.4 (d). It was found that the grain size increased with increasing sintering temperature, as

shown in Figure 5.5 (a). The bulk density and apparent density are measured and plotted as a function of sintering temperature, as shown in Figure 5.5 (b). Both bulk and apparent density are found maximum at 1100 °C and then decrease at 1200 °C. This is due to phase transformation from β -TCP to α -TCP and also formation of α -TCP at 1200 °C prevents densification of hydroxyapatite further. The densification is also influenced by phase transformation as the density of beta TCP is higher than that of alpha TCP (Carrodegua and De Aza 2011).

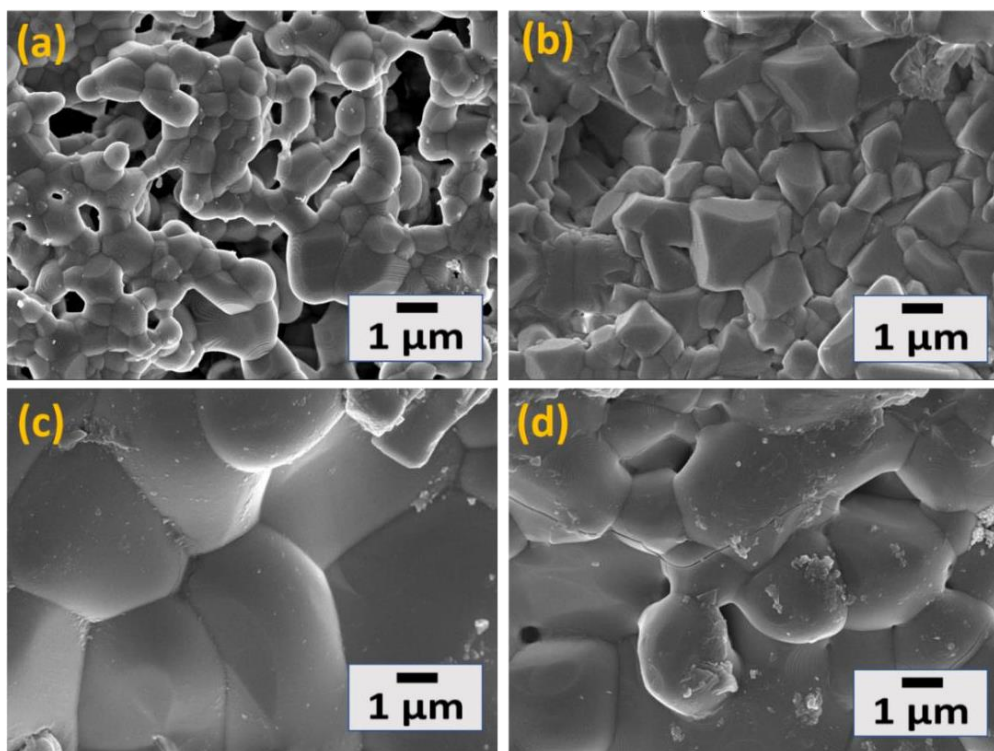


Fig. 5.4 Microstructure of biphasic calcium phosphate specimens sintered at (a) 900 °C, (b) 1000 °C, (c) 1100 °C, and (d) 1200 °C.

The compression strength is measured at various sintering temperatures, and it is found that it is maximum at 1100 °C, as shown in Figure 5.6 (a). Figure 5.5 (c) shows the stress-strain curve for sintered pellets at various temperatures and it was found that pellet sintered at 1100 °C exhibited maximum compressive strength of 56.8MPa compared to other pellets. The open porosity of sintered pellets decreased with an increase in sintering temperature, as shown in Figure 5.6 (b). The EDX was performed to explore surface chemical composition after sintering. Figures 5.7 (a) & 5.7 (b) show

the elemental analysis from EDX of biphasic calcium phosphates at 1100 and 1200 °C, respectively. It confirms the presence of stoichiometric elements Ca, P, O and other trace elements like Fe, Mg, Si, and Na. The atomic percentages are reported in Figures 5.7 (a) & 5.7 (b). The variation in chemical composition between the sintered samples at 1100 and 1200 °C is mainly reported. The Ca/P ratios for the samples sintered at 1100 and 1200 °C are 1.57 and 1.56, respectively.

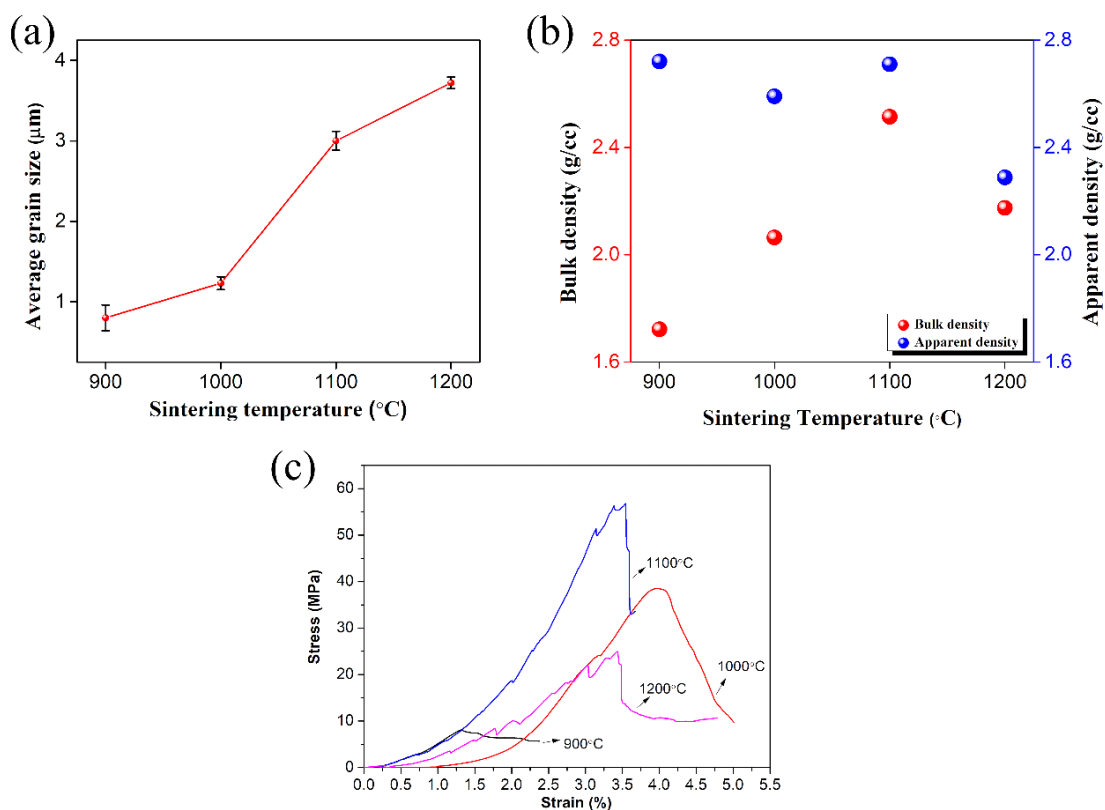


Fig. 5.5. (a) Average grain size as a function of sintering temperature (b) apparent density and bulk density as a function of sintering temperature, and (c) Stress-strain curve of sintered pellets at various temperatures.

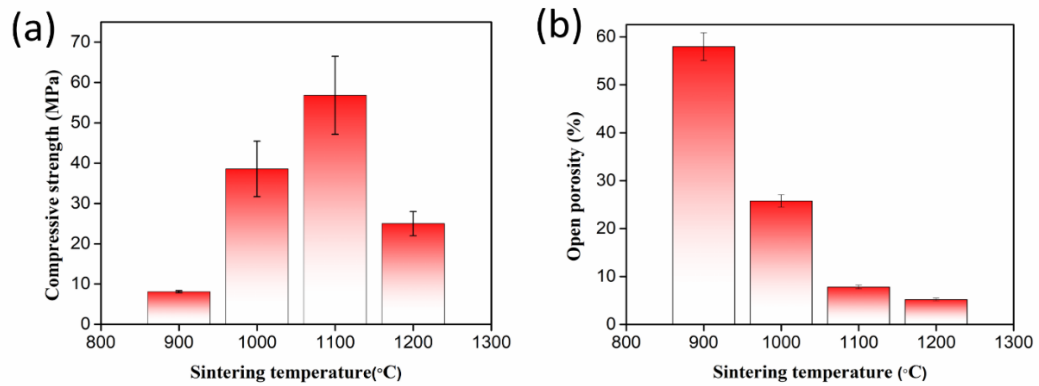


Fig. 5.6. Variation of (a) compression strength and (b) open porosity with sintering temperature

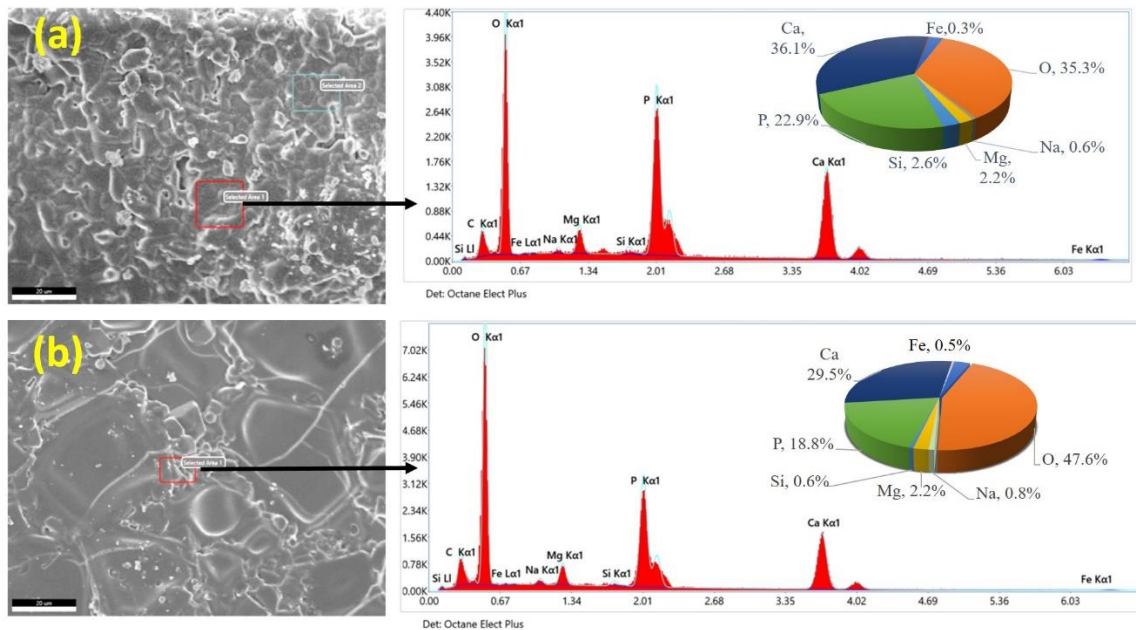


Fig. 5.7. Topological SEM images of BCP specimens at (a) 1100 °C and (b) 1200 °C with Energy-dispersive X-ray spectroscopic analysis.

X-ray photoelectron spectroscopy is carried out for the biphasic calcium phosphates at 1100 °C and 1200 °C to determine the chemical elements present and identify their chemical states. XPS wide scan spectrum as shown in Figure 5.8 (a) confirms the peaks of the elements C 1s, O 1s, Ca 2p, P 2p, Si 2p, Na 1s, and Mg 1s. Figure 5.8 shows the survey spectrum and deconvoluted high-resolution spectra of various elements of BCP at 1100 °C. XPS spectra of Ca 2p peaks are identified at 347.03 eV ($2p_{3/2}$) and 350.57 eV ($2p_{1/2}$) (Figure 5.8(b)), which corresponds to β -TCP (Chusuei

et al. 1999; Nagpure et al. 2012). Figure 5.8(c) displays the high-resolution spectra of O 1s peaks where binding energy at 530.83 eV is due to the presence of β -TCP (Chusuei et al. 1999), and binding energies at 532.05 eV, 533.15 eV are due to HA (Ortiz et al. 2022). Figure 5.8(d) displays the high-resolution spectra of P 2p peaks where binding energies are identified at 132.95 eV and 133.91 eV. Binding energy at 132.95 eV attributes to β -TCP, and binding energy at 133.91 eV belongs to HA (Chusuei et al. 1999). Figure 5.8(e) shows the high-resolution spectra of Na 1s where binding energy at 1071.21 eV is assigned to the +1 state (Bharathi et al. 2019). Figure 5.8(f) shows the high-resolution spectra of Si 2p, where binding energy at 102.67 eV is assigned to the +2 state (Dora et al. 2020). Figure 5.8(g) shows the high-resolution spectra of Mg 1s where binding energy at 1303.76 eV belongs to MgO (La et al. 2017). HA is stable whereas TCP is soluble in body fluid. To achieve an optimum dissolution rate of bone graft materials, biphasic calcium phosphates composed of HA and TCP are mainly focused.

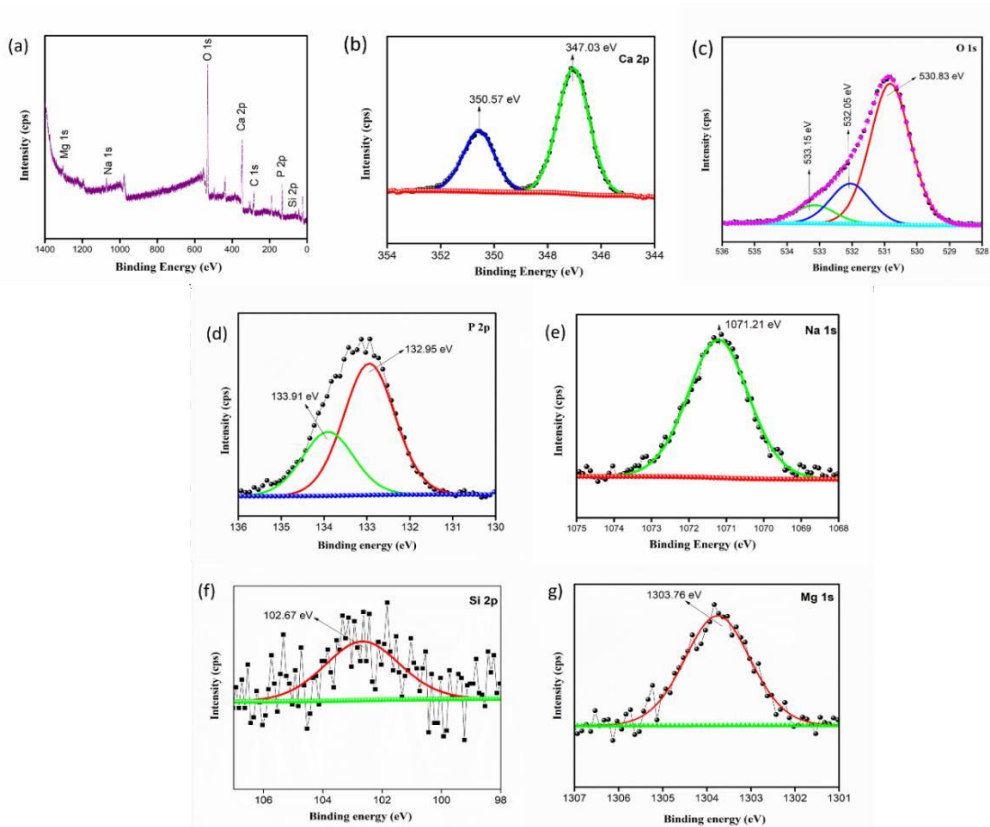


Fig. 5.8. XPS analysis shows (a) Survey spectrum and deconvoluted high-resolution spectra of (b) Ca 2p, (c) O 1s, (d) P 2p, (e) Na 1s, (f) Si 2p, and (g) Mg 1s at 1100 °C.

Figure 5.9 shows the survey spectrum and deconvoluted high-resolution spectra of various elements of BCP at 1200 °C. XPS spectra of Ca 2p peaks are identified at 346.83 eV (2p_{3/2}), 350.45 eV (2p_{1/2}), and 351.85 eV (2p_{1/2}) (Figure 5.9 (b)). The binding energy at 346.83 eV and 350.45 eV corresponds to the O-Ca-O bond in α -TCP (Nagpure et al. 2012). The binding energy at 351.85 eV represents the Ca-O bond in hydroxyapatite (Liu et al. 2014). Figure 5.9 (c) displays the high-resolution spectra of O 1s peaks where binding energies at 530.76 eV, 532.7, 534.61, 536.38 and 537.21 eV attribute to the Ca-O bond in α -TCP (Ortiz et al. 2022), C-O (Ortiz et al. 2022), C-OH bond (Hadagalli et al. 2020), hydroxyl group of HA (Hadagalli et al. 2019) and O-O bond (Hadagalli et al. 2020). Figure 5.9 (d) displays the high-resolution spectra of P 2p where binding energy at 133.30 is due to the formation of α -TCP (Chusuei et al. 1999). Figure 5.9 (e) displays the high-resolution spectra of Na 1s where binding energy at 1070.82 eV is related to Na⁺ ions (Bharathi et al. 2019; Kalapsazova et al. 2017). Binding energy at 134.93 eV correlates to hydroxyapatite and other components at 137.29eV, and 138.76eV corresponds to the phosphate group of HA (Hadagalli et al. 2019). Figure 5.9 (f) displays the high-resolution spectra of Si 2p where binding energy at 102.59 eV is assigned to the +2 state and binding energy at 106.36 eV is assigned to the +3 state (Dong et al. 2016; Dora et al. 2020). Figure 5.9 (g) displays the high-resolution spectra of Mg 1s where binding energy at 1303.29 eV belongs to MgO (Hadagalli et al. 2020; La et al. 2017). Table 5.1 represents XPS core levels of different calcium phosphates.

Table 5.1. XPS core levels of different calcium phosphates

Phase	P 2p(eV)	Ca 2p _{1/2} (eV)	Ca 2p _{3/2} (eV)	O 1s(eV)
HA	133.91	351.85	-	532.05,533.15
β -TCP	132.95	350.57	347.03	530.83
α -TCP	133.3	350.45	346.83	530.76

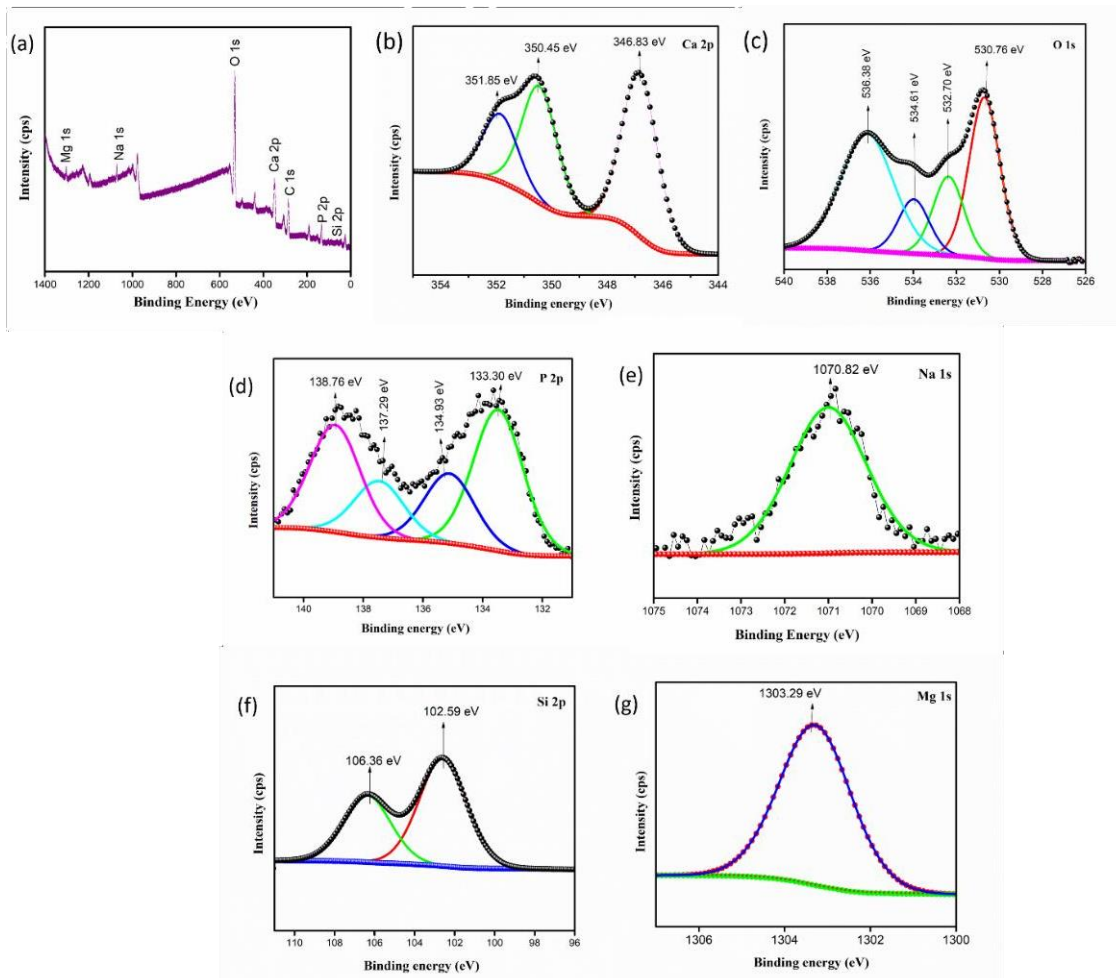


Fig. 5.9. XPS analysis shows (a) Survey spectrum and deconvoluted high-resolution spectra of (b) Ca 2p, (c) O 1s, (d) P 2p, (e) Na 1s, (f) Si 2p, and (g) Mg 1s at 1200 °C.

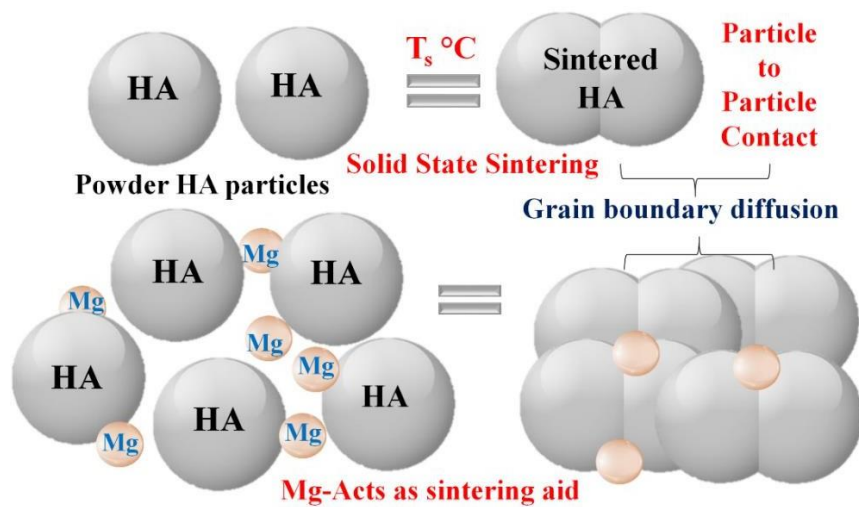


Fig. 5.10. Schematic of the root cause for high strength at 1100 °C

Figure 5.10 shows the schematic representation of solid-state sintering to show the root cause for high strength, where magnesium acts as a sintering aid (Tan et al. 2013). The presence of Mg in the form of MgO (Figure 5.8 (g)) at grain boundaries plays a vital role in grain boundary diffusion to suppress grain growth and enhance the densification and compressive strength of biphasic calcium phosphates (Tan et al. 2013). MgO at grain boundaries is beneficial to suppress discontinuous grain growth and promote the sintering of biphasic calcium phosphate, leading to a dense and strong finer homogeneous structure, as shown in Figure 5.4 (c). The values of physical properties and microstructure at 1100 °C clearly showed that maximum strength was obtained due to dense structure. Sintered specimens at 900 and 1000 °C are characterized by high porosity and relatively low apparent density and bulk density. As a result, these specimens exhibited less compressive strength. Sintered specimens at 1100 °C with porosity in the range of about 10 % exhibited the highest compressive strength. At 1100 °C dense morphology is responsible for high apparent density and bulk density. This dense morphology is because of MgO effect at grain boundaries which is responsible for high strength.

5.4 Conclusion

Prawn shell bio-waste has been explored as a source of calcium carbonate with nature-inbuilt trace elements. The wet chemical synthesis method was employed to synthesize the biphasic calcium phosphate. SEM and EDS revealed well-sintered uniaxial grains and the presence of trace elements like Fe, Mg, Si, and Na, respectively, which aid the sintering process to obtain biphasic calcium phosphates. A comprehensive XPS study determines the presence and chemical state of chemical elements. Especially, Mg in the form of MgO plays a role in grain boundary diffusion to suppress grain growth and enhance densification resulting in the high compressive strength of biphasic calcium phosphate. In the XRD pattern, pellets sintered at 900, 1000, and 1100 °C have BCP phases (combination of HA and β -TCP), and pellet sintered at 1100 °C exhibited a compressive strength of 56.8 MPa. The phase change was observed when the sintering temperature changed from 1100 °C to 1200 °C as β -TCP was converted into α -TCP. The spectrum of physical and mechanical properties makes prawn shell biowaste- biphasic calcium phosphate a new generation of

implantable biomaterial for potential application projected in high-strength hard tissue replacements. In biphasic calcium phosphate, hydroxyapatite has bone-bonding ability on its surface in the body environment. On the other hand, β -tricalcium phosphate has high bio-resorbability in body environments. Therefore, biphasic calcium phosphate could have better functions as bioactive ceramics.

CHAPTER 6

DEVELOPMENT OF HA-KAOLINITE COMPOSITE FOR BONE REGENERATION

6.1 Introduction

Hydroxyapatite (HA, $\text{Ca}_{10}(\text{PO}_4)_6(\text{OH})_2$) is an important bio-ceramic material which is extensively used in bone tissue engineering due to its chemical composition that is like human bone and teeth. It has distinctive biological properties, such as osteoconductive, bioactive, nontoxic, noninflammatory, biodegradable and has excellent biocompatibility (Yuan et al. 2022). Since HA strongly bonds to surrounding tissue when implanted in the human body, it has been successfully used for orthopaedics and dentistry from past few decades (Venkatesan and Anil 2021). However, due to its inadequate mechanical properties, HA is unable to serve as a load-bearing implant (Prakasam et al. 2017). So, the use of HA as a filler for bone defects has been limited to non-load bearing areas and coatings on metallic implants for firm fixation with host bone (Bikramjit Basu n.d.). Therefore, additives like ZrO_2 , Al_2O_3 , SiC and metal fibers can be included in order to enhance the mechanical reliability of HA, but they are ruinous to the biological properties of HA. So, the addition of clays has gained considerable attention. As clays are nontoxic, their composites can be used in biomedical applications such as tissue engineering, bone cement, wound healing, drug delivery and enzyme immobilization (Sandomierski et al. 2022). As bone tissue engineering (BTE) is mainly based on formation of tissue and bone mechanics, scaffold, cells, growth factors are three main components of BTE. The significance of bone tissue engineering has been elevated due to the multifaceted roles of bone, encompassing its structural support for the body, safeguarding vital organs, enabling mobility, and serving as a reservoir for essential calcium and phosphate minerals (Dorozhkin 2011; MURUGAN and RAMAKRISHNA 2005). Additionally, the growing importance of bone tissue engineering has been influenced by the rise in knee and hip replacement procedures over the last few years as well as the drawbacks of existing treatment options such as allografts, autografts, ceramic and metallic implants (Salgado et al. 2004). Scaffolds are three dimensional porous structures which play a crucial role in tissue

engineering investigations. Although HA can be used to prepare scaffolds most of the BTE studies entails the use of polymers (both synthetic and natural) and fillers for the fabrication of composite scaffolds.

Different types of clays namely montmorillonite (MMT) and kaolin clays have been reported in the literature for their role in enhancing the mechanical characteristics of the bio composite scaffolds (Kwaśniewska et al. 2020). Kaolin is one of the most important clay minerals used in the industry. It comprises majorly kaolinite mineral which is a hydrated aluminum silicate, $\text{Al}_2\text{Si}_2\text{O}_5(\text{OH})_4$. Kaolinite is also called china clay and it is composed of layers of silicate, with one octahedral sheet of alumina (AlO_6) octahedra attached through oxygen atoms to one tetrahedral sheet of silica (SiO_4) (FROST and KRISTOF 2004). Kaolinite is earthy, soft and generally white in colour which is produced via weathering/ chemical oxidation of mineral ores of aluminium silicates. It has low cation exchange capacity (CEC) which lies in the range of 1-15 meq/100 g (Torres-Luna and Carriazo 2019). Kaolin has found its applications in paper (Tunç et al. 2016), cement (Lemma et al. 2015), textile (Elmoubarki et al. 2015), paint (Murray 1991), rubber industries (Nasruddin et al. 2021), ceramics industries (Dondi et al. 2008) and in civil engineering applications (Abdullah et al. 2018). Kaolin can also be used to produce fiberglass (Murray 2000). Fiberglass has many numbers of applications which include insulation, plastics reinforcement, textile yarn, substrates for electronic circuit boards (Marsh 2008). Kaolin can be used as a filler in plastics because it helps to produce a better surface finish (Mareri et al. 1998). Kaolin has certain advantages like high specific surface area and low cost (Song et al. 2014). Reports indicate that by incorporating kaolin, the scaffold demonstrated a more stable and favorable pH environment, along with an improved capacity for protein adsorption (Obada et al. 2021).

MMT clay with hydroxyapatite layer can be used as a filler with remineralizing potential in composites for dental applications (Sandomierski et al. 2020). To enhance the strength of a HA/polymer composite, MMT can be used as a reinforcing agent for the application of bone replacement. Katti et al. reported that MMT clay addition in HA/chitosan/MMT composite increased the hardness and elastic modulus of the composite (Katti et al. 2008). Other studies revealed that addition of

MMT clay in MMT/chitosan/HA-ZrO₂ (Bhowmick et al. 2016) and MMT/chitosan/HA-ZnO (Bhowmick et al. 2018) composites improved the tensile strength. Obada et al. reinforced HA with kaolin clay using sol-gel method to improve the mechanical and biological properties of bioceramics (Obada et al. 2021). The reported mechanical measurement data affirms that reinforced hydroxyapatite scaffolds can be served as an alternative for human trabecular bone whose compressive strength lies in the range of 2-12 MPa (Morgan et al. 2018). However, the brittleness and lack of mechanical stability of HA-clay composite scaffolds are some of the significant drawbacks, preventing its application in extensive bone regeneration. Reinforcement of hydroxyapatite with inorganic clays could open an advanced direction of preparing scaffolds with improved mechanical properties, improved sinterability thereby increased strength with retained porosity, improved durability, cost effectiveness and superior cell proliferation within the realm of bone tissue engineering. The scaffold must possess robust mechanical integrity, given that cortical bone typically exhibits an elastic modulus ranging from 1 to 20 GPa and a strength of 1 to 100 MPa, similar to cancellous bone, which boasts an elastic modulus of 0.1 to 1.0 GPa and a strength of 1 to 10 MPa (Sabree et al. 2015).

In the present study, prawns shell exoskeleton waste was utilized as a Ca rich raw source to synthesis HA. Kaolin clay was selected as a reinforcing material to prepare HA-kaolin clay (0, 10, 20, 30 wt.%) composites by mechanical mixing and uniaxial pressing method. In order to maintain high compressive strength in the HA kaolin clay composites while retaining high porosity, the sintering scheme and kaolin clay addition were optimized. X-ray diffraction, Raman spectra, field emission scanning electron microscopy and Fourier-transform infrared spectroscopy (FTIR) for bare HA, HA-clay composite, and bare kaolin were carried out to examine the phases present in HA. The differential scanning calorimetry (DSC) and thermogravimetric analysis (TGA) gave insight into the thermal activity during sintering of the HA-clay composite. To assess the mechanical properties, compression strength is determined and to assess physical properties bulk and apparent densities and open porosities were estimated by Archimedes' principle.

6.2. Materials and methods

6.2.1 Materials

Prawn shell (*Fenneropenaeus indicus*) waste was collected from the local fish market and shells were separated. Prawn exoskeleton is a source of calcium carbonate. Prawn shell is thoroughly washed with tap water and hot distilled water. After being washed, the prawn shells were dried for six hours at 150 °C in an oven before being pulverized into powder. Kaolin (200 mesh) is purchased from Molychem chemicals, Mumbai.

6.2.2 Preparation of hydroxyapatite kaolin clay composite from the prawn shells

The wet chemical synthesis method was employed to prepare hydroxyapatite using prawn shell derived CaO as outlined in chapter 3. The procedure to obtain HA-clay composite is shown in Figure 6.1.

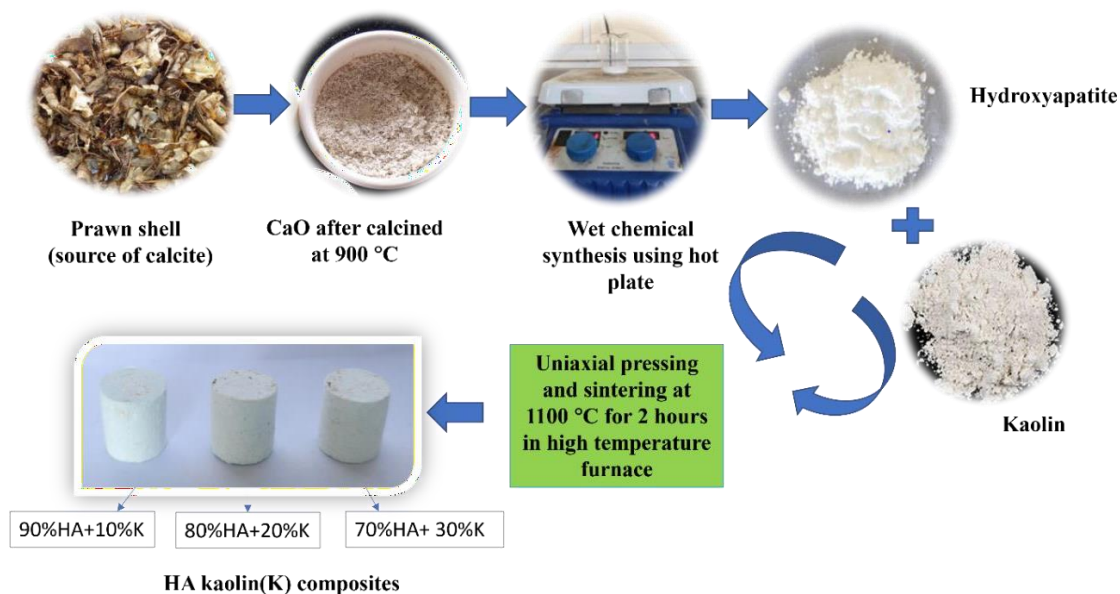


Fig. 6.1. Process flow diagram of HA-clay composite preparation.

HA powder and different wt.% (10, 20 and 30) of kaolin clay are mechanically mixed using agate mortar and pestle and the resulting powder is subjected to uniaxial pressing to obtain the green pellets with a compressive load of 12.5 kN. The green pellets were sintered in air at 1100 °C for 2 hours in programmable high-temperature furnace [Nabertherm, Germany] results in HA-Kaolin clay composites.

6.2.3 Characterization tools

To determine the phases, present in the synthesized powders, X-ray diffractometer (Empyrean, Malvern PANalytical, Netherlands) with Cu K α radiation at a scan rate of 2 °/min was used. Field emission scanning electron microscopy (FESEM 7610FPLUS, Jeol, Japan) with 5 kV as an accelerating voltage was utilized to determine the microstructure of the sintered HA-clay composites. Fourier transform infrared spectroscopy was used (Alpha II, Bruker, Germany) to detect the functional groups present in the samples. FTIR spectra were taken at an average scan rate of 24 scans and 4 cm⁻¹ resolution in the wavenumber range of 550-4000 cm⁻¹. Raman spectroscopy (Renishaw, UK) was used to determine the vibrational states and characteristic bonds in the samples. Raman spectra were taken in the wavenumber range of 100-4000 cm⁻¹. Differential scanning calorimetry (DSC, Netzsch 404 F1, Germany) was carried out to detect exothermic and endothermic transitions at a constant heating rate of 10 °C/min in the temperature range of 30 °C – 950 °C. The weight loss changes in the samples are observed within temperature range of 20 °C – 900 °C, at a constant heating rate of 10 °C/min using Thermogravimetric analyser (PerkinElmer, Singapore). The compressive strength was measured for sintered HA-clay composite specimens by using a universal testing machine (UTM, Shimadzu, Japan). The physical properties like apparent density, bulk density, and open porosity of the sintered HA-clay composite specimens,

were measured using a density measurement kit (CAS 44, Contech) by Archimedes' principle method as per standard ASTM-C373-88. The bulk density, apparent density, and % open porosities were calculated by estimating soaked, immersed and dry weights of sintered specimens.

6.3 Results and discussion

6.3.1 Structural and vibrational analysis

XRD pattern of bare HA, HA-clay composites and bare kaolin are shown in Figure 6.2 (a)-(e) respectively. XRD pattern of sintered HA powder is shown in Figure 6.2 (a), and observed that major reflection at 31.69° which matches to pure HA with the reflection in ICDD number 01-074-0565 and the other prominent reflections are found at 16.92° , 25.94° , 28.12° , 32.74° , 34.1° . XRD patterns of sintered HA-clay composites show kaolin peaks at 21.68° in addition to HA peaks which is shown in Figure 6.2 (b)-(d). In Figure 6.2 (e), XRD pattern of kaolin shows two notable reflections at 12.36° and 24.89° which matches with the Bragg's reflections in ICDD 01-089-6538. A series of peaks are found to be 19.9° , 20.34° , 21.26° , 35.97° , 38.44° which confirms the phase purity of kaolin powder. Figure 6.2 (b)-(d) show peaks around 21.68° along with other series of peaks which confirms the formation of HA-clay composites. However major reflections of kaolin at 12.36° and 24.89° are absent in HA-clay composites due to phase transformations that occur during sintering process (Kłosek-Wawrzyn et al. 2013). These phase transformations can be clearly analyzed from the DSC thermal analysis performed on kaolin.

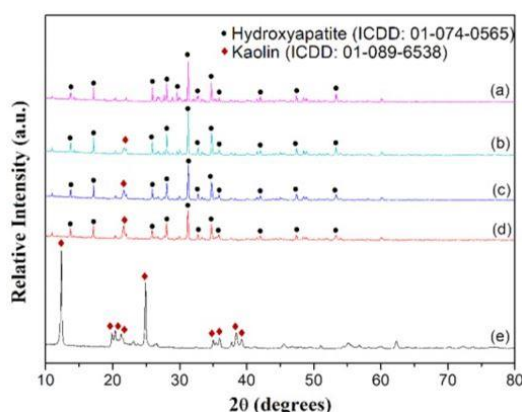


Fig. 6.2. XRD pattern of (a) sintered HA (b) 90 % HA+10 % Kaolin (c) 80 % HA+20 % Kaolin (d) 70 % HA+30 % Kaolin (e) Kaolin.

The FTIR spectra of HA, kaolin and HA with different wt. % kaolin clay composites are shown in Figure 6.3. In Figure 6.3 (a), the FTIR spectrum of HA reveals the characteristic peaks around wavenumbers 563, 597, 724, 966, 1027, 1098 cm^{-1} due to the presence of a phosphate group in the HA (Prekajski et al. 2016). The IR bands observed at 563, 597, 724 cm^{-1} signify phosphate bending vibrations, and those at 966, 1027, 1098 cm^{-1} are due to phosphate stretching vibrations. A weaker peak at 1540 cm^{-1} is due to traces of carbonate ions, and this was attributed to the environmental reactions with CO_2 present in atmosphere. Another broad peak detected at 3426 cm^{-1} attributed to the stretching of the structural OH^- band (Hadagalli et al. 2020). Likewise, the asymmetric stretching, asymmetric bending modes were observed for phosphate and carbonyl groups (Prekajski et al. 2016). Figure 6.3 (b)-(d) show the similar characteristic peaks of HA where kaolin amount varies from 10 to 30 wt%. In accordance with the stretching frequencies of OH groups, kaolin possesses absorption bands between 3500 and 3700 cm^{-1} as shown in Figure 6.3 (e). The FTIR spectrum related to kaolin reveals the presence of two bands at 3688, 3614 cm^{-1} due to the stretching vibrations of O-H bond (Tironi et al. 2012). The bands observed at 1117, 1025, 1005 cm^{-1} in pure kaolin were attributed to Si-O stretching vibration (Tironi et al. 2012). The Al-OH absorption peak was revealed at 910 cm^{-1} (Benkacem et al. 2021). The bands located at 792, 751 cm^{-1} are assigned to vibrations of Si-O-Al groups (Tironi et al. 2012). The band located at 675 cm^{-1} is attributed to vibration of Al-OH group (Tironi et al. 2012). The band located at 560 cm^{-1} is corresponding to vibration of Si-O-Al group. The kaolin structure is chaotic and simpler to dehydrate when the band at 3688 cm^{-1} vanishes. Figure 6.3 (b)-(d) show the peaks around 1117, 1025, 563 cm^{-1} which confirms the presence of kaolin in HA-clay composites (Mgbemena et al. 2013). The assigned vibrational bands from the FTIR spectrum are shown in Table 6.1.

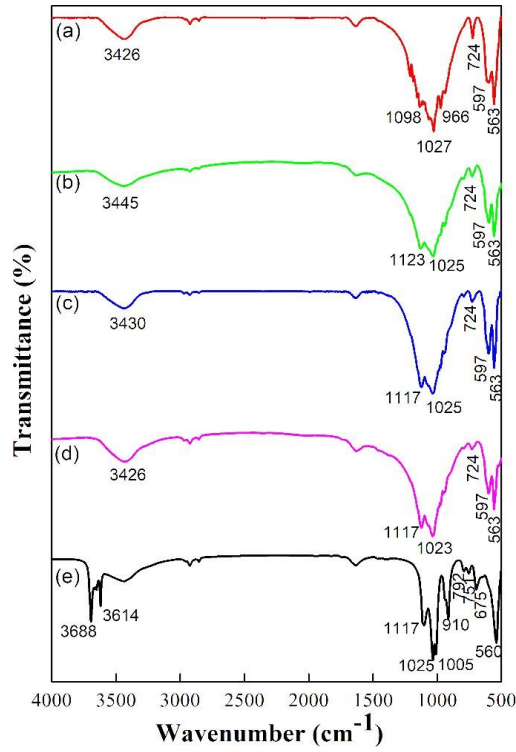


Fig. 6.3 FTIR spectra of (a) sintered HA (b) 90% HA+10% Kaolin (c) 80% HA+20% Kaolin (d) 70% HA+30% Kaolin (e) Kaolin

Table 6.1. Vibration modes in the FTIR spectrum of HA-clay composites

Wavenumber, [cm ⁻¹]	Stretching mode	Functional group	Source
560, 751, 792	-	Si-O-Al	Kaolin
563, 597, 724	Asymmetric bending	PO ₄ ³⁻	HA
966	Symmetric stretching	PO ₄ ³⁻	HA
1023-1027,1098	Asymmetric stretching	PO ₄ ³⁻	HA
675, 910	-	Al-OH	Kaolin
1005, 1025	In plane stretching	Si-O	Kaolin
1117-1123	Longitudinal mode	Si-O	Kaolin
1540	Asymmetric stretching	CO ₃ ²⁻	atmospheric CO ₂
3426	stretching of OH ⁻	OH ⁻	HA

Figure 6.4 (a)-(d) shows the Raman spectra of HA and HA with 10, 20, 30 wt% of kaolin clay composites, respectively and the peak vibrational mode summary is tabulated in Table 6.2. The band observed at 972 cm^{-1} corresponds to the stretching mode (ν_1) of the symmetric vibrational mode of P–O. Additionally, bands near 412 cm^{-1} and 737 cm^{-1} represent the doubly bending mode (ν_2) and triply degenerate bending mode (ν_4) of the PO_4 vibrational mode, respectively. Furthermore, the vibrational mode of PO_4 triply degenerate antisymmetric stretching mode (ν_3) was detected at 1045 cm^{-1} (Amenta et al. 2018). The peaks at 620 cm^{-1} for 80 % HA+20 % kaolin composite and 615 cm^{-1} for 70 % HA + 30 % kaolin composite are due to translation of Si-O-Al group in kaolin of HA-clay composites (Frost et al. 1997). Figure 6.4e shows the Raman spectra of kaolin where peak intensities could only be observed under an enlarged view (inset of Figure 6.4). The bands at 3696 cm^{-1} and 3620 cm^{-1} correspond to the ν_1 and ν_5 stretching modes of the inner surface hydroxyl groups (Horváth et al. 2010; Peng et al. 2018). These bands are further presented in all HA-clay composites which is represented by shaded area.

Table 6.2. Vibration modes in the Raman spectra of HA-clay composite

Wavenumber, [cm ⁻¹]	Assignment	Vibration groups	Source
972	Symmetric stretching vibrational mode of P-O	$\nu_1 \text{PO}_4^{3-}$	HA
412	Doubly bending mode	$\nu_2 \text{PO}_4^{3-}$	HA
1045	Triply generate antisymmetric stretching mode	$\nu_3 \text{PO}_4^{3-}$	HA
737	Triply degenerate bending mode	$\nu_4 \text{PO}_4^{3-}$	HA
615-620	Si-O-Al translation	Si-O-Al	Kaolin
3620	O-H stretching	$\nu_5 \text{OH}^-$	Kaolin
3696	O-H stretching	$\nu_1 \text{OH}^-$	Kaolin

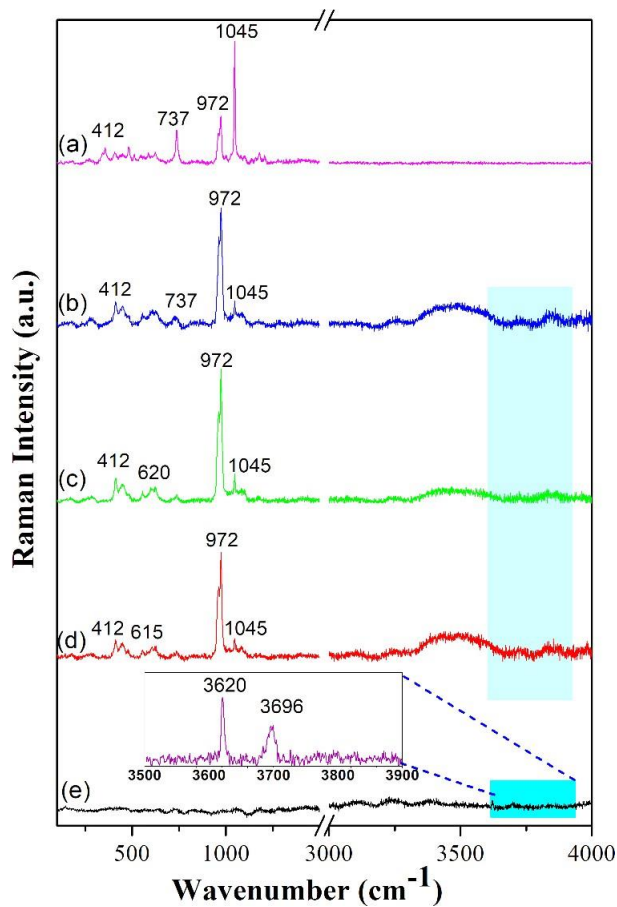


Fig. 6.4. Raman spectra of (a) sintered HA (b) 90 % HA+10 % Kaolin (c) 80 % HA+20 % Kaolin (d) 70 % HA+30 % Kaolin (e) Kaolin

6.3.2. Thermal analysis

Figure 6.5 (a)-(c) represents the DSC analysis of pure HA, kaolin and HA with 20 wt.% of kaolin respectively. In the pure HA, endothermic peak at 80 °C corresponds to the removal of adsorbed water from the lattice. It is reported that heating of apatite at higher temperatures can lead to dehydroxylation, which can be reflected from the exothermic peak at 715 °C in pure HA (Garskaite et al. 2014). Similarly, Skinner et al. reported that the dehydroxylation of HA starts above 700 °C (Skinner et al. 1975). The endothermic peak at 498 °C indicates the dehydroxylation of the kaolinite, which is reflected in the kaolin and HA kaolin composite (Ondro and Trník 2018; Peng et al. 2018). Here, dehydroxylation of the crystalline kaolinite structure took place; resulted in the formation of calcined metakaolin phase. Also, the exothermic peak at 716 °C in Figure 6.5 (c) shows the dehydroxylation of HA.

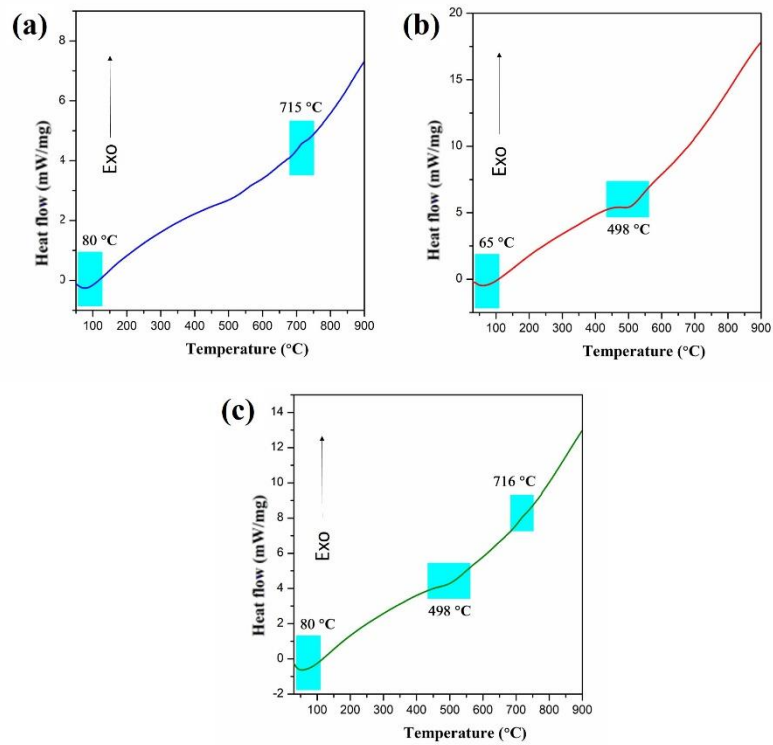


Fig. 6.5. DSC analysis of (a) pure HA (b) Kaolin (c) 80 % HA+20 % Kaolin.

The thermal behavior of the pure HA along with kaolin and blended HA (20 wt.% kaolin) is studied by thermogravimetric analysis (TGA). The percentage weight loss of pure HA, kaolin and HA with 20 wt.% of kaolin, represented in Figure 6.6 (a)-(c) respectively. The weight loss occurred around 210 °C could be attributed due to dehydration and dehydroxylation of absorbed water, expelled from the mineral lattice of HA as shown in Figure 6.6 (a). By interpolation of TG-curve of Figure 6.6 (c), the percentage weight loss of kaolinite mineral in HA with 20 wt. % kaolin was found to be around 8 %. The corresponding TGA peak between 515 °C and 750 °C is a clear indication of weight loss occurred due to dehydroxylation of kaolinite clay mineral within the composite (Faqir et al. 2019).

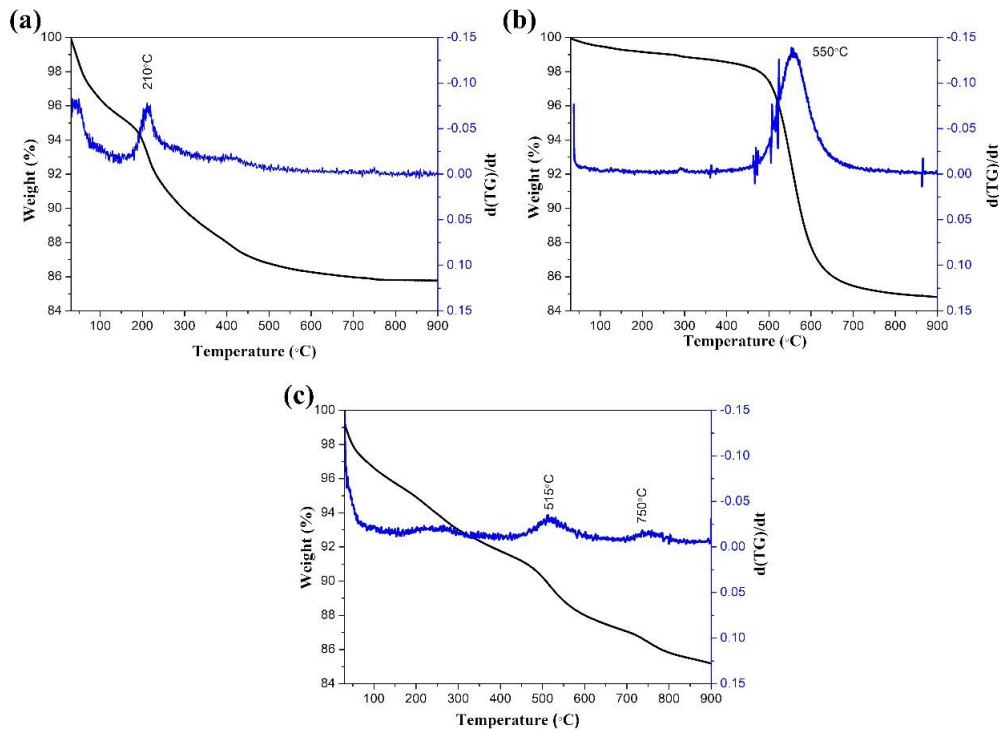


Fig. 6.6. Thermogravimetric analysis of (a) pure HA (b) Kaolin (c) 80 % HA+20 % Kaolin

6.3.3. Morphological analysis

The morphological study is conducted using FESEM for sintered HA, kaolin, HA clay composites and images are shown in Figure 6.7 (a), 6.7 (b), 6.7 (c), 6.7 (d) and 6.7 (e), respectively. The dense morphology and well sintered uni-axial grains were observed for sintered HA as shown in Figure 6.7 (a). Flake-like morphology (Li et al. 2015a) and more agglomeration was observed for pure kaolin clay as shown in Figure 6.7 (b). Figures 6.7 (c)-(e) show the micrographs of HA-clay composites with kaolin addition (10, 20, 30 wt. %) which are sintered at 1100 °C for 2 hours. It is observed that the flake-like structures of kaolin clay reinforced with HA creating porosities within the nanocomposite leads to flocculating morphology as shown in Figures 6.7 (c)-(e) (Dwari and Mishra 2019).

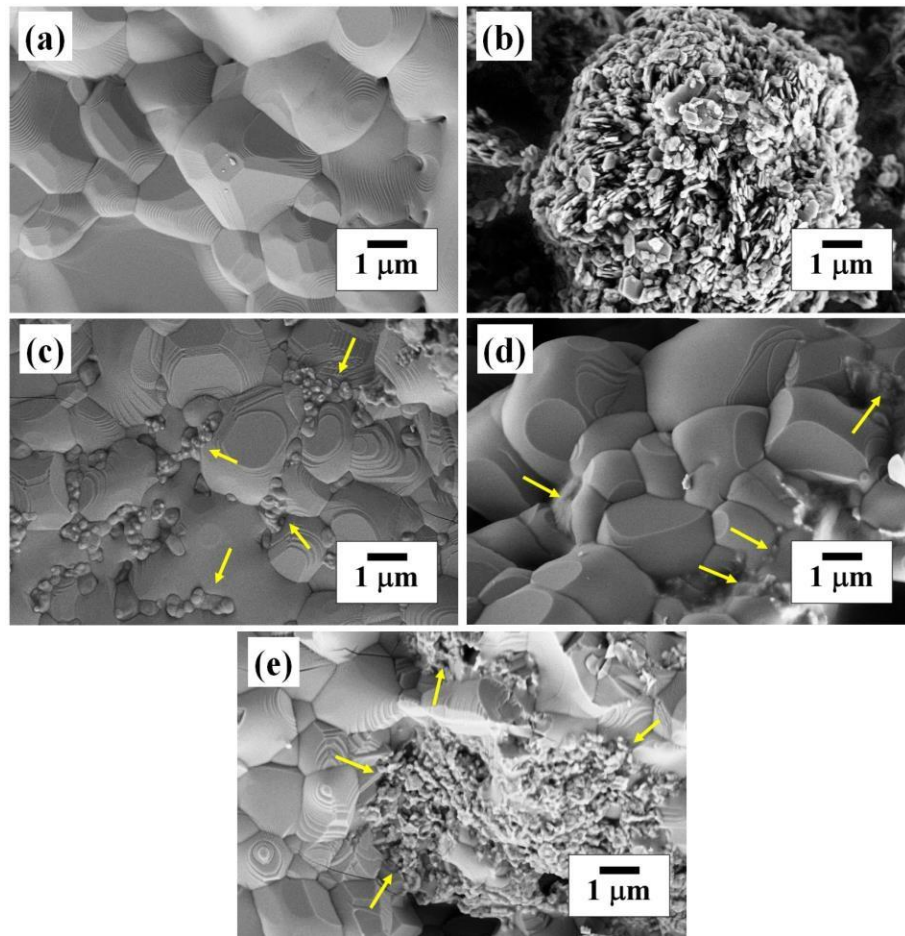


Fig. 6.7. Microstructure of (a) sintered HA (b) Kaolin (c) 90 % HA+10 % Kaolin (d) 80 % HA+20 % Kaolin (e) 70 % HA+30 % Kaolin (Yellow arrow marks represent the presence of kaolin)

6.3.4 Mechanical and physical properties

With reference to mechanical properties, Figure 6.8(A) shows the stress strain curves of sintered HA (Figure 6.8(A)a) and various (10 - 30 wt.%) HA-clay composites (Figure 6.8(A)b-6.8(A)d). It is observed that bare HA exhibited a compressive strength of 26 ± 1.2 MPa; whereas addition of clay component in 90 % HA + 10 % Kaolin and 80 % HA+20 % kaolin displayed an increase in compressive strength from 30 ± 2.8 MPa to 34.76 ± 6.7 MPa. Further addition of Kaolin in 70 % HA+30 % Kaolin exhibited a decrease in compressive strength to 33 ± 0.4 MPa, as shown in Figure 6.8(B). It was found that an increment in mechanical properties of HA with the addition of kaolin up to 20 wt. %, then further addition led to a decline in strength (Pan and Xiong 2009). Obada et.al reported compressive strengths of HA-kaolin clay composites (15 wt.% of

kaolin) under various sintering temperatures. At 900, 1000, and 1100 °C compressive strengths are found to be 5.67, 6.33 and 7.66 MPa which are very much less compared with the present results (Obada et al. 2021). The addition of clay lead to an increment in the compressive strength which may be due to the impact of reinforcement, although there is decrease in the apparent density. The decrement of the density could be due to the flake morphology of the clay which have marginally filled most of the pores (Obada et al. 2021).

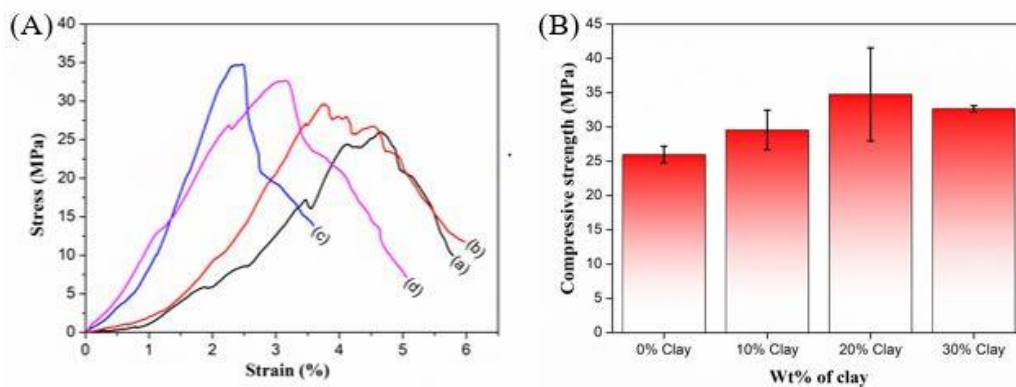


Fig. 6.8. (A) Stress-strain curves of sintered specimens of (a) sintered HA (b) 90% HA+10% Kaolin (c) 80% HA+20% Kaolin (d) 70% HA+30% Kaolin, (B) Variation of compressive strength with different wt.% of clay.

The physical properties of HA-clay composites are determined by open porosities, which originate from the escape of a small amount of water from kaolin during sintering. Figure 6.9 (a) shows the variation in apparent density and bulk density with different weight percentages (0, 10, 20, 30) of the addition of kaolin clay into HA. Figure 6.9 (b) shows the variation in open porosity with different weight % of kaolin clay. The bulk and apparent densities of bare HA, 90 % HA+10 % kaolin, 80 % HA+20 % kaolin and 70 % HA+30 % kaolin clay composites were found to be 2.34 g/cc, 1.75 g/cc, 1.66 g/cc, 1.71 g/cc and 2.67 g/cc, 2.47 g/cc, 2.22 g/cc, 2.22 g/cc, respectively. The open porosity of bare HA was found to be 14 %. But in the case of HA-clay composites, it is observed that open porosity increases up to 33% in 20 wt.% of kaolin addition and further decreases to 29 % in 30 wt.% kaolin clay addition (Yu et al. 2008). It is because of several possible reasons, like dehydroxylation of kaolinite mineral and the complex interaction pattern between hydroxyapatite and clay.

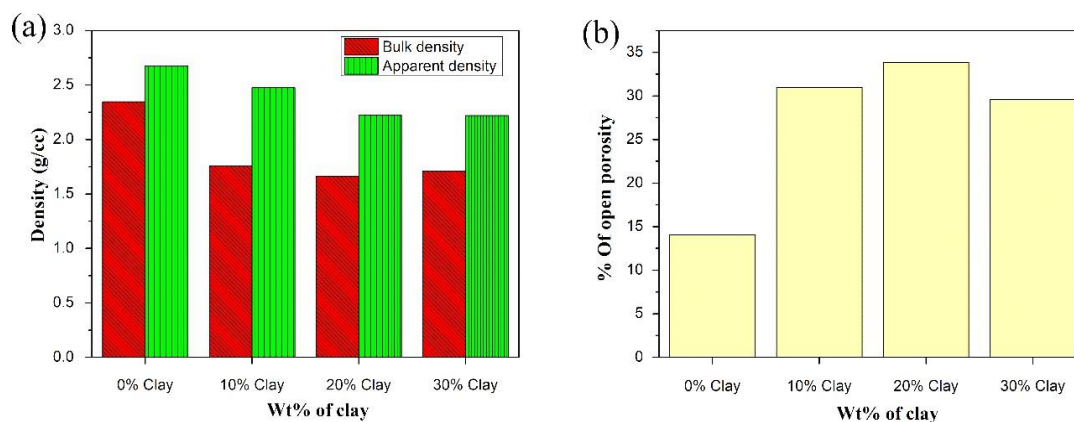


Fig. 6.9. The variation of physical properties of HA-kaolin clay composites with different (0, 10, 20 and 30) wt.% of kaolin clay addition, (a) bulk and apparent densities (b) open porosity

6.4 Conclusion

The utilization of prawn shell (*Fenneropenaeus indicus*) exoskeleton biowaste as a Ca-rich raw source to HA synthesis was demonstrated via wet chemical route and further HA-kaolin clay (10, 20, 30 wt.%) composites were developed by mechanical mixing method. From XRD, the presence of HA and kaolin within the composite is confirmed from the prominent reflections. FTIR analysis show that the characteristic peaks around 1117, 1025, 560 cm^{-1} confirm the presence of kaolin in HA-clay composites. From Raman spectra, the characteristic peaks ranging from 615 to 620 cm^{-1} in HA-clay composite indicate the translation of Si-O-Al group in kaolin. DSC and TGA analysis of the HA-clay composite reveal thermal stability, and the endothermic peak at 498 $^{\circ}\text{C}$ indicates the dehydroxylation of the kaolinite. Dense and flocculating morphology is observed from FESEM in sintered HA and HA-clay composite, respectively, whereas flake morphology is observed in kaolin. Uniaxially pressed HA-clay composite specimens are sintered in air at 1100 $^{\circ}\text{C}$ for 2 hours to determine the physical and mechanical properties. Addition of 20 % kaolin to HA enhanced the compressive strength by 33.7 % in comparison to bare HA. The increase in the open porosity with kaolin addition has caused ~10 % decrease in apparent density. It is observed that there is an increment in compressive strength although there is a considerable increase in open porosity. This improved mechanical property in HA-clay

composites make this class of material an alternative promising material in bone tissue engineering, aimed towards trabecular bone repair and regeneration.

CHAPTER 7

DEVELOPMENT OF HA-BENTONITE COMPOSITE FOR BONE REGENERATION

7.1 Introduction

Because of its similarity to natural bone material, hydroxyapatite is one of the most sought-after biomaterials for bone implantation applications. Polymer materials play an important role in the creation of artificial organs, but their limited biocompatibility and bioactivity limit their technical uses (Geng et al. 2016). However, in tissue engineering applications, HA biomaterial did not exhibit any pyrogenetic reaction, inflammatory response, or toxicity (Kutikov and Song 2013). The best method to improve the ability of biomaterial to support bone and to increase its mechanical vigour (capacity to bear load), is to modify its surface with bioactive ceramics like clay to create nanocomposite. This will extend the biomaterial's lifespan without posing any risks. Natural clay particles are nontoxic, have high adsorption capacity, specific surface area, swelling capacity, and high solubility. Ambre et al. created a mineralized hydroxyapatite nanocomposite that showed tremendous potential for use in medicine using organically modified clay material (Ambre et al. 2015).

Bentonite is a naturally occurring clay mineral that has good features including strong cationic exchange and large surface area that make it useful in tissue engineering applications. Furthermore, bentonite has high swelling ratio, drug carrying capability and high adsorption capacity (Bonifacio et al. 2020; Cavalcanti et al. 2019; Grimes et al. 2018; Li et al. 2019; Stavitskaya et al. 2019). Many qualities of bentonite include a wide interlayer gap, good cationic exchange capacity, high antimicrobial activity (Krishnan and Mahalingam 2017), drug transport and release properties (Verma and Riaz 2018), swelling and absorbability capacity, gel formation tendency, and the capacity to serve as the focal adhesion sites for cells to promote attachment and proliferation (Nones et al. 2015). Numerous studies on bentonite composites for applications such as pharmaceuticals (i.e., drug delivery), biomaterials (i.e., scaffolds), cosmetics (i.e., topical personal care), biosensors (i.e., electrochemical), and medical

devices (i.e., patches and implants) have been carried out because the features of bentonite listed above are conducive to biomedical engineering research.

The current investigation utilized prawn shell exoskeleton biowaste as a calcium-rich raw material for synthesizing hydroxyapatite (HA). Bentonite clay was chosen as a reinforcing agent to fabricate HA-bentonite clay composites (0, 10, 20, 30, 40 wt.%) through mechanical mixing and uniaxial pressing techniques. Optimization of the sintering process and clay incorporation was pursued to maintain high compressive strength in the HA-bentonite clay composites while preserving their porosity. X-ray diffraction, Raman spectroscopy, field emission scanning electron microscopy and Fourier-transform infrared spectroscopy (FTIR) were employed to analyze the phases present in HA, HA-clay composites, and bare bentonite. Differential scanning calorimetry (DSC) and thermogravimetric analysis (TGA) provided insights into the thermal behavior during the sintering of HA-clay composites. Mechanical properties were evaluated through compression strength testing, while physical properties such as bulk and apparent densities, and open porosities were determined using Archimedes' principle.

7.2. Materials and methods

7.2.1 Materials

Prawn shell (*Fenneropenaeus indicus*) waste was collected from the local fish market and shells were separated. Prawn exoskeleton is a source of calcium carbonate. Prawn shell is thoroughly washed with tap water and hot distilled water. After being washed, the prawn shells were dried for six hours at 150 °C in an oven before being pulverized into powder. Bentonite clay is purchased from Molychem chemicals, Mumbai.

7.2.2 Preparation of hydroxyapatite bentonite clay composite from the prawn shells

The wet chemical synthesis method was used to prepare hydroxyapatite using prawn shell derived CaO as outlined in chapter 3. The procedure to obtain HA-bentonite clay composites is shown in Figure 7.1.

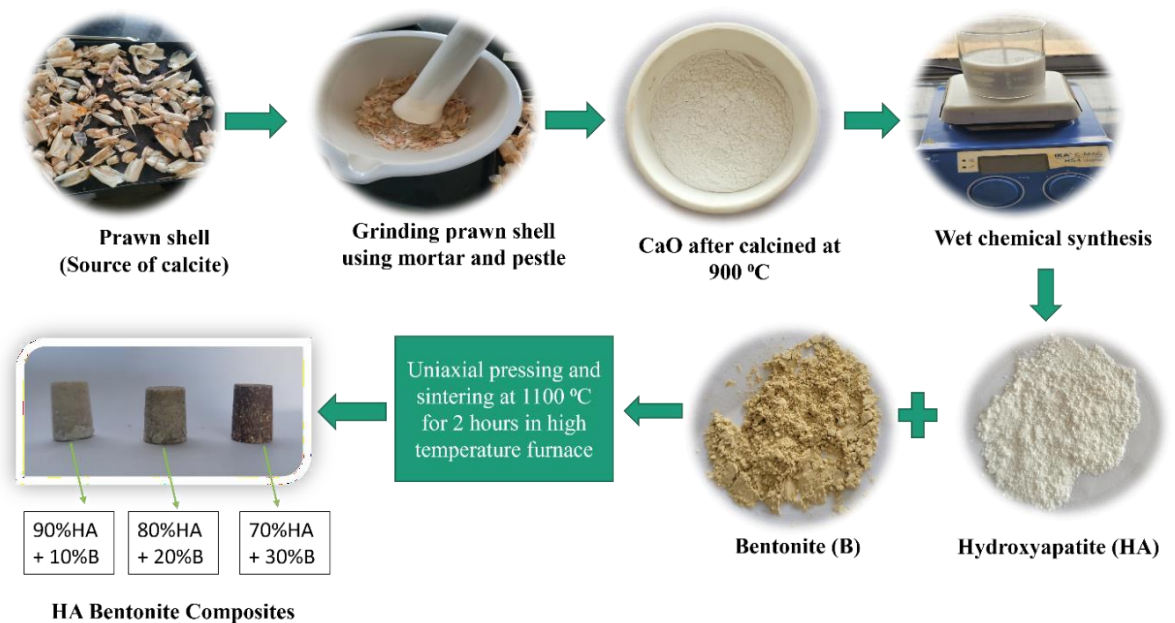


Fig. 7.1 Process flow diagram of HA-bentonite clay composites preparation

Bentonite is mixed physically with HA in various ratios (10 wt.%, 20 wt.%, 30 wt.%, 40 wt.%) and this mixture is pressed uniaxially using die and plunger with a load of 12.5 kN to make pellets. These pellets are then sintered at 1100 °C for 2 hours in a high temperature programmable furnace to obtain HA-bentonite clay composites.

7.2.3 Characterization tools

To determine the phases, present in the synthesized HA-bentonite clay composites, X-ray diffractometer (Empyrean, Malvern PANalytical, Netherlands) with Cu K α radiation at a scan rate of 2 °/min was used. Field emission scanning electron microscopy (FESEM 7610FPLUS, Jeol, Japan) with 5 kV as an accelerating voltage was utilized to determine the microstructure of the sintered HA-bentonite clay composites. Fourier transform infrared spectroscopy was used (Alpha II, Bruker, Germany) to detect the functional groups present in the HA-bentonite clay composite samples. FTIR spectra were taken at an average scan rate of 24 scans and 4 cm⁻¹ resolution in the wavenumber range of 500-4000 cm⁻¹. Raman spectroscopy (Renishaw, UK) was used to determine the vibrational states and characteristic bonds in the HA-bentonite clay composite samples. Raman spectra were taken in the wavenumber range of 100-3500 cm⁻¹. The weight loss changes in the samples are observed within temperature range of 30 °C – 900 °C, at a constant heating rate of 10 °C/min using

Thermogravimetric analyser (PerkinElmer, Singapore). Differential scanning calorimetry (DSC, Netzsch 404 F1, Germany) was carried out to detect exothermic and endothermic transitions at a constant heating rate of 10 °C/min in the temperature range of 30 °C – 900 °C. The compressive strength was measured for sintered HA-bentonite clay composite specimens by using a universal testing machine (UTM, Shimadzu, Japan). The physical properties like apparent density, bulk density, and open porosity of the sintered HA-bentonite clay composite specimens, were measured using a density measurement kit (CAS 44, Contech) by Archimedes' principle method as per standard ASTM-C373-88. The bulk density, apparent density, and % open porosities were calculated by estimating soaked, immersed and dry weights of sintered specimens.

7.3 Results and discussion

7.3.1 Structural and vibrational analysis

XRD pattern of bare HA, HA-bentonite clay composites and bare bentonite are shown in Figure 7.2 (a)-(f) respectively. The XRD pattern of sintered HA powder, as depicted in Figure 7.2 (a), exhibits a prominent peak at 31.69°, corresponding to the reflection found in ICDD number 01-074-0565, indicative of pure HA. Additionally, notable peaks are observed at 16.92°, 25.94°, 28.12°, 32.74°, and 34.1°, suggesting distinct crystallographic planes within the material. XRD patterns of HA-Bentonite clay composites (10, 20, 30, 40 wt.% of bentonite) show bentonite peaks at 26.64° in addition to HA peaks which is shown in Figure 7.2 (b)-(e). In Figure 7.2 (f), XRD pattern of bentonite shows two notable reflections at 12.3° and 26.62° which matches with the Bragg's reflections in ICDD 01-088-0891. A series of other peaks are found to be 19.84°, 20.81°, 24.86°, 34.74° which confirms the phase purity of bentonite powder. However, these reflections of bentonite are absent in HA-bentonite clay composites due to phase transformations that occur during sintering process.

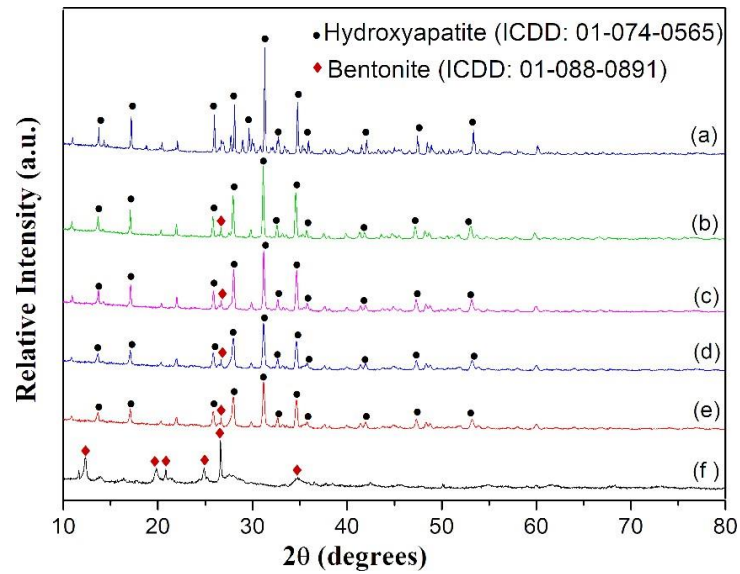


Fig. 7.2 XRD pattern of (a) sintered HA (b) 90 % HA+10 % Bentonite (c) 80 % HA+20% Bentonite (d) 70% HA+30% Bentonite (e) 60% HA+40% Bentonite (f) Bentonite.

The FTIR spectra of HA, bentonite and HA with different wt. % bentonite clay (10, 20, 30 and 40 wt. %) composites are shown in Figure 7.3. In Figure 7.3 (a), the FTIR spectrum of HA reveals the characteristics peaks around wavenumbers 563, 597, 724, 966, 1027, 1098 cm^{-1} due to the presence of a phosphate group in the HA (Prekajski et al. 2016). IR bands at 563, 597, 724 cm^{-1} are due to phospahte bending vibrations, and those at 966, 1027, 1098 cm^{-1} are due to to phospahte streching vibrations. A weaker peak at 1540 cm^{-1} was due to traces of carbonate ions, and this was due to the environmental reactions with CO_2 present in the atmosphere. Another broad peak found at 3426 cm^{-1} indicates the stretching of the structural OH^- band (Hadagalli et al. 2020). The IR spectrum of the raw-bentonite is given in Figure 7.3 (f). The structural OH stretching vibrations are observed at 3453 cm^{-1} , while the Si–O stretching vibration and

the OH bending modes are evident in the range of 1300–550 cm^{-1} . Additionally, the peak at 1638 cm^{-1} corresponds to the OH deformational mode of water, and the peak at 1111 cm^{-1} represents the longitudinal Si–O stretching mode. The FTIR spectra of HA/bentonite clay composites show functional groups of HA and bentonite clay respectively. Si–O stretching of the bentonite clay in HA/bentonite clay composites was noticed around 1119 cm^{-1} . The Si–O–Si stretching peak of the tetrahedral layer was clearly observed at around 1046 cm^{-1} . The OH bending peaks of octahedral layer were detected at 910 and 851 cm^{-1} .

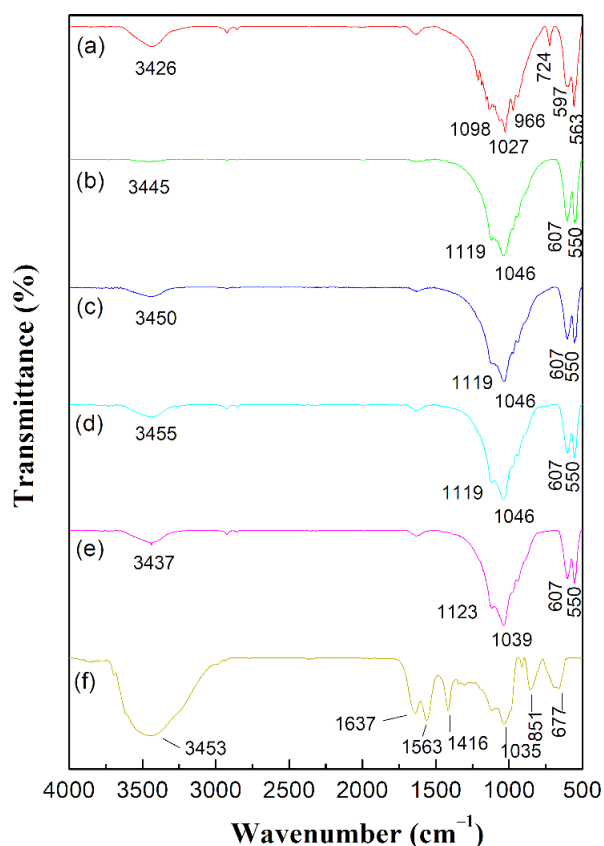


Fig. 7.3. FTIR spectra of (a) sintered HA (b) 90 % HA+10 % Bentonite (c) 80 % HA+20 % Bentonite (d) 70 % HA+30 % Bentonite (e) 60 % HA+40 % Bentonite (f) Bentonite.

Figure 7.4 (a) show the Raman spectra of HA. The 972 cm^{-1} band signifies the symmetric vibrational mode of P–O, termed as ν_1 (stretching mode). Additionally, the bands positioned at approximately 412 cm^{-1} and 737 cm^{-1} represent the vibrational modes ν_2 (doubly bending mode) and ν_4 (triply degenerate bending mode) of PO_4 ,

respectively. Another important vibrational mode, ν_3 (triply degenerate antisymmetric stretching mode) of PO_4 , manifests at 1045 cm^{-1} (Amenta et al., 2018). From the Raman spectra illustrated in Figure 7.4 (b)-(e), the prominent peak observed at 961 cm^{-1} in HA-bentonite clay composites primarily arises from the symmetric stretching vibration of Si–O, where O represents non-bridging oxygen. This peak also confirms the presence of dioctahedral phyllosilicates in the bentonite clay, as indicated by the presence of Raman peaks ranging from $1300\text{--}1900 \text{ cm}^{-1}$. The peaks at around 1184 cm^{-1} in HA-bentonite clay composites are attributed to the SiO_4 vibration mode. The OH/ H_2O vibrational modes in the spectrum of HA-bentonite clay composites are also confirmed from the sharp peaks at 3342 cm^{-1} . Typically, the vibrational modes associated with OH/ H_2O in clays are observed within the range of 3600 to 3000 cm^{-1} .

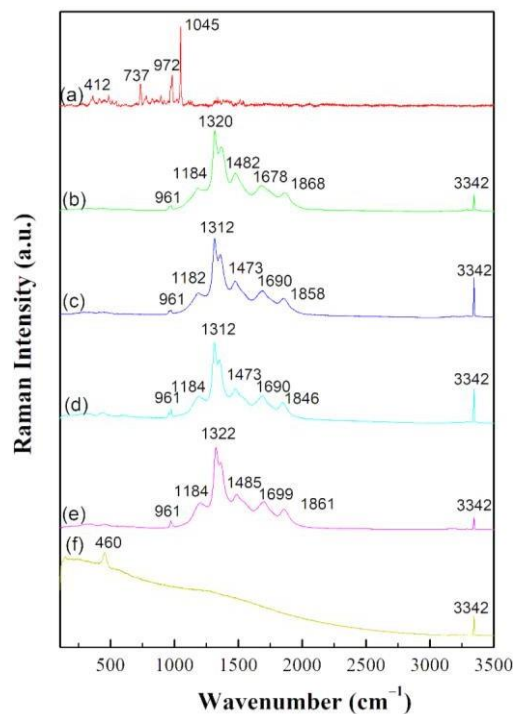


Fig. 7.4. Raman spectra of (a) sintered HA (b) 90 % HA+10 % Bentonite (c) 80 % HA+20 % Bentonite (d) 70 % HA+30 % Bentonite (e) 60 % HA+40 % Bentonite (f) Bentonite.

7.3.2 Thermal analysis

Figure 7.5 (a)-(c) depicts the results of the DSC analysis conducted on pure hydroxyapatite (HA), bentonite, and HA blended with 30 wt.% of bentonite,

respectively. In the case of pure HA, the endothermic peak observed at 80°C corresponds to the removal of adsorbed water from the lattice. Studies by Garskaite et al. have indicated that heating apatite to higher temperatures can result in dehydroxylation, as evidenced by the exothermic peak at 715 °C in pure HA (Garskaite et al. 2014). Similarly, Skinner et al. reported that dehydroxylation of HA typically initiates above 700°C (Skinner et al. 1975). Endothermic peaks are observed at 80 °C in bentonite and 67 °C in HA-bentonite clay composite due to the release of adsorbed and exchangeable water (Zivica and Palou 2015). The presence of minor endothermic peaks is observed in bentonite and HA-bentonite clay composite within the temperature range of 470-480 °C suggests the occurrence of dehydroxylation of bentonite clay (Zivica and Palou 2015).

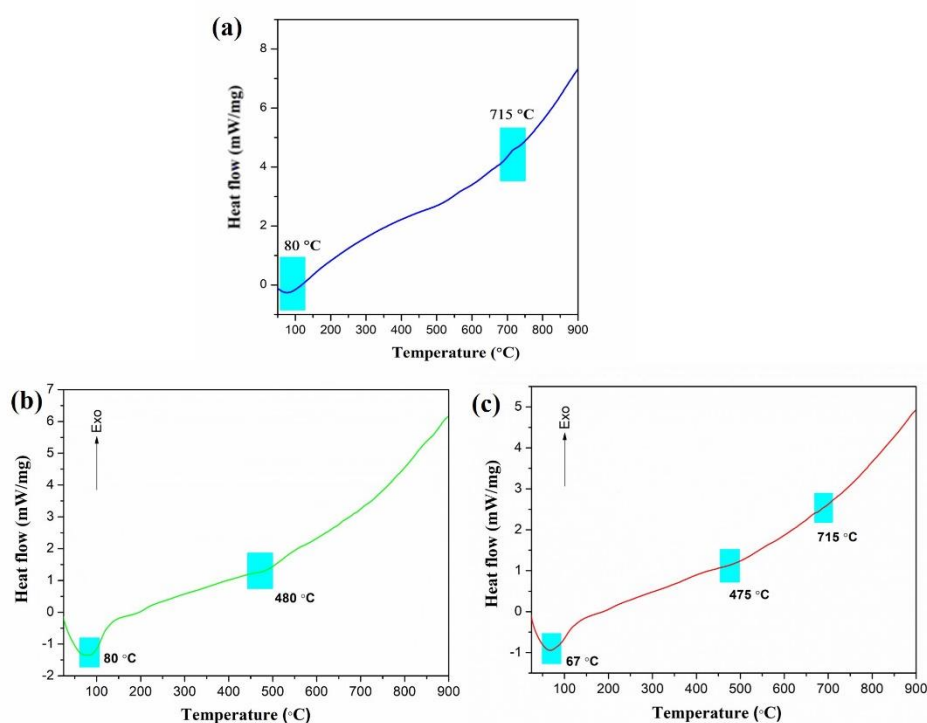


Fig. 7.5. DSC analysis of (a) pure HA (b) Bentonite (c) 70 % HA+30 % Bentonite

The thermal behavior of the pure HA along with bentonite and blended HA (30wt.% bentonite) is studied by thermogravimetric analysis (TGA). The percentage weight loss of pure HA, bentonite and HA with 30 wt.% of bentonite, represented in Figure 7.6 (a)-(c) respectively. The weight loss observed at approximately 210 °C may

be attributed to the dehydration and dehydroxylation processes, wherein absorbed water is released from the mineral lattice of the HA. The weight loss of 5 % was observed at around 505 °C due to dehydroxylation of bentonite. By interpolation of TG-curve, the percentage weight loss of bentonite clay mineral in HA with 30 wt. % bentonite was found to be around 4 %. The corresponding TGA peak at around 502 °C is a clear indication of weight loss occurred due to dehydroxylation of bentonite clay within the composite.

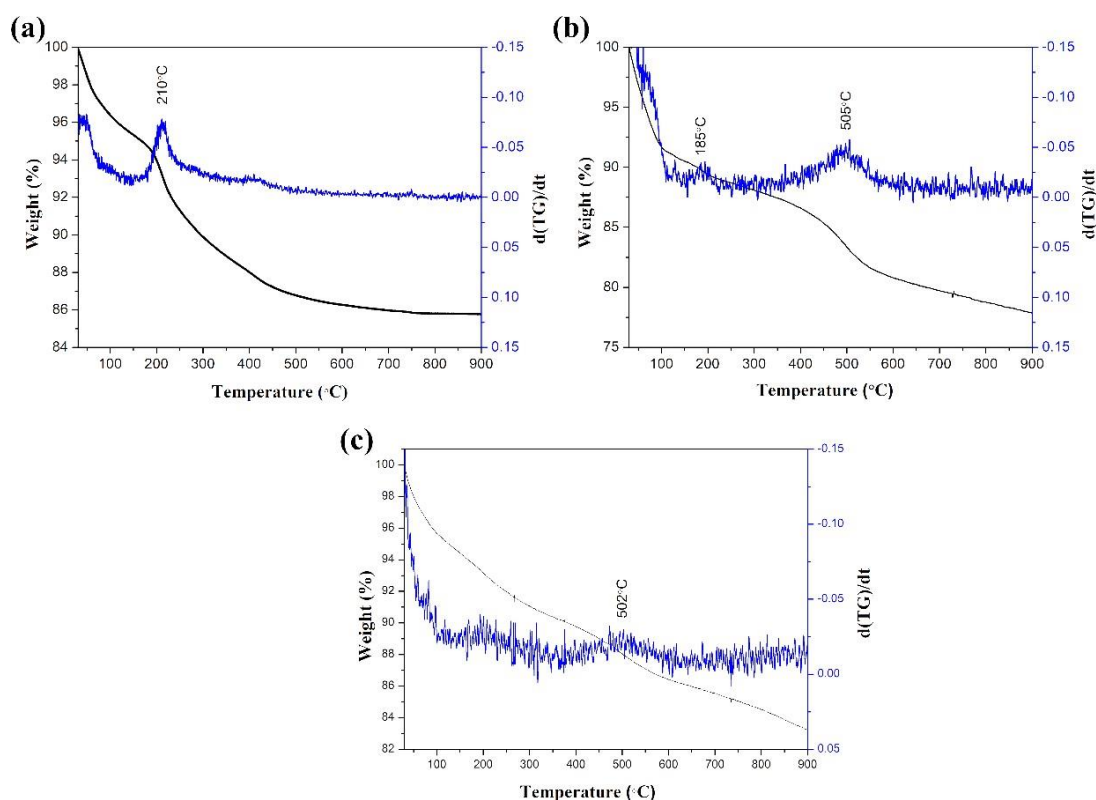


Fig. 7.6. Thermogravimetric analysis of (a) pure HA (b) Bentonite (c) 70 % HA+30 % Bentonite

7.3.3 Morphological analysis

SEM images of HA, bentonite clay and HA-bentonite clay composites in different weight ratios are depicted in Figure 7.7. The dense morphology and well sintered uniaxial grains were observed for sintered HA as shown in Figure 7.7 (a). The morphology of the bentonite clay indicates fiber structure as shown in Figure 7.7 (b) (Kawatra and Ripke 2001). Figures 7.7 (c)-(f) show the micrographs of HA- clay composites with bentonite addition (10, 20, 30, 40 wt. %) which are sintered at 1100 °C for 2 hours.

However, after incorporation of bentonite clay in HA, rod shaped particles were formed with particle quantity becoming more on increasing the quantity of clay in HA. This clearly confirms the formation of HA-bentonite clay composites.

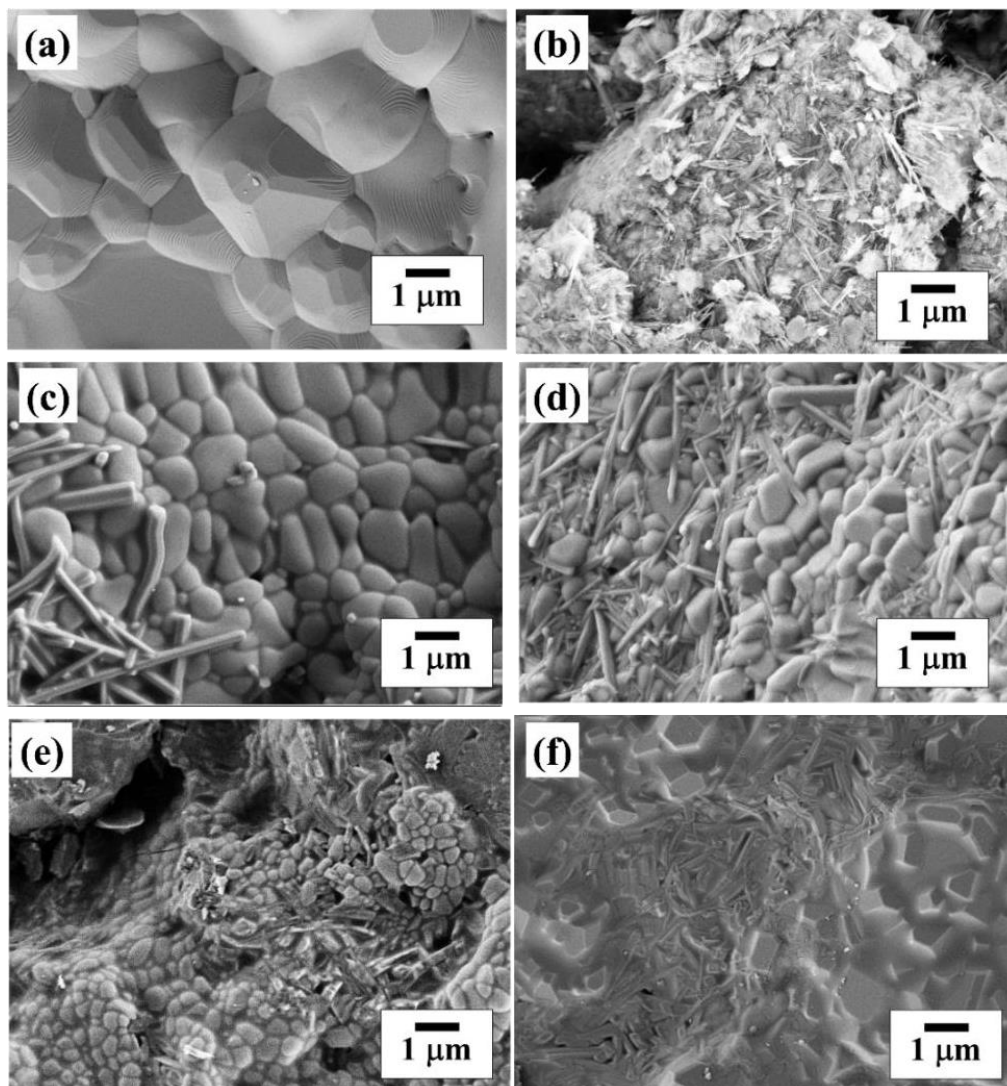


Fig. 7.7. Microstructure of (a) sintered HA (b) Bentonite (c) 90 % HA+10 % Bentonite (d) 80 % HA+20 % Bentonite (e) 70 % HA+30 % Bentonite (f) 60 % HA+40 % Bentonite

7.3.4 Mechanical and physical properties

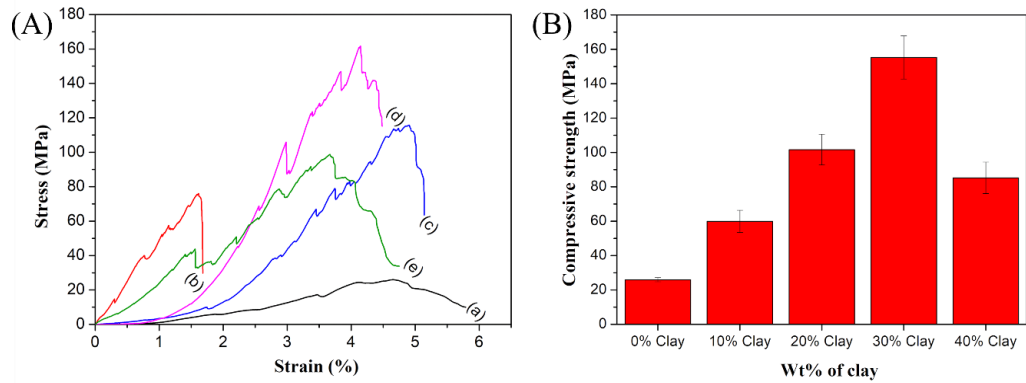


Fig. 7.8 (A) Stress-strain curves of sintered specimens of (a) sintered HA (b) 90% HA+10% Bentonite (c) 80% HA+20% Bentonite (d) 70% HA+30% Bentonite (e) 60%HA+40% Bentonite, (B) Variation of compressive strength with different wt.% of bentonite clay.

Figure 7.8 shows the stress strain curves of sintered HA and various (10 - 40 wt.%) HA-bentonite clay composites (Figure 7.8 b-e). It is observed that addition of bentonite clay component in 90 % HA + 10 % bentonite, 80 % HA+20 % bentonite, 70 % HA+30 % bentonite displayed compressive strength values 59.89 ± 6.4 MPa, 101.64 ± 8.9 MPa, 155.27 ± 12.5 MPa. Further addition of bentonite in 60 % HA+40 % bentonite exhibited a decrease in compressive strength to 85.27 ± 9.2 MPa, as shown in Figure 7.8 (B). This is due to large accumulation of bentonite along the boundaries, which itself acts as a source for cracks, thereby reducing its compressive strength. The high compressive strength with 30% bentonite clay addition was attributed to positive effect of bentonite clay in the deformation of structure of the apatite. From the Hall-Petch equation the compressive strength is related to grain size; as it is inversely proportional to square root of average grain size. Since the grain size is reducing here, the compressive strength is increasing. Moreover, the crack deflection and pull out can increase the strength. The bulk and apparent densities of bare HA, and composites are shown in Figure 7.9 (a). With the addition of bentonite in HA-bentonite clay composites, it is observed that open porosity decreases up to 11.5 % in case of 10 % bentonite clay addition, 10.3 % in case of 20 % bentonite clay addition, 6.9 % in case of 30 % bentonite clay addition and 3.9 % in case of 40 % bentonite clay addition. It is observed that open porosity decreased with increase in bentonite clay addition as shown in Figure 7.9 (b). This might be attributed due to high specific surface area of bentonite.

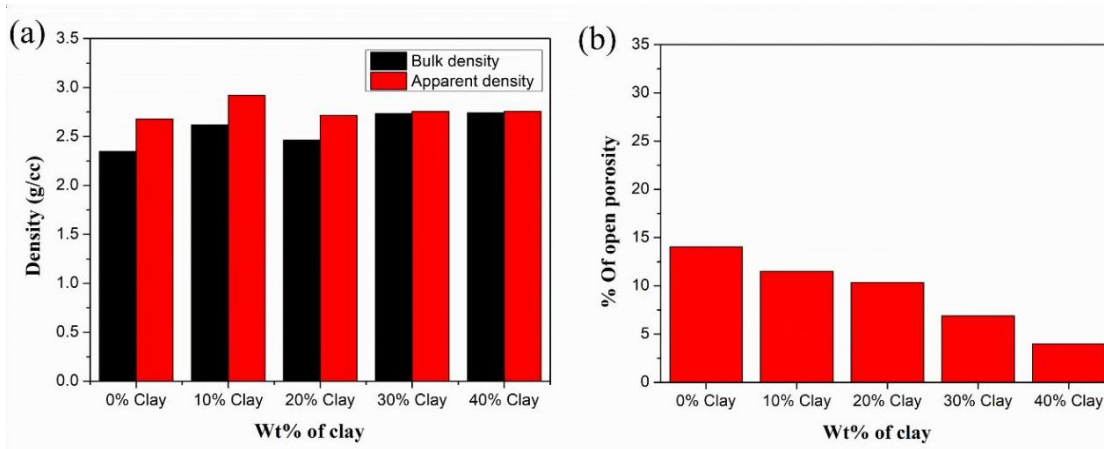


Fig. 7.9. The variation of physical properties of HA-bentonite clay composites with different (0, 10, 20, 30 and 40) wt.% of bentonite clay addition, (a) bulk and apparent densities (b) open porosity

7.4 Conclusion

This study demonstrates the use of prawn shell (*Fenneropenaeus indicus*) exoskeleton biowaste as a calcium-rich raw material for synthesizing hydroxyapatite via a wet chemical synthesis route. Subsequently, composite materials comprising hydroxyapatite and bentonite clay (at 10, 20, 30 and 40 wt.%) are developed using a mechanical mixing method. From XRD, the presence of HA and bentonite within the composite is confirmed from the prominent reflections. FTIR analysis show that the characteristic peaks around 851, 910, 1046, 1119 cm^{-1} confirms the presence of bentonite in HA-bentonite clay composites. From Raman spectra, the characteristic peaks at 961 cm^{-1} in HA-bentonite clay composites indicate Si-O symmetric stretching. DSC and TGA analysis of the HA-bentonite clay composite reveal thermal stability, and the endothermic peak at 475 °C corresponds to the dehydroxylation of the bentonite. Dense and rod like morphology is observed from FESEM in sintered HA and HA-bentonite clay composite, respectively, whereas fibre morphology is observed in bentonite. Uniaxially pressed specimens of HA-clay composite are subjected to sintering in air at 1100°C for a duration of 2 hours to evaluate their physical and mechanical properties. Addition of 30% bentonite to HA enhanced the compressive strength by 485 % in comparison to bare HA. The high compressive strength was attributed to positive effect of bentonite clay in the deformation of structure of the

apatite. The enhanced mechanical properties observed in HA-bentonite clay composites position this material as a promising alternative for bone tissue engineering, specifically targeting cortical bone repair and regeneration.

CHAPTER 8

CONCLUSIONS

In the present thesis, marine biowaste such as prawn (*Fenneropenaeus indicus*) exoskeleton-based calcite was used to synthesize various calcium phosphates namely hydroxyapatite, β -tri calcium phosphate, biphasic calcium phosphates by various methods like wet chemical synthesis and solid-state synthesis. Dense calcium phosphate scaffolds were developed by sintering method and their physical and mechanical properties were evaluated. Secondly, composites were developed by mixing hydroxyapatite with various clays namely kaolinite and bentonite and their physical and mechanical properties were evaluated. Based on the experimental results and analysis, the following conclusions are made.

- The scalable synthesis of biogenic phase-pure HA from prawn exoskeleton was established via wet chemical synthesis method and XRD pattern of HA confirmed the formation of phase-pure HA with hexagonal crystal structure without any secondary phase formation. The Ca/P ratio of obtained HA is 1.65.
- Sintered dense HA at 1100 °C showed compressive strength value of 26.5 MPa with an open porosity of 14 %, which can be a suitable candidate for biomedical applications which include bone repairs and bone filling.
- Biphasic calcium phosphates were synthesised from wet chemical synthesis method. It is found that BCP sintered at 1100 °C exhibited high compressive strength of 56.8 MPa.
- In the X-ray diffraction (XRD) pattern, pellets sintered at 900°C, 1000°C, and 1100°C show the presence of biphasic calcium phosphate (BCP) phases, which are a combination of hydroxyapatite (HA) and β -tricalcium phosphate (β -TCP). A phase change was observed when the sintering temperature increased from 1100°C to 1200°C, resulting in the conversion of β -TCP into α -tricalcium phosphate (α -TCP).
- Phase-pure β -TCP was successfully synthesized using prawn shell biowaste as the raw source, via solid-state reaction method. XRD patterns of β -TCP confirmed the formation of phase-pure β -TCP with rhombohedral crystal

structure and also the elemental analysis at 1100 °C revealed the Ca:P ratio of 1.51 which is equivalent to theoretical ratio of β -TCP (Ca:P =1.5).

- The compressive strength of sintered β -TCP specimens increased with increase in sintering temperature. It is observed that β -TCP scaffolds sintered at 1100 °C exhibited compressive strength value of 6.24 ± 0.4 MPa.
- In β -TCP, it is found that increase in crystallite size with an increase in sintering temperature is observed till 1100 °C and then, it decreases at 1200 °C. This could be due to reconstructive transformation from β -TCP to α -TCP at 1125°C.
- SEM and EDS revealed well-sintered uniaxial grains and the presence of trace elements like Fe, Mg, Si, and Na directly promote the many metabolic processes related to bone metabolism in bone regeneration and repair.
- The significantly higher compressive strength of HA compared to β -TCP can be attributed to its denser morphology. In contrast sintered β -TCP with its inherently higher porosity and lower density resulted in reduced mechanical strength.
- In HA-Kaolin clay composites, FTIR analysis revealed characteristic peaks at 1117 cm^{-1} , 1025 cm^{-1} , and 560 cm^{-1} , confirming the presence of kaolin. Additionally, Raman spectra exhibited characteristic peaks ranging from 615 to 620 cm^{-1} , indicating the translational motion of Si-O-Al groups in kaolin within the composite material.
- DSC and TGA analysis of the HA-clay composite reveal thermal stability, and the endothermic peak at 498 °C, exothermic peak at 716 °C corresponds to the dehydroxylation of the kaolinite and hydroxyapatite respectively.
- Addition of 20% kaolin to HA exhibited compressive strength value of 34.76 ± 6.7 MPa and enhanced the compressive strength by 33.7 % in comparison to bare HA.
- FTIR analysis revealed characteristic peaks at 851 cm^{-1} , 910 cm^{-1} , 1046 cm^{-1} , and 1119 cm^{-1} , confirming the presence of bentonite in the HA-bentonite clay composites. Furthermore, Raman spectra exhibited characteristic peaks at 961 cm^{-1} , indicating Si-O symmetric stretching within the HA-bentonite clay composites.

- Addition of 30 % bentonite to HA exhibited compressive strength value of 155.27 ± 12.5 MPa and enhanced the compressive strength by 485% in comparison to bare HA. The high compressive strength was attributed to positive effect of bentonite clay in the deformation of structure of the apatite.
- The improved mechanical properties observed in HA-kaolin and HA-bentonite clay composites make them promising candidates for bone tissue engineering applications, particularly in the repair and regeneration of trabecular and cortical bones.

8.1 Scope for future work

The result and analysis of the present study aimed at achieving cost-effective synthesis of biogenic hydroxyapatite and its composites from prawn shell biowaste. Biogenic hydroxyapatite (HA) and HA-clay composite dense scaffolds represent a promising novel category of biomaterials, particularly within the field of tissue engineering. Porous scaffolds can be made with tailored porosity in HA-clay composites. *In vitro* cell proliferation and cytotoxicity assays with cultured cells can be conducted with biogenic HA and HA-clay composites.

APPENDIX

Differential scanning calorimetry (DSC) analysis of calcite (CaCO_3) obtained from prawn shell

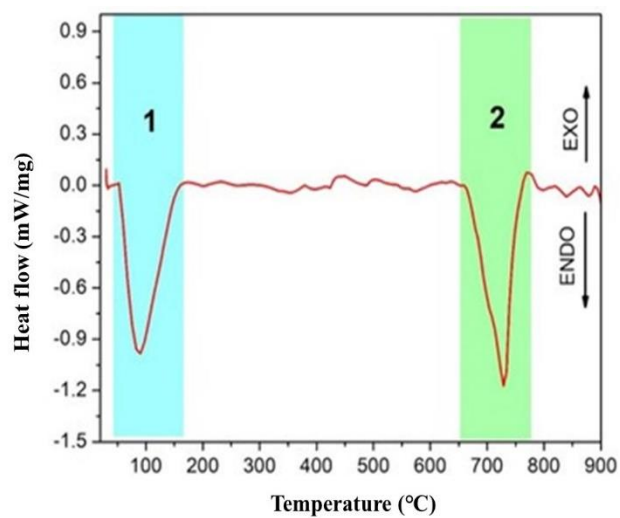


Fig. A-I: DSC analysis of calcite (CaCO_3) obtained from prawn shell
(*Fenneropenaeus indicus*)

REFERENCES

- Abdullah, M. E., Jaya, R. P., Shahafuddin, M. N. A., Yaacob, H., Wan Ibrahim, M. H., Nazri, F. M., Ramli, N. I., and Mohammed, A. A. (2018). "Performance of Kaolin Clay on the Concrete Pavement." *IOP Conf Ser Mater Sci Eng*, 358, 012049.
- Aboudi Mana, S. C., Hanafiah, M. M., and Chowdhury, A. J. K. (2017). "Environmental characteristics of clay and clay-based minerals." *Geology, Ecology, and Landscapes*, 1(3), 155–161.
- Ağaoğullari, D., Kel, D., Gökçe, H., Duman, I., Öveçoğlu, M. L., Akarsubaşı, A. T., Bilgiç, D., and Oktar, F. N. (2012). "Bioceramic Production from Sea Urchins." *Acta Phys Pol A*, 121(1), 23–25.
- Ajmal, A. W., Masood, F., and Yasin, T. (2018). "Influence of sepiolite on thermal, mechanical and biodegradation properties of poly-3-hydroxybutyrate-co-3-hydroxyvalerate nanocomposites." *Appl Clay Sci*, 156, 11–19.
- Akao, M., Aoki, H., Kato, K., and Sato, A. (1982). "Dense polycrystalline beta-tricalcium phosphate for prosthetic applications." *J Mater Sci*, 17(2), 343–346.
- Akram, M., Ahmed, R., Shakir, I., Ibrahim, W. A. W., and Hussain, R. (2014). "Extracting hydroxyapatite and its precursors from natural resources." *J Mater Sci*, 49(4), 1461–1475.
- Albuquerque, R., Queiroga, H., Swearer, S. E., Calado, R., and Leandro, S. M. (2016). "Harvest locations of goose barnacles can be successfully discriminated using trace elemental signatures." *Sci Rep*, 6(1), 27787.
- Alrefeai, M. H., Alhamdan, E. M., Al-Saleh, S., Alqahtani, A. S., Al-Rifaiy, M. Q., Alshiddi, I. F., Farooq, I., Vohra, F., and Abduljabbar, T. (2021). "Application of β -tricalcium phosphate in adhesive dentin bonding." *Polymers (Basel)*, 13(17).
- Al-Sanabani, J. S., Madfa, A. A., and Al-Sanabani, F. A. (2013). "Application of Calcium Phosphate Materials in Dentistry." *Int J Biomater*, 2013, 1–12.
- Al-Shalawi, F. D., Mohamed Ariff, A. H., Jung, D.-W., Mohd Ariffin, M. K. A., Seng Kim, C. L., Brabazon, D., and Al-Osaimi, M. O. (2023). "Biomaterials as Implants in the Orthopedic Field for Regenerative Medicine: Metal versus Synthetic Polymers." *Polymers (Basel)*, 15(12), 2601.
- Alshemary, A. Z., Akram, M., Taha, A., Tezcaner, A., Evis, Z., and Hussain, R. (2018). "Physico-chemical and biological properties of hydroxyapatite extracted from chicken beaks." *Mater Lett*, 215, 169–172.
- Amaral Corrêa, T. H., and França Holanda, J. N. (2019). "Fish bone as a source of raw material for synthesis of calcium phosphate." *Materials Research*, 22.

- Ambre, A. H., Katti, D. R., and Katti, K. S. (2015). "Biomaterialized hydroxyapatite nanoclay composite scaffolds with polycaprolactone for stem cell-based bone tissue engineering." *J Biomed Mater Res A*, 103(6), 2077–2101.
- Amenta, E., King, H. E., Petermann, H., Uskoković, V., Tommasini, S. M., and Macica, C. M. (2018). "Vibrational spectroscopic analysis of hydroxyapatite in HYP mice and individuals with X-linked hypophosphatemia." *Ther Adv Chronic Dis*, 9(12), 268–281.
- Aminatun, Supardi, A., Nisa, Z. I., Hikmawati, D., and Siswanto. (2019). "Synthesis of Nanohydroxyapatite from Cuttlefish Bone (*Sepia* sp.) Using Milling Method." *Int J Biomater*, 2019, 1–6.
- Ana, I. D., Satria, G. A. P., Dewi, A. H., and Ardhani, R. (2018). "Bioceramics for Clinical Application in Regenerative Dentistry." 309–316.
- Anjaneyulu, U., Pattanayak, D. K., and Vijayalakshmi, U. (2016). "Snail Shell Derived Natural Hydroxyapatite: Effects on NIH-3T3 Cells for Orthopedic Applications." *Materials and Manufacturing Processes*, 31(2), 206–216.
- Antoniac, I. V., Lesci, I. G., Blajan, A. I., Vitioanu, G., and Antoniac, A. (2016). "Bioceramics and Biocomposites from Marine Sources." *Key Eng Mater*, 672, 276–292.
- Aoba, T. (1997). "The Effect of Fluoride On Apatite Structure and Growth." *Critical Reviews in Oral Biology & Medicine*, 8(2), 136–153.
- Archunan, M. W., and Petronis, S. (2021). "Bone Grafts in Trauma and Orthopaedics." *Cureus*.
- Awasthi, A., Jadhao, P., and Kumari, K. (2019). "Clay nano-adsorbent: structures, applications and mechanism for water treatment." *SN Appl Sci*, 1(9), 1076.
- Barakat, N. A. M., Khil, M. S., Omran, A. M., Sheikh, F. A., and Kim, H. Y. (2009). "Extraction of pure natural hydroxyapatite from the bovine bones bio waste by three different methods." *J Mater Process Technol*, 209(7), 3408–3415.
- Basu, S., Basu, B. (2019). "Unravelling Doped Biphasic Calcium Phosphate: Synthesis to Application". *ACS Appl. Bio Mater.*, 2, 5263-5297.
- Bee, S.-L., and Hamid, Z. A. A. (2019). "Characterization of chicken bone waste-derived hydroxyapatite and its functionality on chitosan membrane for guided bone regeneration." *Compos B Eng*, 163, 562–573.
- Ben, Y., Zhang, L., Wei, S., Zhou, T., Li, Z., Yang, H., Wong, C., and Chen, H. (2017). "Improved forming performance of β -TCP powders by doping silica for 3D ceramic printing." *Journal of Materials Science: Materials in Electronics*, 28(7), 5391–5397.
- Benkacem, S., Boudeghdegh, K., Zehani, F., Hamidouche, M., and Belhocine, Y. (2021). "Preparation, microstructure studies and mechanical properties of glazes ceramic sanitary ware based on kaolin." *Science of Sintering*, 53(2), 209–221.

- Bharathi, K. K., Moorthy, B., Dara, H. K., Durai, L., and Kim, D. K. (2019). "Electrochemical properties of Na_{0.5}Bi_{0.5}TiO₃ perovskite as an anode material for sodium ion batteries." *J Mater Sci*, 54(20), 13236–13246.
- Bhattacharjee, P., Begam, H., Chanda, A., and Nandi, S. K. (2014). "Animal trial on zinc doped hydroxyapatite: A case study." *Journal of Asian Ceramic Societies*, 2(1), 44–51.
- Bhowmick, A., Banerjee, S. L., Pramanik, N., Jana, P., Mitra, T., Gnanamani, A., Das, M., and Kundu, P. P. (2018). "Organically modified clay supported chitosan/hydroxyapatite-zinc oxide nanocomposites with enhanced mechanical and biological properties for the application in bone tissue engineering." *Int J Biol Macromol*, 106, 11–19.
- Bhowmick, A., Jana, P., Pramanik, N., Mitra, T., Banerjee, S. L., Gnanamani, A., Das, M., and Kundu, P. P. (2016). "Multifunctional zirconium oxide doped chitosan based hybrid nanocomposites as bone tissue engineering materials." *Carbohydr Polym*, 151, 879–888.
- Bian, J. J., Kim, D. W., and Hong, K. S. (2004). "Phase transformation and sintering behavior of Ca₂P₂O₇." *Mater Lett*, 58(3–4), 347–351.
- Bigi, A. (1997). "Isomorphous substitutions in β-tricalcium phosphate: The different effects of zinc and strontium." *J Inorg Biochem*, 66(4), 259–265.
- Bikramjit Basu. (2017). *Biomaterials Science and Tissue Engineering: Principles and Methods*.
- Bogdanoviciene, I., Beganskiene, A., Tõnsuaadu, K., Glaser, J., Meyer, H. J., and Kareiva, A. (2006). "Calcium hydroxyapatite, Ca₁₀(PO₄)₆(OH)₂ ceramics prepared by aqueous sol–gel processing." *Mater Res Bull*, 41(9), 1754–1762.
- Bohner, M., Brunner, T. J., Doebelin, N., Tang, R., and Stark, W. J. (2008). "Effect of thermal treatments on the reactivity of nanosized tricalcium phosphate powders." *J Mater Chem*, 18(37), 4460.
- Bohner, M., Lemaître, J., and Ring, T. A. (1997). "Kinetics of Dissolution of β-Tricalcium Phosphate." *J Colloid Interface Sci*, 190(1), 37–48.
- Bohner, M., Santoni, B. L. G., and Döbelin, N. (2020). "β-tricalcium phosphate for bone substitution: Synthesis and properties." *Acta Biomater*, 113, 23–41.
- Bonifacio, M. A., Cochis, A., Cometa, S., Scalzone, A., Gentile, P., Procino, G., Milano, S., Scalia, A. C., Rimondini, L., and Giglio, E. De. (2020). "Advances in cartilage repair: The influence of inorganic clays to improve mechanical and healing properties of antibacterial Gellan gum-Manuka honey hydrogels." *Materials Science and Engineering: C*, 108, 110444.

Boonyang, U., Chaopanich, P., Wongchaisuwat, A., Senthongkaew, P., and Siripaisarnpipat, S. (2010). "Effect of Phosphate Precursor on the Production of Hydroxyapatite from Crocodile Eggshells." *J Biomim Biomater Tissue Eng*, 5, 31–37.

Bouler, J.-M., Trcant, M., Delcrin, J., Royer, J., Passuti, N., and Daculsi, G. (1996). "Macroporous biphasic calcium phosphate ceramics: Influence of five synthesis parameters on compressive strength." *J Biomed Mater Res*, 32(4), 603–609.

Bow, J.-S., Liou, S.-C., and Chen, S.-Y. (2004). "Structural characterization of room-temperature synthesized nano-sized β -tricalcium phosphate." *Biomaterials*, 25(16), 3155–3161.

Brazete, D., Torres, P. M. C., Abrantes, J. C. C., and Ferreira, J. M. F. (2018). "Influence of the Ca/P ratio and cooling rate on the allotropic $\alpha \leftrightarrow \beta$ -tricalcium phosphate phase transformations." *Ceram Int*, 44(7), 8249–8256.

Brovold, M., Almeida, J. I., Pla-Palacín, I., Sainz-Arnal, P., Sánchez-Romero, N., Rivas, J. J., Almeida, H., Dachary, P. R., Serrano-Aulló, T., Soker, S., and Baptista, P. M. (2018). "Naturally-Derived Biomaterials for Tissue Engineering Applications." *Adv Exp Med Biol*, 1077, 421-449.

Brunner, T. J., Bohner, M., Dora, C., Gerber, C., and Stark, W. J. (2007). "Comparison of amorphous TCP nanoparticles to micron-sized α -TCP as starting materials for calcium phosphate cements." *J Biomed Mater Res B Appl Biomater*, 83(2), 400–407.

Buschmann, J. (2016). "Biomimetic Phosphate Nanocomposites for Bone-Tissue Regeneration." *Nanocomposites for Musculoskeletal Tissue Regeneration*, Elsevier Inc., 285–305.

Cai, Y., Mei, D., Jiang, T., and Yao, J. (2010). "Synthesis of oriented hydroxyapatite crystals: Effect of reaction conditions in the presence or absence of silk sericin." *Mater Lett*, 64(24), 2676–2678.

Canillas, M., Pena, P., Aza, A. H. de, and Rodríguez, M. A. (2017). "Calcium phosphates for biomedical applications." *Boletín de la Sociedad Española de Cerámica y Vidrio*, 56(3), 91–112.

Carbajal, L., Caballero, A., and Sainz, M. A. (2012). "Design and processing of ZnO doped tricalcium phosphate-based materials: Influence of β/α polymorph phase assemblage on microstructural evolution." *J Eur Ceram Soc*, 32(3), 569–577.

Carrodegua, R. G., and Aza, S. De. (2011). " α -Tricalcium phosphate: Synthesis, properties and biomedical applications." *Acta Biomater*, Elsevier Ltd.

Catros, S., Guillemot, F., Lebraud, E., Chanseau, C., Perez, S., Bareille, R., Amédée, J., and Fricain, J. C. (2010). "Physico-chemical and biological properties of a nano-hydroxyapatite powder synthesized at room temperature." *IRBM*, 31(4), 226–233.

- Cavalcanti, G. R. S., Fonseca, M. G., Silva Filho, E. C. da, and Jaber, M. (2019). “Thiabendazole/bentonites hybrids as controlled release systems.” *Colloids Surf B Biointerfaces*, 176, 249–255.
- Chair, H., Labjar, H., and Britel, O. (2017). “Synthesis of β -tricalcium phosphate.” *Morphologie*, 101(334), 120–124.
- Chen, C., Li, J., Huang, Z., Cheng, X., Yu, J., Wang, H., Chi, R., and Hu, Y. (2011). “Phase transformation process and step growth mechanism of hydroxyapatite whiskers under constant impulsion system.” *J Cryst Growth*, 327(1), 154–160.
- Chen, F.-M., and Liu, X. (2016). “Advancing biomaterials of human origin for tissue engineering.” *Prog Polym Sci*, 53, 86–168.
- Chen, J., Wen, Z., Zhong, S., Wang, Z., Wu, J., and Zhang, Q. (2015). “Synthesis of hydroxyapatite nanorods from abalone shells via hydrothermal solid-state conversion.” *Mater Des*, 87, 445–449.
- Chen, Y., and Miao, X. (2004). “Effect of fluorine addition on the corrosion resistance of hydroxyapatite ceramics.” *Ceram Int*, 30(7), 1961–1965.
- Cheng, X., Huang, Z., Li, J., Liu, Y., Chen, C., Chi, R., and Hu, Y. (2010). “Self-Assembled Growth and Pore Size Control of the Bubble-Template Porous Carbonated Hydroxyapatite Microsphere.” *Cryst Growth Des*, 10(3), 1180–1188.
- Chun H J, Park K, Kim C, and Khang G. (2018). *Novel Biomaterials for Regenerative Medicine*. (H. J. Chun, K. Park, C.-H. Kim, and G. Khang, eds.), Singapore: Springer Singapore.
- Chusuei, C. C., Goodman, D. W., Stipdonk, M. J. van, Justes, D. R., and Schweikert, E. A. (1999). “Calcium Phosphate Phase Identification Using XPS and Time-of-Flight Cluster SIMS.” *Anal Chem*, 71(1), 149–153.
- Coelho, T. M., Nogueira, E. S., Steimacher, A., Medina, A. N., Weinand, W. R., Lima, W. M., Baesso, M. L., and Bento, A. C. (2006). “Characterization of natural nanostructured hydroxyapatite obtained from the bones of Brazilian river fish.” *J Appl Phys*, 100(9).
- Cuzzo, R. C., Sartoretto, S. C., Resende, R. F. B., Alves, A. T. N. N., Mavropoulos, E., Prado da Silva, M. H., and Calasans-Maia, M. D. (2020). “Biological evaluation of zinc-containing calcium alginate-hydroxyapatite composite microspheres for bone regeneration.” *J Biomed Mater Res B Appl Biomater*, 108(6), 2610–2620.
- Daculsi, G., Legeros, R. Z., Nery, E., Lynch, K., and Kerebel, B. (1989). “Transformation of biphasic calcium phosphate ceramics in vivo: Ultrastructural and physicochemical characterization.” *J Biomed Mater Res*, 23(8), 883–894.
- Dahlan, K., and Nuzulia, N. A. (2015). “Synthesis of Chicken’s Eggshells-Based β -Tricalcium Phosphate Bioceramics.” *Adv Mat Res*, 1112, 458–461.

Degli Esposti, L., Dotti, A., Adamiano, A., Fabbi, C., Quarta, E., Colombo, P., Catalucci, D., Luca, C. De, and Iafisco, M. (2020). “Calcium Phosphate Nanoparticle Precipitation by a Continuous Flow Process: A Design of Experiment Approach.” *Crystals (Basel)*, 10(10), 953.

Descamps, M., Boilet, L., Moreau, G., Tricoteaux, A., Lu, J., Leriche, A., Lardot, V., and Cambier, F. (2013). “Processing and properties of biphasic calcium phosphates bioceramics obtained by pressureless sintering and hot isostatic pressing.” *J Eur Ceram Soc*, 33(7), 1263–1270.

Destainville, A., Champion, E., Bernache-Assollant, D., and Laborde, E. (2003). “Synthesis, characterization and thermal behavior of apatitic tricalcium phosphate.” *Mater Chem Phys*, 80(1), 269–277.

Díaz-Cuenca, A., Rabadjieva, D., Sezanova, K., Gergulova, R., Ilieva, R., and Tepavitcharova, S. (2022). “Biocompatible calcium phosphate-based ceramics and composites.” *Mater Today Proc*, 61, 1217–1225.

Dickens, B., Schroeder, L. W., and Brown, W. E. (1974). “Crystallographic studies of the role of Mg as a stabilizing impurity in β -Ca₃(PO₄)₂. The crystal structure of pure β -Ca₃(PO₄)₂.” *J Solid State Chem*, 10(3), 232–248.

Dondi, M., Iglesias, C., Dominguez, E., Guarini, G., and Raimondo, M. (2008). “The effect of kaolin properties on their behaviour in ceramic processing as illustrated by a range of kaolins from the Santa Cruz and Chubut Provinces, Patagonia (Argentina).” *Appl Clay Sci*, 40(1–4), 143–158.

Dong, G., Zheng, Y., He, L., Wu, G., and Deng, C. (2016). “The effect of silicon doping on the transformation of amorphous calcium phosphate to silicon-substituted α -tricalcium phosphate by heat treatment.” *Ceram Int*, 42(1), 883–890.

Dora, J. K., Nayak, D., Ghosh, S., Adyam, V., Yedla, N., and Kundu, T. K. (2020). “A facile and green synthesis approach to derive highly stable SiO_x-hard carbon based nanocomposites for use as the anode in lithium-ion batteries.” *Sustain Energy Fuels*, 4(12), 6054–6065.

Dorozhkin, S. (2009). “Calcium Orthophosphates in Nature, Biology and Medicine.” *Materials*, 2(2), 399–498.

Dorozhkin, S. (2013). “Calcium Orthophosphate-Based Bioceramics.” *Materials*, 6(9), 3840–3942.

Dorozhkin, S. V. (2003). “Mechanism of solid-state conversion of non-stoichiometric hydroxyapatite to diphasic calcium phosphate.” *Russian Chemical Bulletin*, 52(11), 2369–2375.

Dorozhkin, S. V. (2011). “Calcium orthophosphates.” *Biomatter*, 1(2), 121–164.

Dorozhkina, E. I., and Dorozhkin, S. V. (2002). “Mechanism of the Solid-State Transformation of a Calcium-Deficient Hydroxyapatite (CDHA) into Biphasic Calcium

- Phosphate (BCP) at Elevated Temperatures.” *Chemistry of Materials*, 14(10), 4267–4272.
- DRISKELL T. D. (1973). “Significance of resorbable bioceramics in the repair of bone defect.” *Proc. Annu. Conf. Eng. Med. Bio.*, 15, 119.
- Ducheyne, P., and Qiu, Q. (1999). “Bioactive ceramics: the effect of surface reactivity on bone formation and bone cell function.” *Biomaterials*, 20(23–24), 2287–2303.
- Duta, L., Oktar, F. N., Stan, G. E., Popescu-Pelin, G., Serban, N., Luculescu, C., and Mihailescu, I. N. (2013). “Novel doped hydroxyapatite thin films obtained by pulsed laser deposition.” *Appl Surf Sci*, 265, 41–49.
- Dwari, R. K., and Mishra, B. K. (2019). “Evaluation of flocculation characteristics of kaolinite dispersion system using guar gum: A green flocculant.” *Int J Min Sci Technol*, 29(5), 745–755.
- Eder, C., Meissner, J., Bretschneider, W., Schildböck, S., and Ogon, M. (2014). “Analysis of a β -TCP bone graft extender explanted during revision surgery after 28 months in vivo.” *European Spine Journal*, 23(S2), 157–160.
- Ehrlich, H., Elkin, Y. N., Artyukov, A. A., Kozlovskaya, E., Stonik, V. A., Safronov, P. P., Kurek, D. V., Bazhenov, V. V., Kummer, K., Vyalikh, D., Molodtsov, S. L., Sivkov, V. N., Born, R., Ruhnnow, M., Meissner, H., and Richter, G. (2010). “The Spines of Sand Dollar & Scaphechinus mirabilis (Agassiz 1863): Analytical and Structural Study.” *Journal of Advanced Microscopy Research*, 5(2), 100–109.
- Eliaz, N., and Metoki, N. (2017). “Calcium Phosphate Bioceramics: A Review of Their History, Structure, Properties, Coating Technologies and Biomedical Applications.” *Materials*, 10(4), 334.
- Elmoubarki, R., Mahjoubi, F. Z., Tounsadi, H., Moustadraf, J., Abdennouri, M., Zouhri, A., Albani, A. El, and Barka, N. (2015). “Adsorption of textile dyes on raw and decanted Moroccan clays: Kinetics, equilibrium and thermodynamics.” *Water Resour Ind*, 9, 16–29.
- Enderle, R., Götz-Neunhoeffler, F., Göbbels, M., Müller, F. A., and Greil, P. (2005). “Influence of magnesium doping on the phase transformation temperature of β -TCP ceramics examined by Rietveld refinement.” *Biomaterials*, 26(17), 3379–3384.
- Ergun, C., Evis, Z., Webster, T. J., and Sahin, F. C. (2011). “Synthesis and microstructural characterization of nano-size calcium phosphates with different stoichiometry.” *Ceram Int*, 37(3), 971–977.
- Erhart, S., Kammerlander, C., El-Attal, R., and Schmoelz, W. (2012). “Is augmentation a possible salvage procedure after lateral migration of the proximal femur nail antirotation?” *Arch Orthop Trauma Surg*, 132(11), 1577–1581.

Evis, Z., and Webster, T. J. (2011). “Nanosize hydroxyapatite: doping with various ions.” *Advances in Applied Ceramics*, 110(5), 311–321.

Fadeeva, I. v., Lazoryak, B. I., Davidova, G. A., Murzakhanov, F. F., Gabbasov, B. F., Petrakova, N. v., Fosca, M., Barinov, S. M., Vadalà, G., Uskoković, V., Zheng, Y., and Rau, J. v. (2021a). “Antibacterial and cell-friendly copper-substituted tricalcium phosphate ceramics for biomedical implant applications.” *Materials Science and Engineering: C*, 129, 112410.

Fadli, A., Akbar, F., Putri, P., Pratiwi, D. I., and Muhara, I. (2014). *Hydroxyapatite Powder Prepared by Low Temperature Hydrothermal Method from Sea Shells*.

Faksawat, K., Sujinnapram, S., Limsuwan, P., Hoonnivathana, E., and Naemchanthara, K. (2015). “Preparation and Characteristic of Hydroxyapatite Synthesized from Cuttlefish Bone by Precipitation Method.” *Adv Mat Res*, 1125, 421–425.

Famery, R., Richard, N., and Boch, P. (1994). “Preparation of α - and β -tricalcium phosphate ceramics, with and without magnesium addition.” *Ceram Int*, 20(5), 327–336.

Faqir, N. M., Shawabkeh, R., Al-Harhi, M., and Wahhab, H. A. (2019). “Fabrication of Geopolymers from Untreated Kaolin Clay for Construction Purposes.” *Geotechnical and Geological Engineering*, 37(1), 129–137.

Farzadi, A., Solati-Hashjin, M., Bakhshi, F., and Aminian, A. (2011). “Synthesis and characterization of hydroxyapatite/ β -tricalcium phosphate nanocomposites using microwave irradiation.” *Ceram Int*, 37(1), 65–71.

Fathi, M. H., Hanifi, A., and Mortazavi, V. (2008). “Preparation and bioactivity evaluation of bone-like hydroxyapatite nanopowder.” *J Mater Process Technol*, 202(1–3), 536–542.

Felício-Fernandes, G., and Laranjeira, M. C. M. (2000). “Calcium phosphate biomaterials from marine algae. Hydrothermal synthesis and characterisation.” *Quim Nova*, 23(4), 441–446.

Fernandez de Grado, G., Keller, L., Idoux-Gillet, Y., Wagner, Q., Musset, A.-M., Benkirane-Jessel, N., Bornert, F., and Offner, D. (2018). “Bone substitutes: a review of their characteristics, clinical use, and perspectives for large bone defects management.” *J Tissue Eng*, 9, 204173141877681.

Firdaus Hussin, M. S., Abdullah, H. Z., Idris, M. I., and Abdul Wahap, M. A. (2022). “Extraction of natural hydroxyapatite for biomedical applications—A review.” *Heliyon*, 8(8), e10356.

Forero-Sossa, P. A., Salazar-Martínez, J. D., Giraldo-Betancur, A. L., Segura-Giraldo, B., and Restrepo-Parra, E. (2021). “Temperature effect in physicochemical and bioactive behavior of biogenic hydroxyapatite obtained from porcine bones.” *Sci Rep*, 11(1), 11069.

- FROST, R. L., and KRISTOF, J. (2004). "Raman and Infrared Spectroscopic Studies of Kaolinite Surfaces Modified by Intercalation." 184–215.
- Frost, R. L., Thu Ha, T., and Kristof, J. (1997). "FT-Raman spectroscopy of the lattice region of kaolinite and its intercalates." *Vib Spectrosc*, 13(2), 175–186.
- Gaharwar, A. K., Cross, L. M., Peak, C. W., Gold, K., Carrow, J. K., Brokesh, A., and Singh, K. A. (2019). "2D Nanoclay for Biomedical Applications: Regenerative Medicine, Therapeutic Delivery, and Additive Manufacturing." *Advanced Materials*, 31(23).
- Galán, E., and Ferrell, R. E. (2013). "Genesis of Clay Minerals." 83–126.
- Galea, L., Alexeev, D., Bohner, M., Doebelin, N., Studart, A. R., Aneziris, C. G., and Graule, T. (2015). "Textured and hierarchically structured calcium phosphate ceramic blocks through hydrothermal treatment." *Biomaterials*, 67, 93–103.
- Galea, L., Bohner, M., Thuring, J., Doebelin, N., Aneziris, C. G., and Graule, T. (2013). "Control of the size, shape and composition of highly uniform, non-agglomerated, sub-micrometer β -tricalcium phosphate and dicalcium phosphate platelets." *Biomaterials*, 34(27), 6388–6401.
- Gallinetti, S., Canal, C., and Ginebra, M. (2014). "Development and Characterization of Biphasic Hydroxyapatite/ β -TCP Cements." *Journal of the American Ceramic Society*, 97(4), 1065–1073.
- Gao, J., Wang, M., Shi, C., Wang, L., Wang, D., and Zhu, Y. (2016). "Synthesis of trace element Si and Sr codoping hydroxyapatite with non-cytotoxicity and enhanced cell proliferation and differentiation." *Biol Trace Elem Res*, 174(1), 208–217.
- Garskaite, E., Gross, K.-A., Yang, S.-W., Yang, T. C.-K., Yang, J.-C., and Kareiva, A. (2014). "Effect of processing conditions on the crystallinity and structure of carbonated calcium hydroxyapatite (CHAp)." *CrystEngComm*, 16(19), 3950.
- Ge, M., Ge, K., Gao, F., Yan, W., Liu, H., Xue, L., Jin, Y., Ma, H., and Zhang, J. (2018). "Biomimetic mineralized strontium-doped hydroxyapatite on porous poly (L-lactic acid) scaffolds for bone defect repair." *Int J Nanomedicine*, Volume 13, 1707–1721.
- Geng, Z., Wang, R., Li, Z., Cui, Z., Zhu, S., Liang, Y., Liu, Y., Huijing, B., Li, X., Huo, Q., Liu, Z., and Yang, X. (2016). "Synthesis, characterization and biological evaluation of strontium/magnesium-co-substituted hydroxyapatite." *J Biomater Appl*, 31(1), 140–151.
- George, P., Abdul Hamid, Z., Abu Bakar@Zakaria, M. Z., Perimal, E. K., and Bharatham, H. (2019). "A Short Review on Cockle Shells as Biomaterials in the Context of Bone Scaffold Fabrication." *Sains Malays*, 48(7), 1539–1545.
- Gergely, G., Wéber, F., Lukács, I., Illés, L., Tóth, A., Horváth, Z., Mihály, J., and Balázs, C. (2010a). "Nano-hydroxyapatite preparation from biogenic raw materials." *Open Chem*, 8(2), 375–381.

Gergely, G., Wéber, F., Lukács, I., Tóth, A. L., Horváth, Z. E., Mihály, J., and Balázs, C. (2010b). "Preparation and characterization of hydroxyapatite from eggshell." *Ceram Int*, 36(2), 803–806.

Ghadiri, M., Chrzanowski, W., and Rohanzadeh, R. (2015). "Biomedical applications of cationic clay minerals." *RSC Adv*, 5(37), 29467–29481.

Ghanaati, S., Barbeck, M., Orth, C., Willershausen, I., Thimm, B. W., Hoffmann, C., Rasic, A., Sader, R. A., Unger, R. E., and Peters, F. (2010). "Influence of β -tricalcium phosphate granule size and morphology on tissue reaction in vivo." *Acta Biomater*, 6(12), 4476–4487.

Gibbs, P. E., and Bryan, G. W. (1972). "A study of strontium, magnesium, and calcium in the environment and exoskeleton of decapod crustaceans, with special reference to *Uca burgersi* on barbuda, west Indies." *J Exp Mar Biol Ecol*, 9(1), 97–110.

Gibson, I. R., Rehman, I., Best, S. M., and Bonfield*, W. (2000). "Characterization of the transformation from calcium-deficient apatite to β -tricalcium phosphate." *J Mater Sci Mater Med*, 11(9), 533–539.

Gomes, G. C., Borghi, F. F., Ospina, R. O., López, E. O., Borges, F. O., and Mello, A. (2017). "Nd: YAG (532 nm) pulsed laser deposition produces crystalline hydroxyapatite thin coatings at room temperature." *Surf Coat Technol*, 329, 174–183.

Gómez Vázquez, N. S., Luque Morales, P. A., Gomez Gutierrez, C. M., Nava Olivas, O. de J., Villarreal Sánchez, R. C., Vilchis Nestor, A. R., and Chinchillas Chinchillas, M. de J. (2020). "Hydroxyapatite Biosynthesis Obtained from Sea Urchin Spines (*Strongylocentrotus purpuratus*): Effect of Synthesis Temperature." *Processes*, 8(4), 486.

Gopi, D., Bhalaji, P. R., Prakash, V. C. A., Ramasamy, A. K., Kavitha, L., and Ferreira, J. M. F. (2011). "An effective and facile synthesis of hydroxyapatite powders using oxalic acid–ethylene glycol mixture." *Current Applied Physics*, 11(3), 590–593.

Grigoraviciute-Puroniene, I., Tsuru, K., Garskaite, E., Stankeviciute, Z., Beganskiene, A., Ishikawa, K., and Kareiva, A. (2017). "A novel wet polymeric precipitation synthesis method for monophasic β -TCP." *Advanced Powder Technology*, 28(9), 2325–2331.

Grimes, W., Luo, Y., McFarland, A., and Mills, D. (2018). "Bi-Functionalized Clay Nanotubes for Anti-Cancer Therapy." *Applied Sciences*, 8(2), 281.

Guerrero-Gironés, J., Alcaina-Lorente, A., Ortiz-Ruiz, C., Ortiz-Ruiz, E., Pecci-Lloret, M. P., Ortiz-Ruiz, A. J., Rodríguez-Lozano, F. J., and Pecci-Lloret, M. R. (2021). "Biocompatibility of a HA/ β -TCP/C Scaffold as a Pulp-Capping Agent for Vital Pulp Treatment: An In Vivo Study in Rat Molars." *Int J Environ Res Public Health*, 18(8), 3936.

- Guinier, A. (1952). “Phase Transformations in Solids” edited by R. Smoluchowski, J. E. Mayer and W. A. Weyl.” *Acta Crystallogr*, 5(6), 857–858.
- Gunduz, O., Sahin, Y. M., Agathopoulos, S., Ben-Nissan, B., and Oktar, F. N. (2014). “A New Method for Fabrication of Nanohydroxyapatite and TCP from the Sea Snail *Cerithium vulgatum*.” *J Nanomater*, 2014, 1–6.
- Guo, F., Aryana, S., Han, Y., and Jiao, Y. (2018). “A Review of the Synthesis and Applications of Polymer–Nanoclay Composites.” *Applied Sciences*, 8(9), 1696.
- Guo, G., Sun, Y., Wang, Z., and Guo, H. (2005). “Preparation of hydroxyapatite nanoparticles by reverse microemulsion.” *Ceram Int*, 31(6), 869–872.
- Guo, Y.-P., Yao, Y., Ning, C.-Q., Guo, Y.-J., and Chu, L.-F. (2011). “Fabrication of mesoporous carbonated hydroxyapatite microspheres by hydrothermal method.” *Mater Lett*, 65(14), 2205–2208.
- Haberko, K., Bućko, M. M., Brzezińska-Miecznik, J., Haberko, M., Mozgawa, W., Panz, T., Pyda, A., and Zarębski, J. (2006). “Natural hydroxyapatite—its behaviour during heat treatment.” *J Eur Ceram Soc*, 26(4–5), 537–542.
- Hadagalli, K., Kumar, R., Mandal, S., and Basu, B. (2020). “Structural, compositional and spectral investigation of prawn exoskeleton nanocomposite: UV protection from mycosporine-like amino acids.” *Mater Chem Phys*, 249.
- Hadagalli, K., Panda, A. K., Mandal, S., and Basu, B. (2019). “Faster Biomineralization and Tailored Mechanical Properties of Marine-Resource-Derived Hydroxyapatite Scaffolds with Tunable Interconnected Porous Architecture.” *ACS Appl Bio Mater*, 2(5), 2171–2184.
- Hammari, L. El, Merroun, H., Coradin, T., Cassaignon, S., Laghzizil, A., and Saoiabi, A. (2007). “Mesoporous hydroxyapatites prepared in ethanol–water media: Structure and surface properties.” *Mater Chem Phys*, 104(2–3), 448–453.
- Han, Y., Li, S., and Wang, X. (2009). “A novel thermolysis method of colloidal protein precursors to prepare hydroxyapatite nanocrystals.” *Crystal Research and Technology*, 44(3), 336–340.
- Han, Y., Li, S., Wang, X., Jia, L., and He, J. (2007). “Preparation of hydroxyapatite rod-like crystals by protein precursor method.” *Mater Res Bull*, 42(6), 1169–1177.
- Hanh, L., Hai, L. van, The Hoang, N., Thi Hong Hanh, D., Minh Hai, L., and Viet Nam, N. (2021). “In vitro biodegradation behavior of biodegradable hydroxyapatite coated AZ31 alloy treated at various pH values.” *J Appl Biomater Funct Mater*, 19, 228080002110100.
- Hansen, M. E., and Illanes, A. (1994). “Applications of crustacean wastes in biotechnology.” *Fisheries Processing*, Boston, MA: Springer US, 174–205.

- Hazar Yoruç, A. B., and İpek, Y. (2012). "Sonochemical Synthesis of Hydroxyapatite Nanoparticles with Different Precursor Reagents." *Acta Phys Pol A*, 121(1), 230–232.
- He, D., Xiao, X. F., Liu, F., and Liu, R. F. (2007). "Hydroxyapatite nanospindles by biomimetic synthesis with chitosan as template." *Materials Science and Technology*, 23(10), 1228–1232.
- Herliansyah, M. K., Hamdi, M., Ide-Ektessabi, A., Wildan, M. W., and Toque, J. A. (2009). "The influence of sintering temperature on the properties of compacted bovine hydroxyapatite." *Materials Science and Engineering: C*, 29(5), 1674–1680.
- Hong, M.-H., Lee, J. H., Jung, H. S., Shin, H., and Shin, H. (2022). "Biom mineralization of bone tissue: calcium phosphate-based inorganics in collagen fibrillar organic matrices." *Biomater Res*, 26(1), 42.
- Horváth, E., Kristóf, J., and Frost, R. L. (2010). "Vibrational Spectroscopy of Intercalated Kaolinites. Part I." *Appl Spectrosc Rev*, 45(2), 130–147.
- Hou, X., Zhang, L., Zhou, Z., Luo, X., Wang, T., Zhao, X., Lu, B., Chen, F., and Zheng, L. (2022). "Calcium Phosphate-Based Biomaterials for Bone Repair." *J Funct Biomater*, 13(4), 187.
- Hsu, C.-K. (2003). "The preparation of biphasic porous calcium phosphate by the mixture of $\text{Ca}(\text{H}_2\text{PO}_4)_2 \cdot \text{H}_2\text{O}$ and CaCO_3 ." *Mater Chem Phys*, 80(2), 409–420.
- Huang, Y.-C., Hsiao, P.-C., and Chai, H.-J. (2011). "Hydroxyapatite extracted from fish scale: Effects on MG63 osteoblast-like cells." *Ceram Int*, 37(6), 1825–1831.
- Hughes, E. A. B., Robinson, T. E., Bassett, D. B., Cox, S. C., and Grover, L. M. (2019). "Critical and diverse roles of phosphates in human bone formation." *J Mater Chem B*, 7(47), 7460–7470.
- Huzum, B., Puha, B., Necoara, R., Gheorghevici, S., Puha, G., Filip, A., Sirbu, P., and Alexa, O. (2021). "Biocompatibility assessment of biomaterials used in orthopedic devices: An overview (Review)." *Exp Ther Med*, 22(5), 1315.
- Iafisco, M., Delgado-López, J. M., Gómez-Morales, J., Hernández-Hernández, M. A., Rodríguez-Ruiz, I., and Roveri, N. (2011). "Formation of calcium phosphates by vapour diffusion in highly concentrated ionic micro-droplets." *Crystal Research and Technology*, 46(8), 841–846.
- Impens, S., Schelstraete, R., Luyten, J., Mullens, S., Thijs, I., Humbeeck, J. van, and Schrooten, J. (2009). "Production and characterisation of porous calcium phosphate structures with controllable hydroxyapatite/ β -tricalcium phosphate ratios." *Advances in Applied Ceramics*, 108(8), 494–500.
- Ishikawa, K., Ducheyne, P., and Radin, S. (1993). "Determination of the Ca/P ratio in calcium-deficient hydroxyapatite using X-ray diffraction analysis." *J Mater Sci Mater Med*, 4(2), 165–168.

- Ishikawa, K., Miyamoto, Y., Yuasa, T., Ito, A., Nagayama, M., and Suzuki, K. (2002). "Fabrication of Zn containing apatite cement and its initial evaluation using human osteoblastic cells." *Biomaterials*, 23(2), 423–428.
- Ismail, H., and Mohamad, H. (2021). "Bioactivity and Biocompatibility Properties of Sustainable Wollastonite Bioceramics from Rice Husk Ash/Rice Straw Ash: A Review." *Materials*, 14(18), 5193.
- Ito, A., Otsuka, M., Kawamura, H., Ikeuchi, M., Ohgushi, H., Sogo, Y., and Ichinose, N. (2005). "Zinc-containing tricalcium phosphate and related materials for promoting bone formation." *Current Applied Physics*, 5(5), 402–406.
- Jain, S., and Datta, M. (2014). "Montmorillonite-PLGA nanocomposites as an oral extended drug delivery vehicle for venlafaxine hydrochloride." *Appl Clay Sci*, 99, 42–47.
- Jarcho, M., Salsbury, R. L., Thomas, M. B., and Doremus, R. H. (1979). "Synthesis and fabrication of β -tricalcium phosphate (whitlockite) ceramics for potential prosthetic applications." *J Mater Sci*, 14(1), 142–150.
- Jaw, K. S. (2006). "Preparation of a biphasic calcium phosphate from $\text{Ca}(\text{H}_2\text{PO}_4)_2 \cdot \text{H}_2\text{O}$ AND CaCO_3 ." *J Therm Anal Calorim*, 83(1), 145–149.
- Jeong, J., Kim, J. H., Shim, J. H., Hwang, N. S., and Heo, C. Y. (2019). "Bioactive calcium phosphate materials and applications in bone regeneration." *Biomater Res*, 23(1), 4.
- Jiang, G. P., Yang, J.F., Gao, J.Q., (2009) "Characterization of porous silicon nitride ceramics using bentonite as binder and sintering additive." *Materials Characterization*, 456-460.
- Jillavenkatesa, A., and Condrate, R. A. (1998). "The infrared and raman spectra of β - and α - tricalcium phosphate ($\text{Ca}_3(\text{PO}_4)_2$)." *Spectroscopy Letters*, 31(8), 1619–1634.
- Jinawath, S., Polchai, D., and Yoshimura, M. (2002). "Low-temperature, hydrothermal transformation of aragonite to hydroxyapatite." *Materials Science and Engineering: C*, 22(1), 35–39.
- Jinlong, N., Zhenxi, Z., and Dazong, J. (2001). "Investigation of phase evolution during the thermochemical synthesis of tricalcium phosphate." *Journal of Materials Synthesis and Processing*, 9(5), 235–240.
- Jitaru, S., Hodisan, I., Timis, L., Lucian, A., and Bud, M. (2016). "THE USE OF BIOCERAMICS IN ENDODONTICS - LITERATURE REVIEW." *Med Pharm Rep*, 89(4), 470–473.
- Johnstone, M. B., Ellis, S., and Mount, A. S. (2008). "Visualization of shell matrix proteins in hemocytes and tissues of the Eastern oyster, *Crassostrea virginica*." *J Exp Zool B Mol Dev Evol*, 310B (3), 227–239.

Jun, Y., Hong, S., and Kong, Y. (2006). "Effect of Co-Precipitation on the Low-Temperature Sintering of Biphasic Calcium Phosphate." *Journal of the American Ceramic Society*, 89(7), 2295–2297.

Jyoth, S. T., Kundu, B., and Mandal, S. (2017). *Low Temperature Development of Nano-Hydroxyapatite from Austromegabalanus psittacus, Star fish and Sea urchin*.

Kalapsazova, M. L., Zhecheva, E. N., Tyuliev, G. T., Nihtianova, D. D., Mihaylov, L., and Stoyanova, R. K. (2017). "Effects of the particle size distribution and of the electrolyte salt on the intercalation properties of P3-Na_{2/3}Ni_{1/2}Mn_{1/2}O₂." *Journal of Physical Chemistry C*, 121(11), 5931–5940.

Kalpana, M., and Nagalakshmi, R. (2023). "Effect of reaction temperature and pH on structural and morphological properties of hydroxyapatite from precipitation method." *Journal of the Indian Chemical Society*, 100(4), 100947.

Kamal, M.M., Mahmud, S., Plabon, I.A., Kader, M.A., Islam, M.N. (2024). "Effects of sintering temperature on the physical, structural, mechanical and antimicrobial properties of extracted hydroxyapatite ceramics from Anabas testudineus bone and head skull for biomedical applications." *Results in Materials*, 22(2024), 100590.

Kanazawa, T., Umegaki, T., and Uchiyama, N. (1982). "Thermal crystallisation of amorphous calcium phosphate to α -tricalcium phosphate." *Journal of Chemical Technology and Biotechnology*, 32(2), 399–406.

Kandori, K., Kuroda, T., Togashi, S., and Katayama, E. (2011). "Preparation of Calcium Hydroxyapatite Nanoparticles Using Microreactor and Their Characteristics of Protein Adsorption." *J Phys Chem B*, 115(4), 653–659.

Kannan, S., Goetz-Neunhoeffler, F., Neubauer, J., and Ferreira, J. M. F. (2007). "Ionic Substitutions in Biphasic Hydroxyapatite and β -Tricalcium Phosphate Mixtures: Structural Analysis by Rietveld Refinement." *Journal of the American Ceramic Society*, 91(1), 1–12.

Kannan, S., Goetz-Neunhoeffler, F., Neubauer, J., and Ferreira, J. M. F. (2009). "Synthesis and Structure Refinement of Zinc-Doped β -Tricalcium Phosphate Powders." *Journal of the American Ceramic Society*, 92(7), 1592–1595.

Katti, K. S., Katti, D. R., and Dash, R. (2008). "Synthesis and characterization of a novel chitosan/montmorillonite/hydroxyapatite nanocomposite for bone tissue engineering." *Biomedical Materials*, 3(3), 034122.

Kel, D., Gökçe, H., Bilgiç, D., Ağaoğulları, D., Duman, I., Öveçoğlu, M. L., Kayali, E. S., Kiyici, I. A., Agathopoulos, S., and Oktar, F. N. (2011). "Production of Natural Bioceramic from Land Snails." *Key Eng Mater*, 493–494, 287–292.

Kim, B.-S., Kang, H. J., Yang, S.-S., and Lee, J. (2014). "Comparison of *in vitro* and *In vivo* bioactivity: cuttlefish-bone-derived hydroxyapatite and synthetic

hydroxyapatite granules as a bone graft substitute.” *Biomedical Materials*, 9(2), 025004.

Kjellin, P., Rajasekharan, A. K., Currie, F., and Handa, P. (2016). “Investigation of calcium phosphate formation from calcium propionate and triethyl phosphate.” *Ceram Int*, 42(12), 14061–14065.

Kłosek-Wawrzyn, E., Małolepszy, J., and Murzyn, P. (2013). “Sintering Behavior of Kaolin with Calcite.” *Procedia Eng*, 57, 572–582.

Koutsopoulos, S., Barlos, K., Gatos, D., and Dalas, E. (2004). “The effect of various Prothymosin α fragments on the crystal growth of hydroxyapatite in aqueous solution.” *J Cryst Growth*, 267(1–2), 306–311.

Kreethawate, L., Tong-On, S., Siriarchavatana, P., and Larпкиattaworn, S. (2014). “Microstructure and Properties of TCP/HA Composite Materials.” *Key Eng Mater*, 608, 259–263.

Krishnan, B., and Mahalingam, S. (2017). “Facile synthesis and antimicrobial activity of manganese oxide/bentonite nanocomposites.” *Research on Chemical Intermediates*, 43(4), 2351–2365.

Kumar, R., and Mohanty, S. (2022). “Hydroxyapatite: A Versatile Bioceramic for Tissue Engineering Application.” *J Inorg Organomet Polym Mater*, 32(12), 4461–4477.

Kutikov, A. B., and Song, J. (2013). “An amphiphilic degradable polymer/hydroxyapatite composite with enhanced handling characteristics promotes osteogenic gene expression in bone marrow stromal cells.” *Acta Biomater*, 9(9), 8354–8364.

Kwaśniewska, A., Chocyk, D., Gładyszewski, G., Borc, J., Świetlicki, M., and Gładyszewska, B. (2020). “The Influence of Kaolin Clay on the Mechanical Properties and Structure of Thermoplastic Starch Films.” *Polymers (Basel)*, 12(1), 73.

La, D. D., Patwari, J. M., Jones, L. A., Antolasic, F., and Bhosale, S. v. (2017). “Fabrication of a GNP/Fe–Mg Binary Oxide Composite for Effective Removal of Arsenic from Aqueous Solution.” *ACS Omega*, 2(1), 218–226.

Lam, M. T., and Wu, J. C. (2012). “Biomaterial applications in cardiovascular tissue repair and regeneration.” *Expert Rev Cardiovasc Ther*, 10(8), 1039–1049.

Lee, E. J., Kasper, F. K., and Mikos, A. G. (2014). “Biomaterials for Tissue Engineering.” *Ann Biomed Eng*, 42(2), 323–337.

Lee, S. J., and Oh, S. H. (2003). “Fabrication of calcium phosphate bioceramics by using eggshell and phosphoric acid.” *Mater Lett*, 57(29), 4570–4574.

- Lee, W., and Fu, Y. (2003). "Effect of montmorillonite on the swelling behavior and drug-release behavior of nanocomposite hydrogels." *J Appl Polym Sci*, 89(13), 3652–3660.
- LeGeros, R. Z., Lin, S., Rohanizadeh, R., Mijares, D., and LeGeros, J. P. (2003). "Biphasic calcium phosphate bioceramics: preparation, properties and applications." *J Mater Sci Mater Med*, 14(3), 201–209.
- Lemma, R., Irassar, E. F., and Rahhal, V. (2015). "Calcined Illitic Clays as Portland Cement Replacements." 269–276.
- Lemos, A. F., Rocha, J. H. G., Quaresma, S. S. F., Kannan, S., Oktar, F. N., Agathopoulos, S., and Ferreira, J. M. F. (2006). "Hydroxyapatite nano-powders produced hydrothermally from nacreous material." *J Eur Ceram Soc*, 26(16), 3639–3646.
- Li B, and Webster T. (2017). *Orthopedic Biomaterials*. (B. Li and T. Webster, eds.), Cham: Springer International Publishing.
- Li, C. (2009). "Crystalline behaviors of hydroxyapatite in the neutralized reaction with different citrate additions." *Powder Technol*, 192(1), 1–5.
- Li, C., and Meng, F. (2008). "Nano-crystalline hydroxyapatite synthesized by neutralization with the assist of citric acid." *Mater Lett*, 62(6–7), 932–934.
- Li, C., Zhao, L., Han, J., Wang, R., Xiong, C., and Xie, X. (2011). "Synthesis of citrate-stabilized hydrocolloids of hydroxyapatite through a novel two-stage method: A possible aggregates–breakdown mechanism of colloid formation." *J Colloid Interface Sci*, 360(2), 341–349.
- Li, G. L., Zhou, C. H., Fiore, S., and Yu, W. H. (2019). "Interactions between microorganisms and clay minerals: New insights and broader applications." *Appl Clay Sci*, 177, 91–113.
- Li, H., Zhu, M., Li, L., and Zhou, C. (2008). "Processing of nanocrystalline hydroxyapatite particles via reverse microemulsions." *J Mater Sci*, 43(1), 384–389.
- Li, X., Ouyang, J., Zhou, Y., and Yang, H. (2015a). "Assembling strategy to synthesize palladium modified kaolin nanocomposites with different morphologies." *Sci Rep*, 5(1), 13763.
- Li, Z., Huang, B., Mai, S., Wu, X., Zhang, H., Qiao, W., Luo, X., and Chen, Z. (2015b). "Effects of fluoridation of porcine hydroxyapatite on osteoblastic activity of human MG63 cells." *Sci Technol Adv Mater*, 16(3), 035006.
- Lima, I. R. de, Alves, G. G., Fernandes, G. V. de O., Dias, E. P., Soares, G. de A., and Granjeiro, J. M. (2010). "Evaluation of the in vivo biocompatibility of hydroxyapatite granules incorporated with zinc ions." *Materials Research*, 13(4), 563–568.

- LIN, F., CHEN, C., CHENG, W., and KUO, T. (2006). "Modified montmorillonite as vector for gene delivery." *Biomaterials*, 27(17), 3333–3338.
- Lin, F.-H., Liao, C.-J., Chen, K.-S., and Sun, J.-S. (1998). "Preparation of high-temperature stabilized β -tricalcium phosphate by heating deficient hydroxyapatite with $\text{Na}_4\text{P}_2\text{O}_7 \cdot 10\text{H}_2\text{O}$ addition." *Biomaterials*, 19(11–12), 1101–1107.
- Liu, B., and Lun, D. (2012). "Current Application of β -tricalcium Phosphate Composites in Orthopaedics." *Orthop Surg*, 4(3), 139–144.
- Liu, C., Ji, X., and Cheng, G. (2007). "Template synthesis and characterization of highly ordered lamellar hydroxyapatite." *Appl Surf Sci*, 253(16), 6840–6843.
- Liu, S., Zhou, H., Liu, H., Ji, H., Fei, W., and Luo, E. (2019). "Fluorine-contained hydroxyapatite suppresses bone resorption through inhibiting osteoclasts differentiation and function in vitro and in vivo." *Cell Prolif*, 52(3).
- Liu, Z., Qu, S., Zheng, X., Xiong, X., Fu, R., Tang, K., Zhong, Z., and Weng, J. (2014). "Effect of polydopamine on the biomimetic mineralization of mussel-inspired calcium phosphate cement in vitro." *Materials Science and Engineering: C*, 44, 44–51.
- Lobo, S. E., and Livingston Arinze, T. (2010). "Biphasic Calcium Phosphate Ceramics for Bone Regeneration and Tissue Engineering Applications." *Materials*, 3(2), 815–826.
- Lukić, M., Stojanović, Z., Škapin, S. D., Maček-Kržmanc, M., Mitrić, M., Marković, S., and Uskoković, D. (2011). "Dense fine-grained biphasic calcium phosphate (BCP) bioceramics designed by two-step sintering." *J Eur Ceram Soc*, 31(1–2), 19–27.
- Lukina, Y., Safronova, T., Smolentsev, D., and Toshev, O. (2023). "Calcium Phosphate Cements as Carriers of Functional Substances for the Treatment of Bone Tissue." *Materials*, 16(11), 4017.
- M. J. Buerger. (1948). "The role of temperature in mineralogy." *American Mineralogist*, 33(3–4), 101–121.
- Macha, I. J., Sevgi Ozyegin, L., Chou, J., Samur, R., Oktar, F. N., and Ben-Nissan, B. (2013). *An Alternative Synthesis Method for Di Calcium Phosphate (Monetite) Powders from Mediterranean Mussel (Mytilus galloprovincialis) Shells. Journal of The Australian Ceramic Society.*
- Maciejewski, M., Brunner, T. J., Loher, S. F., Stark, W. J., and Baiker, A. (2008). "Phase transitions in amorphous calcium phosphates with different Ca/P ratios." *Thermochim Acta*, 468(1–2), 75–80.
- Makarov, C., Gotman, I., Jiang, X., Fuchs, S., Kirkpatrick, C. J., and Gutmanas, E. Y. (2010). "In situ synthesis of calcium phosphate-polycaprolactone nanocomposites with high ceramic volume fractions." *J Mater Sci Mater Med*, 21(6), 1771–1779.

- Malla, K. P., Regmi, S., Nepal, A., Bhattarai, S., Yadav, R. J., Sakurai, S., and Adhikari, R. (2020). "Extraction and Characterization of Novel Natural Hydroxyapatite Bioceramic by Thermal Decomposition of Waste Ostrich Bone." *Int J Biomater*, 2020, 1–10.
- Maloo, L. M., Patel, A., Toshniwal, S. H., and Bagde, A. D. (2022). "Smart Materials Leading to Restorative Dentistry: An Overview." *Cureus*.
- Manjubala, I., and Sivakumar, M. (2001). "In-situ synthesis of biphasic calcium phosphate ceramics using microwave irradiation." *Mater Chem Phys*, 71(3), 272–278.
- Mareri, P., Bastide, S., Binda, N., and Crespy, A. (1998). "Mechanical behaviour of polypropylene composites containing fine mineral filler: Effect of filler surface treatment." *Compos Sci Technol*, 58(5), 747–752.
- Marsh, G. (2008). "Electronics – a major market for reinforced plastics." *Reinforced Plastics*, 52(5), 38–41.
- Martins, M. A., Santos, C., Almeida, M. M., and Costa, M. E. V. (2008). "Hydroxyapatite micro- and nanoparticles: Nucleation and growth mechanisms in the presence of citrate species." *J Colloid Interface Sci*, 318(2), 210–216.
- Matsunaga, K. (2008). "First-principles study of substitutional magnesium and zinc in hydroxyapatite and octacalcium phosphate." *J Chem Phys*, 128(24).
- Meski, S., Ziani, S., Khireddine, H., Yataghane, F., and Ferguene, N. (2011). "Elaboration of the hydroxyapatite with different precursors and application for the retention of the lead." *Water Science and Technology*, 63(10), 2087–2096.
- Mgbemena, C. O., Ibekwe, N. O., Sukumar, R., and Menon, A. R. R. (2013). "Characterization of kaolin intercalates of oleochemicals derived from rubber seed (*Hevea brasiliensis*) and tea seed (*Camelia sinensis*) oils." *J King Saud Univ Sci*, 25(2), 149–155.
- Miculescu, F., Cristina Luta, Constantinescu, A.E., Maidaniuc, A. (2020). "Considerations and influencing parameters in EDS microanalysis of biogenic hydroxyapatite." *J. Funct. Biomater.* 2020, 11, 82.
- Milovac, D., Gamboa-Martínez, T. C., Ivankovic, M., Gallego Ferrer, G., and Ivankovic, H. (2014). "PCL-coated hydroxyapatite scaffold derived from cuttlefish bone: In vitro cell culture studies." *Materials Science and Engineering: C*, 42, 264–272.
- Ming, F. H., Perng, L.H., Chin, T.S., Perng, H.G. (2001) "Phase purity of solgel-derived hydroxyapatite ceramic." *Biomaterials*, 2601-2607
- Mohd Pu'ad, N. A. S., Koshy, P., Abdullah, H. Z., Idris, M. I., and Lee, T. C. (2019). "Syntheses of hydroxyapatite from natural sources." *Heliyon*, 5(5), e01588.

- Mondal, S., Mahata, S., Kundu, S., and Mondal, B. (2010). "Processing of natural resourced hydroxyapatite ceramics from fish scale." *Advances in Applied Ceramics*, 109(4), 234–239.
- Morgan, E. F., Unnikrisnan, G. U., and Hussein, A. I. (2018). "Bone Mechanical Properties in Healthy and Diseased States." *Annu Rev Biomed Eng*, 20(1), 119–143.
- Motameni, A., Dalgic, A. D., Alshemary, A. Z., Keskin, D., and Evis, Z. (2020). "Structural and Biological Analysis of Mesoporous Lanthanum Doped β TCP For Potential Use as Bone Graft Material." *Mater Today Commun*, 23, 101151.
- Mozafari, M., Rabiee, M., Azami, M., and Maleknia, S. (2010). "Biomimetic formation of apatite on the surface of porous gelatin/bioactive glass nanocomposite scaffolds." *Appl Surf Sci*, 257(5), 1740–1749.
- Mullins, W. W. (1956). "Two-Dimensional Motion of Idealized Grain Boundaries." *J Appl Phys*, 27(8), 900–904.
- Murray, H. H. (1991). "Overview — clay mineral applications." *Appl Clay Sci*, 5(5–6), 379–395.
- Murray, H. H. (2000). "Traditional and new applications for kaolin, smectite, and palygorskite: a general overview." *Appl Clay Sci*, 17(5–6), 207–221.
- Murray, H. H. (2006). "Clays." *Ullmann's Encyclopedia of Industrial Chemistry*, Wiley.
- MURUGAN, R., and RAMAKRISHNA, S. (2005). "Development of nanocomposites for bone grafting." *Compos Sci Technol*, 65(15–16), 2385–2406.
- Murugan, R., Sampath Kumar, T. S., and Panduranga Rao, K. (2002). "Fluorinated bovine hydroxyapatite: preparation and characterization." *Mater Lett*, 57(2), 429–433.
- Murugesan, S., and Scheibel, T. (2020). "Copolymer/Clay Nanocomposites for Biomedical Applications." *Adv Funct Mater*, 30(17).
- Nagpure, I. M., Duvenhage, M. M., Pitale, S. S., Ntwaeaborwa, O. M., Terblans, J. J., and Swart, H. C. (2012). "Synthesis, Thermal and Spectroscopic Characterization of Caq2 (Calcium 8-Hydroxyquinoline) Organic Phosphor." *J Fluoresc*, 22(5), 1271–1279.
- Nahar, N., Uddin, M., Gurley, E. S., Jahangir Hossain, M., Sultana, R., and Luby, S. P. (2015). "Cultural and Economic Motivation of Pig Raising Practices in Bangladesh." *Ecohealth*, 12(4), 611–620.
- Nandi, S. K., Kundu, B., Mukherjee, J., Mahato, A., Datta, S., and Balla, V. K. (2015). "Converted marine coral hydroxyapatite implants with growth factors: In vivo bone regeneration." *Materials Science and Engineering: C*, 49, 816–823.

Nasiri-Tabrizi, B., Honarmandi, P., Ebrahimi-Kahrizsangi, R., and Honarmandi, P. (2009). "Synthesis of nanosize single-crystal hydroxyapatite via mechanochemical method." *Mater Lett*, 63(5), 543–546.

Nasruddin, Agustini, S., and Sholeh, M. (2021). "Utilization of Kaolin as a Filling Material for Rubber Solid Tire Compounds for Two-wheeled Electric Scooters." *IOP Conf Ser Mater Sci Eng*, 1143(1), 012010.

Natasha, A. N., Singh, R., Abd Shukor, M. H. Bin, Young, T. C., Purbolaksono, J., Sopyan, I., and Toulouei, R. (2014). "Synthesis and Properties of Biphasic Calcium Phosphate Prepared by Different Methods." *Adv Mat Res*, 970, 20–25.

Nayak, G., Bhuyan, S. K., Bhuyan, R., Sahu, A., Kar, D., and Kuanar, A. (2022). "Marine sources as an unexplored bone tissue reconstruction material -A review." *Egyptian Journal of Basic and Applied Sciences*, 9(1), 477–498.

Nayar, S., and Guha, A. (2009). "Waste utilization for the controlled synthesis of nanosized hydroxyapatite." *Materials Science and Engineering: C*, 29(4), 1326–1329.

Neelakandeswari, N., Sangami, G., and Dharmaraj, N. (2011). "Preparation and Characterization of Nanostructured Hydroxyapatite Using a Biomaterial." *Synthesis and Reactivity in Inorganic, Metal-Organic, and Nano-Metal Chemistry*, 41(5), 513–516.

Nilen, R. W. N., and Richter, P. W. (2008). "The thermal stability of hydroxyapatite in biphasic calcium phosphate ceramics." *J Mater Sci Mater Med*, 19(4), 1693–1702.

Nones, J., Riella, H. G., Trentin, A. G., and Nones, J. (2015). "Effects of bentonite on different cell types: A brief review." *Appl Clay Sci*, 105–106, 225–230.

Obada, D. O., Osseni, S. A., Sina, H., Salami, K. A., Oyedeji, A. N., Dodoo-Arhin, D., Bansod, N. D., Csaki, S., Atta, A. Y., Fasanya, O. O., Sowunmi, A. R., Kuburi, L. S., Dauda, M., Abifarin, J. K., and Dauda, E. T. (2021). "Fabrication of novel kaolin-reinforced hydroxyapatite scaffolds with robust compressive strengths for bone regeneration." *Appl Clay Sci*, 215.

Ofudje, E. A., Akinwunmi, F., Sodiya, E. F., Alayande, S. O., Ogundiran, A. A., and Ajayi, G. O. (2022). "Biogenic preparation of biphasic calcium phosphate powder from natural source of snail shells: bioactivity study." *SN Appl Sci*, 4(5), 144.

Oliveira, A. P., Motisuke, M., Leal, C. v., and Beppu, M. M. (2007). "A Comparative Study between β -TCP Prepared by Solid State Reaction and by Aqueous Solution Precipitation: Application in Cements." *Key Eng Mater*, 361–363, 355–358.

Olivier, F., Rochet, N., Delpeux-Ouldriane, S., Chancolon, J., Sarou-Kanian, V., Fayon, F., and Bonnamy, S. (2020). "Strontium incorporation into biomimetic carbonated calcium-deficient hydroxyapatite coated carbon cloth: Biocompatibility with human primary osteoblasts." *Materials Science and Engineering: C*, 116, 111192.

- Ondro, T., and Trník, A. (2018). “Kinetic behaviour of thermal transformations of kaolinite.” 020033.
- Ooi, C. Y., Hamdi, M., and Ramesh, S. (2007). “Properties of hydroxyapatite produced by annealing of bovine bone.” *Ceram Int*, 33(7), 1171–1177.
- Ortiz, C. H., Aperador, W., and Caicedo, J. C. (2022). “Electrochemical response of (β -TCP and HA) individual coatings and [β -TCP/HA] multilayers coatings exposed to biocompatible environments.” *Surf Coat Technol*, 435.
- Ozyegin, L. S., Sima, F., Ristoscu, C., Kiyici, I. A., Mihailescu, I. N., Meydanoglu, O., Agathopoulos, S., and Oktar, F. N. (2011). “Sea Snail: An Alternative Source for Nano-Bioceramic Production.” *Key Eng Mater*, 493–494, 781–786.
- Pajor, K., Pajchel, L., and Kolmas, J. (2019). “Hydroxyapatite and Fluorapatite in Conservative Dentistry and Oral Implantology—A Review.” *Materials*, 12(17), 2683.
- Palazzo, B., Walsh, D., Iafisco, M., Foresti, E., Bertinetti, L., Martra, G., Bianchi, C. L., Cappelletti, G., and Roveri, N. (2009). “Amino acid synergetic effect on structure, morphology and surface properties of biomimetic apatite nanocrystals.” *Acta Biomater*, 5(4), 1241–1252.
- Pan, Y., and Xiong, D. (2009). “Study on compressive mechanical properties of nanohydroxyapatite reinforced poly (vinyl alcohol) gel composites as biomaterial.” *J Mater Sci Mater Med*, 20(6), 1291–1297.
- Parithimarkalaignan, S., and Padmanabhan, T. V. (2013). “Osseointegration: An Update.” *The Journal of Indian Prosthodontic Society*, 13(1), 2–6.
- Park, H. C., Baek, D. J., Park, Y. M., Yoon, S. Y., and Stevens, R. (2004). “Thermal stability of hydroxyapatite whiskers derived from the hydrolysis of -TCP.” *J Mater Sci*, 39(7), 2531–2534.
- Park, J. H., Jo, S. Bin, Lee, J.-H., Lee, H.-H., Knowles, J. C., and Kim, H.-W. (2023). “Materials and extracellular matrix rigidity highlighted in tissue damages and diseases: Implication for biomaterials design and therapeutic targets.” *Bioact Mater*, 20, 381–403.
- Paul, S., Pal, A., Choudhury, A. R., Bodhak, S., Balla, V. K., Sinha, A., and Das, M. (2017). “Effect of trace elements on the sintering effect of fish scale derived hydroxyapatite and its bioactivity.” *Ceram Int*, 43(17), 15678–15684.
- Peng, B., Xu, Y., Liu, K., Wang, X., and Mulder, F. M. (2017). “High-Performance and Low-Cost Sodium-Ion Anode Based on a Facile Black Phosphorus–Carbon Nanocomposite.” *ChemElectroChem*, 4(9), 2140–2144.
- Peng, H., Vaughan, J., and Vogrin, J. (2018). “The effect of thermal activation of kaolinite on its dissolution and re-precipitation as zeolites in alkaline aluminate solution.” *Appl Clay Sci*, 157, 189–197.

- Piccirillo, C., Pullar, R. C., Costa, E., Santos-Silva, A., E. Pintado, M. M., and L. Castro, P. M. (2015). “Hydroxyapatite-based materials of marine origin: A bioactivity and sintering study.” *Materials Science and Engineering: C*, 51, 309–315.
- Pilliar, R. M., Filiaggi, M. J., Wells, J. D., Grynblas, M. D., and Kandel, R. A. (2001). “Porous calcium polyphosphate scaffolds for bone substitute applications — in vitro characterization.” *Biomaterials*, 22(9), 963–972.
- Pokhrel, S. (2018). “Hydroxyapatite: Preparation, Properties and Its Biomedical Applications.” *Advances in Chemical Engineering and Science*, 08(04), 225–240.
- Posati, T., Benfenati, V., Sagnella, A., Pistone, A., Nocchetti, M., Donnadio, A., Ruani, G., Zamboni, R., and Muccini, M. (2014). “Innovative Multifunctional Silk Fibroin and Hydroxycalcite Nanocomposites: A Synergic Effect of the Components.” *Biomacromolecules*, 15(1), 158–168.
- Prakasam, M., Locs, J., Salma-Ancane, K., Loca, D., Largeteau, A., and Berzina-Cimdina, L. (2015). “Fabrication, Properties and Applications of Dense Hydroxyapatite: A Review.” *J Funct Biomater*, 6(4), 1099–1140.
- Prakasam, M., Locs, J., Salma-Ancane, K., Loca, D., Largeteau, A., and Berzina-Cimdina, L. (2017). “Biodegradable materials and metallic implants-A review.” *J Funct Biomater*, MDPI AG.
- Prekajski, M., Mirković, M., Todorović, B., Matković, A., Marinović-Cincović, M., Luković, J., and Matović, B. (2016). “Ouzo effect—New simple nanoemulsion method for synthesis of strontium hydroxyapatite nanospheres.” *J Eur Ceram Soc*, 36(5), 1293–1298.
- Ptáček, P. (2016). “Introduction to Apatites.” *Apatites and their Synthetic Analogues - Synthesis, Structure, Properties and Applications*, InTech.
- Putri, T. S., Sugiura, Y., Tsuru, K., and Ishikawa, K. (2020). “Fabrication of an interconnected porous β -tricalcium phosphate structure by polyacrylic acid-mediated setting reaction and sintering.” *J. Ceram. Soc. Japan*, 128(8), 555–559.
- Qiu, C., Xiao, X., and Liu, R. (2008). “Biomimetic synthesis of spherical nano-hydroxyapatite in the presence of polyethylene glycol.” *Ceram Int*, 34(7), 1747–1751.
- Qu, T., Verma, D., Alucozai, M., and Tomar, V. (2015). “Influence of interfacial interactions on deformation mechanism and interface viscosity in α -chitin–calcite interfaces.” *Acta Biomater*, 25, 325–338.
- Raabe, D., Sachs, C., and Romano, P. (2005). “The crustacean exoskeleton as an example of a structurally and mechanically graded biological nanocomposite material.” *Acta Mater*, 53(15), 4281–4292.
- Rabiei, M., Palevicius, A., Monshi, A., Nasiri, S., Vilkauskas, A., and Janusas, G. (2020). “Comparing methods for calculating nano crystal size of natural hydroxyapatite using X-ray diffraction.” *Nanomaterials*, 10(9), 1–21.

- Radin, S. R., and Ducheyne, P. (1994). "Effect of bioactive ceramic composition and structure on *in vitro* behavior. III. Porous versus dense ceramics." *J Biomed Mater Res*, 28(11), 1303–1309.
- Ramesh, S., Tan, C.Y., Tolouei, R., Amiriyan, M., Sopyan, I., Teng, W.D. (2012) "Sintering behavior of hydroxyapatite prepared from different routes." *Materials and design*, 34, 148-154.
- Rangavittal, N., Landa-Cnovas, A. R., Gonzalez-Calbet, J. M., and Vallet-Reg, M. (2000). "Structural study and stability of hydroxyapatite and beta-tricalcium phosphate: Two important bioceramics." *J Biomed Mater Res*, 51(4), 660–668.
- RAO, R. R., ROOPA, H. N., and KANNAN, T. S. (1997). "Solid state synthesis and thermal stability of HAP and HAP – β -TCP composite ceramic powders." *J Mater Sci Mater Med*, 8(8), 511–518.
- Ratnayake, J., Gould, M., Ramesh, N., Mucalo, M., and Dias, G. J. (2024). "A Porous Fluoride-Substituted Bovine-Derived Hydroxyapatite Scaffold Constructed for Applications in Bone Tissue Regeneration." *Materials*, 17(5), 1107.
- Raymond, S., Maazouz, Y., Montufar, E. B., Perez, R. A., González, B., Konka, J., Kaiser, J., and Ginebra, M.-P. (2018). "Accelerated hardening of nanotextured 3D-plotted self-setting calcium phosphate inks." *Acta Biomater*, 75, 451–462.
- Raynaud, S., Champion, E., Bernache-Assollant, D., and Thomas, P. (2002). "Calcium phosphate apatites with variable Ca/P atomic ratio I. Synthesis, characterisation and thermal stability of powders." *Biomaterials*, 23(4), 1065–1072.
- Roberts, T. T., and Rosenbaum, A. J. (2012). "Bone grafts, bone substitutes and orthobiologics." *Organogenesis*, 8(4), 114–124.
- Rodrigues, A. I., Reis, R. L., Blitterswijk, C. A. van, Leonor, I. B., and Habibović, P. (2017). "Calcium phosphates and silicon: exploring methods of incorporation." *Biomater Res*, 21(1), 6.
- Rodríguez-Lugo, V., Hernández, J. S., Arellano-Jimenez, Ma. J., Hernández-Tejeda, P. H., and Recillas-Gispert, S. (2005). "Characterization of Hydroxyapatite by Electron Microscopy." *Microscopy and Microanalysis*, 11(6), 516–523.
- Rodríguez-Lugo, V., Salinas-Rodríguez, E., Vázquez, R. A., Alemán, K., and Rivera, A. L. (2017). "Hydroxyapatite synthesis from a starfish and β -tricalcium phosphate using a hydrothermal method." *RSC Adv*, 7(13), 7631–7639.
- Roy, R. K., and Lee, K. (2007). "Biomedical applications of diamond-like carbon coatings: A review." *J Biomed Mater Res B Appl Biomater*, 83B (1), 72–84.
- Ruiz-Aguilar, C., Olivares-Pinto, U., Aguilar-Reyes, E. A., López-Juárez, R., and Alfonso, I. (2018). "Characterization of β -tricalcium phosphate powders synthesized by sol–gel and mechanosynthesis." *Boletín de la Sociedad Española de Cerámica y Vidrio*, 57(5), 213–220.

- Sabree, I., Gough, J. E., and Derby, B. (2015). "Mechanical properties of porous ceramic scaffolds: Influence of internal dimensions." *Ceram Int*, 41(7), 8425–8432.
- Sadat-Shojai, M., Khorasani, M.-T., Dinpanah-Khoshdargi, E., and Jamshidi, A. (2013). "Synthesis methods for nanosized hydroxyapatite with diverse structures." *Acta Biomater*, 9(8), 7591–7621.
- Safronova, T. V., Putlyaev, V. I., Sergeeva, A. I., Kunenkov, E. V., and Tret'yakov, Yu. D. (2009). "Synthesis of nanocrystalline calcium hydroxyapatite from calcium saccharates and ammonium hydrogen phosphate." *Doklady Chemistry*, 426(2), 118–123.
- Safronova, T. V., Selezneva, I. I., Tikhonova, S. A., Kiselev, A. S., Davydova, G. A., Shatalova, T. B., Larionov, D. S., and Rau, J. V. (2020). "Biocompatibility of biphasic α,β -tricalcium phosphate ceramics in vitro." *Bioact Mater*, 5(2), 423–427.
- Sahin, Y. M., Orman, Z., and Yucel, S. (2020). "In vitro studies of α -TCP and β -TCP produced from *Clinocardium ciliatum* seashells." *Journal of the Australian Ceramic Society*, 56(2), 477–488.
- Salgado, A. J., Coutinho, O. P., and Reis, R. L. (2004). "Bone Tissue Engineering: State of the Art and Future Trends." *Macromol Biosci*, 4(8), 743–765.
- Sandomierski, M., Buchwald, Z., and Voelkel, A. (2020). "Calcium montmorillonite and montmorillonite with hydroxyapatite layer as fillers in dental composites with remineralizing potential." *Appl Clay Sci*, 198, 105822.
- Sandomierski, M., Zielińska, M., Adamska, K., Patalas, A., and Voelkel, A. (2022). "Calcium montmorillonite as a potential carrier in the release of bisphosphonates." *New Journal of Chemistry*, 46(7), 3401–3408.
- Sanosh, K. P., Chu, M.-C., Balakrishnan, A., Kim, T. N., and Cho, S.-J. (2010). "Sol-gel synthesis of pure nano sized β -tricalcium phosphate crystalline powders." *Current Applied Physics*, 10(1), 68–71.
- Santhosh, S., and Balasivanandha Prabu, S. (2012). "Characterization of Hydroxyapatite Synthesized from Sea Shells and Electrospin Coating of Hydroxyapatite for Biomedical Applications." *Adv Mat Res*, 584, 435–439.
- Santis, R. de, Gloria, A., and Ambrosio, L. (2017). "Composite materials for hip joint prostheses." *Biomedical Composites*, 237–259.
- Sariibrahimoglu, K., Wolke, J. G. C., Leeuwenburgh, S. C. G., Yubao, L., and Jansen, J. A. (2014). "Injectable biphasic calcium phosphate cements as a potential bone substitute." *J Biomed Mater Res B Appl Biomater*, 102(3), 415–422.
- Schuh, J. C. L., and Funk, K. A. (2019). "Compilation of International Standards and Regulatory Guidance Documents for Evaluation of Biomaterials, Medical Devices, and 3-D Printed and Regenerative Medicine Products." *Toxicol Pathol*, 47(3), 344–357.

- Shahidi, F., Arachchi, J. K. V., and Jeon, Y.-J. (1999). "Food applications of chitin and chitosans." *Trends Food Sci Technol*, 10(2), 37–51.
- Shanthi, P. M. S. L., Mangalaraja, R. V., Uthirakumar, A. P., Velmathi, S., Balasubramanian, T., and Ashok, M. (2010). "Synthesis and characterization of porous shell-like nano hydroxyapatite using Cetrinide as template." *J Colloid Interface Sci*, 350(1), 39–43.
- Sheikhi, A., Afewerki, S., Oklu, R., Gaharwar, A. K., and Khademhosseini, A. (2018). "Effect of ionic strength on shear-thinning nanoclay–polymer composite hydrogels." *Biomater Sci*, 6(8), 2073–2083.
- Shepherd, D. V., Kauppinen, K., Brooks, R. A., and Best, S. M. (2014). "An *in vitro* study into the effect of zinc substituted hydroxyapatite on osteoclast number and activity." *J Biomed Mater Res A*, 102(11), 4136–4141.
- Shi, C., Yuan, Z., Han, F., Zhu, C., and Li, B. (2016). "Polymeric biomaterials for bone regeneration." *Ann Jt*, 1, 27–27.
- Shkilnyy, A., Brandt, J., Manton, A., Paris, O., Schlaad, H., and Taubert, A. (2009). "Calcium Phosphate with a Channel-like Morphology by Polymer Templating." *Chemistry of Materials*, 21(8), 1572–1578.
- Silva, L. M. da, Tavares, D. dos S., and Santos, E. A. dos. (2020). "Isolating the Effects of Mg²⁺, Mn²⁺ and Sr²⁺ Ions on Osteoblast Behavior from those Caused by Hydroxyapatite Transformation." *Materials Research*, 23(2).
- Singh, N. B. (2022). "Clays and Clay Minerals in the Construction Industry." *Minerals*, 12(3), 301.
- Sinusaite, L., Popov, A., Antuzevics, A., Mazeika, K., Baltrunas, D., Yang, J. C., Horng, J. L., Shi, S., Sekino, T., Ishikawa, K., Kareiva, A., and Zarkov, A. (2020). "Fe and Zn co-substituted beta-tricalcium phosphate (β -TCP): Synthesis, structural, magnetic, mechanical and biological properties." *Materials Science and Engineering C*, 112.
- Siva Rama Krishna, D., Siddharthan, A., Seshadri, S. K., and Sampath Kumar, T. S. (2007). "A novel route for synthesis of nanocrystalline hydroxyapatite from eggshell waste." *J Mater Sci Mater Med*, 18(9), 1735–1743.
- Sivakumar, M., Kumar, T. S. S., Shantha, K. L., and Rao, K. P. (1996). "Development of hydroxyapatite derived from Indian coral." *Biomaterials*, 17(17), 1709–1714.
- Skinner, H. C. W., Kittelberger, J. S., and Beebe, R. A. (1975). "Thermal instability in synthetic hydroxyapatites." *J Phys Chem*, 79(19), 2017–2019.
- SL Shanthi, P. M., Ashok, M., Balasubramanian, T., Riyasdeen, A., and Akbarsha, M. A. (2009). "Synthesis and characterization of nano-hydroxyapatite at ambient temperature using cationic surfactant." *Mater Lett*, 63(24–25), 2123–2125.

- Sobczak, A., Kida, A., Kowalski, Z., and Wzorek, Z. (2009). "Evaluation of the biomedical properties of hydroxyapatite obtained from bone waste." *PJCT*, 11(1), 37–43.
- Somrani, S., Rey, C., and Jemal, M. (2003). "Thermal evolution of amorphous tricalcium phosphate." *J Mater Chem*, 13(4), 888–892.
- Song, J., Liu, Y., Zhang, Y., and Jiao, L. (2011). "Mechanical properties of hydroxyapatite ceramics sintered from powders with different morphologies." *Materials Science and Engineering: A*, 528(16–17), 5421–5427.
- Song, S., Dong, L., Zhang, Y., Chen, S., Li, Q., Guo, Y., Deng, S., Si, S., and Xiong, C. (2014). "Lauric acid/intercalated kaolinite as form-stable phase change material for thermal energy storage." *Energy*, 76, 385–389.
- Sossa, P. A. F., Giraldo, B. S., Garcia, B. C. G., Parra, E. R., and Arango, P. J. A. (2018). "Comparative study between natural and synthetic hydroxyapatite: Structural, morphological and bioactivity properties." *Revista Materia*, 23(4).
- Stähli, C., Thüring, J., Galea, L., Tadier, S., Bohner, M., and Döbelin, N. (2016). "Hydrogen-substituted β -tricalcium phosphate synthesized in organic media." *Acta Crystallogr B Struct Sci Cryst Eng Mater*, 72(6), 875–884.
- Stastny, P., Sedlacek, R., Suchy, T., Lukasova, V., Rampichova, M., and Trunec, M. (2019). "Structure degradation and strength changes of sintered calcium phosphate bone scaffolds with different phase structures during simulated biodegradation in vitro." *Materials Science and Engineering: C*, 100, 544–553.
- Stavitskaya, A., Batasheva, S., Vinokurov, V., Fakhrullina, G., Sangarov, V., Lvov, Y., and Fakhrullin, R. (2019). "Antimicrobial Applications of Clay Nanotube-Based Composites." *Nanomaterials*, 9(5), 708.
- Sun, T., Wang, M., Shao, Y., Wang, L., and Zhu, Y. (2018). "The Effect and Osteoblast Signaling Response of Trace Silicon Doping Hydroxyapatite." *Biol Trace Elem Res*, 181(1), 82–94.
- Sun, Y., Guo, G., Wang, Z., and Guo, H. (2006). "Synthesis of single-crystal HAP nanorods." *Ceram Int*, 32(8), 951–954.
- Swain, S. K., and Sarkar, D. (2011). "A comparative study: Hydroxyapatite spherical nanopowders and elongated nanorods." *Ceram Int*, 37(7), 2927–2930.
- Szcześ, A., Hołysz, L., and Chibowski, E. (2017). "Synthesis of hydroxyapatite for biomedical applications." *Adv Colloid Interface Sci*, 249, 321–330.
- Tadjiev, T. R., Chun, S. S., and Kim, S. Y. (2007). "Mechano-Chemical Synthesis of Biphasic Calcium Phosphates with the Various Ratio of HA and β -TCP." *Key Eng Mater*, 330–332, 7–10.

- Tahmasebifar, A., and Evis, Z. (2013). *Structural and mechanical characteristics of hydroxyapatite and tri-calcium phosphates doped with Al³⁺ and F-ions. Article in Journal of Ceramic Processing Research.*
- Tămășan, M., Ozyegin, L. S., Oktar, F. N., and Simon, V. (2013). “Characterization of calcium phosphate powders originating from *Phyllacanthus imperialis* and *Trochidae Infundibulum concavus* marine shells.” *Materials Science and Engineering: C*, 33(5), 2569–2577.
- Tan, C. Y., Yaghoubi, A., Ramesh, S., Adzila, S., Purbolaksono, J., Hassan, M. A., and Kutty, M. G. (2013). “Sintering and mechanical properties of MgO-doped nanocrystalline hydroxyapatite.” *Ceram Int*, 39(8), 8979–8983.
- Tan, J., Chen, M., and Xia, J. (2009). “Water-dispersible hydroxyapatite nanorods synthesized by a facile method.” *Appl Surf Sci*, 255(21), 8774–8779.
- Tang, Z., Li, X., Tan, Y., Fan, H., and Zhang, X. (2018). “The material and biological characteristics of osteoinductive calcium phosphate ceramics.” *Regen Biomater*, 5(1), 43–59.
- Tao, J., Jiang, W., Pan, H., Xu, X., and Tang, R. (2007). “Preparation of large-sized hydroxyapatite single crystals using homogeneous releasing controls.” *J Cryst Growth*, 308(1), 151–158.
- Tao, J., Jiang, W., Zhai, H., Pan, H., Xu, X., and Tang, R. (2008). “Structural Components and Anisotropic Dissolution Behaviors in One Hexagonal Single Crystal of β -Tricalcium Phosphate.” *Cryst Growth Des*, 8(7), 2227–2234.
- Tao, J., Pan, H., Zhai, H., Wang, J., Li, L., Wu, J., Jiang, W., Xu, X., and Tang, R. (2009). “Controls of Tricalcium Phosphate Single-Crystal Formation from Its Amorphous Precursor by Interfacial Energy.” *Cryst Growth Des*, 9(7), 3154–3160.
- TenHuisen, K. (1998). “Formation of calcium-deficient hydroxyapatite from α -tricalcium phosphate.” *Biomaterials*, 19(23), 2209–2217.
- TenHuisen, K. S., and Brown, P. W. (1999). “Phase Evolution during the Formation of α -Tricalcium Phosphate.” *Journal of the American Ceramic Society*, 82(10), 2813–2818.
- Terkula Iber, B., Azman Kasan, N., Torsabo, D., and Wese Omuwa, J. (2022). “A Review of Various Sources of Chitin and Chitosan in Nature.” *J Renew Mater*, 10(4), 1097–1123.
- Tironi, A., Trezza, M. A., Irassar, E. F., and Scian, A. N. (2012). “Thermal Treatment of Kaolin: Effect on the Pozzolanic Activity.” *Procedia Materials Science*, 1, 343–350.
- Todros, S., Todesco, M., and Bagno, A. (2021). “Biomaterials and their biomedical applications: From replacement to regeneration.” *Processes*, MDPI.

Torres, P. M. C., Abrantes, J. C. C., Kaushal, A., Pina, S., Döbelin, N., Bohner, M., and Ferreira, J. M. F. (2016). "Influence of Mg-doping, calcium pyrophosphate impurities and cooling rate on the allotropic $\alpha \leftrightarrow \beta$ -tricalcium phosphate phase transformations." *J Eur Ceram Soc*, 36(3), 817–827.

Torres-Luna, J. A., and Carriazo, J. G. (2019). "Porous aluminosilicic solids obtained by thermal-acid modification of a commercial kaolinite-type natural clay." *Solid State Sci*, 88, 29–35.

Toyoma, T., Nakasima, K., and Yasue, T. (2002). "Hydrothermal Synthesis of Beta - Tricalcium Phosphate from Amorphous Calcium Phosphate." *Journal of the Ceramic Society of Japan*, 110(1284), 716–721.

Tunç, S., Duman, O., and Polat, T. G. (2016). "Effects of montmorillonite on properties of methyl cellulose/carvacrol based active antimicrobial nanocomposites." *Carbohydr Polym*, 150, 259–268.

Vaiani, L., Boccaccio, A., Uva, A. E., Palumbo, G., Piccininni, A., Guglielmi, P., Cantore, S., Santacroce, L., Charitos, I. A., and Ballini, A. (2023). "Ceramic Materials for Biomedical Applications: An Overview on Properties and Fabrication Processes." *J Funct Biomater*, 14(3), 146.

Vani, R., Giriya, E. K., Elayaraja, K., Prakash Parthiban, S., Kesavamoorthy, R., and Narayana Kalkura, S. (2009). "Hydrothermal synthesis of porous triphasic hydroxyapatite/ (α and β) tricalcium phosphate." *J Mater Sci Mater Med*, 20(S1), 43–48.

Vasilakos, S. P., and Tarantili, P. A. (2012). "In vitro drug release studies from organoclay/poly (dimethyl siloxane) nanocomposite matrices." *J Biomed Mater Res B Appl Biomater*, 100B (7), 1899–1910.

Vecbiskena, L., Gross, K. A., Riekstina, U., and Yang, T. C.-K. (2015). "Crystallized nano-sized alpha-tricalcium phosphate from amorphous calcium phosphate: microstructure, cementation and cell response." *Biomedical Materials*, 10(2), 025009.

Vecchio, K. S., Zhang, X., Massie, J. B., Wang, M., and Kim, C. W. (2007). "Conversion of bulk seashells to biocompatible hydroxyapatite for bone implants." *Acta Biomater*, 3(6), 910–918.

Veljović, Dj., Palcevskis, E., Dindune, A., Putić, S., Balać, I., Petrović, R., and Janačković, Dj. (2010a). "Microwave sintering improves the mechanical properties of biphasic calcium phosphates from hydroxyapatite microspheres produced from hydrothermal processing." *J Mater Sci*, 45(12), 3175–3183.

Veljović, Dj., Zalite, I., Palcevskis, E., Smiciklas, I., Petrović, R., and Janačković, Dj. (2010b). "Microwave sintering of fine-grained HAP and HAP/TCP bioceramics." *Ceram Int*, 36(2), 595–603.

- Venkatesan, J., and Anil, S. (2021). "Hydroxyapatite Derived from Marine Resources and their Potential Biomedical Applications." *Biotechnology and Bioprocess Engineering*, Korean Society for Biotechnology and Bioengineering.
- Venkatesan, J., Qian, Z. J., Ryu, B., Thomas, N. V., and Kim, S. K. (2011). "A comparative study of thermal calcination and an alkaline hydrolysis method in the isolation of hydroxyapatite from *Thunnus obesus* bone." *Biomedical Materials*, 6(3), 035003.
- Venkatesan, J., Rekha, P. D., Anil, S., Bhatnagar, I., Sudha, P. N., Dechsakulwatana, C., Kim, S.-K., and Shim, M. S. (2018). "Hydroxyapatite from Cuttlefish Bone: Isolation, Characterizations, and Applications." *Biotechnology and Bioprocess Engineering*, 23(4), 383–393.
- Verma, A., and Riaz, U. (2018). "Sonolytically intercalated poly (anisidine-co-toluidine)/bentonite nanocomposites: pH responsive drug release characteristics." *J Drug Deliv Sci Technol*, 48, 49–58.
- Verwilghen, C., Chkir, M., Rio, S., Nzihou, A., Sharrock, P., and Depelsenaire, G. (2009). "Convenient conversion of calcium carbonate to hydroxyapatite at ambient pressure." *Materials Science and Engineering: C*, 29(3), 771–773.
- Vinoth Kumar, K. C., Jani Subha, T., Ahila, K. G., Ravindran, B., Chang, S. W., Mahmoud, A. H., Mohammed, O. B., and Rathi, M. A. (2021). "Spectral characterization of hydroxyapatite extracted from Black Sumatra and Fighting cock bone samples: A comparative analysis." *Saudi J Biol Sci*, 28(1), 840–846.
- Walsh, P. J., Buchanan, F. J., Dring, M., Maggs, C., Bell, S., and Walker, G. M. (2008). "Low-pressure synthesis and characterisation of hydroxyapatite derived from mineralise red algae." *Chemical Engineering Journal*, 137(1), 173–179.
- Wang, P., Li, C., Gong, H., Jiang, X., Wang, H., and Li, K. (2010). "Effects of synthesis conditions on the morphology of hydroxyapatite nanoparticles produced by wet chemical process." *Powder Technol*, 203(2), 315–321.
- Wang, S., Castro, R., An, X., Song, C., Luo, Y., Shen, M., Tomás, H., Zhu, M., and Shi, X. (2012). "Electrospun laponite-doped poly (lactic-co-glycolic acid) nanofibers for osteogenic differentiation of human mesenchymal stem cells." *J Mater Chem*, 22(44), 23357.
- Wang, W., and Yeung, K. W. K. (2017). "Bone grafts and biomaterials substitutes for bone defect repair: A review." *Bioact Mater*, 2(4), 224–247.
- Webster, T. J., Ergun, C., Doremus, R. H., and Bizios, R. (2002). "Hydroxylapatite with substituted magnesium, zinc, cadmium, and yttrium. II. Mechanisms of osteoblast adhesion." *J Biomed Mater Res*, 59(2), 312–317.

Wei, G., Reichert, J., Bossert, J., and Jandt, K. D. (2008). “Novel Biopolymeric Template for the Nucleation and Growth of Hydroxyapatite Crystals Based on Self-Assembled Fibrinogen Fibrils.” *Biomacromolecules*, 9(11), 3258–3267.

Wu, C., Xue, L.-D., Su, L.-W., Xie, J.-L., Jiang, H., Yu, X.-J., and Liu, H.-M. (2019). “Magnesium promotes the viability and induces differentiation of neural stem cells both *in vitro* and *in vivo*.” *Neurol Res*, 41(3), 208–215.

Wu, S.-C., Hsu, H.-C., Wang, H.-F., Liou, S.-P., and Ho, W.-F. (2023). “Synthesis and Characterization of Nano-Hydroxyapatite Obtained from Eggshell via the Hydrothermal Process and the Precipitation Method.” *Molecules*, 28(13), 4926.

Xu, Y., Wang, D., Yang, L., and Tang, H. (2001). “Hydrothermal conversion of coral into hydroxyapatite.” *Mater Charact*, 47(2), 83–87.

Yamada, Y., Inui, T., Kinoshita, Y., Shigemitsu, Y., Honda, M., Nakano, K., Matsunari, H., Nagaya, M., Nagashima, H., and Aizawa, M. (2019). “Silicon-containing apatite fiber scaffolds with enhanced mechanical property express osteoinductivity and high osteoconductivity.” *Journal of Asian Ceramic Societies*, 7(2), 101–108.

Yang, D. J., Tadjiev, T. R., Kim, J. W., You, C. K., Choi, S. K., Park, K. B., Ryoo, K. H., and Kim, S. Y. (2006). “Comparative Study of the Degradation Behavior of Mechanically Mixed and Chemically Precipitated Biphasic Calcium Phosphates.” *Key Eng Mater*, 309–311, 227–230.

Yang, X., and Wang, Z. (1998). “Synthesis of biphasic ceramics of hydroxyapatite and β -tricalcium phosphate with controlled phase content and porosity.” *J Mater Chem*, 8(10), 2233–2237.

Ye, F., Guo, H., and Zhang, H. (2008). “Biomimetic synthesis of oriented hydroxyapatite mediated by nonionic surfactants.” *Nanotechnology*, 19(24), 245605.

Ye, F., Guo, H., Zhang, H., and He, X. (2010). “Polymeric micelle-templated synthesis of hydroxyapatite hollow nanoparticles for a drug delivery system.” *Acta Biomater*, 6(6), 2212–2218.

Yilmaz, B., Alshemary, A. Z., and Evis, Z. (2019). “Co-doped hydroxyapatites as potential materials for biomedical applications.” *Microchemical Journal*, 144, 443–453.

Yoganand, C. P., Selvarajan, V., Goudouri, O. M., Paraskevopoulos, K. M., Wu, J., and Xue, D. (2011). “Preparation of bovine hydroxyapatite by transferred arc plasma.” *Current Applied Physics*, 11(3), 702–709.

Yu, H., Matthew, H. W., Wooley, P. H., and Yang, S. (2008). “Effect of porosity and pore size on microstructures and mechanical properties of poly- ϵ -caprolactone-hydroxyapatite composites.” *J Biomed Mater Res B Appl Biomater*, 86B(2), 541–547.

Yu, L., and Wei, M. (2021). “Biom mineralization of Collagen-Based Materials for Hard Tissue Repair.” *Int J Mol Sci*, 22(2), 944.

Yu, W., Sun, T.-W., Qi, C., Ding, Z., Zhao, H., Zhao, S., Shi, Z., Zhu, Y.-J., Chen, D., and He, Y. (2017). "Evaluation of zinc-doped mesoporous hydroxyapatite microspheres for the construction of a novel biomimetic scaffold optimized for bone augmentation." *Int J Nanomedicine*, Volume 12, 2293–2306.

Yuan, X., Xu, Y., Lu, T., He, F., Zhang, L., He, Q., and Ye, J. (2022). "Enhancing the bioactivity of hydroxyapatite bioceramic via encapsulating with silica-based bioactive glass sol." *J Mech Behav Biomed Mater*, 128.

Zaharia, A., Sarbu, A., Radu, A.-L., Jankova, K., Daugaard, A., Hvilsted, S., Perrin, F.-X., Teodorescu, M., Munteanu, C., and Fruth-Oprisan, V. (2015). "Preparation and characterization of polyacrylamide-modified kaolinite containing poly [acrylic acid-co-methylene bisacrylamide] nanocomposite hydrogels." *Appl Clay Sci*, 103, 46–54.

Zhang, Y., Liu, Y., and Ji, X. (2011a). "Fabrication of flower-like hydroxyapatite agglomerates with the assistant of bamboo membrane." *Mater Lett*, 65(12), 1982–1985.

Zhang, Y., Liu, Y., Ji, X., Banks, C. E., and Song, J. (2011b). "Flower-like agglomerates of hydroxyapatite crystals formed on an egg-shell membrane." *Colloids Surf B Biointerfaces*, 82(2), 490–496.

Zhang, Y., and Lu, J. (2008a). "The transformation of single-crystal calcium phosphate ribbon-like fibres to hydroxyapatite spheres assembled from nanorods." *Nanotechnology*, 19(15), 155608.

Zhang, Y., and Lu, J. (2008b). "A Mild and Efficient Biomimetic Synthesis of Rodlike Hydroxyapatite Particles with a High Aspect Ratio Using Polyvinylpyrrolidone as Capping Agent." *Cryst Growth Des*, 8(7), 2101–2107.

Zhang, Y., Lu, J., Wang, J., Yang, S., and Chen, Y. (2009). "Synthesis of nanorod and needle-like hydroxyapatite crystal and role of pH adjustment." *J Cryst Growth*, 311(23–24), 4740–4746.

Zhang, Y., Yokogawa, Y., and Kameyama, T. (2007a). "Bimodal Porous Bi-Phasic Calcium Phosphate Ceramics and Its Dissolution in SBF Solution." *Key Eng Mater*, 330–332, 91–94.

Zhang, Y., Yokogawa, Y., and Kameyama, T. (2007b). "Preparation of Biphasic Calcium Phosphate Porous Ceramics Prepared from Fine Powders with Different Particle Size and its Dissolution Behavior in Simulated Body Fluid." *Key Eng Mater*, 336–338, 1688–1691.

Zhao, H., He, W., Wang, Y., Zhang, X., Li, Z., Yan, S., and Zhou, W. (2008a). "Biomimetic Synthesis and Characterization of Hydroxyapatite Crystal with Low Phase Transformation Temperature." *J Chem Eng Data*, 53(12), 2735–2738.

Zhao, H., He, W., Wang, Y., Zhang, X., Li, Z., Yan, S., Zhou, W., and Wang, G. (2008b). "Biom mineralization of large hydroxyapatite particles using ovalbumin as biosurfactant." *Mater Lett*, 62(20), 3603–3605.

Zhu, G., Hu, Y., Yang, Y., Zhao, R., and Tang, R. (2015). "Solvothermal synthesis of β -tricalcium phosphate porous nanospheres by using organic phosphorus source and their biomedical potentials." *RSC Adv*, 5(30), 23958–23964.

Zhu, R., Yu, R., Yao, J., Wang, D., and Ke, J. (2008). "Morphology control of hydroxyapatite through hydrothermal process." *J Alloys Compd*, 457(1–2), 555–559.

Zivica, V., and Palou, M. T. (2015). "Physico-chemical characterization of thermally treated bentonite." *Compos B Eng*, 68, 436–445.

LIST OF PUBLICATIONS

Perabathula Satish, Ashritha Salian, Komalakrushna Hadagalli, Saumen Mandal, “Preparation and structural characteristics of biphasic calcium phosphates from prawn shell bio-waste”, **Advances in Applied Ceramics**, 122,69-78 (2023). (I.F. 2.2)

Perabathula Satish, Komalakrushna Hadagalli, Lakkimsetti Lakshmi Praveen, Mahin Saif Nowl, Asiful H Seikh, Ibrahim A Alnaser, Hany S Abdo, Saumen Mandal, “Hydroxyapatite–Clay Composite for Bone Tissue Engineering: Effective Utilization of Prawn Exoskeleton Biowaste”, **Inorganics** 11,427 (2023). (I.F. 3.14)

Perabathula Satish, Lakkimsetti Lakshmi Praveen, Vishal Gautam, Komalakrushna Hadagalli, Saumen Mandal, “Effect of temperature on solid state reaction of prawn shell derived phase-pure β -tricalcium phosphate”, **Journal of Materials Engineering and Performance**, (2024) (I.F. 2.3)

Perabathula Satish, Komalakrushna Hadagalli, Mahin Saif Nowl, Rahul Siddeswara, Shankamma Kalikeri, Saumen Mandal, “Enhancing strength properties of hydroxyapatite composites with bentonite clay”, **Transaction of Indian Ceramic Society**. (Under Review)

LIST OF CONFERENCE PRESENTATIONS

Perabathula Satish, Lakkimsetti Lakshmi Praveen, Komalakrushna Hadagalli, Saumen Mandal, “Effect of temperature on solid state reaction of prawn shell derived phase-pure β -tricalcium phosphate”, 4th International Conference on Processing and Characterization of Materials, NIT Rourkela, December, 9 – 11, 2022. [Oral]

Perabathula Satish, Saumen Mandal, “Hydroxyapatite–Clay Composite for Bone Tissue Engineering: Effective Utilization of Prawn Exoskeleton Biowaste”, International Conference on Advances in Minerals, Metals, Materials, Manufacturing and Modelling (ICAM5-2023), NIT Warangal, IN, September 22-23, 2023. [Oral].

BIODATA

Name : Perabathula Satish
Father's Name : Perabathula Venkata swamy naidu
Date of birth : 15th August 1988
Permanent Address : #1-5, Vilasa,
Near American eye hospital,
Ainavilli Mandal, East Godavari Dist.
Andhra Pradesh, India -533577
Mobile : +91-9381793493
E-mail : confidence.satish@gmail.com

Academic qualification:

Bachelor of Technology (B.Tech.) in Mechanical Engineering from B.V.C. Engineering college, Odalarevu, Andhra Pradesh (78.72 % out of 100 %)

Master of Technology (M.Tech.) in Nano Technology from National Institute of Technology Calicut, Kerala (CGPA: 7.88 out 10)